Washington University in St. Louis
Washington University Open Scholarship

All Theses and Dissertations (ETDs)

1-1-2011

Aerosol Synthesis Of Cathode Materials For Li-Ion Batteries

Xiaofeng Zhang
Washington University in St. Louis

Follow this and additional works at: https://openscholarship.wustl.edu/etd

Recommended Citation
Zhang, Xiaofeng, "Aerosol Synthesis Of Cathode Materials For Li-Ion Batteries" (2011). *All Theses and Dissertations (ETDs)*. 674.
https://openscholarship.wustl.edu/etd/674

This Dissertation is brought to you for free and open access by Washington University Open Scholarship. It has been accepted for inclusion in All Theses and Dissertations (ETDs) by an authorized administrator of Washington University Open Scholarship. For more information, please contact digital@wumail.wustl.edu.

WASHINGTON UNIVERSITY IN ST. LOUIS
School of Engineering and Applied Science
Department of Energy, Environmental and Chemical Engineering

Dissertation Examination Committee:
Richard Axelbaum, Chair
Ilias Belharouak
Pratim Biswas
William Buhro
Daren Chen
Venkat Subramanian

AEROSOL SYNTHESIS OF CATHODE MATERIALS FOR LI-ION BATTERIES

by

Xiaofeng Zhang

A dissertation presented to the
Graduate School of Arts and Sciences
of Washington University in partial fulfillment of the
requirements for the degree of

DOCTOR OF PHILOSOPHY

August 2011
Saint Louis, Missouri

ABSTRACT OF THE DISSERTATION

Aerosol Synthesis of Cathode Materials for Li-ion Batteries

by

Xiaofeng Zhang

Doctor of Philosophy in Energy, Environmental and Chemical Engineering

Washington University in St. Louis, 2011

Research Advisor: Professor Richard L. Axelbaum

Rapid advancement of technologies for production of next-generation Li-ion batteries will be critical to address the Nation's need for clean, efficient and secure transportation system and renewable energy storage system. Advancements in materials are believed to be essential to meet the growing demand of high-performance materials for Li-ion batteries, as well as to bring down the battery cost (material cost) to a reasonable level. In the past decade, the primary focus in the Li-ion battery research has been to develop new materials, which are essential to improve the performance of the electrodes in terms of energy density, power density and cycle life. However, no single material has satisfied all the necessary criteria because there is a trade-off between energy and power in Li-ion batteries. Fortunately, by tailoring the nano-scale architectures, some of the "less robust" high-energy materials have yielded superior power density over their bulk materials, and these nanostructured materials have come to the forefront of the battery material research. A typical example is the Li-excess composite materials adopting nanostructured morphology. These materials can attain

nearly twice the capacity of commercial $LiCoO_2$. This high capacity has traditionally been a challenge to bulk composite materials, especially at elevated charge/discharge current density and at low temperature.

Despite rapid advances in material development, to date, less attention has been placed on developing approaches to commercial scale production of materials with nano to micron features. Conventional processes such as solid-state reaction and wet-chemistry processes have notable challenges for large-scale material synthesis of nanostructured materials, including difficulty in controlling particle size, morphology and sometimes stoichiometry. They can also be energy-intensive, and have challenges associated with consistent production of uniform powders at scale-up. Motivated by the above, this work aims to develop new processes that are commercially viable for large-scale production of state-of-the-art battery materials. Aerosol synthesis is a standard industrial method for producing powders with controlled particle size. The materials producing in aerosol processes can have a variety of morphologies, from one-dimensional to three-dimensional structures. Spherical particles are desirable in the Li-ion battery industry because high packing density is required. In this research, spray pyrolysis and flame spray pyrolysis are successfully developed to produce high-quality, spherical cathode materials. These processes have many advantages over conventional processes including: (1) the ability to consistently produce uniform porous spherical particles, (2) low-cost, (3) simplicity, and (4) precise control over particle composition and crystal structure. This research will not only provide a basic understanding of the aerosol process for synthesizing nanostructured cathode materials, but also strategies for industry practice in aerosol processing of state-of-the-art battery materials.

The dissertation includes the following achievements in developing an aerosol approach to synthesis of cathode materials. This work, for the first time, demonstrates the synthesis of spherical-shape spinel cathode powders using a hydrogen diffusion flame. A basic understanding of the relationship between flame temperature and structure, physical and chemical properties of the produced powder, and electrochemical system are provided. In particular, flame-made nanostructured 4 V $LiMn_2O_4$ and 5 V $LiNi_{0.5}Mn_{1.5}O_4$ cathode materials have shown comparable performance to those from conventional processes. A spray pyrolysis was also developed to address the synthetic conditions for synthesizing the integrated layered-layered $x Li_2MnO_3 \cdot (1-x) LiNi_{0.5}Mn_{0.5}O_2$ and layered-spinel $Li_{(1.2-\delta)}Ni_{0.2}Mn_{0.6}O_{(2-\delta/2)}$ composite materials for high-energy Li-ion batteries. The composite materials obtained from spray pyrolysis shared some common morphological characteristics: spherical in shape, meso- to macro porous, polycrystalline, highly uniform inter- and intra-particles. In particular, the layered $Li_{1.2}Ni_{0.2}Mn_{0.6}O_2$ (equivalent to $0.5Li_2MnO_3 \cdot 0.5LiNi_{0.5}Mn_{0.5}O_2$) material displayed the highest capacity (*c.a.* 250 $mAhg^{-1}$) among all cathode materials ever made with spray pyrolysis. Furthermore, the nanostructured composite materials showed electrochemical performance comparable to, and in some aspect better than those materials produced *via* coprecipitation, the standard method of synthesis.

Acknowledgments

I owe my gratitude to all those people who have made this dissertation possible and whom I have been working with that make my work successful. My deepest gratitude is to my advisor Dr. Richard Axelbaum who provided me the opportunity to explore new fields and exciting understandings, and who ignited my passion for academic excellence. His guidance, support and insights, and work ethic tremendously helped in completing this dissertation.

I would like to thank my committee members Dr. Ilias Belharouak, Dr. Pratim Biswas, Dr. William Buhro, Dr. Daren Chen and Dr. Venkat Subramanian for their review of my proposal and this dissertation, as well as providing valuable comments and suggestions. Attending their lectures and my discussions with them have been extremely enjoyable, inspiring and helpful. My sincere thanks are given to Dr. Vincent Battaglia and Honghe Zheng at Lawrence Berkeley National Laboratory, who systematically and patiently trained me on Li-ion battery fabrication and testing. Their efforts and knowledge helped this work proceed smoothly and are gratefully acknowledged. I would also like to thank Dr. Steve Harris at General Motors for sharing his battery knowledge with me at the ECS meetings.

I would like to thank Dr. Tyrone Daulton at the Center for Materials Innovation, Dr. Dong Qin, Dr. Yujie Xiong and Kristy Wendt at the Nano Research Facility and Patty Wurm with the EECE department for their training and assistance on the dedicated instruments and facilities.

I'm grateful to all the members and alumni in the Laboratory for Advanced Combustion & Energy Research and my colleagues in the EECE department. A special thanks to Chad Unrau, Scott Skeen, Ben Kumfer, Jinghun Jiang, Fan Mei, Lin Li, Huijing Fu, Miklos Lengyel and others, their outstanding work ethic motivated me to move forward in this endeavor. Gratitude is also expressed to Melissa Holtmeyer who keeps the lab a safe place to work and

who managed the waste chemicals generated in this research. Thanks to all the department staff for their administrative assistance.

This work was funded in part by the National Science Foundation and the Center for Materials Innovation at Washington University in St. Louis, both of which are gratefully acknowledged. Part of the technology described herein was licensed to Xtend Energy LLC and their efforts to commercialize the technology are gratefully acknowledged.

My very special thanks to my parents whom I owe everything that I am today. Everyday I could sense their unwavering love and support overseas. I would like to thank my wife for her tolerance, patience, understanding and faith in me through these years, who has made my life relaxing and full of joy.

Xiaofeng Zhang

Washington University in St. Louis

August 2011

Dedicated to my parents, Xiurong Ma and Chenglin Zhang
and
my wife, Wan C. Sheu

"The purpose of life is ...
to be useful, to be honorable, to be compassionate,
to have it make some difference
that you have lived and lived well."

- Ralph Waldo Emerson
(1803-1882)

Contents

Abstract ii

Acknowledgments v

Contents ix

List of Tables xii

List of Figures xiii

Preface xix

1 Background 1
- 1.1 Demand for Li-ion Batteries 2
- 1.2 Fundamentals of Li-ion Batteries 4
  - 1.2.1 Reaction Mechanism in Lithium-ion Batteries 4
  - 1.2.2 Electrochemistry of Li-ion Batteries 8
- 1.3 Materials for Li-ion Batteries 12
  - 1.3.1 Anode Materials for Li-ion Batteries 12
  - 1.3.2 Cathode Materials in Li-ion Batteries 14
  - 1.3.3 Summary of Status of Advanced Battery Development 24
- 1.4 Overview of Synthesis Processes for Cathode Materials 25
  - 1.4.1 Solid-State Reactions 25
  - 1.4.2 Wet-Chemistry Processes 27
  - 1.4.3 Aerosol Synthesis 31
- 1.5 Objectives and Dissertation Outline 38
  - 1.5.1 Objectives 38
  - 1.5.2 Dissertation Outline 41

2 Research Methodology 42
- 2.1 Powder Synthesis 43
  - 2.1.1 Spray Pyrolysis 43
  - 2.1.2 Diffusion Flame Pyrolysis 45
- 2.2 Post-Treatment of the As-Synthesize Powders 47
- 2.3 *In-situ* Particle Size Measurements 48
- 2.4 Crystallographic Analysis 49
  - 2.4.1 Powder Diffraction 49
  - 2.4.2 Cell Refinement 51
- 2.5 Morphology Studies 52
- 2.6 Battery Performance Evaluation 53
  - 2.6.1 Cell Fabrication 53

2.6.1 Li-ion Battery Test Protocol 55

3 Flame Synthesis of 4 V Spinel $LiMn_2O_4$ 57
3.1 Precursor Chemistry 60
3.2 Flame Structures 62
3.3 Crystallographic Analysis 65
3.4 Powder Morphology 67
3.5 Battery Performance Test 70
3.5.1 Voltage Profile and Capacity 70
3.5.2 Rater Performance 72
3.6 Summary 74

4 Synthesis of 5 V Spinel-$LiNi_{0.5}Mn_{1.5}O_4$ with Superior Cycle-Life 75
4.1 Flame Structures 77
4.1 Crystallographic Analysis 82
4.2 Powder Morphology 85
4.3 Electrochemical Performance of 5 V Spinel-$LiNi_{0.5}Mn_{1.5}O_4$ 87
4.3.1 Voltage Profile and Capacity 87
4.3.2 Cycle Performance 89
4.3.3 Rate Performance 90
4.4 Summary 92

5 Layered-Layered Li-Ni-Mn-Oxide Composite Materials for High-Energy Li-ion Batteries 94
5.1 Material Synthesis *via* Spray Pyrolysis 97
5.2 Elemental Analysis 98
5.3 Particle Size Distribution 99
5.4 Crystallographic Analysis 100
5.4.1 X-Ray Powder Diffraction 100
5.4.2 Rietveld Cell Refinement 103
5.5 Powder Morphology 106
5.6 Electrochemical Performance 109
5.6.1 Voltage Profile and Capacity 109
5.6.2 Cycle Performance 112
5.6.3 Rate Performance 115
5.7 Annealing Conditions 117
5.8 Summary 122

6 Integrated Layered-Spinel Li-Ni-Mn-Oxide Composite Materials for High-Energy Li-ion Batteries 124
6.1 Material Synthesis *via* Spray Pyrolysis 126
6.2 Elemental Analysis 127
6.3 Particle Size Distribution 128
6.4 Crystallographic Analysis 129
6.4.1 X-Ray Powder Diffraction 129
6.4.2 WPF Cell Refinement 133

6.4.3 Integrated Layered-Spinel Structure 135
6.5 Powder Morphology 138
6.6 Electrochemical Performance 143
6.6.1 Voltage Profile and Capacity 143
6.6.2 Cycle Performance 147
6.6.3 Rate Performance 152
6.7 Summary 154

7 Summary and Recommendations for Future Work 156
7.1 Summary of Results 157
7.1.1 Flame Pyrolysis 158
7.1.1 Spray Pyrolysis 160
7.2 Recommendations for Future Work 163
7.2.1 Flame Pyrolysis 163
7.2.2 Spray Pyrolysis 164

Appendix A Spray Pyrolysis Synthesis of Spinel $LiMn_2O_4$ 166
A.1 Precursor Effects on Particle Morphology 166
A.2 Effects of Reactor Temperature 171
A.3 Particle Size Distribution and Morphology 173
A.4 Electrochemical performance 175

Appendix B Spray Pyrolysis Synthesis of Spinel $LiNi_{0.5}Mn_{1.5}O_4$ 177
B.1 Effects of Reactor Temperature and Annealing Temperature 177
B.2 Electrochemical performance 183

Appendix C Battery Performance Validation at National Laboratories 186

Appendix D Fabrication Procedure for Li-ion Coin Cells 188
D.1 NMP-Based Binder Solution Preparation 188
D.2 Electrode Preparation 191
D.3 Coin Cell Assembly 194

References 198

Curriculum Vitae 212

List of Tables

Table 1.1 Selected Li-ion Battery System Applied for PHEVs. 25

Table 1.2 Precursors and reaction conditions in the solid-state reactions for cathode materials originated by Goodenough *et al*. 26

Table 4.1 Different pyrolysis flames and the crystallographic data of the as-synthesized powders. 82

Table 5.1 ICP-MS analysis of $xLi_2MnO_3 \cdot (1-x)LiNi_{0.5}Mn_{0.5}O_2$ precursor solution ... 99

Table 5.2 ICP-MS elemental analysis of $0.5Li_2MnO_3 \cdot 0.5LiNi_{0.5}Mn_{0.5}O_2$ (or $Li_{1.2}Ni_{0.2}Mn_{0.6}O_2$) precursor and the powders under different heat treatment. 99

Table 5.3 Rietveld cell refinement parameters and results of the $0.5Li_2MnO_3 \cdot 0.5LiNi_{0.5}Mn_{0.5}O_2$ (or $Li_{1.2}Ni_{0.2}Mn_{0.6}O_2$) powder annealed at 800 °C for 2 hr. 105

Table 5.4 Theoretical capacity of the layered composite materials $xLi_2MnO_3 \cdot (1-x)LiNi_{0.5}Mn_{0.5}O_2$ and the corresponding chemical formula in the solid-solution format. 112

Table 6.1 ICP-MS results for the precursor solution and theoretical charge/discharge capacities 128

Table A.1 Physical properties of the precursors. 167

Table A.2 Particle morphology with various precursors. 169

Table C.1 Electrode composition and test condition for flame-made $LiNi_{0.5}Mn_{1.5}O_4$ powder. 186

Table D.1 Example of binder solution composition for $LiMn_2O_4$ 189

Table D.2 Example of binder solution composition for $Li_{1.2}Ni_{0.2}Mn_{0.6}O_2$ 190

Table D.3 Example of cathode slurry composition for $LiMn_2O_4$:PVdF:Carbon = 92:5:3 192

List of Figures

Figure 1.1 A comparison of energy density of different battery technologies (Ref. [1]). 3

Figure 1.2 A schematic of the charge/discharge mechanism of a Li-ion cell. 6

Figure 1.3 A schematic illustration of solid-solution reaction (left) and two-phase reaction (right). 8

Figure 1.4 Discharge profile of current cathode materials. (Source: *Directions for Energy Storage R&D in the Vehicle Technologies Program*, DOE, 2010) 11

Figure 1.5 The 3-D crystal structure of layered $Li[M]O_2$, where M=Co, Ni, Mn. 16

Figure 1.6 The 3-D crystal structure of layered Li_2MnO_3. 18

Figure 1.7 The 3-D crystal structure of spinel $LiMn_2O_4$. 19

Figure 1.8 Open circuit voltage profile of $Li_xMn_2O_4$ (Ref. [40]). 21

Figure 1.9 The 3-D crystal structure of olivine $LiFePO_4$. 23

Figure 1.10 Various powder morphologies from wet-chemistry processes. 28

Figure 1.11 A schematic of coprecipitation process for high-energy $Li_{1.2}Ni_{0.2}Mn_{0.6}O_2$ synthesis (Ref. [37]). 30

Figure 1.12 A schematic of key steps in spray pyrolysis (source: Web Based Aerosol Science and Technology Educational Resources Workshop) 34

Figure 1.13 Typical morphology of cathode powders from spray pyrolysis: (a) spherical shape $LiFePO_4$ as observed by SEM [141]; (b) hollow $LiNi_{0.5}Mn_{1.5}O_4$ as observed by TEM [116]. 35

Figure 1.14 Aggregated morphology of (a) $LiCoO_2$ and (b) $LiMn_2O_4$ powders from FSP processes (Ref. [123, 142]). 36

Figure 2.1 A schematic of the spray pyrolysis system with a two-stage aerosol flow reactor. 44

Figure 2.2 A schematic diagram of experiment system: 1. pressure gauge; 2. flow meter; 3. bubbler; 4. BGI Collison atomizer; 5. burner system; 6.

honeycomb; 7. quartz shield; 8. collection funnel; 9. filter; 10. vacuum pump. 46

Figure 3.1 TGA measurements of the individual precursor $LiNO_3$, $Mn(NO_3)_2 \cdot 4H_2O$, $Ni(NO_3)_2 \cdot 6H_2O$, and their stoichiometric mixture. 62

Figure 3.2 Measured temperature profile as a function of height above burner (HAB). Temperatures are not corrected for radiative heat loss from the thermocouple. 63

Figure 3.3 XRD patterns of the flame-synthesized $LiMn_2O_4$ powder: (a) before annealing and (b) after annealing at 700 °C for 2hr. 66

Figure 3.4 Morphology of the $LiMn_2O_4$: (a) SEM of the powder before annealing; (b) TEM of the powder before annealing; (c) SEM of the powder after annealing; (d) TEM of the powder after annealing at 700 °C for 2hr. (SEM scale bar = 1 μm; TEM scale bar = 100 nm). 68

Figure 3.5 Size distribution of the flame-synthesized $LiMn_2O_4$ powder: (a) before annealing and (b) after annealing at 700 °C for 2 hr. 69

Figure 3.6 Initial charge/discharge curve of the flame-synthesized $LiMn_2O_4$ powder: (a) before annealing and (b) after annealing at 700 °C for 2hr (dash line: charge curve; solid line: discharge curve). 71

Figure 3.7 Rate performance of flame-made $LiMn_2O_4$. 73

Figure 4.1 Images of Flame-A producing the spinel $LiNi_{0.5}Mn_{1.5}O_4$ powder (left) measured flame temperature profile (middle) and flame without precursors (right). Temperature is in Celsius. 79

Figure 4.2 XRD pattern of the as-produced $LiNi_{0.5}Mn_{1.5}O_4$ powder from different flames. 81

Figure 4.3 XRD patterns of the flame-synthesized $LiNi_{0.5}Mn_{1.5}O_4$ powder: (a) as-synthesized; (b) after annealing at 700 °C for 2hr. 84

Figure 4.4 Morphology of the $LiMn_{0.5}Ni_{1.5}O_4$: (a) SEM photo of the powder before annealing; (b) TEM photo of the powder before annealing; (c) SEM photo of the powder after annealing; (d) TEM photo of the powder after annealing. Embedded figure in c is the elemental mapping of the particle surface using SEM-EDX (Red: Mn; Green: Ni). 86

Figure 4.5 First charge/discharge curves of Li/$LiNi_{0.5}Mn_{1.5}O_4$ cell at C/10 rate at 30 °C. Powder for cathode was produced in Flame-A and annealed at 800 °C for 2 hr. 88

Figure 4.6 Cycle performance of Li/$LiNi_{0.5}Mn_{1.5}O_4$ cell at C/10 rate at 30 °C. Powder for cathode was produced in Flame-A and annealed at 800 °C for 2 hr. (Solid circle: discharge capacity; open circle: charge capacity; cross: coulombic efficiency) 90

Figure 4.7 Rate performance of Li/$LiNi_{0.5}Mn_{1.5}O_4$ cell at room temperature. Powder for cathode was produced in Flame-A and annealed at 800 °C for 2 hr. (Solid circle: discharge capacity; open circle: charge capacity; cross: coulombic efficiency) 91

Figure 4.8 Discharge voltage profile of Li/$LiNi_{0.5}Mn_{1.5}O_4$ cell at elevated C-rates. .. 92

Figure 5.1 Particle size distribution of the as-synthesized composite material $xLi_2MnO_3 \cdot (1\text{-}x)LiNi_{0.5}Mn_{0.5}O_2$ as measured using ELPI. 100

Figure 5.2 XRD pattern of as-produced (non-annealed) nanostructured $xLi_2MnO_3 \cdot (1\text{-}x)LiNi_{0.5}Mn_{0.5}O_2$ (where x = 0.3, 0.5 and 0.7) powders from spray pyrolysis. 101

Figure 5.3 XRD pattern of composite material $xLi_2MnO_3 \cdot (1\text{-}x)LiNi_{0.5}Mn_{0.5}O_2$ (x = 0.3, 0.4, 0.5, 0.6 and 0.7) annealed at 800 °C for 2 hr. 103

Figure 5.4 Single-phase Rietveld cell refinement of $0.5Li_2MnO_3 \cdot 0.5LiNi_{0.5}Mn_{0.5}O_2$ (or $Li_{1.2}Ni_{0.2}Mn_{0.6}O_2$) powder annealed at 800 °C for 2 hr. The structure parameter and the refined results are shown in Table 5.3. 104

Figure 5.5 SEM photographs of as-produced (non-annealed) nanostructured $0.5Li_2MnO_3 \cdot 0.5LiNi_{0.5}Mn_{0.5}O_2$ (or simply $Li_{1.2}Ni_{0.2}Mn_{0.6}O_2$) powders from spray pyrolysis. 107

Figure 5.6 Porous morphology of composite materials $xLi_2MnO_3 \cdot (1\text{-}x)LiNi_{0.5}Mn_{0.5}O_2$ as observed by SEM: (a) x=0.3; (b) x=0.5; (c) x=0.7. The powders were annealed at 800 °C for 2 hr. 108

Figure 5.7 Initial charge-discharge voltage profile vs. capacity of the composite materials $xLi_2MnO_3 \cdot (1\text{-}x)LiNi_{0.5}Mn_{0.5}O_2$ (*e.g.,* x=0.3, 0.4, 0.5 and 0.6). The current density is 11.5 mAg^{-1}, with a cut-off voltage between 2.0 and 4.9 V. The test is performed at room temperature, 23°C 111

Figure 5.8 Cycling performance of the composite material $xLi_2MnO_3 \cdot (1\text{-}x)LiNi_{0.5}Mn_{0.5}O_2$ (where x=0.3, 0.4, 0.5 and 0.6). The current density is 23 mAg^{-1}, with a cut-off voltage between 2.0 and 4.8 V. The test is performed at room temperature, 23°C. 114

Figure 5.9 Cycle performance of $0.5Li_2MnO_3 \cdot 0.5LiNi_{0.5}Mn_{0.5}O_2$ (or $Li_{1.2}Ni_{0.2}Mn_{0.6}O_2$) after annealing at 800°C for 2 hr: (a) cycle life at

elevated C-rates; and (b) corresponding voltage profile at elevated C-rates. 116

Figure 5.10 XRD pattern of $0.5Li_2MnO_3 \cdot 0.5LiNi_{0.5}Mn_{0.5}O_2$ (or $Li_{1.2}Ni_{0.2}Mn_{0.6}O_2$) after annealing at 800°C for 2 hr and 10 hr. Arrows indicate the broadening of peaks towards lower degrees (2θ). 118

Figure 5.11 Porous morphology of composite materials $x Li_2MnO_3 \cdot (1-x)LiNi_{0.5}Mn_{0.5}O_2$ preserved after annealing at 800 °C for 10 hr and 2 hr. 119

Figure 5.12 Cycle performance of $0.5Li_2MnO_3 \cdot 0.5LiNi_{0.5}Mn_{0.5}O_2$ (or $Li_{1.2}Ni_{0.2}Mn_{0.6}O_2$) after annealing at 800°C for 2 hr and 10 hr, at 23 mAg^{-1} between 2.0 and 4.8 V. 120

Figure 6.1 Particle size distribution of the as-synthesized composite material $Li_{(1.2-\delta)}Ni_{0.2}Mn_{0.6}O_{(2-\delta/2)}$ as measured using ELPI 129

Figure 6.2 XRD pattern of the $Li_{(1.2-\delta)}Ni_{0.2}Mn_{0.6}O_{(2-\delta/2)}$ (δ=0, 1/20, 1/10) powders after annealing treatment: (a) δ=0; (b) δ =1/20; and (c) δ =1/10. The arrows indicate the broadening of the peaks. Solid circles show the splitting and separation of peaks, indicating the formation of Li_2MnO_3-type structures. 132

Figure 6.3 Stacking of XRD patterns of spinel-$LiNi_{0.5}Mn_{1.5}O_4$, layered $Li_{1.2}Ni_{0.2}Mn_{0.6}O_2$ and layered-spinel $Li_{1.1}Ni_{0.2}Mn_{0.6}O_{1.95}$. 133

Figure 6.4 As-estimated lattice parameters of $Li_{(1.2-\delta)}Ni_{0.2}Mn_{0.6}O_{(2-\delta/2)}$ for different Li-content using WPF method. 134

Figure 6.5 Microstructures of the powders obtained by HR-TEM and FFT: (a) $Li_{1.2}Ni_{0.2}Mn_{0.6}O_2$ (800 °C), and (b) $Li_{1.1}Ni_{0.2}Mn_{0.6}O_{1.95}$ (700 °C). Circles indicate the nano-domains of spinel structure that are integrated with the layered structure. 137

Figure 6.6 SEM photographs of the powders after annealing at 700 °C and 800 °C: (a, b) $Li_{1.2}Ni_{0.2}Mn_{0.6}O_2$; (c, d) $Li_{1.15}Ni_{0.2}Mn_{0.6}O_{1.975}$; and (e, f) $Li_{1.1}Ni_{0.2}Mn_{0.6}O_{1.95}$. The annealing temperature is shown on each photograph. 140

Figure 6.7 TEM photograph of the $Li_{1.2}Ni_{0.2}Mn_{0.6}O_2$ (800 °C) powders: (a) morphology of particle; and (b) a cross-section of the particles sliced using microtome. 142

Figure 6.8 Initial charge/discharge voltage profiles of the cells at a constant current density of 11.5 mAg^{-1} between 2.0 and 4.9 V: (a) $Li_{1.2}Ni_{0.2}Mn_{0.6}O_2$; (b) $Li_{1.15}Ni_{0.2}Mn_{0.6}O_{1.975}$; and (c) $Li_{1.1}Ni_{0.2}Mn_{0.6}O_{1.95}$. (dash line: annealing temperature 700 °C; solid line: annealing temperature at 800 °C) 144

Figure 6.9 Cycling performance of the cells at a constant current density of 23 mAg^{-1} between 2.0 and 4.8 V: (a) $Li_{1.2}Ni_{0.2}Mn_{0.6}O_2$; (b) $Li_{1.15}Ni_{0.2}Mn_{0.6}O_{1.975}$; and (c) $Li_{1.1}Ni_{0.2}Mn_{0.6}O_{1.95}$. (triangles: annealing temperature is 700 °C; circles: annealing temperature is 800 °C).....149

Figure 6.10 Cycling performance of the cells electrochemically activated at a constant current density of 11.5 mAg^{-1} between 2.0 and 4.9 V, and then cycled at 23 mAg^{-1} between 2.0 and 4.8 V: (a) $Li_{1.2}Ni_{0.2}Mn_{0.6}O_2$; (b) $Li_{1.15}Ni_{0.2}Mn_{0.6}O_{1.975}$; and (c) $Li_{1.1}Ni_{0.2}Mn_{0.6}O_{1.95}$. Annealing temperature is 800 °C for 10 hr. 151

Figure 6.11 Rate performance of the cells at elevated current density between 2.0 and 4.9 V: (a) $Li_{1.2}Ni_{0.2}Mn_{0.6}O_2$ (800 °C); and (b) $Li_{1.1}Ni_{0.2}Mn_{0.6}O_{1.95}$ (700 °C). Coulombic efficiency corresponding to each charge/discharge cycle is calculated and plotted, as shown in the figures 153

Figure A.1 Solubility of Li nitrate and acetate in water. 167

Figure A.2 Particle morphology as observed on TEM. Precursor and reactor temperature are listed in Table A1. 170

Figure A.3 XRD patterns of $LiMn_2O_4$ powder synthesized at 600 ºC (bottom), 700 ºC (middle) and 800 ºC (top). 172

Figure A.4 XRD patterns of $LiMn_2O_4$ powders made in the aerosol flow reactor: (a) before annealing and (b) after annealing at 700 °C for 2 hr. 172

Figure A.5 Particle size distribution of $LiMn_2O_4$ from spray pyrolysis. 173

Figure A.6 Morphology of $LiMn_2O_4$ powders made in two-stage flow reactor: (a) before annealing and (b) after annealing at 700 °C for 2 hr. 174

Figure A.7 Initial charge-discharge curves of $LiMn_2O_4$ powders (dash lines: as-synthesized powder; solid line: annealed powder). 175

Figure A.8 Cycling performance of $LiMn_2O_4$ annealed at 700 °C, at C/10 rate. 176

Figure B.1 XRD pattern of as-synthesized $LiNi_{0.5}Mn_{1.5}O_4$ at various temperatures *via* spray pyrolysis. 178

Figure B.2 XRD pattern of $LiNi_{0.5}Mn_{1.5}O_4$ after annealing at 600 °C, 700 °C and 800 °C. Powder is produced at 700 °C *via* spray pyrolysis. 178

Figure B.3 Morphology of $LiNi_{0.5}Mn_{1.5}O_4$ as observed on TEM: (a) as-synthesize powder; (b) annealed at 600 °C for 2 hr; (c) annealed at 800 °C for 2hr. The 600 °C annealed powder shows an identical morphology to the as-synthesized powder. 180

Figure B.4 Figure B.4 TGA analysis of the powders annealed at 600 °C (a) and 800 °C (b). 182

Figure B.5 Discharge voltage profile of electrodes with $LiNi_{0.5}Mn_{1.5}O_{4-\delta}$ (800 °C) and $LiNi_{0.5}Mn_{1.5}O_4$ (600 °C) powders.. 184

Figure B.6 Rate performance of $LiNi_{0.5}Mn_{1.5}O_{4-\delta}$ (800 °C) and $LiNi_{0.5}Mn_{1.5}O_4$ (600 °C) powders. 185

Figure C.1 Charge-discharge voltage profiles of $LiNi_{0.5}Mn_{1.5}O_4$ electrodes assembled at WU and LBNL. 187

Figure D.1 Assembly of a 2032 coin cell. 196

Preface

Energy supplies have become critical to maintain sustainable global development in the 21st century. With the rapidly growing economies and populations there is an increasing global demand for energy, especially crude oil. According to the Energy Information Administration (EIA), the U.S. consumed approximately 19 million barrels of oil per day in 2009, of which over 50% were imported. Early in his presidency, President Obama defined a long-term strategic goal to reduce our dependence on imported oil, and during his 2011 State of the Union Address he put substance to this by setting a goal of putting 1 million electric vehicles (includes plug-in hybrid, hybrid and all electric vehicles) on the road by 2015. Furthermore, it is anticipated that 100 million to 200 million electric vehicles will be deployed by 2030, which would reduce the projected demand for imported oil by approximately 4 million barrels/day.

Furthermore, the consumption of petroleum in transportations leads to the emission of green house gases, which can have adverse effects on global climate. Electric vehicles offer the potential to reduce these effects by introducing vehicles that have zero tailpipe emission; plug-in hybrid and hybrid electric vehicles, to a lesser extent, can reduce these emissions and maximize the efficiency. Developments in U.S. Department of Energy's (DOE's) Vehicle Technologies Program focus on lithium ion based electrochemical energy storage system due to the high theoretical capacity and electrochemical potential. Li-ion battery technology can provide a reliable rechargeable system to meet the demand

for clean and high-efficiency transportation. Aside from the demand of electric-powered vehicles, of particular interest is the electric energy generated from intermittent renewable resources, *e.g.*, solar and wind, which requires electric energy storage with superior cycle life and calendar life to ensure a steady supply of electricity. Germany is the leading country in wind-power utilization; however, in 2006 15% of the energy was lost due to the lack of suitable electrical energy storage. Lithium-ion batteries are projected to provide stationary storage, enabling the effective use of renewable energies.

Regardless of the applications of Li-ion batteries, high performance, long-life, safe and low cost batteries are always desirable. Performance is constrained mainly by energy density and power density at low and high temperatures. Life refers to battery cycle life and calendar life. For example, hybrid electric vehicles require battery packs with an estimated 10-15 year lifetime and a goal of 300,000 cycles. Safety is also critical in that short circuit, thermal runaway and explosions must be prevented. As a commercial product, the materials applied in battery systems should have little and no toxicity. Currently, the cost of Li-based batteries is approximately $800 to $1,000/kWh, a factor of about two to five too high. The high cost is constrained by the raw materials cost, material processing, module packaging and manufacturing cost. Materials account for approximately 30% to 60% of the total cost of a PHEV battery pack, with the cathode sharing *c.a.* 50% of the material cost. The above-mentioned technology challenges and barriers are essentially material-related (chemistry and manufacturing). Poor power density and low-temperature performance are mainly diffusion problems in the cell, and loss of power and capacity is due to fatal structure fracture, phase transition, and

consumption of electrolyte. Moreover, the high production costs of state-of-the-art active materials creates serious cost barriers that must be addressed to achieve and satisfy a long-term battery market. Therefore, the goal of his work is to develop commercially viable material synthesizing processes to reduce the processing cost without sacrificing the performance of the Li-ion batteries.

Chapter 1

Background

1.1 Demand for Li-ion Batteries

Since the invention of the zinc/copper Voltaic Pile battery in 1800, batteries have become the most common energy storage devices for daily use and for many industrial applications. An electric battery contains one or more electrochemical cells that convert between chemical energy and electrical energy. The batteries are classified mainly into two categories: primary and secondary batteries. The primary battery can only convert chemical energy to electrical energy, thus they consist of non-rechargeable cells. Batteries that can restore their chemical energy or original chemical composition by supplying an electrical current are called secondary (or rechargeable) batteries. The first rechargeable battery, the lead-acid cell, was invented in 1859. A lead-acid cell consists of a lead anode and a lead oxide cathode immersed in a sulfuric acid solution, with the redox shuttle between elemental Pb and Pb^{n+} supplying the current. The lead-acid battery is still widely used today in automobiles. Despite the low material cost, a lead-acid battery has a very low energy density (per unit of mass or volume). In the mid 1900s, the nickel-cadmium (NiCd) and nickel-metal hydride (NiMH) secondary batteries were developed. These have an improved energy density, 40-60 $Whkg^{-1}$ and 30-80 $Whkg^{-1}$, respectively. Nonetheless, the metal Cd and rare earth elements used in these batteries are very expensive, so NiCd and NiMH batteries are not suitable for large-scale applications. Since the first demonstration of intercalation chemistry in a rechargeable Li-ion cell in the 1970s, the Li-ion battery technology has been undergoing rapid expansion in research, industry and market, because it has the highest volumetric and gravimetric energy densities among the conventional battery technologies, as shown in Figure 1.1. Li-ion

batteries are considered to be the most promising electronic energy storage intermediates for portable electronics, transportation and large energy storage facilities for renewable energies that require higher energy densities. The electric storage needs range from milli-watts to mega-watts for these applications.

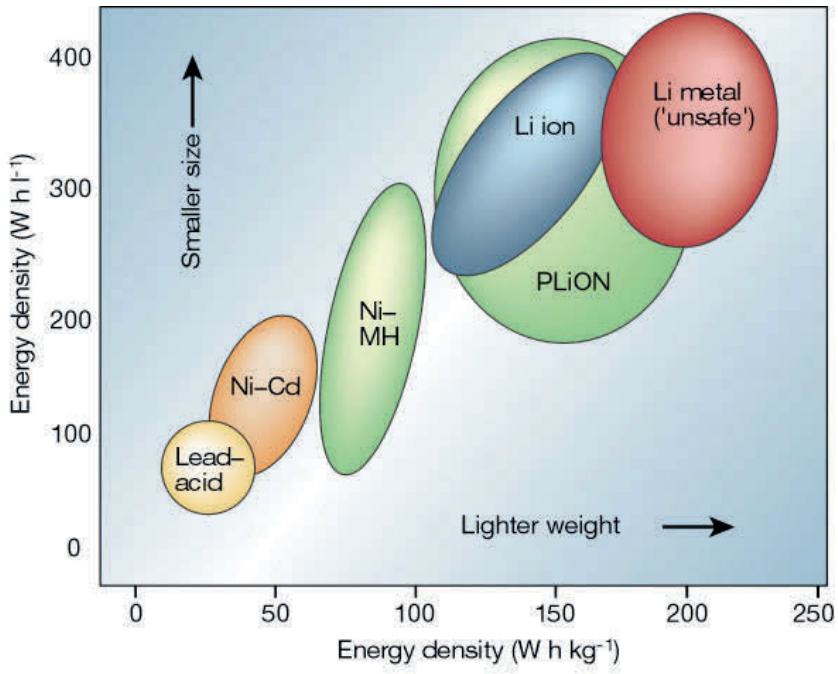

Figure 1.1 A comparison of energy density of different battery technologies (Ref. [1]).

Currently, the main driving force for the fast development of Li-ion battery technologies is to address the need for high-efficient and green ground transportation systems. Hybrid-electric-vehicles (HEVs) initially drew much attention due to their improved efficiency (saving gasoline), where the battery is charged during braking [2] or spinning of an electric-generator by an on-board IC engine that operates a peak cycle performance. The battery in the HEV is repeatedly charged and discharged during normal driving, which requires good battery *cycleability* at shallow discharge (*e.g.*, > 300,000 cycles, 30% state

of charge, SOC). The next generation of electric vehicles might be plug-in hybrid electric vehicles (PHEVs), in which a larger battery pack is used and it can be fully charged by plugging it into an external electric power source. Similar to a HEV, a PHEV combines an internal combustion engine and an electric motor. At normal operating conditions, the battery pack powers the vehicle, and when the battery is nearly depleted the internal combustion engine kicks on as a backup, giving a long driving range. Meanwhile, the heat from the internal combustion engine can provide heat and defogging/deicing at low-temperature environments [2]. The PHEV battery needs to supply high energy with weight and volume constraints for long-range driving, and it needs to be functional after deep cycles (5,000 cycles, ≥ 50% SOC). All electric vehicles (EVs) rely on batteries that need to be recharged or swapped out after draining the battery. Concerns about EVs include: driving range, price and availability of charge stations. For all these applications, in order to achieve commercial success the batteries need to be low cost, have long cycle and calendar life, high energy/power density, and be tolerant to abusive conditions, have low toxicity and safely operate.

1.2 Fundamentals of Li-ion Batteries

1.2.1 Reaction Mechanism in Lithium-ion Batteries

Batteries (or cells) are comprised of an *anode* and a *cathode*, separated by a porous separator. In conventional electrochemistry, the *anode* supplies electrons to the external

circuit during discharge, and is being oxidized. The *cathode* then accepts electrons and is being reduced. Considering the external electron circuit, the anode is the source of electrons, thus it is the *negative electrode*, and the cathode is the *positive electrode*. In a Li-ion secondary cell, the anode and cathode are soaked in electrolyte and separated by an ionic conductive separator, as shown in Figure 1.2. Li ions migrate between the cathode and anode through the separator during charge and discharge. Electrons can only migrate through the external circuit thus avoiding internal short-circuit of the battery. During charge, the Li cations move toward the anode and electrons are released to the external circuit. Discharge is the reversed process where Li ions are transported back to the cathode host from the anode and electrons move back to the cathode through the external circuit. The anode material is typically porous carbon (*e.g.*, graphite), lithium titanate ($Li_4Ti_5O_{12}$) or lithium alloys. The cathode materials are typically transition metal oxides, such as layered $Li[M]O_2$ (M = Co, Ni, Mn), spinel $Li[M']_2O_4$ (M' = Ni, Mn or combination of them), olivine-type $Li[M'']PO_4$ (M'' = Fe, Mn) and their derivatives [3, 4].

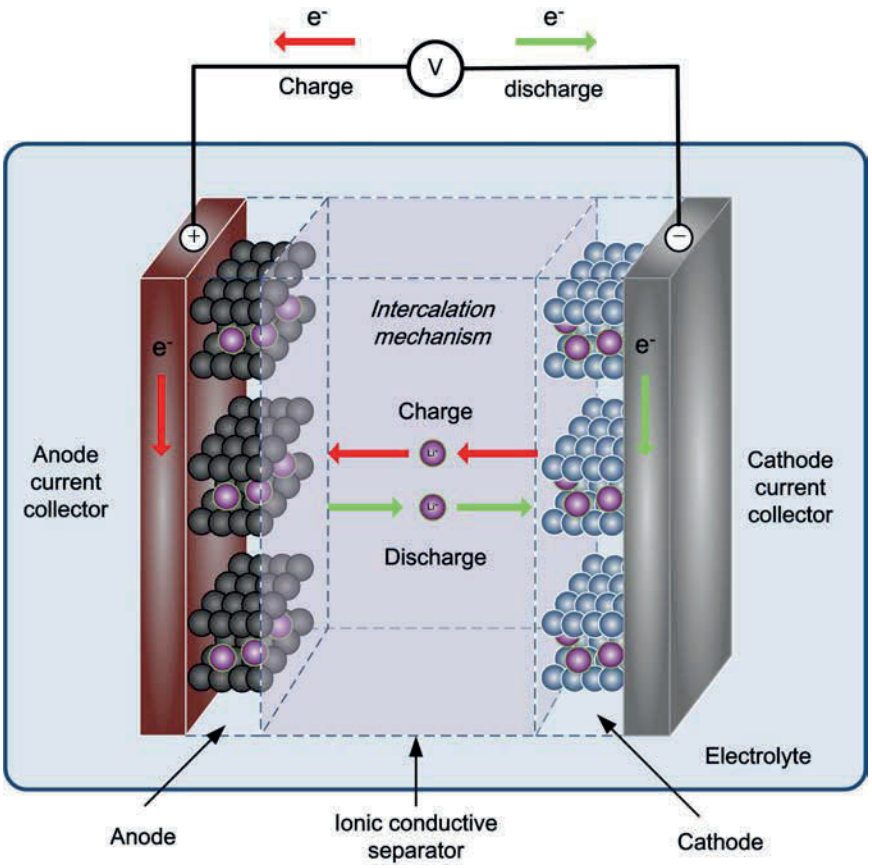

Figure 1.2 A schematic of the charge/discharge mechanism of a Li-ion cell.

The *intercalation* reaction or *de-intercalation* reaction is the most important reaction mechanism for Li-ion rechargeable batteries, and involves the insertion of the guest species, *i.e.,* Li ions, into *interstitial sites* in the crystal without changing the basic crystal structure. The intercalation chemistry in the Li-ion battery system was first proposed by M.S. Whittingham, who studied the Li insertion reaction into layered-type cathode materials, *i.e.*, Li_xTiS_2 [5]. The intercalation reaction is a reversible process, in which Li ion can be repeatedly be extracted from or inserted into the host materials. If both the anode and cathode are intercalatable in a way that the Li ions can be transported between the two electrodes during charge and discharge, this is commonly referred to as the

"rocking chair" mechanism [6]. A common examples of "rocking chair" type batteries is graphite(-)/$LiCoO_2$(+) or graphite(-)/$LiMn_2O_4$(+). The insertion reactions normally occur when the host has an open framework or a *layered-type crystal structure*, so that small ions like Li can reside in the space available in a continuous manner as seen in Figure 1.3(left), which is called *solid-solution reaction*. The voltage of the cell varies continuously with Li content in the host material. The reaction in the cathode can be written as the following:

$$x\,Li + M \rightarrow Li_xM \qquad (1.1)$$

where *M* is the solid-solution host material on the cathode side and *x* indicates stoichiometric coefficient for Li. Layered $LiCoO_2$ and $LiNi_{1/3}Mn_{1/3}Co_{1/3}O_2$ are solid-solution type cathode materials displaying a smooth voltage profile at discharge. On the other hand, sometimes multi-phase reactions occur during insertion/extraction of Li, where there is an interface separating the host into two regions. Thermodynamically, the multiphase reconstitution occurs resulting in a set of constant-voltage plateaus. The reaction can be written as:

$$Li + M' \rightarrow LiM' \qquad (1.2)$$

Where *M'* is the host material on the cathode side, and *LiM'* is the lithiated phase during the two-phase reaction. There is an interface between lithiated *LiM'* and *M'*, which moves as more Li ions being inserted. For example, spinel $LiMn_2O_4$ and olivine $LiFePO_4$ show two-phase reactions with at least one voltage plateau.

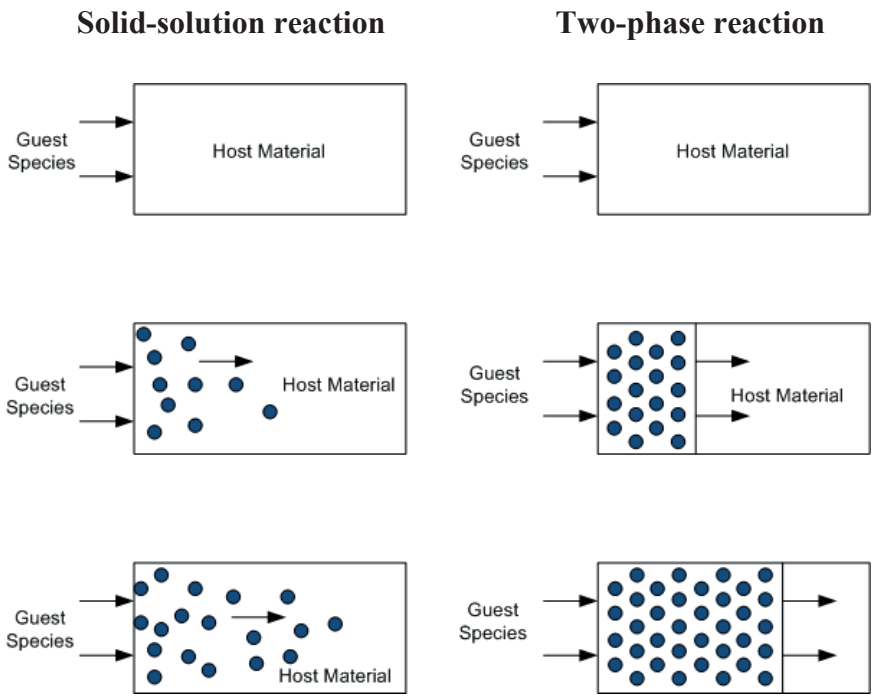

Figure 1.3 A schematic illustration of solid-solution reaction (left) and two-phase reaction (right).

1.2.2 Electrochemistry of Li-Ion Batteries

The driving force for the reactions across the cell is the difference in chemical potentials of the two electrodes. It is expressed as *the standard Gibbs free energy* change per mole of the reaction, ΔG_r^o, determined as the difference in the standard Gibbs free energy change of formation between products and reactants. The balance between ΔG_r^o and molar electrostatic energy of electrically charged species $-zFE_{th}$ is

$$\Delta G_r^0 = -zFE_{th} \qquad (1.3)$$

where E_{th} is the theoretical voltage of the cell under equilibrium conditions, F is the Faraday constant (96,487 Coulombs per equivalent), z is the charge number of the ionic

species (*e.g.*, $z = 1$ for Li^+). The cell can hold an electrostatic potential with extremely slow self-discharge because the separator only allows the penetration of Li^+. The electrolyte and separator are ionic conductive, thus the transportation of electrons between the two electrodes in the cell is eliminated. Note that the practical voltage of a cell E_{out} is not always equal to E_{th}. *Impedance* always exists due to the transport of ions in the cell and this may cause a voltage drop. The *impedance Z* is the instantaneous ratio of the applied voltage to the response (*i.e.*, current) across the circuit, when time-dependent changes in structure or composition occur. When the current flows internally in the cell, the output voltage can be written as:

$$E_{out} = E_{th} - I_{out}Z_i \qquad (1.4)$$

Several parameters are important to determine the electrochemical performance of a cell or an electrode material. *Specific energy density* is the energy available per unit weight ($Whkg^{-1}$). On the other hand, *energy density* refers to the amount of energy per unit volume (WhL^{-1}). Energy density is very important for PHEVs and EVs where there is limited space available for battery packs. *Specific capacity*, or simply *capacity* ($mAhg^{-1}$, or $Ahkg^{-1}$) is normally used in galvanic cells at certain working potential. Maximum theoretical specific capacity can be calculated from the chemistry of the reactant engaged in the reaction. In reaction (1.1), the theoretical capacity of Li_xBX is simply calculated as

$$Specific\ capacity\ (mAhg^{-1}) = \frac{xzF}{3.6\ MW_t} \qquad (1.5)$$

where x is equivalent of Li in Li_xBX, z is the net charge of Li ions, MW_t is the molecular weight of Li_xBX, in $gmol^{-1}$. Also note that the product of xzF is total charge in Coulombs per equivalent involved in the reactions. For instance, the theoretical capacity of $LiMn_2O_4$ is *c.a.* 148 $mAhg^{-1}$ if all Li is extracted from the spinel structure during charging. It's not hard to see that higher Li-content in the host materials may contribute to higher galvanic capacities.

The charge/discharge voltage profile is normally plotted against specific capacity, or *state of charge* (SOC) or *depth of discharge* (DOD). SOC is the battery's charge level, usually expressed as a percentage of full charge (0-100%). DOD is another term to describe the level of depletion in the battery. DOD is opposite to SOC, thus their sum equals 100%. Figure 1.4 shows the voltage profile of common cathode materials plotted against specific capacity. $LiFePO_4$ shows a typical two-phase reaction mechanism that the voltage displays as a plateau, as discussed earlier. The layered compounds $LiCoO_2$, $LiNi_{1/3}Mn_{1/3}Co_{1/3}O_2$, $LiNi_{0.8}Co_{0.15}Al_{0.05}O_2$ (NCA) and the Li-excess composite material (composition unknown) have displayed a typical single-phase solid solution behavior in that the voltage declines slowly at discharge. The integration of the voltage with respect to the specific capacity gives the theoretical *specific energy density* (Whg^{-1} or $kWhg^{-1}$) of the cathode material, as well as the *energy density* (WhL^{-1}) if divided by the material density. Additionally, Figure 1.4 shows that the excess-Li composite material has the highest energy density among these cathode materials, making it very attractive for high-energy applications.

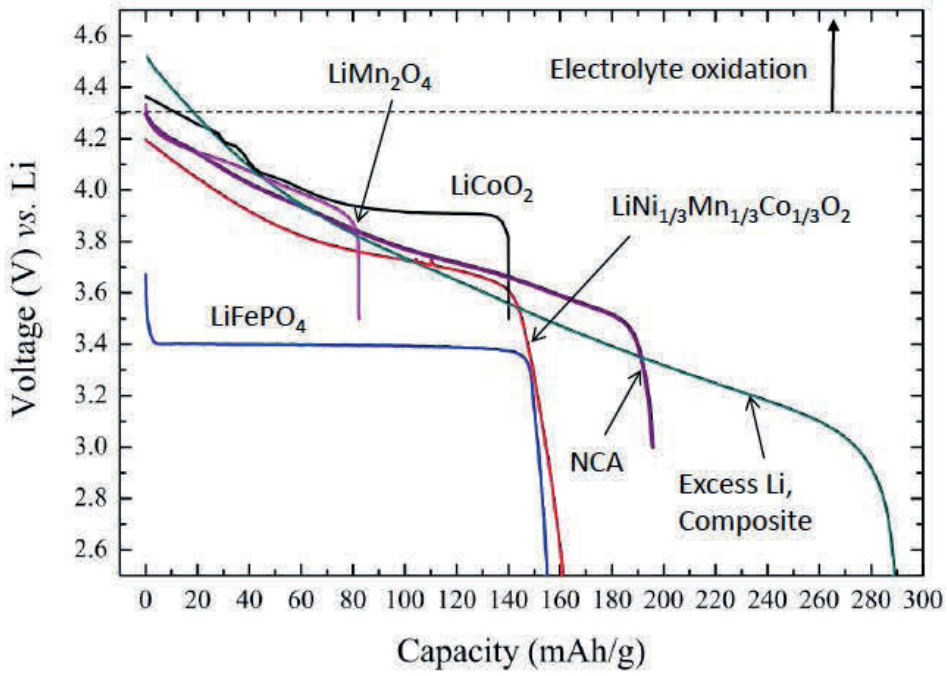

Figure 1.4 Discharge profile of current cathode materials. (Source: *Directions for Energy Storage R&D in the Vehicle Technologies Program*, DOE, 2010)

Cycle life is critical for a Li-ion cell, and refers to the number of times a cell can be effectively recharged before its capacity becomes too low. *Coulombic efficiency* is the fraction of the prior charge capacity that is available during the discharge. Higher coulombic efficiency means a better cycleability of a cell. Another important parameter is the *C-rate*, the rate at which a battery is discharged. C-rate is normally expressed as C/R, where R is the number of hours required to completely discharge a cell within this normal capacity range. For example, a $LiMn_2O_4$ cell normally has a practical specific capacity of 120 $mAhg^{-1}$. At a C/10 discharge rate, the cell can be fully discharged in 10 hr and the corresponding current density will be 12 mAg^{-1}. At elevated C-rates, the observed voltage will depart from the equilibrium for kinetic reasons. In fact, there may not be sufficient time to attain compositional or structural changes that should occur under equilibrium

conditions. In particular, battery discharge is a diffusion-controlled process, whereas Li ions diffuse between the anode and cathode hosts through the separator. Therefore, diffusion of Li becomes the rate-limiting factor at low temperature or high C-rates. Micro- and nano-scaled particles can minimize the diffusion path length in slow-diffusion phase and also accommodate volume change with minimal risk in structural failure, hence making this attractive for high-power batteries. Models based on Fick's second law, Ohm's law and Butler-Volmer kinetics have been developed to parameterize the transport phenomena, *e.g.*, diffusion coefficient, and predict the battery performance (specific energy density and cycle life).

1.3 Materials for Li-ion Batteries

1.3.1 Anode Materials for Li-ion Batteries

Elemental lithium was used as the anode material in the early development of Li-ion batteries. However, when elemental Li is used, problems arise with respect to poor cycle life or failure of the cell. The reason for this is the formation of branched dendrites, which will penetrate the membrane separator and short-circuit the cell. Another reason for avoiding Li metal is safety concerns associated with elemental Li at elevated temperatures, especially in electric vehicles. Alternatives materials with novel micro- or nanostructures have been developed to improve the cycle life or energy density of the anode in the Li-ion batteries.

Carbon, specifically graphite, has been extensively studied as an anode material because of the extremely low cost. Li can be inserted between graphene layers of the host graphite structures to form graphite intercalation compounds (GIC) [7, 8]. The practical capacity of the graphite electrode is about 372 $mAhg^{-1}$, and the half reaction can be written as

$$x\ Li^{+} + x\ e^{-} + 6\ C \rightarrow Li_x C_6 \qquad (1.6)$$

Graphite arranges in a stack of layers of carbon planes and the interplanar spacing provides a host for Li ions. The graphite structure is commonly described as *-A-B-A-B-* stacking (*A, B*: carbon layers), in which the *B* layers are shifted with respect to the *A* layers. By the insertion of lithium, the structure will change to *-A-I-A-I-* stacking (*I*: guest layers or intercalated layers) [7]. The carbon layers stack together and become equivalent to each other after complete insertion of Li. One important problem with Li-graphite anode is that the maximum concentration of lithium in the graphite structure is achieved with one Li per six carbons (LiC_6), resulting a low carbon usage and low energy density. In addition to that, some irreversible capacity loss has been observed during the first few cycles due to the formation of solid electrolyte interface (SEI layer) on the carbonaceous electrode [9, 10]. Recently, a variety of carbon-base materials with novel micro- and nanostructures have been studied to improve the capacity and cycling performance of the anode, *e.g.*, carbon fibers (CFs) [11, 12], carbon nanotubes (single-walled or multi-walled) [13, 14] and mesocarbon microbeads (MCMB) [15-17]. The spherical shape of MCMB particles offers a high packing density, and its low surface area reduces the amount of side reactions resulting in good cycleability.

Another attractive anode material is silicon, which has a low discharge potential *vs.* Li and the highest known theoretical capacity (4,200 $mAhg^{-1}$, charging) [18]. In an Si anode, maximum intercalatable Li is 4.4 per Si [19], resulting in a high energy density. However, the severe volume expansion (about 300%) of the Li-Si anode will cause structural failure after repetitive insertion/extraction of Li at full SOC, deteriorating the capacity and cycling performance [20]. Recent studies have shown that nanostructured Si, *e.g.*, Si nanotubes [19] and nanowires [18, 21], core-shell Si/C, can reduce volume expansion and improve the cycle life.

1.3.2 Cathode Materials in Li-ion Batteries

A) Materials with the Layered Structures $Li[M]O_2$

Many materials have been demonstrated to be electrochemically active (intercalation) compounds for the cathode in Li-ion batteries. The first Li intercalation reaction was demonstrated with a Li/TiS_2 cell in 1976 [5, 22]. The cathode material TiS_2, shows a two-dimensional layered structure, and can form Li_xTiS_2 (where $0 \leq x \leq 1$) with the insertion of Li. The Li/TiS_2 cell shows an open circuit voltage of 2.5 V and an energy density of 480 $Whkg^{-1}$. However, the Li/TiS_2 cells were found to be unsafe due to the elemental Li anode with the liquid electrolyte [1]. Although, Li-Al alloy anodes were later developed to replace elemental Li, the volume change of such lithium alloy deteriorated the cycleability of the cells [1].

Another important two-dimensional layer-structured cathode material $LiCoO_2$ was discovered by Goodenough in the 1980s [23]. $LiCoO_2$ is iso-structural to α-$NaFeO_2$ ($R\bar{3}m$ symmetry) with the oxygen atoms in a cubic-close-packed (*ccp*) arrangement, as seen in Figure 1.5. In the ideal layered materials, Li and Co atoms occupy the octahedral interstitial sites, and CoO_2 layers are formed consisting of edge-sharing [CoO_6] octahedra when the Li/transition-metal ratio is unity or less [4, 24]. After complete extraction of Li, the oxygen layers will rearrange themselves and form hexagonal-closed-packed (*hcp*) structures of the oxygen atoms in CoO_2. However, only one half of the Li in $LiCoO_2$ is reversibly cycled, because deep removal of Li will cause a phase change *(-ABCA-* to *-ABA-* stacking sequence) leading to poor structural stability. Moreover, upon completely extraction of Li (overcharge), the voltage of Li/$LiCoO_2$ cell can ramp up to 4.7 V, which causes decomposition/oxidation of the organic electrolyte [24]. Moreover, the heat released during the overcharge may cause thermal runaway, being unsafe for consumers. Thus, the charging of $LiCoO_2$ cell is restricted and its capacity is expected to be *c.a.* 130-150 $mAhg^{-1}$ between 2.5 and 4.3 V *vs.* Li/Li^+. The C/$LiCoO_2$ batteries (C: graphite anode) lead to the first large-scale commercialization of Li-ion secondary batteries by SONY Corp. in early 1990s [4]. Although $LiCoO_2$ has dominated the current Li-ion battery market for years, the limited availability of cobalt makes it rather expensive for larger scale applications, *e.g.*, HEVs and EVs. Thus, $LiCoO_2$ is limited to the cathode battery material for small electronics, *e.g.*, cell phone batteries and laptop batteries.

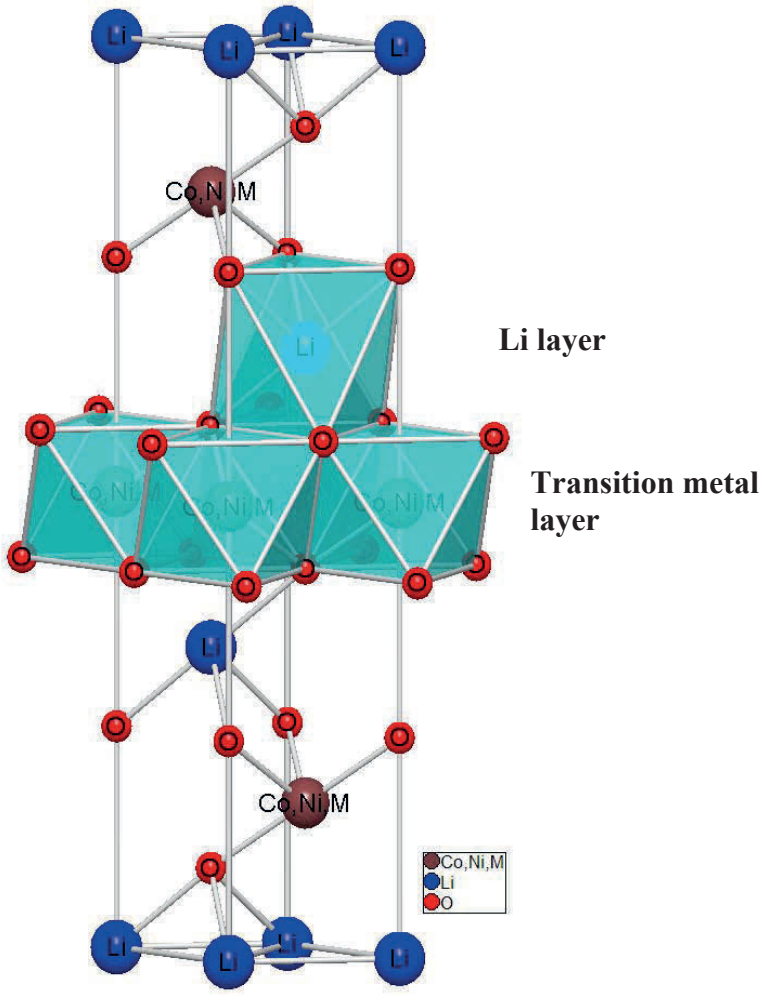

Figure 1.5 The 3-D crystal structure of layered $Li[M]O_2$, where M=Co, Ni, Mn.

Alternatively, different layer-structured lithium metal oxides with the general formula of $Li[M]O_2$ (M = Ni, Mn or a combination with Co) have also been developed. $LiNiO_2$ is considered as an isostructural to α-$NaFeO_2$ with $R\bar{3}m$ symmetry. The redox potential of $LiNiO_2$ is 0.25 V lower than that of $LiCoO_2$ electrode, making it more stable against electrolyte oxidation. Meanwhile, about 0.65 Li per unit formula in $LiNiO_2$ can be intercalated, which can provide a capacity of over 150 $mAhg^{-1}$ between 2.5 and 4.2 V [25]. Unfortunately, stoichiometric $LiNiO_2$ is difficult for synthesis due to the disordering

of Li and Ni ions [26]. In the disordered $LiNiO_2$, Ni ions at 3(a) sites will displace with Li ions at 3(b) sites and these Ni ions presumably will block Li diffusion pathways. Therefore, $LiNiO_2$ often shows very poor electrochemical performance during repeated Li insertion/extraction. Both synthetic optimization and partial substitution of Ni with Co or Mn have been studied to limit the Li-Ni disordering. $LiNi_{0.5}Mn_{0.5}O_2$ and $LiNi_{1/3}Mn_{1/3}Co_{1/3}O_2$ have successfully shown improved structural stability during cycling.

$LiMnO_2$ synthesized at high temperature (*e.g.*, 800 °C) is thermodynamically stable as an orthorhombic structure with *Pmmn* symmetry. o-$LiMnO_2$ can convert to the more stable spinel structure upon cycling, thus yielding a poor cycleabilty of the electrode [4, 24]. Within the Li-Mn-O system, Li_2MnO_3 is another layered-type material with rock-salt structure, in which the Li and Mn occupy all the octahedral sites to form a layer of Li ions and a mixed layer of Li and Mn ions [27, 28], as seen in Figure 1.6. Hence Li_2MnO_3 can be reformulated as $Li[Li_{1/3}Mn_{2/3}]O_2$ in a solid-solution expression. Since all the Mn is tetravalent and it can't be further oxidized, therefore Li_2MnO_3 is considered to be electrochemically inactive for Li-intercalation reactions [28, 29]. Despite the inactivity, Li_2MnO_3 is an attractive alternative for $LiCoO_2$ because of the high theoretical capacity, *c.a.* 458 $mAhg^{-1}$ if assuming all the Li can be extracted [30]. It has been reported that Li_2MnO_3 can deliver 140 to 200 $mAhg^{-1}$ after the removal of Li_2O by acid etching [31, 32], ion exchange [29] or electrochemical activation [33]. Li_2MnO_3 is an interesting material because it can integrate with layered $Li[M]O_2$ forming a "composite" material with advanced electrochemical properties [33-37]. These composite materials will be discussed in the chapters to follow.

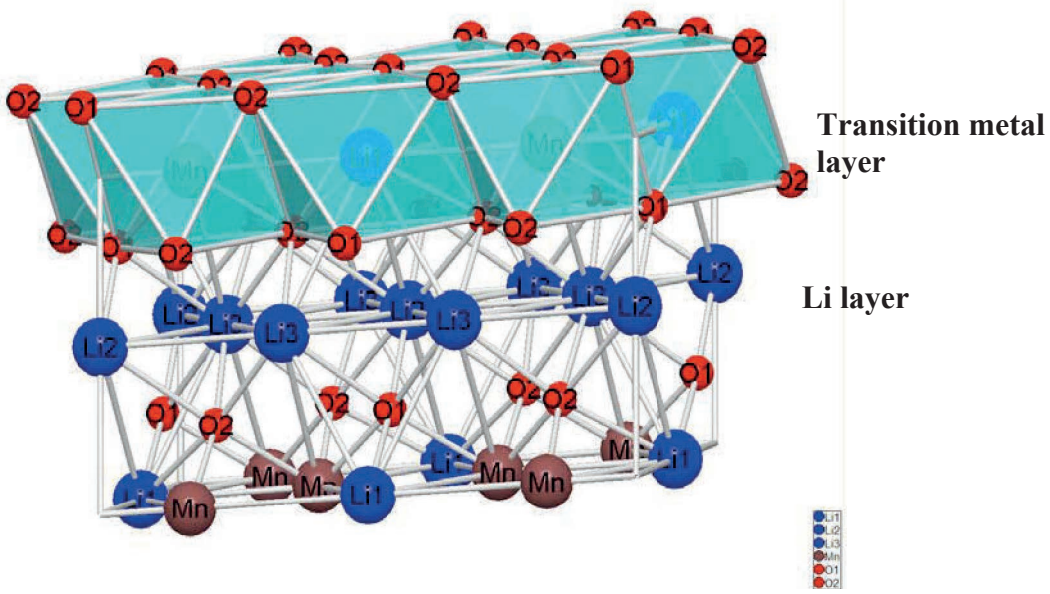

Figure 1.6 The 3-D crystal structure of layered Li_2MnO_3.

B) Materials with the Spinel Structure $Li[M_2]O_4$

The cubic spinel has a general formula $Li[M_2]O_4$ possessing a $Fd\bar{3}m$ space group structure. As seen in Figure 1.7, the oxygen anions form cubic-close-packed (*ccp*) arrays occupying the *32e* sites; the Li cations occupy 1/8 of the tetrahedral sites (8a), and the M cations occupy half of the octahedral sites (16d) [38]. In the spinel $LiMn_2O_4$ structure, the lithium and manganese ions occupy the tetrahedral (8a) and octahedral (16d) sites respectively, and oxygen atoms form *ccp* arrays. The spinel shows a 3-D framework structure, thus, Li can be intercalated at a higher rate. The fast insertion/extraction of Li can lead to high power density, thus it is very important for the application of fast charge/discharge batteries.

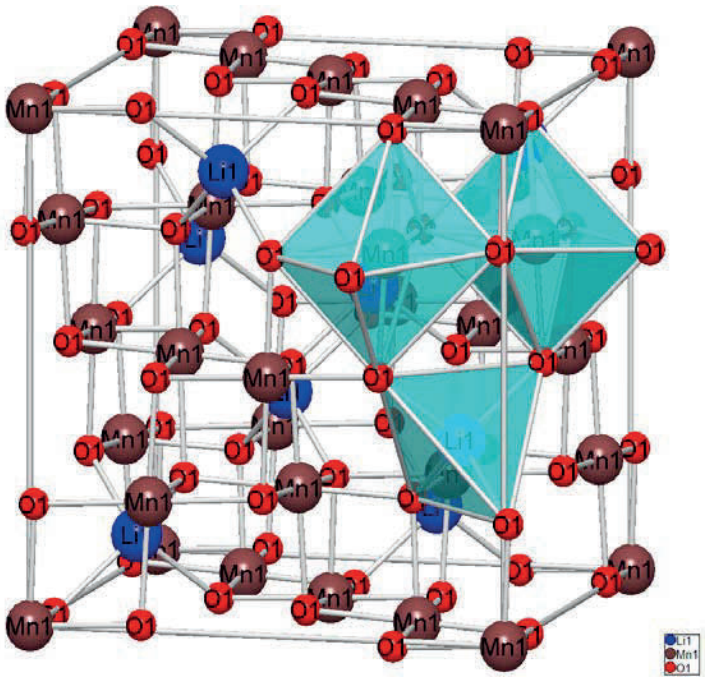

Figure 1.7 The 3-D crystal structure of spinel $LiMn_2O_4$.

The intercalation reaction in cubic spinel $LiMn_2O_4$ was initially studied by Goodenough, *et. al* in 1983 [39]. Spinel $LiMn_2O_4$ is thermodynamically more stable than layered $LiMnO_2$, and also shows a flat potential plateau in the 3 to 4 V region, as seen in Figure 1.7 [40]. As Mn is cheaper and more abundant than Co, this material has gained attention as an alternative to $LiCoO_2$. The insertion/extraction of Li ions in the spinel framework involves two distinct steps: lithium insertion/extraction into tetrahedral sites (8a), which occurs at about 4 V; at 3 V, lithium insert/extraction into the octahedral (16c) sites forming a tetragonal spinel $Li_2Mn_2O_4$. The Li-extraction reaction across the cell can be written as:

$$4\,V : LiMn_2O_4 \rightarrow Li_{(1-x)}Mn_2O_4 + x\,Li^+ + x\,e^- \qquad (1.7)$$

$$3\,V : Li_{(1+x)}Mn_2O_4 \rightarrow LiMn_2O_4 + x\,Li^+ + x\,e^- \qquad (1.8)$$

As seen in Figure 1.8, as the Li content in the $Li_xMn_2O_4$ electrode changes at discharge, there are series of reactions occurring, which can be characterized into three regions [40]. In region I, where two cubic phases coexist, a plateau near 4.1 V can be seen. In region II, the voltage profile turns into an "S" shape and drops slowly, where it is considered as a single-phase (cubic) solid-solution. In region III, a cubic and a tetragonal phase coexist, thus a two-phase plateau is observed. However, in the 3 V region, a cubic-to-tetragonal transition from $LiMn_2O_4$ to $Li_2Mn_2O_4$ will cause structure failure, which is known as Jahn-Teller distortion, and thereof severe capacity fading. The distortion will lead to 16% increase in the *c/a* ratio and 6.5% volume increase of a unit cell. This severe change of the electrode will deteriorate the structure integrity during charge/discharge cycles, thus showing rapid capacity fade (loss of capacity) at 3 V. Thus, spinel $LiMn_2O_4$ is categorized as a 4 V cathode material. The theoretical capacity of spinel $LiMn_2O_4$ is 148 $mAhg^{-1}$ in both 4 V and 3 V regions. However, normally 120 $mAhg^{-1}$ can be achieved, whereas about 0.4 Li per Mn is intercalatable practically at 4 V. However, $LiMn_2O_4$ still exhibits capacity fade during cycling at 4 V. The reason for the fading is believed to be the Jahn-Teller distortion associated with the Mn^{3+} ion, loss of crystallinity, as well as decomposition of the electrolyte at high temperature and high charge/discharge voltage. It is generally accepted that by doping the spinel with foreign metal cations (e.g., Li, Co, Ni, Cr, Fe, Al, and Mg) to stabilize the structure, the Li-ion battery performance can be improved, eventually reducing capacity fading [41]. Some studies have indicated that the cycleabilty of $LiMn_2O_4$ electrodes at 3 V can be improved and the kinetics of reversible insertion can be achieved by decreasing grain size into the tens of nanometers range [42,

43]. The reason was understood to be that the strain within the particle that was induced from Jahn-Teller distortion dissipates in random directions, preventing structural failure.

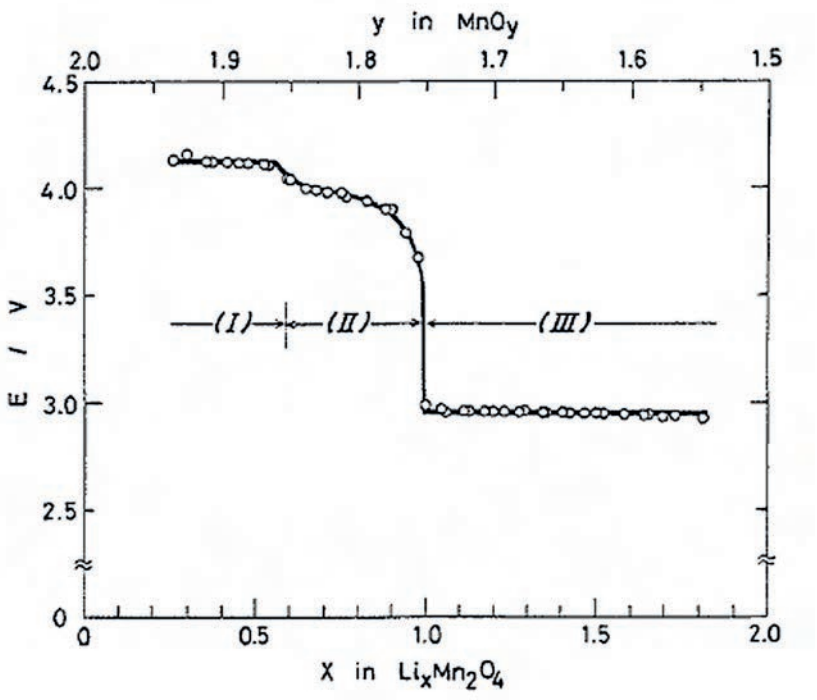

Figure 1.8 Open circuit voltage profile of $Li_xMn_2O_4$ (Ref. [40]).

Recently, it has been reported that with significant increases in the substitution of Mn, *i.e.*, 25% substitution, with transition metals, the doped spinel shows a higher working potential near 5 V and also retains a good discharge capacity [44-47]. Among the 5 V spinels, nanostructured $LiNi_{0.5}Mn_{1.5}O_4$ (Ni^{2+}, Mn^{4+}) has drawn special interest for its specific electrochemical characteristics: high capacity (130 -140 $mAhg^{-1}$), a working voltage plateau at 4.7 V and good cycling performance at elevated charge/discharge rates [46, 48, 49]. The high-voltage plateau of $LiNi_{0.5}Mn_{1.5}O_4$ during cycling is known to be the result of the Ni^{2+}/Ni^{4+} redox couple, compared to the Mn^{3+}/Mn^{4+} redox couple in the

traditional 4 V spinels. $LiNi_{0.5}Mn_{1.5}O_4$ has two stable crystallographic structures: disordered $Fd\bar{3}m$ space group and ordered $P4_332$ space group, which are stable at different synthetic conditions [46, 50, 51]. It has also been found that nano-sized disordered spinel-$LiNi_{0.5}Mn_{1.5}O_4$ ($Fd\bar{3}m$) shows better cycling performance at high-discharge rate than the ordered structure [50, 52, 53].

C) Olivine-Type Lithium Phosphates Li[M]PO_4

Olivine-type lithium iron phosphate $LiFePO_4$ is considered as another promising material for large-scale applications. Olivine-phase $LiFePO_4$ was first discovered by Padhi, et al. in 1997 and synthesized by a solid-state reaction [54]. $LiFePO_4$ has a high theoretical capacity of 170 mA h/g, and a flat potential plateau at 3.5 V versus Li/Li^+. The flat voltage curve indicates that the insertion and extraction of Li during charge and discharge proceeds through the reaction:

$$LiFePO_4 \rightarrow Li_{(1-x)}FePO_4 + x\ FePO_4 + x\ Li^+ + x\ e^- \qquad (1.9)$$

Olivine $LiFePO_4$ (M_2XO_4) belongs to the NASICON framework family (a family of Na super-ionic conductors) that shows high stability and allows good insertion and extraction of lithium ions [55, 56]. $LiFePO_4$ has an olivine structure (space group: *Pnma*), in which FeO_6 octahedra share common corners with each other, as shown in Figure 1.9 [1]. Li^+ and Fe^{2+} occupy half of the octahedral sites and P^{5+} is in 1/8 of the tetrahedral sites, in an *hcp* oxygen array. Olivine $LiFePO_4$ can also be considered as a special case of spinel $X[M_2]O_4$, but the M sites are crystallographically distinct and different in size.

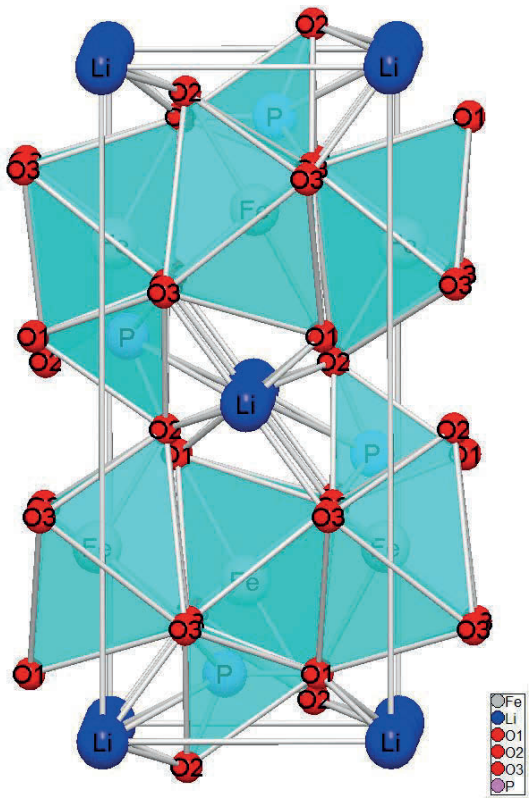

Figure 1.9 The 3-D crystal structure of olivine $LiFePO_4$.

Nevertheless, pure $LiFePO_4$ has a very low conductivity at room temperature (10^{-9} Scm^{-1}), compared to other well-known lithium cathode materials, e.g., $LiCoO_2$ (10^{-3} Scm^{-1}) [57] and $LiMn_2O_4$ (10^{-4} Scm^{-1}) [58]. This low conductivity results in losses of capacity during high-rate discharge at room temperature [59]. The reason for the low conductivity is widely accepted as the one-dimensional Li diffusion pathway and the low interfacial diffusivity of Li^+ ions. As a result, the current density is small for $LiFePO_4$ electrodes at room temperature. Many efforts have been made to overcome the low conductivity of $LiFePO_4$, by, for example, coating the material with carbon to form $LiFePO_4$/C composites [60-64], reducing particle size [65-67], and doping with metallic elements [68-71], which adds to the manufacturing complexity and cost.

1.3.3 Summary of Status of Advanced Battery Development

Table 1.1 summarizes the characteristics of some promising lithium-ion batteries in various stages of development mainly for PHEVs and HEVs in the year of 2007 [72]. Graphite and lithium titanate are the key candidates for the anode in Li-ion batteries due to the low material cost and ease of manufacturing. NCA-graphite and LFP-graphite batteries are both in pilot-scale development, however, thermal runaway in NCA electrodes and high manufacturing cost for preparing nano-sized $LiFePO_4$ material appear to be the main technical barriers that need to be resolved [72]. A spinel-spinel coupled battery system applies spinel-type materials in the cathode and anode. Despite the fact that the spinel-type batteries have a low specific capacity and low operation voltage, the high power output and excellent cycle life make them still attractive. MN-graphite system has the highest capacity, which can lead to a reduction in battery weight. MN ($Li_{1.2}Ni_{0.2}Mn_{0.5}O_2$) can be considered as a Li-excess composite material, which integrates more than one phase at the molecular level. The state-of-the-art composite materials require further development because proper material processing and nanostructured architecture are critical for achieving superior performance.

Table 1.1 Selected Li-ion Battery System Applied for PHEVs.

System	NCA-Graphite	LFP-Graphite	MS-TiO	MNS-TiO	MN-Graphite
Cathode Material	$LiNi_{0.8}Co_{0.15}Al_{0.05}O_2$	$LiFePO_4$	$LiMn_2O_4$	$LiNi_{0.5}Mn_{1.5}O_4$	$Li_{1.2}Ni_{0.2}Mn_{0.6}O_2$
Capacity ($mAhg^{-1}$)	155	162	100	130	275
Anode Material	Graphite	Graphite	$Li_4Ti_5O_{12}$	$Li_4Ti_5O_{12}$	Graphite
Capacity ($mAhg^{-1}$)	290	290	170	170	290
Voltage at 50% SOC	3.6	3.35	2.52	3.14	3.9
Safety	Fair	Good	Excellent	Excellent	Excellent
Life Potential	Good	Good	Excellent	Unknown	Unknown
Cost	Moderate	Moderate	Low	Moderate	Moderate
Status	Pilot Scale	Pilot Scale	Develop.	Research	Research

1.4 Overview of Synthesis Processes for Cathode Materials

1.4.1 Solid-State Reactions

Solid-state reaction is also called dry-media reaction as a solvent is not used during the chemical reaction. Solid-state reaction is widely used in many industries, because the process costs are low and it is very simple. Layered $LiCoO_2$, the first commercialized Li-ion battery cathode material, was initially synthesized *via* the solid-state reaction of lithium carbonate and cobalt carbonate [23]. Later, this group developed two other attractive cathode materials: spinel-$LiMn_2O_4$ and olivine-type $LiFePO_4$ *via* solid-state

reaction methods, as seen in Table 1.2 [39, 54]. Since then, solid-state reaction has become a conventional approach to the synthesis of lithium transition metal oxides and lithium iron phosphate and their derivatives for Li-ion batteries [73-81]. The characteristics of the powders are affected by the properties and purity of the precursors [82]. Moreover, long time calcination for complete reaction and grain growth is required, and mechanical grinding is needed to obtain the desired particle size and morphology [83-85]. Generally, long mechanical milling is required to grind the powder to the desired sizes. As a result, particle size, morphology and homogeneity are difficult to control. It is known that a finer particle size is needed to improve electrochemical performance, *e.g.*, rate capabilities. The size obtained with a solid-state reaction is practically limited and thus significant improvements in performance are not anticipated with this method. Alternative synthetic routes have been developed trying to overcome the disadvantages of the solid-state reaction method described above, such as co-precipitation [86-88], sol-gel method [89-91], and the hydrothermal method [92-94].

Table 1.2 Precursors and reaction conditions in the solid-state reactions for cathode materials originated by Goodenough *et al.*

Materials	Li source	Transition metal source	Heating / °C	Time / hr	Post heating / °C	Time / hr
$LiCoO_2$ [23]	Li_2CO_3	$CoCO_3$	900	20	Yes	N/A
$LiMn_2O_4$ [39]	Li_2CO_3	Mn_2O_3	650	12	850	24
$LiFePO_4$ [54]	Li_2CO_3	$Fe(C_2H_3O_2)_2$	300-350	N/A	800	24

1.4.2 Wet-Chemistry Processes

Wet-chemistry processes require solvents and sometime additives to produce materials with desired chemical composition and morphology, and they are more sophisticated than solid-state reactions. Typical wet-chemistry processes involve hydrothermal, sol-gel and coprecipitation methods. A variety of materials can be produced *via* wet-chemistry processes, including SnO_2, V_2O_5, layered $LiMO_2$ (M=Li, Co, Mn, Ni, or a combination of them), spinel $LiMn_2O_4$, Olivine $LiFePO_4$ and $LiMnPO_4$. Compared to solid-state reactions, wet-chemistry is a low temperature synthesis process, therefore, the as-produced powders are very small in size, sometimes showing unique morphologies such as aggregates [95], wires [96], rods [97], flakes [98] and spheres [37, 99], as shown in Figure 1.10.

The sol-gel method can be described as a four-step process: (1) mixing of the precursors and gelation agents with control over pH; (2) sol formation (*e.g.*, at 70 to 80 °C); (3) gel formation (*e.g.*, at 70 to 80 °C); (4) calcination of the gel to form solid powders at *c.a.* 300 °C. Normally post-calcination at a higher temperature is required to obtain the desirable crystalline phase. The Li and other metal precursors are selected from metal hydrates, nitrates, acetyl-acetonates *etc*. The organic gelation agents should have hydrophilic functional groups, like citric acid, polyacrylic acid (PAA) and polyvinyl-pyrrolidone (PVP) [100].

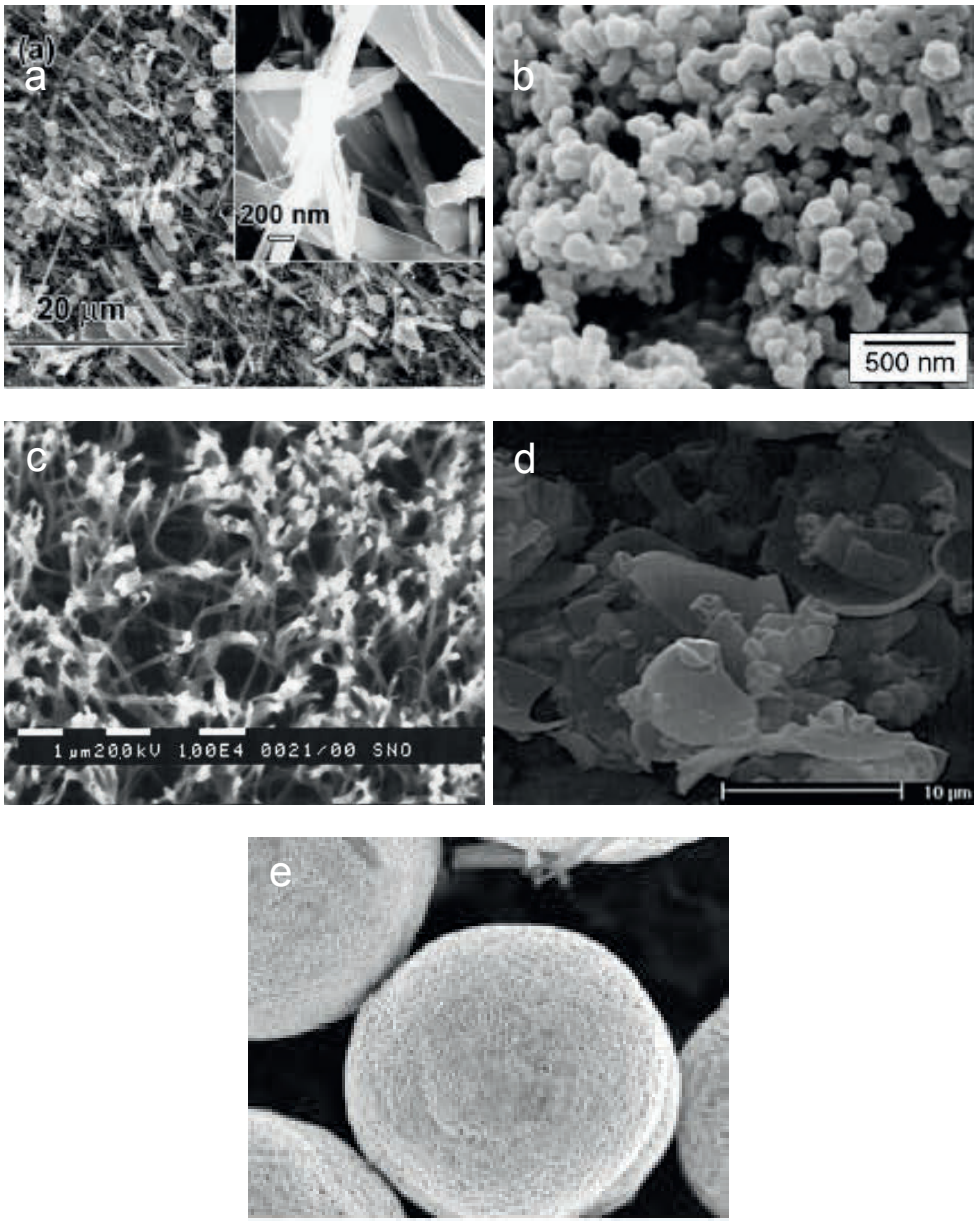

Figure 1.10 Various powder morphologies from wet-chemistry processes.

The hydrothermal process is similar to the sol-gel process, except for the absence of the gelation agent and the different heating temperatures. The precursor solution containing metal salts and surfactant is placed in a low temperature environment, normally in an autoclave heated between 120 °C and 400 °C for a couple of hours. After the reaction is complete, the resulting precipitates will be cooled, washed, dried and further calcined at a

higher temperature, *c.a.* 600 °C to obtain the crystalline phase and remove the carbonaceous surfactant (if applied). Both sol-gel and hydrothermal processes require long-tem moderate temperature heating to obtain the precursor powders. Organic gelation agent and surfactant are required to obtain uniform products with homogenous compositions, which adds to the material manufacturing cost. Therefore, they are generally not considered commercially viable for large-scale applications.

Recently, the coprecipitation process has become very popular, as the organic gelation agent or surfactant is absent. Under certain conditions, spherical particles can be produced, as shown in Figure 1.10e, which allows for a good packing density of the electrodes. Taking the high-energy cathode material $Li_{1.2}Ni_{0.2}Mn_{0.6}O_2$ as an example, the coprecipitation process developed at Argonne National Laboratory is shown schematically in Figure 1.11 [37, 99]. The first step is the coprecipitation of $Mn_{0.75}Ni_{0.25}CO_3$ precursors from manganese and nickel salts, sodium carbonate and a chelating agent (NH_4OH) in a continuous stirred tank reactor. The temperature, pH, stirring speed and concentration are controlled to obtain homogenous precipitates, the carbonate powders, which serve as a solid precursor for $Li_{1.2}Ni_{0.2}Mn_{0.6}O_2$ synthesis. In the reactor, $Mn_{0.75}Ni_{0.25}CO_3$ precipitates will take hours to grow into spherical particles in the size of 10 to 15 microns. The resulting $Mn_{0.75}Ni_{0.25}CO_3$ powders are collected, washed and dried under vacuum for hours to completely remove residual chemicals (Na salts) and water content. Thereafter, a stoichiometric amount of Li_2CO_3 will be mixed with $Mn_{0.75}Ni_{0.25}CO_3$ forming a uniform mixture, which will be calcined at 600 °C for 15 hr to decompose the carbonate precursors following by lithiation at 900 °C for 15 hr.

Although the materials from the coprecipitation process have shown good electrochemical performance, the process potentially has issues of reproducibility during scale-up. Even with identical chemical composition, the powders can have different colors due to a phase separation, *i.e.*, Li_2MnO_3 phase, which can be very detrimental to the battery performance (source: presentation slides from Argonne, 2010).

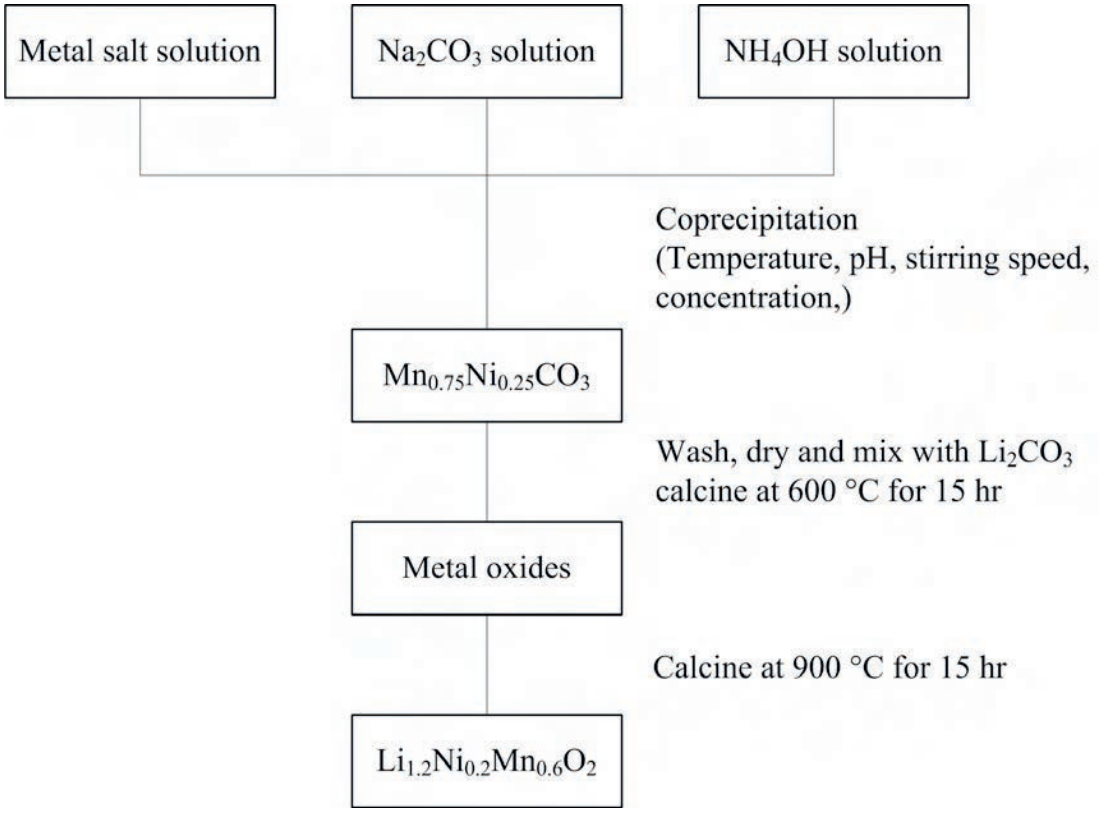

Figure 1.11 A schematic of coprecipitation process for high-energy $Li_{1.2}Ni_{0.2}Mn_{0.6}O_2$ synthesis (Ref. [37]).

In summary, wet-chemistry is a multi-step process and requires precise control over precursor chemistry, reaction temperature, pH and long-time calcinations. The key step in wet-chemistry process is the formation of a uniform precipitate (or gel precursor) with

controlled stoichiometry. However sometimes, undesired precipitates are produced. With the coprecipitation process as an example, Mn-Ni-hydroxides may precipitate during the $Mn_{0.75}Ni_{0.25}CO_3$ formation in the reactor, especially when the local environment (*e.g.*, pH, temperature, concentration) is not ideal. Therefore, the control over the stoichiometry of Li, Ni and Mn is challenging, especially at large scale.

1.4.3 Aerosol Synthesis

Aerosol synthesis technology has been rapidly developing in the past years. The term aerosol generally means small particulates (solid or liquid) suspended in the gas phase. The particle size can range from a few angstroms to 100 microns. The particles can be spherical, fiber-like, or irregular shapes, and they also can be dense or hollow in terms of their internal structures. In addition to improving our understanding in health and environmental science, aerosol technology has enabled the fast development of synthesis of functional micron- and nanostructured materials through a variety of processes. In particular, electrochemists have started to apply aerosol-based processes for the production of electrochemically active materials for energy conversion and storage applications. Compared to the solid-state reaction, aerosol processes provide a bottom-up, scalable, and continuous approach to produce novel nanostructured powders with narrow size distribution, and good uniformity. As discussed earlier, nanostructured cathode materials have shown good electrochemical performance with respect to rate capability and tolerance in volume change of the nanoparticles. Thus aerosol methods show great potential for material production for energy storage applications.

Aerosol methods involve gas-to-particle reactions and liquid-droplet-to-particle reactions for powder synthesis. During the gas-to-particle process, particles are formed by intraparticle reactions or by nucleation and growth of low-vapor-pressure species [101]. One example of gas-to-particle synthesis is the vapor-grown carbon fiber (VGCF) for anode materials in Li-ion batteries [102, 103]. Also, carbon nanotubes synthesized in gas phase potentially can be used as anode materials [104-106]. Nonetheless, gas-to-particle reactions are not commonly used for synthesizing cathode materials. It has been reported that by using chemical vapor deposition (CVD), polycrystalline $LiCoO_2$ and $LiMn_2O_4$ thin films can be prepared using metal organic precursors under certain conditions [107]. In this research, the gas-to-particle conversion was studied for the flame synthesis of $LiMn_2O_4$ with lithium acetyl-acetonate and manganese acetyl-acetonate precursors. However, the experiment turned out to be nonviable due to the difficulty in controlling the ratio of Li and Mn precursors in the vapor phase and the instability of these precursors. From these observations, the disadvantages of the gas-to-particle route for cathode materials synthesis generally include: (1) difficulty in controlling stoichiometry for multicomponent materials, (2) expensive and unstable precursors, (3) complexity over solid-state reactions and droplet-to-particle routes, and (4) agglomerated morphology.

For the above reasons, the liquid droplet-to-particle (or droplet-to-solid, liquid-to-solid) reactions are applied in this research for the synthesis of lithium transition metal oxides. Technologies for droplet-to-particle conversion mainly include: spray pyrolysis [82, 108-122], flame spray pyrolysis (or flame synthesis) [123-129] and spray drying [130-134]. Spray pyrolysis and flame spray pyrolysis are chemical processes where the precursors

undergo chemical reactions to form a product containing some of the elements in the precursors. The spray drying process is a physical process, whereas the chemical reactions generally do not take place, and the composition of the precursors and the products are the same. Therefore, post-treatment is normally required in order to obtain a different product for physical processes. Spray drying is not studied in this dissertation.

Spray pyrolysis and flame spray pyrolysis processes consist of the following basic steps: (1) formation of droplets containing precursors by means of an aerosol generator; (2) transport of the droplets into a high-temperature environment, *e.g.*, a heated reactor or a flame; (3) evaporation of the solvent; (4) thermal conversion of the precursors into the final products. A schematic of the key steps in a spray pyrolysis process is shown in Figure 1.12. These steps involve a wide range of physical and chemical phenomena (evaporation, sintering, diffusion, decomposition, combustion, *etc.*) that occur at different length scales and time scales. For example, the length scale ranges from the reactor size down to the nano-size of the crystallites, and the time scale ranges from the precursor decomposition time up to the residence time of the droplets or particles in the reactor. When a combustible solvent, *e.g.*, ethanol or methanol, is applied to suspend the precursors, combustion of the droplets has to be considered in the experiment. These phenomena along with other factors, such as reactor temperature, thermostability of the products, will determine the morphology, chemical composition and crystal structure of the final powders. In this dissertation, some of the factors are discussed in the following chapters and appendix.

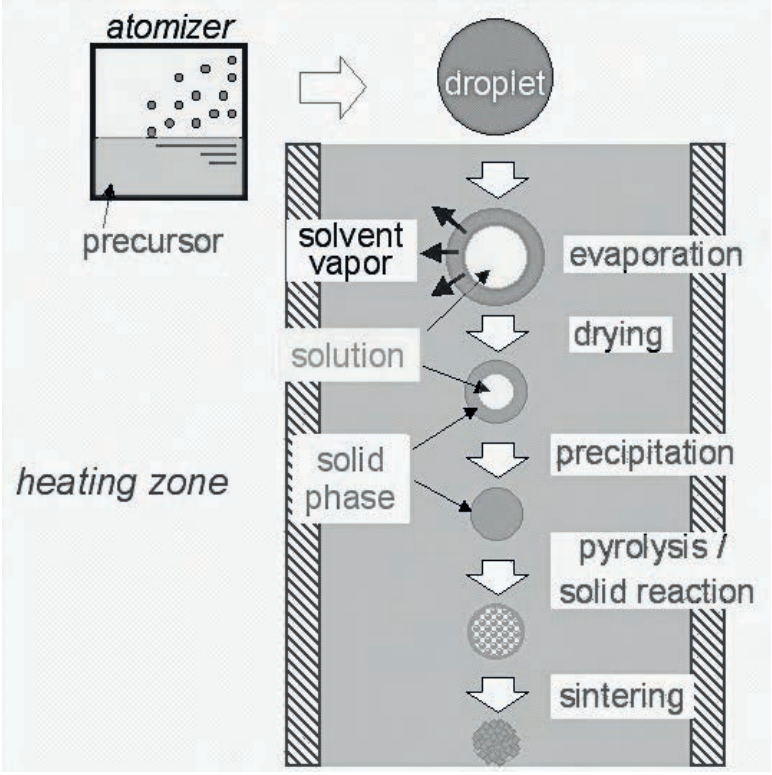

Figure 1.12 A schematic of key steps in spray pyrolysis (source: Web Based Aerosol Science and Technology Educational Resources Workshop)

A) Spray Pyrolysis

Spray pyrolysis methods have been reported to produce layered $LiCoO_2$ [108, 135, 136], $LiNiO_2$ [137], spinel $LiMn_2O_4$ [112, 113, 138], $LiNi_{0.5}Mn_{1.5}O_4$ [49, 118, 139] and olivine-type $LiFePO_4$ powders [121, 140, 141]. Spherical particles of micron sizes are typically formed in the spray pyrolysis process, and these particles are also polycrystalline. The $LiMn_2O_4$ particles from spray pyrolysis can have a nanocrystalline structure and they have demonstrated a good cyclic performance without doping [113, 138]. It also has been found that a portion of the particles prepared by the ultrasonic spray pyrolysis method were found to have a shell structure, and this lowered the volumetric

density of as-prepared powders [113, 116], as shown in Figure 1.13. By tuning the pH values in the precursor solution, hollow structure can be converted into a solid structure during the synthesis of $LiNi_{0.5}Mn_{1.5}O_4$ [116].

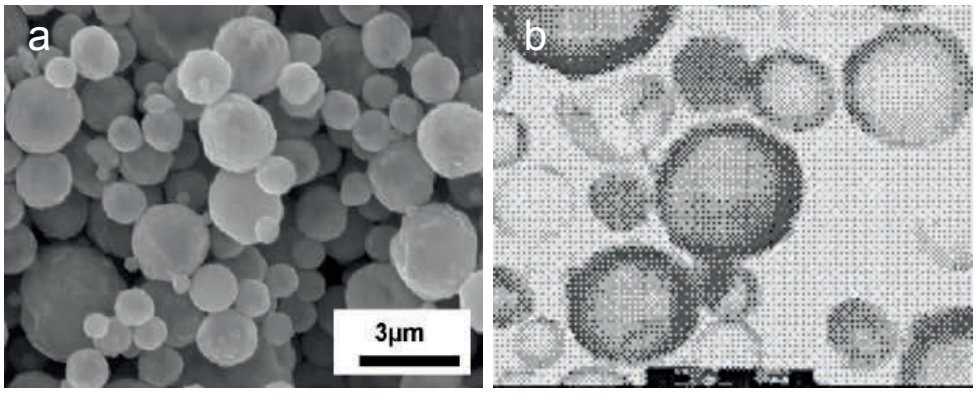

Figure 1.13 Typical morphology of cathode powders from spray pyrolysis: (a) spherical shape $LiFePO_4$ as observed by SEM [141]; (b) hollow $LiNi_{0.5}Mn_{1.5}O_4$ as observed by TEM [116].

B) Flame Synthesis

Flame synthesis is a proven industrial process that produces millions of tons of fumed metal oxides and carbon black each year. Flame technologies are known to be the desired industrial approach for low-cost, high volume materials. Flame technologies are inherently low cost because the fuel acts as the energy source, the process is continuous, and capital equipment costs are low. In addition, the produced powder can be uniform because the heat is generated uniformly through the flame, as opposed to being transferred from the walls of the reactor. Efforts have demonstrated that nano-sized $LiCoO_2$ and $LiMn_2O_4$ particles can be produced by different flame spray pyrolysis methods (FSP) [123, 142]. Jang, *et al.* synthesized $LiCoO_2$ particles in an H_2 diffusion

pyrolysis flame with lithium and cobalt acetate precursors dissolved in distilled water. As seen in Figure 1.14a, the as-synthesized powder showed a high-aggregation morphology with spherical nano primary particles ranging from 11 to 35 nm. This fractal morphology will lower the packing density of the electrode.

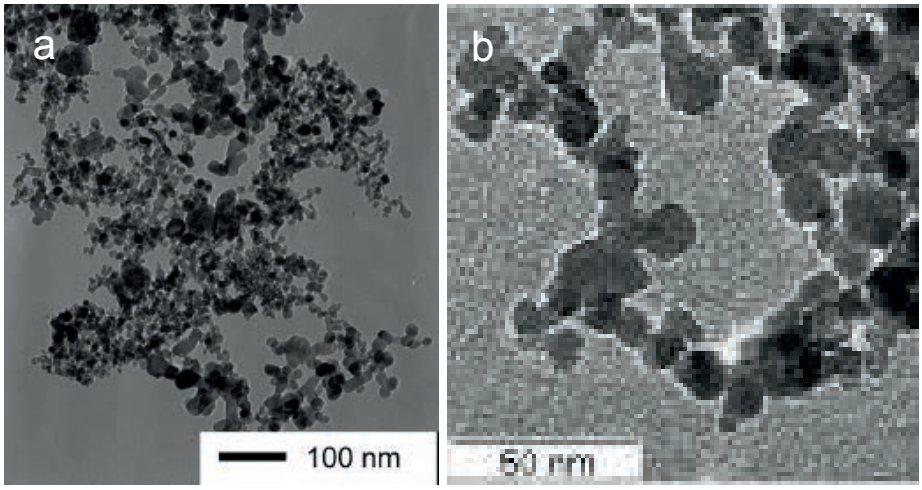

Figure 1.14 Aggregated morphology of (a) $LiCoO_2$ and (b) $LiMn_2O_4$ powders from FSP processes (Ref. [123, 142]).

Another well-known flame spray pyrolysis (FSP) process uses liquid fuel to produce micro- or nanostructured materials, *e.g.*, ZnO_2 [143], TiO_2 [144], and SiO_2 [145]. The FSP experimental apparatus consists of a gas-assisted spray nozzle where a group of CH_4 pilot flames surrounds the spray nozzle to stabilize the flame. Recently, electrochemically active spinel $LiMn_2O_4$, $Li_4Ti_5O_{12}$ and $LiFe_5O_8$ were synthesized by FSP, having a nanocrystalline structure with an average grain size of less than 20 nm (Figure 1.14b) [142]. Thus the powder showed a very high specific surface area, 53 to 203 m^2g^{-1}, which may be detrimental to the electrolyte. The initial discharge capacity of the $LiMn_2O_4$ cell was about 106 $mAhg^{-1}$. The low capacity may be due to the poor crystallinity, leading to

more side-reactions. Moreover, rare organic metallic compounds, *i.e.*, Li-*t*-butoxide in tetrahydrofuran and Mn(III) acetyl-acetonate were used as precursors, which made the process extremely expensive and not commercially viable.

The flame synthesis process has shown the ability to produce electrochemically active materials. Nonetheless, the electrochemical performance of the powders synthesized to date is not comparable to solid-state reaction, hydrothermal and other soft chemistry methods. With the design of new flames, the flame-made powder may become a promising approach to produce raw materials for Li-ion batteries.

1.5 Objectives and Dissertation Outline

1.5.1 Objectives

The overall objective of this dissertation is to develop and demonstrate technologies for producing affordable, high-performance cathode materials, where high-performance refers to high voltage, high capacity, high packing density and promising cycle life. A low-cost process will be employed to synthesize high-energy materials that might have superior properties to those produced by solid-state reaction and wet-chemistry processes. The method of synthesis should also have advantages for large-scale production of materials with uniform properties and consistency. In particular, a spray pyrolysis and a flame spray pyrolysis process will be developed by using a droplet-particle conversion mechanism, which ensures high uniformity of the powders and precise control of chemical composition in the particles and from particle-to-particle. Aside from superior powder properties, spray pyrolysis or flame spray pyrolysis process is less energy-intensive due to the short reaction times and short annealing/calcination times in the post processes. As stated in the previous sections, spray pyrolysis or flame spray pyrolysis process has been applied for the synthesis of cathode materials; however, the powders do not show ideal morphologies nor display superior electrochemical performance. The flame-made powders consist of nano-sized primary particles agglomerated together, which would lower the powder packing density, as seen in Figure 1.14. Some hollow particle can be produced in the spray pyrolysis process for multi-component material

synthesis, as seen in Figure 1.13. In this dissertation, these technical challenges and barriers will be addressed by using the state-of-the-art aerosol synthesis processes.

The performance target for these materials from the as-developed spray pyrolysis/flame spray pyrolysis includes high voltage around 5 V, and high capacity in range of 200-300 $mAhg^{-1}$ with long cycle life. New materials for batteries are critical for achieving a new generation of electrical energy storage system. Before the new materials can be designed, a deep understanding of the relationship between storage capacity, material chemistry and material morphology is desirable. In the Li-ion battery system, nano-scale materials hold promise for high-rate performance for the short ionic transport distance between the cathode and anode. Meanwhile, a stable electrode-electrolyte interface needs to be achieved in order to provide a long cycle life. With this information, cathode materials with well-controlled pore structures could yield an improved electrochemical performance for the batteries. Considering the manufacturing cost along with the as-mentioned desirable electrode properties, Mn-based cathode materials are selected in this research, as listed in the following:

a) 4 V spinel $LiMn_2O_4$;

b) 5 V spinel $LiNi_{0.5}Mn_{1.5}O_4$;

c) layered-layered composite $xLi_2MnO_3 \cdot (1-x)LiNi_{0.5}Mn_{0.5}O_2$;

d) integrated layered-spinel composite $Li_{(1.2-\delta)}Ni_{0.2}Mn_{0.6}O_{(2-\delta/2)}$;

In this dissertation, a unique pyrolysis flame will be developed to produce spherical, non-agglomerated $LiMn_2O_4$ and $LiNi_{0.5}Mn_{1.5}O_4$ powders. The latter material is a quaternary-

metal-oxide, yet has not been successfully synthesized in other flames. Therefore, this work will propose a prototype flame process for the synthesis of multi-metal oxides with low-cost inorganic precursors. Spinel $LiMn_2O_4$ and $LiNi_{0.5}Mn_{1.5}O_4$ have three-dimensional Li transportation pathways, and they are thermodynamically stable. Because $LiNi_{0.5}Mn_{1.5}O_4$ has a higher operation voltage and improved cycle life over $LiMn_2O_4$, it holds promise for high-power applications, such as EVs.

The spray pyrolysis process developed will be able to synthesize the spinels and the composite materials with nano features besides having spherical, non-agglomerate and non-hollow morphologies. Layered-layered composite $xLi_2MnO_3\cdot(1\text{-}x)LiNi_{0.5}Mn_{0.5}O_2$ is a Li-excess layered material that structurally integrates Li_2MnO_3 and $LiNi_{0.5}Mn_{0.5}O_2$ together. Its capacity falls in the target range (200-300 $mAhg^{-1}$) therefore it can be applied in the batteries requiring high-energy densities. $Li_{(1.2-\delta)}Ni_{0.2}Mn_{0.6}O_{(2-\delta/2)}$ integrates $LiNi_{0.5}Mn_{1.5}O_4$ and $xLi_2MnO_3\cdot(1\text{-}x)LiNi_{0.5}Mn_{0.5}O_2$ (where $x = 0.5$). The spinel-type structure ideally incorporates 3-D Li transport sites in the 2-D networks, potentially improving the rate capability. Aside from chemical composition and crystallographic property, the pore structure of the particle plays a more significant role for holding a high capacity at elevated C-rates for the composite materials. Therefore, strategies are needed to optimize porous morphology, primary particle size, crystal structure and chemical composition in order to achieve a stable high-energy and high-power electrode.

1.5.2 Dissertation Outline

With these objectives, the dissertation will have mainly five parts. Chapter two will give a brief introduction about the methodology and experimental apparatus design. Chapter three will discuss the flame spray pyrolysis process for spinel-$LiMn_2O_4$ powder synthesis. Chapter four will discuss the disordered spinel $LiNi_{0.5}Mn_{1.5}O_4$ from the pyrolysis flame displaying superior cycle life. Chapter five will discuss the spray pyrolysis process for nanostructured layered-layered composite materials; and Chapter six will study nanostructured layered-spinel composite materials from spray pyrolysis process.

Chapter 2

Research Methodology

2.1 Powder Synthesis

2.1.1 Spray Pyrolysis

As discussed in Chapter 1, the spray pyrolysis has shown potential for continuous and rapid production of submicron to micron size powders. However, the particle size distribution, morphology, and quality are strongly dependent on precursor chemistry and the process. A wide size distribution and a hollow/shell structure were observed for $LiMn_2O_4$ particles produced with spray pyrolysis method [112, 113]. When the droplets enter the furnace heated to a high temperature (600-800 ºC), the solvent starts to evaporate very fast and the solute becomes supersaturated. The solute will start to precipitate forming crystallites on the surface. As further evaporation of the solvent, the crystallites continue to grow forming a solid shell. Therefore, hollow/shell-structured powder may be produced if the heat-transfer, particle size distribution, or the physical and chemical properties of the precursors are not well controlled. To prevent the formation of these unfavorable structures, a BGI atomizer is applied to generate ultrafine aerosol droplets containing the precursors. The critical droplet size for the onset of solute nucleation decreases as the initial droplet size decreases due to the short diffusion length. For that reason the as-synthesized powder may potentially show a non-hollow internal structure if the aerosolized precursor droplets are fine enough. Additionally, before entering the reaction zone, the precursor droplets enter a low-temperature evaporator, allowing the slow evaporation of water and precipitation of solute. The spray pyrolysis is explored to study the synthetic conditions and optimal morphologies of particles.

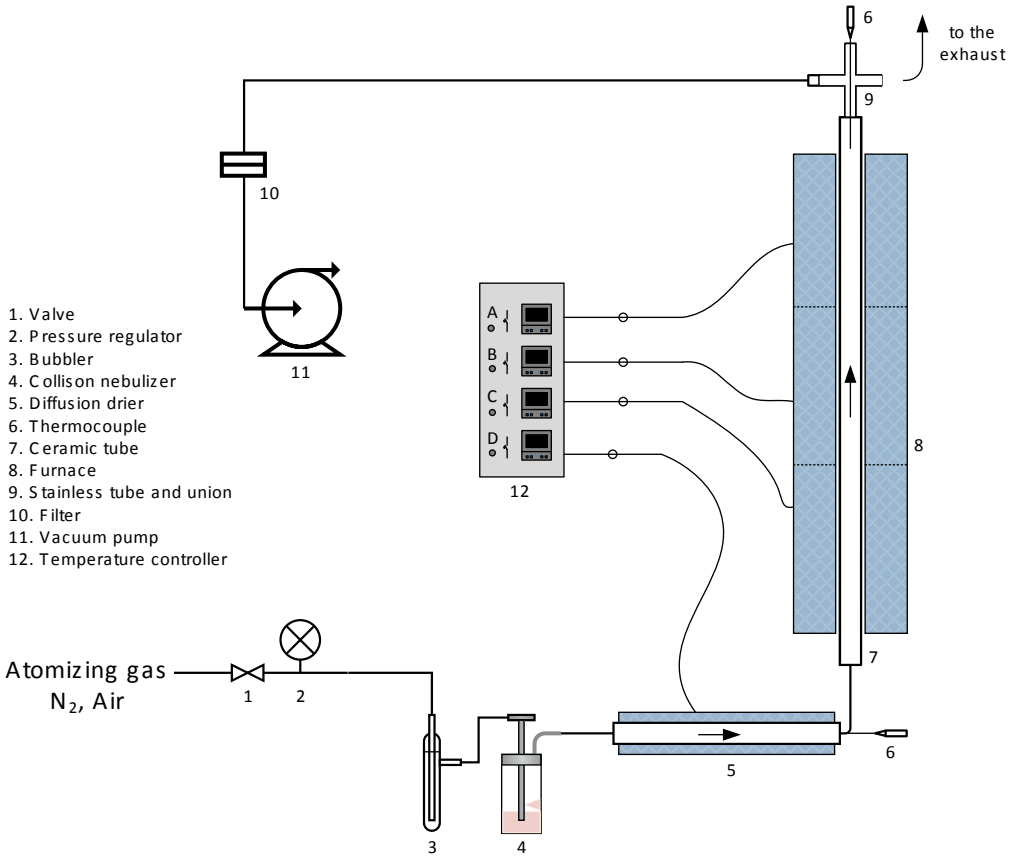

Figure 2.1 A schematic of the spray pyrolysis system with a two-stage aerosol flow reactor.

For the reasons stated above, the design of the spray pyrolysis system considered the following factors affecting the morphological characteristics of the final powders: (1) slow heating in the preheater which allows slow evaporation of solvent without forming solid shells on each individual particles; (2) appropriate furnace temperature profile that is sufficient high to decompose the precursor and calcine the primary particle without inducing impurity phases; (3) initial droplet size and salt concentration in the precursor solution; (4) relative humidity of the carrier gas that may reduce/eliminate evaporation of solvent in precursor reservoir (Collison nebulizer), maintaining a constant concentration

of precursor salts and thereof particle size distribution; (5) residence time associated with reactor dimensions and flow rate of the carrier gas.

The designed two-stage aerosol flow reactor consists of a low-temperature reactor at 300 °C wall temperature, and a hot-wall ceramic tube flow reactor (1 inch OD, ¾ inch ID, 3 ft. long) maintained at 600-800 °C wall temperature. The precursor solution was prepared by dissolving stoichiometric amounts of precursor nitrates in deionized water. A Collison nebulizer is applied to aerosolize the precursor solution. As seen in Figure 2.1, the aerosolized precursors enter the low temperature reactor where the solvent slowly evaporates completely. The gas temperature at the exit of the low-temperature furnace is monitored with a thermocouple, and is kept at about 100-130 ºC. The dried precursors then enter a hot-wall ceramic tube flow reactor maintained at 600-800 °C wall temperature, where the precursors decompose and the desired powder is synthesized. The gas temperature at the exit of the second reactor is also monitored by a thermocouple inserted into the ceramic tube. The powder is collected at the reactor exit.

2.1.2 Diffusion Flame Pyrolysis

As part of this work, a novel flame process has been designed to produce nanostructured $LiMn_2O_4$ and $LiNi_{0.5}Mn_{1.5}O_4$ particles. The pyrolysis flame that produces powders is an aerosol-assisted laminar hydrogen diffusion flame. Figure 2.2 shows the schematic diagram of the hydrogen diffusion flame experimental system. The burner jet has a 12.5 mm inner diameter and is made of 316-stainless steel. A cylindrical quartz chamber

(inner diameter 224 mm) is used as a shield around the jet to prevent disturbances from the surroundings. Honeycomb surrounds the jet, ensuring a uniform laminar flow of air in the quartz chamber. The precursor solution is prepared by dissolving $LiNO_3$ (anhydrous), and $Mn(NO_3)_2 \cdot 4H_2O$ (and $Ni(NO_3)_2 \cdot 6H_2O$ for synthesizing $LiNi_{0.5}Mn_{1.5}O_4$) in methanol at a stoichiometric ratio. The precursor solution is aerosolized with a BGI one-jet Collison nebulizer to generate ultra-fine precursor droplets. Methanol-saturated N_2 carries the precursor droplets into the flame. Downstream of the flame, the as-synthesized

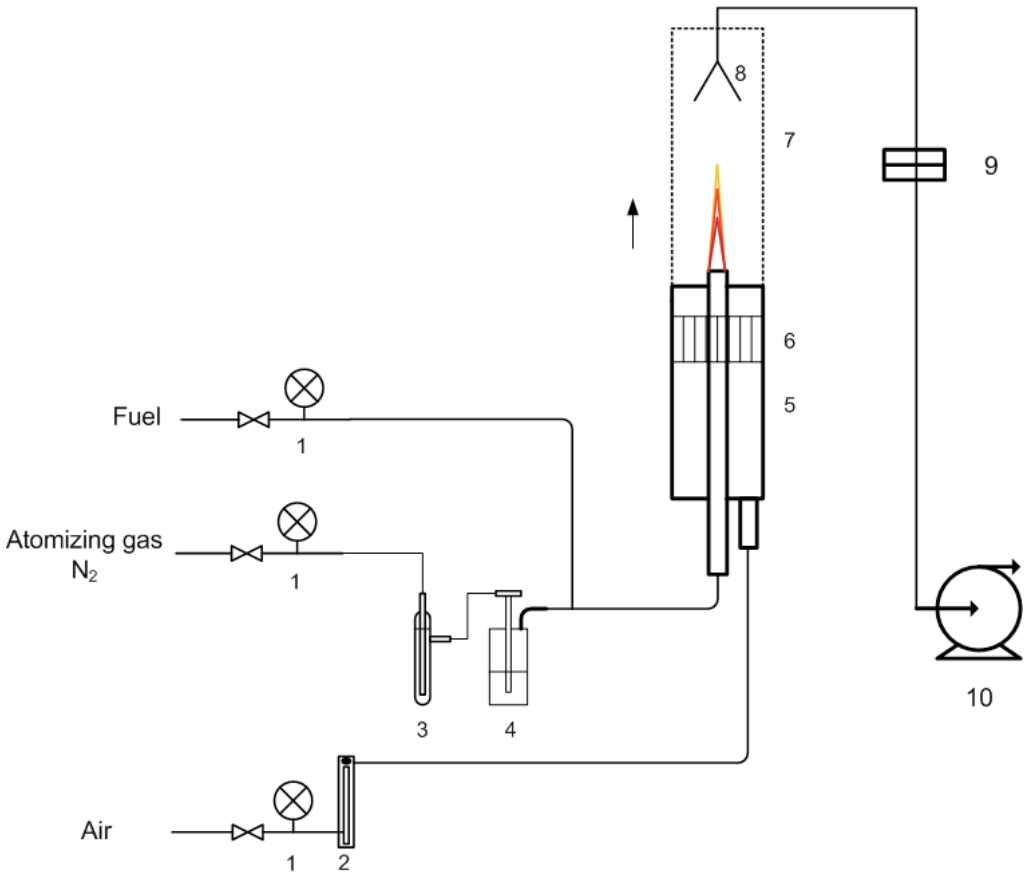

Figure 2.2 A schematic diagram of experiment system: 1. pressure gauge; 2. flow meter; 3. bubbler; 4. BGI Collison atomizer; 5. burner system; 6. honeycomb; 7. quartz shield; 8. collection funnel; 9. filter; 10. vacuum pump.

powder is collected with a Nuclepore Track-etch polycarbonate membrane-filter with a pore size of 0.2 μm. To improve the crystallinity and remove possible impurity-phases, the as-synthesized powders are annealed at 700 to 800 ºC for typically 2 hr followed by slow cooling in air at *c.a.* 3.7 °C/min.

2.2 Post-Treatment of the as-Synthesize Powders

An ideal electrode material should have good structural integrity and should not have impurity phase. Structural integrity may eliminate the side reactions between the electrode and the electrolyte, thus preserving the capacity. Powders from the spray pyrolysis (flow reactor) have an average crystallite size of less than 20 nm. Although at this scale the transportation of Li ions in the electrode may be very fast, the high surface area can lead the dissolution of Mn ions and side reactions with the electrolyte, which reduce the capacity as well. Thus, moderate heat treatment is necessary for the powders from spray pyrolysis to acquire the proper crystalline size.

Impurities may not necessarily deteriorate the cell, but they can lower the specific capacity of the cell. The as-synthesized powders (spinel $LiMn_2O_4$, $LiNi_{0.5}Mn_{1.5}O_4$ and *etc.*) in flames may have some impurity phases and defects. Post heat treatment is necessary to convert the impurities into the desired phase and reduce/eliminate the

oxygen-deficiency defects. In this research, the as-synthesized powder is annealed at elevated temperatures (600-800 ºC), and followed by slow cooling. The annealed powder shows better electrochemical performance than the as-synthesized powder. The detailed result will be discussed in the each of the chapters.

2.3 *In-situ* Particle Size Measurements

A proper particle size distribution is very important to improve the performance of the powders. In our current research, a BGI collision nebulizer was applied to generate fine precursor aerosol droplets. The particle size distribution is not only controlled by the atomizer, but also is controlled by the concentration of the precursor solution. A precursor solution with higher concentration can produce larger particles. In contrast, diluted solutions produce smaller dry precursor particles and this reduces the size of the final powders. A scanning mobility particle sizer (SMPS) is used to *in-situ* measure the particle size distribution of the as-prepared powder if the particles fall into 20-800 nm range. The SMPS charges the particles and only allows the particles with a certain electrical mobility to pass through the differential mobility analyzer (DMA). For larger particles, *c.a.* 1-10 μm, an electric low-pressure impactor (ELPI) is applied to measure particle size distribution. In the ELPI, a corona charger charges the particles in the aerosol stream, and then the charged particles release their charge when they impact on the corresponding stage by inertial force. Signals are collected and processed to generate

the particle size distribution profile. The *geometric mean diameter* $d_{p,g}$ and *geometric standard derivation* σ_g is calculated to describe the lognormal particle size distribution.

$$ln\, d_{p,g} = \frac{\sum n_i\, ln\, d_i}{N} \qquad (2.1)$$

$$ln\, \sigma_g = \sqrt{\frac{\sum n_i (ln\, d_i - ln\, d_{p,g})^2}{N-1}} \qquad (2.2)$$

where n_i is number of particles in i_{th} group, d_i is the midpoint diameter in i_{th} group and N is the total number of particles in the sample.

2.4 Crystallographic Analysis

2.4.1 Powder Diffraction

X-ray powder diffraction is a common physical tool to investigate the crystal structure of the crystalline powders. In this research, X-ray powder diffraction is performed on a Rigaku Geigerflex D-MAX/A Diffractometer using Cu-Kα radiation. The instrument is equipped with a vertical goniometer and a scintillation counter. Maximum power is 1.5 kW operating at 50 kV and 50 mA; however, all work is on geologic materials using 35 kV and 35 mA. Data is collected on the diffractometer using a PC-based Data scan software by MDI and processed using Jade 9 software. Typical scan step size is 0.04 ° (2θ) per step, and scan speed is one step per second.

In an ideal XRD powder diffraction analysis, the diffraction peaks should be sharp and smooth. However, in practice, peak broadening and changes in peak shape or smoothness might occur, arising from instrumental or powder sample contributions. The instrumental contribution is mainly caused by one of the following: (1) poor radiation source that has decayed or is not perfectly monochromatic; (2) shallow powder samples; (3) the dimensions and configuration of the slits in the diffractometer; and (4) misalignment of the diffractometer. The instrumental contributions will give inaccurate XRD data, resulting in misleading information on the crystal structures. Peak broadening mainly arises from nanosized crystallites and inhomogeneous strains in the specimen. The lattice strain is inhomogeneous with the presence of defects, such as dislocations and vacancies. Any change in *d-spacing* from defects in a crystallite can cause a shift in diffraction angle 2θ near Bragg peaks, therefore peak broadening might be observed. Inhomogeneous strain is not studied in this dissertation. Peak broadening is also related to the nanosized crystallite, and it can be applied to estimate crystallite sizes. The Scherrer equation correlates the broadness of the diffraction peaks and the crystallite size (*L*) of the nanostructured materials.

$$L = \frac{K\lambda}{\beta \cos\theta} \qquad (2.3)$$

where K is the shape factor (about 0.9), λ is the radiation wavelength, θ is the usual Bragg angle and β is the *full-width-at-half-maximum (FWHM)* of the peaks. The use of Scherrer formula is limited to the cases where the average crystallite size is less than 1 μm.

2.4.2 Cell Refinement

Cell refinement extracts finite information from the XRD patterns to identify the crystal phase and refine the cell parameters, such as space group and symmetry, lattice parameters and indexing. *Whole pattern fitting (WPF)* approach is applied to refine the crystal structure of powders produced in this work. WPF approach entails the calculation of an XRD pattern, which fits the experimental data as close as possible. This dissertation includes two methods for WPF refinement: (1) Rietveld method, which is conducted by tuning the parameters of already-known crystal structures to best fit the observed pattern; (2) observed pattern method which matches the observed pattern with the reference pattern in the database, such as Crystal Structure Data (CSD) and Powder Diffraction Files (PDF). The commercial software Jade, or example combines Rietveld method and the observation method (WPF function). The essential differences between Rietveld refinement and observed pattern method is that no atom position and site occupancies can be refined in the latter method. With observed pattern method, some structural information may be lost for the crystals with defects. The use of this method is therefore recommended if the phase is pure with less or no defects, and the Bragg peaks are sharp enough and well positioned. Rietveld refinement is the first mathematical model in refining crystal structures based on known crystal XRD diffraction data, and it can describe both the profile parameters (indexing, peak shape and background) and atomic information (atomic coordinates and occupancy). The foundation of Rietveld refinement is a least-square method for the calculation of the entire pattern deduced from the

intensities. In this work, Rietveld method is generally applied to investigate atomic information.

2.5 Morphology Studies

Besides SMPS measurements, a state-of-the-art high-resolution transmission electron microscope (TEM, JEOL JEM-2100F) is employed for characterization of as-prepared powders. TEM imaging is used to identify the internal structure of as-prepared particles, and primary/secondary particle sizes. TEM lattice-fringe imaging is employed for direct identification of crystalline structure of a single crystal in a particle. This instrument is equipped with a Schottky FEG emitter (0.5 nA at 1 nm FWHM) and has a point-to-point resolution of 0.23 nm. In addition to the high-resolution TEM, A Tecnai^{TM} G^2 Spirit TEM with a line resolution of 0.20 nm is also applied in this research.

The particle morphology is examined with scanning electron microscopy (SEM). A Hitachi S-4500 field emission SEM is used in this research. This SEM has a very high spatial resolution at all of its working voltages: 4 nm at 1 kV and 1.5 nm from 15 kV to 30 kV. Porous morphology is observed using a FEI Nova 230 SEM with a resolution of 1.6 nm at 1 kV. Working distance and operation voltage are subject to change in corresponding experiments. A Noran Energy Dispersed Spectrometer (EDS) elemental analysis system allows chemical analysis of all elements heavier than beryllium, and also

provides facilities for digitizing and processing images. Ultramicrotome (Leica EM UC7) is applied to section the particle to obtain the morphology of the internal structure.

In addition to the morphology study, the specific area of the powders is measured by Brunauer-Emment-Teller (BET, Autosorb-1 Series) method in N_2. Thermal gravimetric analysis (TGA) is used to test the decomposition temperature of precursors, hence to understand the chemistry behind the synthesis process.

2.6 Battery Performance Evaluation

2.6.1 Cell Fabrication

A Li-ion cell consists of an anode and a cathode separated by an ionic conductive membrane separator. All the components in a Li-ion cell are soaked in electrolyte containing Li salts, as described in Chapter 1. In this research, the synthesized powders are assembled as cathode-active materials into 2032 coin-type half-cells (cells with elemental lithium as the counter electrode). To prepare the cathodes, a mixture of the synthesized powder, polyvinylidene-fluoride (PVdF) binder, and Super-P conductive-carbon-black at a proper ratio is dissolved in N-methyl-2-pyrrolidene (NMP) and then homogenized to form a homogenous slurry. The amount of PVdF and carbon black varies for different cathode materials in the research, as given in each chapter. The spinels have 3D-diffusion pathways, therefore a high rate capability is expected and less conductive

carbon black is required. For the layered-structured materials, more conductive carbon black is desired in order to achieve a satisfactory rate performance. The cathode slurry is then cast on an Al foil using the doctor blade technique to form a thin cathode film. The cathode film is dried in a vacuum oven at 120-130 °C for 16 hr. To improve adhesion, the cathode is calendared, forming a compressed, thin film. Small, round, cathode plates are punched out from the dry film for the test batteries.

The 2032 coin-type test batteries are assembled in a glove box filled with ultra high purity argon gas. The configuration of the 2032 test cell is shown in the Appendix D. A Li thin foil is employed as an anode and a polypropylene membrane (Celgard 2500) is used as the separator. The electrolyte is chosen among 1M $LiPF_6$ in ethylene carbonate/diethyl carbonate solution (EC:DEC = 1:1 or 1:2 by weight, Ferro) at LBNL, and 1M $LiPF_6$ in ethylene carbonate/dimethyl carbonate solution (EC:DMC = 1:1 by volume, Ferro) and 1M $LiPF_6$ in ethylene carbonate/diethyl carbonate solution/dimethyl carbonate solution (EC:DEC:DMC = 1:1:1 by volume, MTI) at Washington University (WU). The electrochemical performance of the cells is tested with a computer controlled MACCOR (Model 4200) battery tester (LBNL) or MTI battery analyzer (WU) at various charge/discharge rates. The experimental parameters (e.g., current density, cut-off voltage) may vary for different cathode materials, and the test temperature is specified in each chapter.

Some of the battery tests for spinel $LiMn_2O_4$ and $LiNi_{0.5}Mn_{1.5}O_4$ was performed at Lawrence Berkeley Nation Laboratory (LBNL) at the early stage. An independent

validation of the battery test results has been performed at Washington University, which has shown consistency to the data acquired at LBNL. Thus, the fabrication of the coin cells, performed test and the results are considered valid and consistent in the research.

2.6.1 Li-ion Battery Test Protocol

The prepared cathode materials are assembled in half cells (cells with lithium metal as the counter electrode), then it is able to measure the reversible capacity and first cycle irreversible capacity, and even the cyclic voltammetry; however, this approach will not be able to measure long-term cycleability, as lithium forms dendrites and shorts the cell, or any effects of migration of species from cathode to anode as has been seen with many Li-ion chemistries. For this reason, only 50 to 100 cycles are performed to display a trend of the battery cycle life as the cell is cycled. Once the capacity of the first charge of the cathode is known (C/20 to C/10 at the first cycle), cells made with the synthesized powders perform the following tests: rate capability (which is a series of cycles at C/10, C/5, C/2, C3/4, and C/1), and cycle life (C/10 for 50 to 100 cycles).

Cell testing and characterization can take from weeks to months. At C/10 discharge, 50 cycles will take approximately 2 months. Thus, new chemistries can be evaluated on a 3-month interval if includes material synthesis and characterization. This is about the length of time it will take to analyze a given chemistry, understand its benefits and deficiencies, and synthesize a new chemistry. In the beginning, before new chemistries are developed,

we spend some time optimizing our electrode formulations for the baseline chemistry. This involves determining the proper ratio of carbon to binder and inactive material to active material. Once the best formulation is identified, we evaluate solvent content and its effect on electrode casting and performance.

Chapter 3

Flame Synthesis of 4 V Spinel $LiMn_2O_4$ [1]

[1] Published in Journal of Power Sources, 2011

Spinel lithium manganese oxide $LiMn_2O_4$ and its derivatives have gained attention as an alternative to lithium cobalt oxide ($LiCoO_2$), which is currently being used commercially as a cathode material for lithium-ion secondary batteries. Spinel $LiMn_2O_4$ has many desirable advantages, including high rate performance due to its 3-D framework, high energy density, low cost, low toxicity, and simplicity of preparation [73]. The conventional approach to synthesis of $LiMn_2O_4$ spinel is the solid-state reaction of a mixture of lithium and manganese precursors at high temperature [39]. Sometimes, mechanical grinding (*e.g.,* ball milling) is needed to reduce particle size [146]. Other approaches to synthesis have been developed, including the Xerogel method [147], hydrothermal [148], sol-gel method [149], sputtering [150], and coprecipitation [151]. These methods have been shown to produce powders that have narrow size distribution, and uniform composition and morphology, yielding good electrochemical performance. Nonetheless, none of these processes are continuous, and long reaction times are required.

In the past decade, spray pyrolysis, which is a continuous process, has been studied to synthesize fine $LiMn_2O_4$ powder and its derivatives, yielding materials with good electrochemical performance [43, 110, 113, 152-154]. Spray pyrolysis is an aerosol process that can involve gas-, liquid-, and solid-phase reactions. The as-synthesized particles are in the nano- to micron-size range and can have a variety of morphologies. Common spray pyrolysis processes include ultrasonic spray pyrolysis [112, 113], electrospray pyrolysis [152], and spray drying [153]. In the spray pyrolysis process the precursor solution is aerosolized to form fine precursor droplets. The aerosolized precursor is then introduced into a tubular furnace reactor in which the solvent evaporates,

and then the precursors precipitate and decompose forming the desired product [112]. Under certain conditions, shell-structured $LiMn_2O_4$ particles are present in the products and this lowers the packing density of the material [112, 134]. Spray pyrolysis requires external heating to maintain reactor temperature and this non-uniform heating can lead to non-uniformities in product, making it difficult to scale up [139, 155].

Flame synthesis is a widely used technique to synthesize a number of functional powders over a range of sizes from nano- to micrometers, *e.g.,* carbon nanotubes and carbon black [104, 156, 157], metal oxide particles (TiO_2, SiO_2, Y_2O_3:Eu) [158-160], and non-oxide ceramics (Ti, TiB_2, Ta, and AlN) [161-164]. Among them, carbon black is the most successful example with daily production of about 100 tons [157]. In the past few years, flame techniques have been applied to synthesize oxides of multicomponent metal oxide powders for energy applications. Perovskite-type compounds have been produced by flame aerosol synthesis for applications in oxygen-separation membranes [165] and by flame hydrolysis to produce catalyst particles for catalytic combustions [166, 167]. In flame synthesis, the exothermic reaction between fuel and oxidizer generates heat to create a high temperature environment. Thus, it does not require external heating, and the heating is volumetric in flames. By changing the flame temperature and precursor solution composition, crystal structure and particle sizes can be varied. Hence, flame synthesis has the potential to produce cathode materials for lithium-ion batteries at a large scale and low cost.

Jang *et al.* has synthesized $LiCoO_2$ nanoparticles synthesized *via* flame spray pyrolysis (FSP) using H_2 as the fuel [123]. However, the electrochemical properties of the as-synthesized $LiCoO_2$ nanoparticles were not evaluated in that work. Recently, Pratsinis *et al.* developed an alternative FSP process to produce spinel-$LiMn_2O_4$ cathode materials using liquid-phase fuels [126, 142]. In this process, metallic-organic compounds were dissolved in an organic solvent to serve as precursors. The as-produced spinel-$LiMn_2O_4$ showed a good rate capability at 4 V [125]. Nonetheless, the commercial viability of the FSP process is highly dependent on the price, availability, and compatibility of the metallic-organic precursor compounds and solvents. In the present work, a flame-assisted spray technology (FAST) is developed to produce spinel $LiMn_2O_4$ powders using low-cost metal-nitrate precursors.

3.1 Precursor Chemistry

To understand the formation mechanism of the spinel $LiMn_2O_4$ in the pyrolysis flame, the thermal properties of the precursors $LiNO_3$ and $Mn(NO_3)_2{\cdot}4H_2O$ were studied by TGA analysis. Three experiments were performed: (1) $Mn(NO_3)_2{\cdot}4H_2O$ only, (2) $LiNO_3$ only, and (3) a stoichiometric amount of $LiNO_3$ and $Mn(NO_3)_2{\cdot}4H_2O$, all in methanol. The decomposition reaction mechanisms of $Mn(NO_3)_2$ and $LiNO_3$ are known, and their decomposition products are MnO_2 and Li_2O, respectively [168]. As indicated by the dotted-line in Figure 3.1, pure $Mn(NO_3)_2$ decomposed into oxides in the temperature range of 200 to 280 °C, as indicated by the large weight loss. Pure $LiNO_3$ began to

decompose at around 600 °C and was fully decomposed by 750 °C, as indicated by the dash-line. However, as shown by the solid-line, the complete decomposition of the mixture of precursors occurred at 480 °C, more than 200 °C less than that of the pure $LiNO_3$ salt. For a 1:2 molar ratio of $LiNO_3$ and $Mn(NO_3)_2{\cdot}4H_2O$ precursors, the total weight loss was calculated to be 57.5%, assuming complete decomposition of $Mn(NO_3)_2{\cdot}4H_2O$ to MnO_2, and the measured weight loss from TGA was 57.6% at 280 °C. Similarly, for complete decomposition of $LiNO_3$ to Li_2O, the calculated weight loss was 66.9%, compared to a measured weight loss of 67.1% at 480 °C. Thus, the assumed decomposition products were valid even for the mixture of nitrate precursors. Importantly, the decomposition temperature of $LiNO_3$ was much lowered in the mixture than alone. The lower decomposition temperature of $LiNO_3$ for mixtures has also been observed using a mixture of electrolytic manganese dioxide MnO_2 and $LiNO_3$ [169]. This was understood to be due to the presence of MnO_2, acting as a catalyst for the pyrolysis reactions [169]. Figure 3.1 also shows that if $Ni(NO_3)_2{\cdot}6H_2O$ was added, forming a 1:1.5:0.5 (Li:Mn:Ni elemental ratio) mixture, the completed decomposition of the salts occurs near 400 °C. The decomposition reaction of dehydrated $LiNO_3$, $Mn(NO_3)_2$ and $Ni(NO_3)_2$ can be written as below (source: High Temperature Properties and Thermal Decomposition of Inorganic Salts, CRC press, 2001):

$$LiNO_3 \rightarrow \frac{1}{2}Li_2O + NO + NO_2 \qquad (3.1)$$

$$Mn(NO_3)_2 \rightarrow MnO_2 + 2\,NO_2 \qquad (3.2)$$

$$Ni(NO_3)_2 \rightarrow NiO + 2\,NO_2 + \frac{1}{2}\,O_2 \qquad (3.3)$$

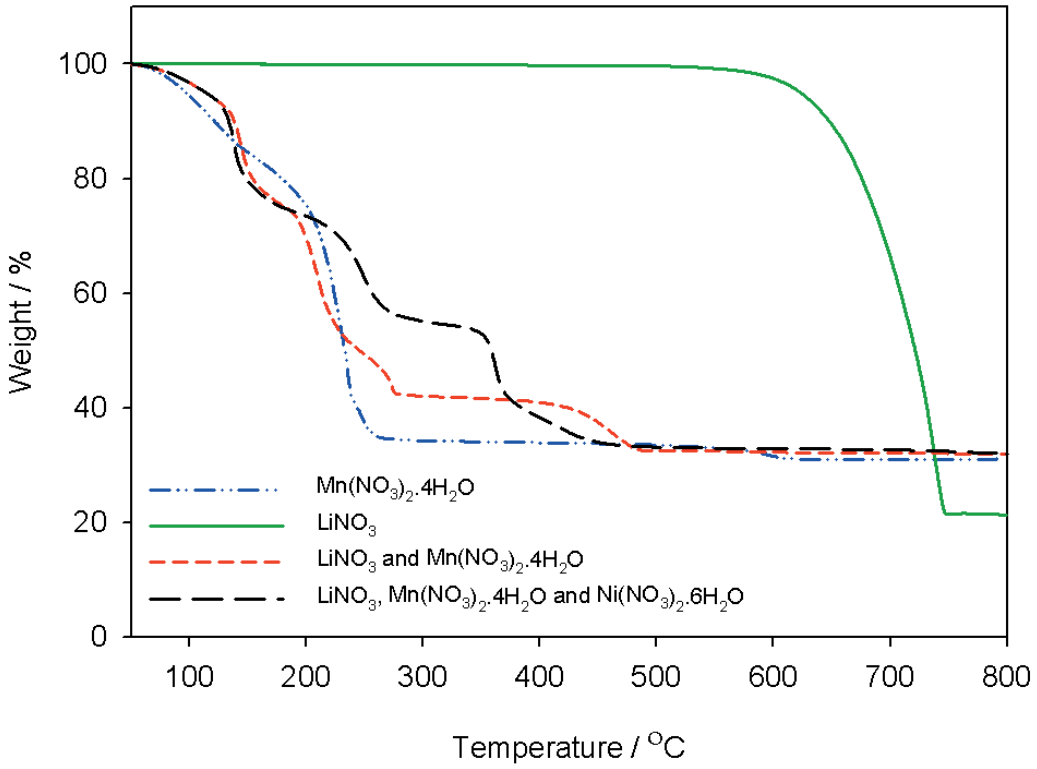

Figure 3.1 TGA measurements of the individual precursor $LiNO_3$, $Mn(NO_3)_2 \cdot 4H_2O$, $Ni(NO_3)_2 \cdot 6H_2O$, and their stoichiometric mixture.

3.2 Flame Structures

The precursor was prepared by dissolving stoichiometric quantities (1:2 molar ratio) of $LiNO_3$ and $Mn(NO_3)_2 \cdot 4H_2O$ in methanol. The concentrations of $LiNO_3$ and $Mn(NO_3)_2$ were 0.5 mole L^{-1} and 1.0 mole L^{-1}, respectively. The flow rates of H_2 and the atomizing gas N_2 were kept at 0.5 L min^{-1} and 2.5 L min^{-1}, respectively. The flame temperature was measured with a Pt/Rh thermocouple inserted into the flame. The data was recorded with an Omega wireless thermocouple connector. The visible flame used to produce spinel

$LiMn_2O_4$ was about 15 cm tall. Both H_2 and methanol are combustible and their oxidation provides heat for the synthesis reaction of spinel $LiMn_2O_4$. Temperature was measured along the axis with a Pt/Rh thermocouple (bead size = 340 μm). Figure 3.2 shows axial temperature profile, uncorrected for radiation heat loss, as a function of the height above the burner (HAB). The highest temperature in the flame was 1100 °C and occurred at 13.4 cm HAB. This temperature was higher than the temperatures associated with the solid-state reaction, spray pyrolysis, and sol-gel methods, which are in the range of 200 to 1000 °C [3, 82, 149]. Nonetheless, the residence time of the aerosol at this temperature (1100 °C) was only milliseconds. The flame temperature could not be lowered further in the current setup without causing the flame to become unstable.

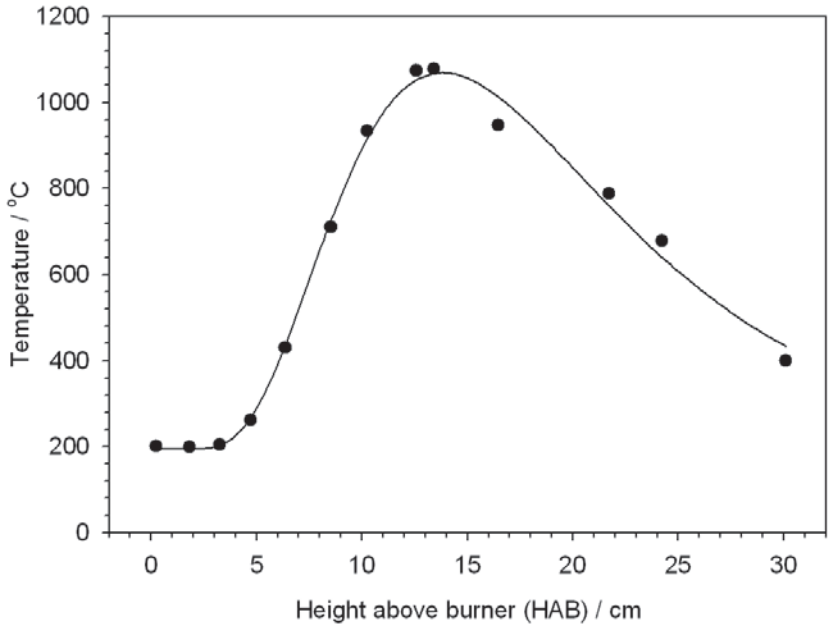

Figure 3.2 Measured temperature profile as a function of height above burner (HAB). Temperatures are not corrected for radiative heat loss from the thermocouple.

The formation of spinel $LiMn_2O_4$ in the flame is expected to follow a sequence of (1) evaporation of the methanol solvent, (2) pyrolysis of the precursors, (3) synthesis reactions of spinel $LiMn_2O_4$, and (4) sintering and coarsening of the primary particles. In the center of the flame, the temperature increased slowly until 5.0 cm HAB and then the temperature increased rapidly, as seen in Figure 3.2. At this point, the solvent methanol would begin to evaporate quickly, as the temperature (> 220°C) was far above its boiling point (*c.a.* 65 °C). After evaporation, the Li and Mn nitrate precursors would begin to precipitate. Based on the TGA data, the precursor $Mn(NO_3)_2$ should start to decompose almost immediately upon evaporation of the solvent in the flame. Up until 7 cm HAB, the temperature was less than 430 °C, where $LiNO_3$ would begin to decompose. The temperature increased rapidly beyond this point, which is expected to lead to rapid thermal decomposition of the $LiNO_3$ and $Mn(NO_3)_2$ precursors. Further downstream in the flame, the particles coarsen and sinter. In the post flame region (15 to 30 cm HAB), the temperature dropped slowly, allowing the nano grains to grow into larger crystallites.

A characteristic residence time of the precursors/product in the flame reactor can be estimated by assuming the particles follow the flow field and neglecting buoyancy in the flame (if buoyancy is considered, the residence time will be shorter). The length scale is considered to be 30 cm because beyond 30 cm HAB, the temperature was less than 400 °C, so sintering of $LiMn_2O_4$ would be negligible. At a total flow rate of 3.0 L min^{-1} (H_2+N_2), the characteristic residence time was calculated to be less than 800 milliseconds, which is the shortest synthesis time among current synthesis methods for spinel $LiMn_2O_4$. For ultrasonic spray pyrolysis, sol-gel and solid-state reaction methods, it takes seconds

to hours to synthesize nanocrystalline $LiMn_2O_4$ powder [39, 113, 149]. The short formation times were due to the rapid evaporation of solvent methanol, followed by rapid decomposition reactions of precursors and synthesis reactions of the spinel in the flame. At the high flame temperature, the solvent methanol also reacted as a fuel supporting local heat release at the flame. Thus, the FAST process is a rapid process to make $LiMn_2O_4$ powder continuously with low energy requirements.

3.3 Crystallographic Analysis

The XRD pattern of the as-synthesized powder matched the spinel $LiMn_2O_4$ structure as indicated by the strong intensities of the (111), (311) and (400) planes, as seen in Figure 3.3a. The wide XRD peaks of the as-synthesized powder indicated a nanocrystalline structure. The elemental ratio of Li and Mn was 1.01:2 as measured by ICP-MS analysis, which is consistent with spinel $LiMn_2O_4$. However, some impurities coexisted with the as-synthesized powder, as indicated by the minor peaks on the XRD spectrum. The impurity was identified as Mn_3O_4, which is known to form at elevated temperatures. Studies have shown that at elevated temperatures, oxygen may be extracted from spinel $LiMn_2O_4$, forming oxygen deficient spinel [75, 170, 171]. If the temperature exceeds 1000 °C, the spinel would eventually decompose into orthorhombic $LiMnO_2$ and Mn_3O_4, and release O_2 in an oxygen extraction reaction [75]. In the flame, the residence time of the particles in the high temperature region was very short, so only a small portion of

spinel $LiMn_2O_4$ decomposed into Mn_3O_4 in the flame. Nonetheless, a post-annealing treatment was necessary to remove the impurity in the flame-synthesized spinel $LiMn_2O_4$.

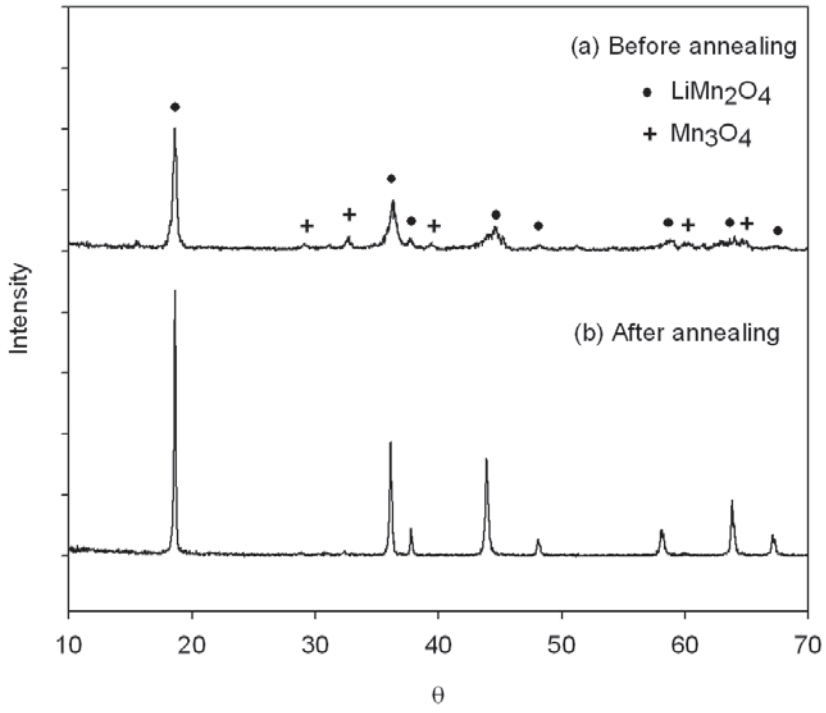

Figure 3.3 XRD patterns of the flame-synthesized $LiMn_2O_4$ powder: (a) before annealing and (b) after annealing at 700 °C for 2hr.

After annealing the as-synthesized powder at 700 °C for 2 hr, the XRD pattern was a good match to the single-phase spinel $LiMn_2O_4$ with a space group $Fd\bar{3}m$, as shown in Figure 3.3b. No Mn_3O_4 impurity was detectable in the XRD spectrum. The crystallinity of the powder was also greatly improved, as indicated by the sharper XRD peaks. After Rietveld cell refinement, the lattice parameter *a* of the annealed powder was 8.234 Å, which is in good agreement with spinel $LiMn_2O_4$. The average grain size of the annealed

powder was 33 nm, as estimated by the Scherrer formula (*fwhm* = 0.268°, 2-Theta = 43.981°, $\lambda_{Cu/K-\alpha 1}$ = 1.54 Å).

3.4 Powder Morphology

The SEM and TEM photographs of $LiMn_2O_4$ powder, before and after annealing are shown in Figure 3.4. The as-synthesized particles were submicron in size, with some particles falling into the nano-size range, as seen from Figure 3.4a. The secondary particles consisted of irregular-shape, nano-size primary particles. The porous morphology of as-synthesized powder was similar to that of the powder made with spray pyrolysis when using $LiNO_3$ and $Mn(NO_3)_2$ as precursors [112, 113], however, the particle surface appeared smoother after annealing. The as-synthesized $LiMn_2O_4$ powder also showed a polycrystalline structure, as seen in the TEM image of Figure 3.4b.

The size distribution of the as-synthesized aerosol is shown in Figure 3.5a as measured by SMPS. The geometric mean diameter of the as-synthesized powder was 160 nm with a geometric standard derivation σ_g of 1.58. After annealing, the nano-sized particles did not exist, as can be seen by comparing the images of Figure 3.4a with 3.4c, and 3.4b with 3.4d, and the powder showed a clearer facet structure, as compared to the as-synthesized powder. By measuring 390 different particles in the SEM images, the size distribution of the annealed powder was obtained, as shown in Figure 3.5b. The geometric mean diameter of the annealed powder was 330 nm with a geometric standard derivation, σ_g, of 1.81.

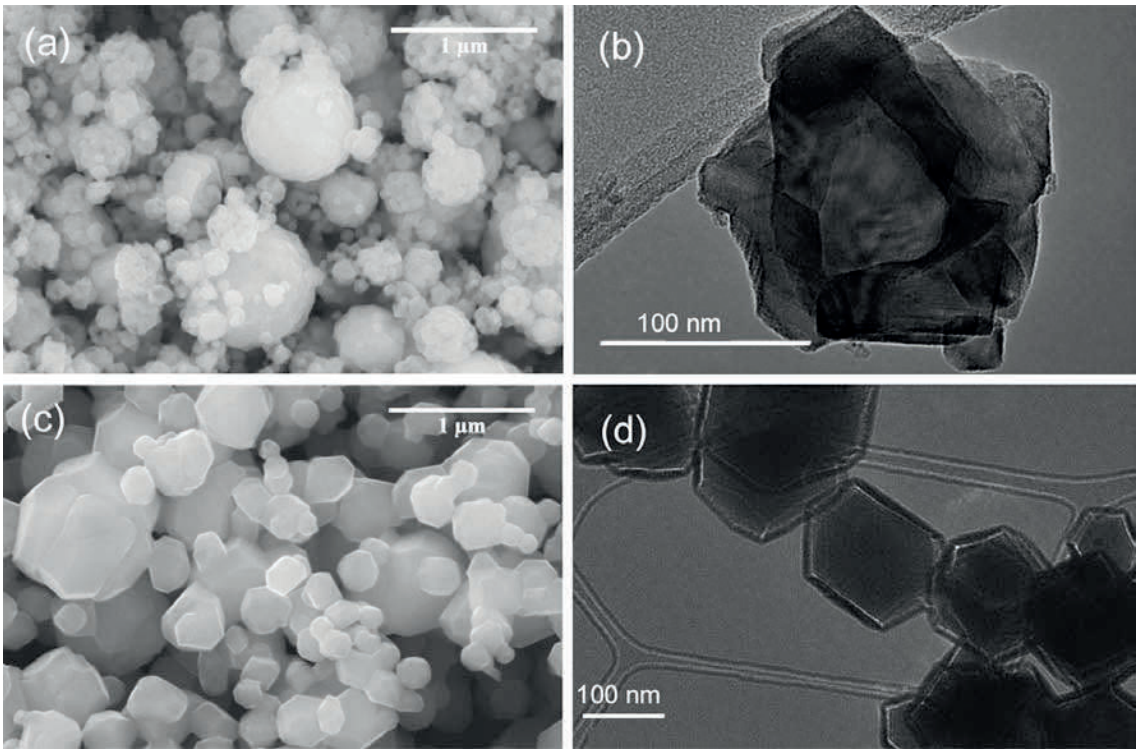

Figure 3.4 Morphology of the $LiMn_2O_4$: (a) SEM of the powder before annealing; (b) TEM of the powder before annealing; (c) SEM of the powder after annealing; (d) TEM of the powder after annealing at 700 °C for 2hr. (SEM scale bar = 1 μm; TEM scale bar = 100 nm).

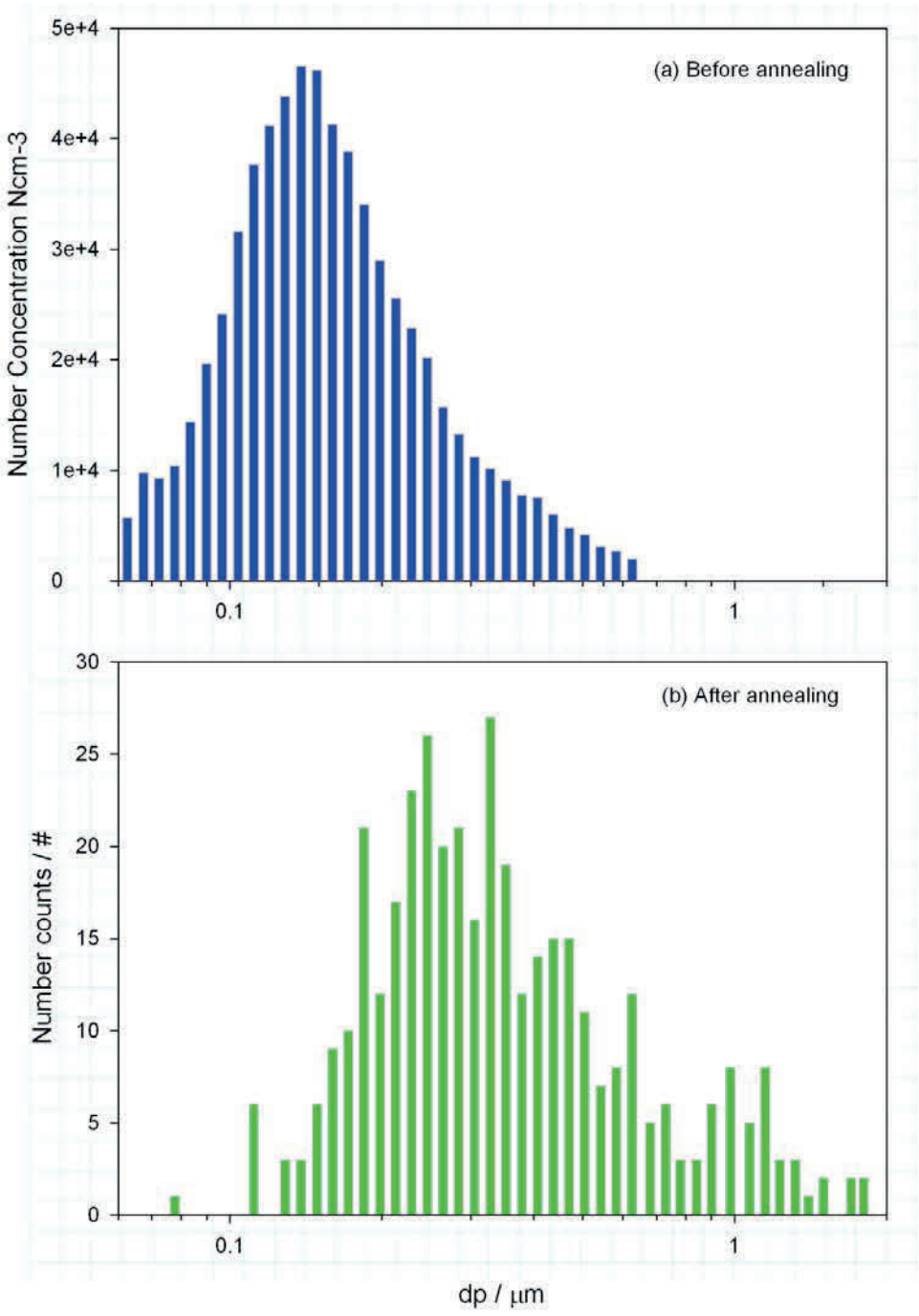

Figure 3.5 Size distribution of the flame-synthesized $LiMn_2O_4$ powder: (a) before annealing and (b) after annealing at 700 °C for 2 hr.

3.5 Battery Performance Test

3.5.1 Voltage Profile and Capacity

2032 coin-type half-cells were assembled with the unannealed (as-synthesized) and annealed $LiMn_2O_4$ powder as active cathode materials, and the cells were charged/ discharged between 2.5 and 4.3 V at C/10 rate (1 C = 120 $mAhg^{-1}$). As seen in Figure 3.6a, the initial charge/discharge curve shows the characteristic voltage plateaus at 2.8 V and 4 V *vs.* Li, corresponding to spinel $LiMn_2O_4$ with an $Fd\bar{3}m$ space group structure. The initial charge and discharge capacity of the unannealed powder was about 70 $mAhg^{-1}$at 4 V, which is much lower than the theoretical capacity of $LiMn_2O_4$ (148 $mAhg^{-1}$). Nonetheless, the result was quite consistent with the measured capacity of nanocrystalline spinel $LiMn_2O_4$, which is from 70 to 100 $mAhg^{-1}$ in the 4 V range [43]. The lower capacity at 4 V than the theoretical value for the as-synthesized powder can be explained by the large surface area, lower crystallinity [42, 43, 172], and also by the level of impurities in the powder. In the 3.0 V range, the initial discharge capacity of unannealed powder was about 60 $mAhg^{-1}$, which is also lower than the theoretical value of spinel $LiMn_2O_4$. This could be due to the oxygen deficiency of the spinel $LiMn_2O_4$ which can lead to a large capacity loss in the 3 V range. As discussed earlier, Mn_3O_4 was detected in the as-synthesized powder. Mn_3O_4 was not electrochemically active, so its presence lowered the capacities in both the 3 V and 4 V range. Due to the low overall capacity, the cell made with unannealed $LiMn_2O_4$ powder was not subject to further testing.

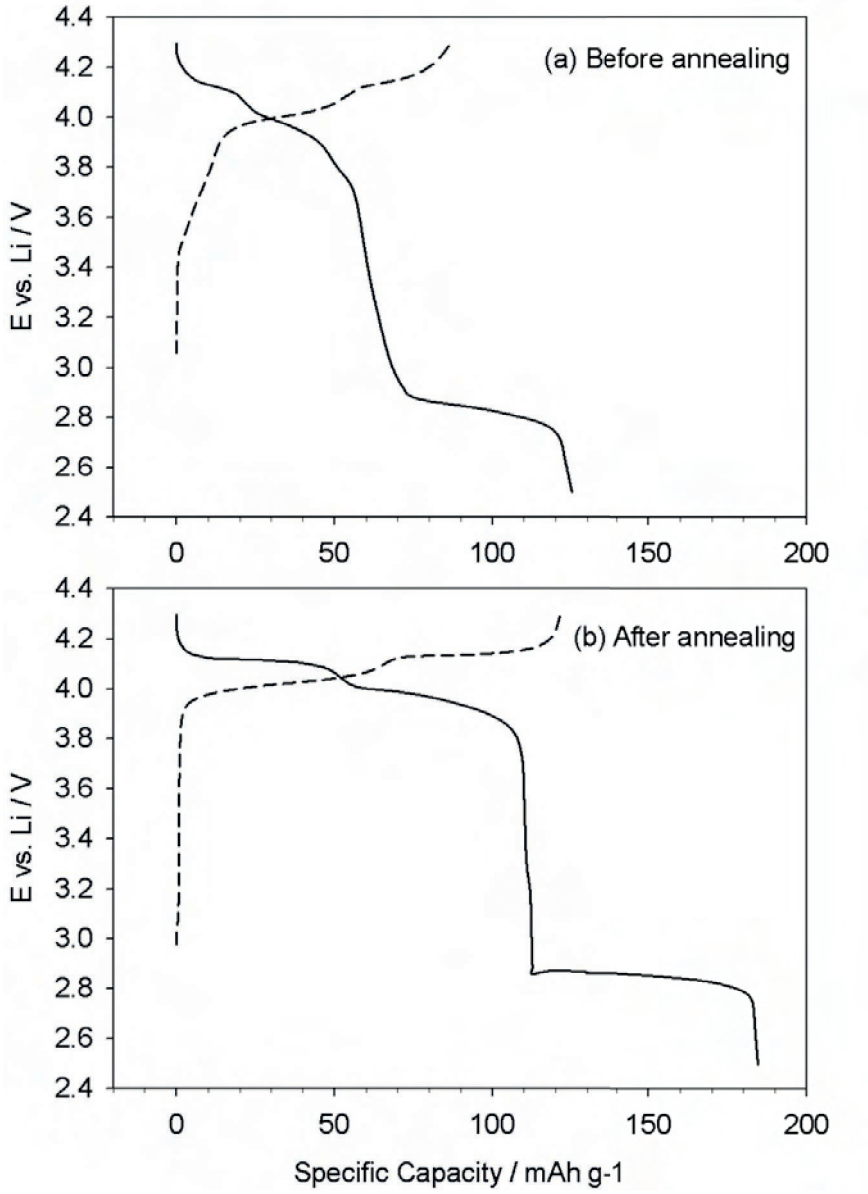

Figure 3.6 Initial charge/discharge curve of the flame-synthesized $LiMn_2O_4$ powder: (a) before annealing and (b) after annealing at 700 °C for 2hr (dash line: charge curve; solid line: discharge curve).

As shown in Figure 3.6b, after annealing, the $LiMn_2O_4$ powder showed a clearer two-staged lithium intercalation behavior at a voltage of 3.9 V and 4.16 V, which is indicative

of a single-phase spinel $LiMn_2O_4$ structure. The initial charge and discharge capacities were about 120 $mAhg^{-1}$ and 115 $mAhg^{-1}$, respectively, in the 4 V range. The reversible discharge capacity was 96% in the first cycle. The initial charge/discharge capacity was dramatically improved when compared to the as-synthesized powder because of the improved crystallinity and lack of impurities. However, the trend of the initial discharge curve in the entire range from 2.5 to 4.3 V was similar to that of slightly oxygen-deficient spinel $LiMn_2O_4$, for which the capacity in the 3 V range was low, about 70 $mAhg^{-1}$ [170]. Although the oxygen extraction reaction, which leads to oxygen deficiency, is a reversible process, the oxygen vacancy in the spinel may not have been completely recovered by annealing at 700 °C for 2 hr.

3.5.2 Rater Performance

The rate capability of the annealed $LiMn_2O_4$ powder was evaluated at various C-rates, from C/10 to 2C (1C =120 $mAhg^{-1}$) with a cut-off voltage of 3.0 to 4.3 V. The charge/discharge rate was increased every five cycles, as indicated in Figure 3.7. In the first 10 cycles, the capacity of the cell rapidly faded from 115 $mAhg^{-1}$ to 104 $mAhg^{-1}$ at a charge/discharge rate from C/10 to C/5. At the 11th cycle, a transitional cycle from C/5 to C/2 rates, the capacity dropped dramatically, and then the cell showed a better capacity retention with an average coulombic efficiency of 99% at C/2 rate. At the transition from 1C to 2C, the cell also showed a large capacity loss with a coulombic efficiency of about 92%. In the next few cycles at 2C, the cell showed less capacity loss with an average

coulombic efficiency of 98%. The capacity fading was also observed in the annealed flame-synthesized spinel $LiMn_2O_4$. The reasons for capacity fading are understood to be manganese dissolution, electrolyte decomposition at high potentials, and the loss of crystallinity during cycling [114]. In addition, the small amount of oxygen deficiency may have been another reason for the capacity fading of the annealed $LiMn_2O_4$ [171]. Nonetheless, considering that only 6 % conductive carbon black was added to the cathode, the annealed flame-synthesized powder showed an acceptable cycling performance at increasing C-rates.

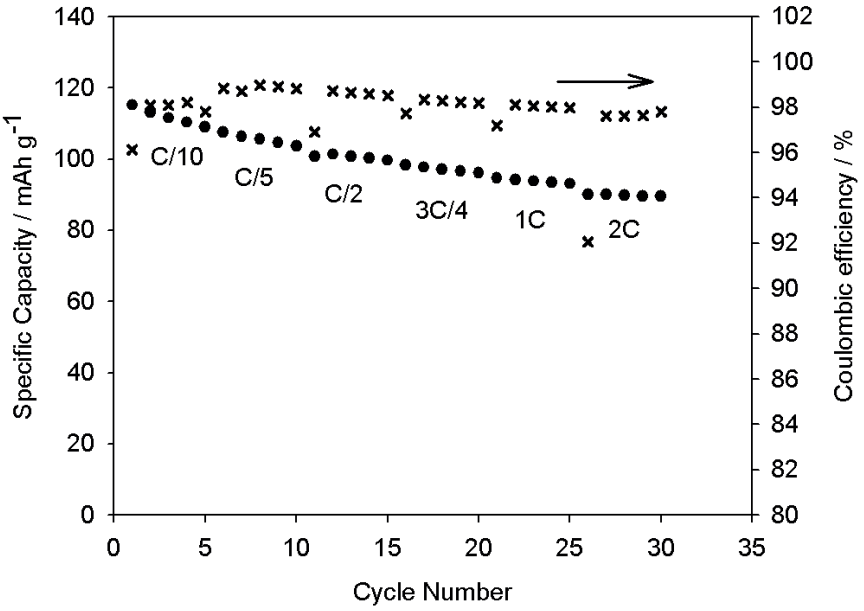

Figure 3.7 Rate performance of flame-made $LiMn_2O_4$.

3.6 Summary

Nanostructured spinel $LiMn_2O_4$ cathode materials for lithium-ion batteries were synthesized by using flame-assisted spray technology (FAST). The as-synthesized powder showed a nanocrystalline structure with uniform morphology. However, the impurity Mn_3O_4 was detected, which resulted from the decomposition reaction of $LiMn_2O_4$ at elevated temperature (>1000 °C). After a post-annealing treatment, the $LiMn_2O_4$ powder showed a single-phase spinel structure. The charge/discharge performance of the powder before and after post-annealing was in good agreement with the electrochemical characteristics of spinel $LiMn_2O_4$. The annealed $LiMn_2O_4$ powder had a much higher capacity than the as-synthesized powder, especially in the 4 V range. Moreover, the annealed $LiMn_2O_4$ powder showed a good rate capability with a small amount of conductive material. This chapter has demonstrated that the FAST process has the potential to rapidly produce electrochemically active materials for lithium-ion secondary batteries at low cost.

Chapter 4

Synthesis of 5 V Spinel-$LiNi_{0.5}Mn_{1.5}O_4$ with Superior Cycle-Life [2]

[2] Published in Proceedings of the Combustion Institute, 2011

Spinel $LiMn_2O_4$ has been studied extensively as a 4 V cathode material due to the low cost and abundance of Mn, ease of preparation, high-rate performance and low toxicity [3]. However, severe capacity fading during charge/discharge at 3-4 V may limit its commercial applications, as discussed in the previous chapter. To address this problem, the Mn cation can be partially substituted with Li or a transition metal forming doped spinel $LiM_xMn_{2-x}O_4$ (where $0 \leq x \leq 1/3$, M = Li, Ni, Co, Cr, and Al, etc.) [114, 173, 174]. This improves the cycling performance at 4 V, however, notable discharge capacity loss will occur because of the inactivity of these transition metal dopants at 4 V. Recently, it has been reported that with significant increases in the substitution of Mn *i.e.*, $x = 0.5$, with transition metals, the doped spinel will show a higher working potential near 5 V and also retain a good discharge capacity [44-47].

Among the 5 V spinels, spinel-$LiNi_{0.5}Mn_{1.5}O_4$ (Ni^{2+}, Mn^{4+}) has drawn interest due to its electrochemical characteristics: high capacity (130 to 140 $mAhg^{-1}$), a working voltage plateau at 4.7 V and good cycling performance at elevated charge/discharge rates [46, 49]. The high-voltage plateau of $LiNi_{0.5}Mn_{1.5}O_4$ during cycling is known to be the result of the Ni^{2+}/Ni^{4+} redox couple, compared to the Mn^{3+}/Mn^{4+} redox couple in the traditional 4 V spinels. $LiNi_{0.5}Mn_{1.5}O_4$ has two stable crystallographic structures: disordered $Fd\bar{3}m$ space group and ordered $P4_332$ space group, which are stable at different synthetic conditions [46, 50, 51]. It has been verified that nano-sized disordered spinel-$LiNi_{0.5}Mn_{1.5}O_4$ shows better cycling performance at high-discharge rate than the ordered structure. At high temperatures both Ni and Mn can be stable in the form of binary oxides M_xO_y, so flame synthesis of this quaternary metal-oxide presents a challenge. In this work, the flame

pyrolysis process was used to synthesize 5 V, spinel-$LiNi_{0.5}Mn_{1.5}O_4$ ($Fd\bar{3}m$) cathode-materials.

4.1 Flame Structures

The precursor solution is prepared by dissolving $LiNO_3$ (anhydrous, Alfa Aesar), $Ni(NO_3)_2 \cdot 6H_2O$ (Alfa Aesar), and $Mn(NO_3)_2 \cdot 4H_2O$ (Alfa Aesar) in methanol at a stoichiometric ratio of 1:0.5:1.5. The precursor solution was aerosolized with a BGI one-jet Collison nebulizer to generate ultra-fine precursor droplets. Methanol-saturated N_2 carried the precursor droplets into the flame. The temperature field was measured with a Pt/Rh thermocouple without correction for radiation heat loss. If the thermocouple were inserted into the pyrolysis flame, the deposition of metal oxides on the thermocouple bead would affect the measurement accuracy. Thus, during the measurements of temperature over the entire flame, only pure methanol (i.e., without the metal nitrate precursors) was atomized to form fine methanol droplets, and then delivered into the same hydrogen flame. The measured temperature profile was plotted based on an average of 20 measurements at each point with a precision of ±5 °C. The enthalpy required to decompose the precursor nitrates was calculated to be less than 0.3% of the total heat of reaction at standard conditions. Thus, it is expected that the nitrate precursors in the pyrolysis flame would have a negligible effect on flame temperature. Experiment showed that the measured peak temperature of the flame without nitrate precursors was 1205 °C compared to 1155 °C for the flame with precursors at 1.5 cm HAB. A possible

explanation for the temperature difference could be the radiative heat loss from the as-synthesized powder. Thus, the H_2/methanol flame temperature profile can be considered to be approximately that of the flame producing $LiNi_{0.5}Mn_{1.5}O_4$ powder.

The flame-assisted pyrolysis technology designed to produce $LiNi_{0.5}Mn_{1.5}O_4$ powders has two distinct colors: crimson red near the burner exit and dark orange in the upper regions of the flame, as shown in Figure 4.1a. The red color is characteristic of Li and indicates the region of decomposition of the $LiNO_3$ precursor. The dark-orange color is believed to result from a combination of emissions from Li (red), Mn (yellowish green), and Ni (green) in the flame. It is also possible that some of the dark-orange color is due to radiation from particles in the flame. When atomizing pure methanol without any metal nitrate precursor, the H_2/methanol/air diffusion flame is blue near the base and has a light red tone near the tip. Thus, the dark-orange luminance was used to identify the synthetic reaction of spinel-$LiNi_{0.5}Mn_{1.5}O_4$ particles in the pyrolysis flame. No soot or other carbonaceous species were observed in the final powder. In the pyrolysis flame, the formation mechanism of the $LiNi_{0.5}Mn_{1.5}O_4$ is expected to sequentially involve the evaporation of the methanol solvent, decomposition of the nitrates and reaction to form the metal oxide.

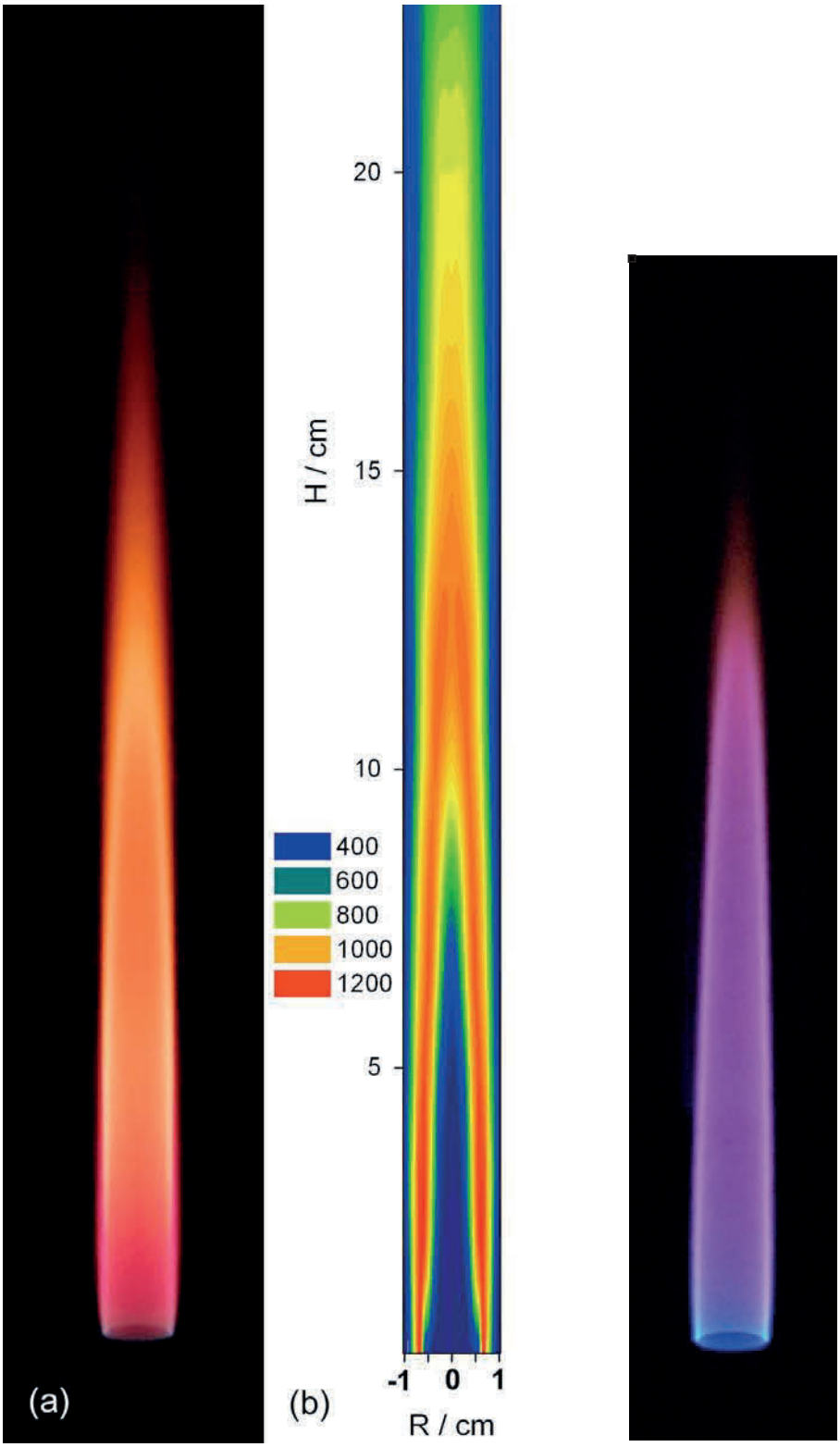

Figure 4.1 Images of Flame-A producing the spinel $LiNi_{0.5}Mn_{1.5}O_4$ powder (left) measured flame temperature profile (middle) and flame without precursors (right). Temperature is in Celsius.

In Figure 4.1b, the measured flame temperature contours for Flame A (the flame conditions used to produce the powders but without the nitrates) are shown opposite a photograph of a pyrolysis flame producing $LiNi_{0.5}Mn_{1.5}O_4$ powder. The flow rate of H_2 is 0.5 lpm and methanol vapor feed rate (from the bubbler) is 0.3 g min^{-1}. The highest temperature of the flame is 1205 °C, which occurs at 1.5 cm above the burner, and the temperature decreases slightly to about 1100 °C at the flame tip. Although both H_2 and methanol behave as fuels, preferential diffusion of H_2 over methanol near the burner exit apparently promotes a higher temperature near the base. Figure 4.1b also shows that the temperature increases slowly in the center of the flame before it reaches 700 °C at a HAB of 8.0 cm, and then the temperature increases quickly. Before reaching 700 °C the solvent methanol has evaporated and the precursors are expected to have decomposed. However, the synthesized powders pass through flame temperatures that are considerably higher than the temperatures normally used in solid-state reactions, spray pyrolysis and sol-gel methods (600 to 1000 °C) [46, 120, 175]. Flame temperatures above 1000 °C may lead to the formation of some impurity phases, such as various metal-oxides; however, the flame temperature could not be lowered further without inducing flame instabilities.

When the flow rate of H_2 is increased and the flow rate of the atomizing gas (methanol-saturated N_2) is decreased, the red flame zone expands and the orange zone shortens. As seen in Table 4.1, the flame temperature at 1.5 cm HAB is 1325 °C in Flame B and 1500 °C in Flame C. The increase in the temperature at the flame tip is less (Table 4.1). The as-produced powders from Flames A, B, and C were collected and the crystal

structures were compared as analyzed by XRD, as seen in Figure 4.2. All the three as-produced powders from different flames have shown the typical XRD pattern of spinel structures. No impurity phase was detected by XRD, except for the splitted peak near 62° for the powder from Flame C (red line). Therefore, the high-flame temperature is not detrimental for the $LiNi_{0.5}Mn_{1.5}O_4$ powder quality if only seeing the XRD spectrums. Moreover, $LiNi_{0.5}Mn_{1.5}O_4$ appears to be more thermodynamically stable over $LiMn_2O_4$.

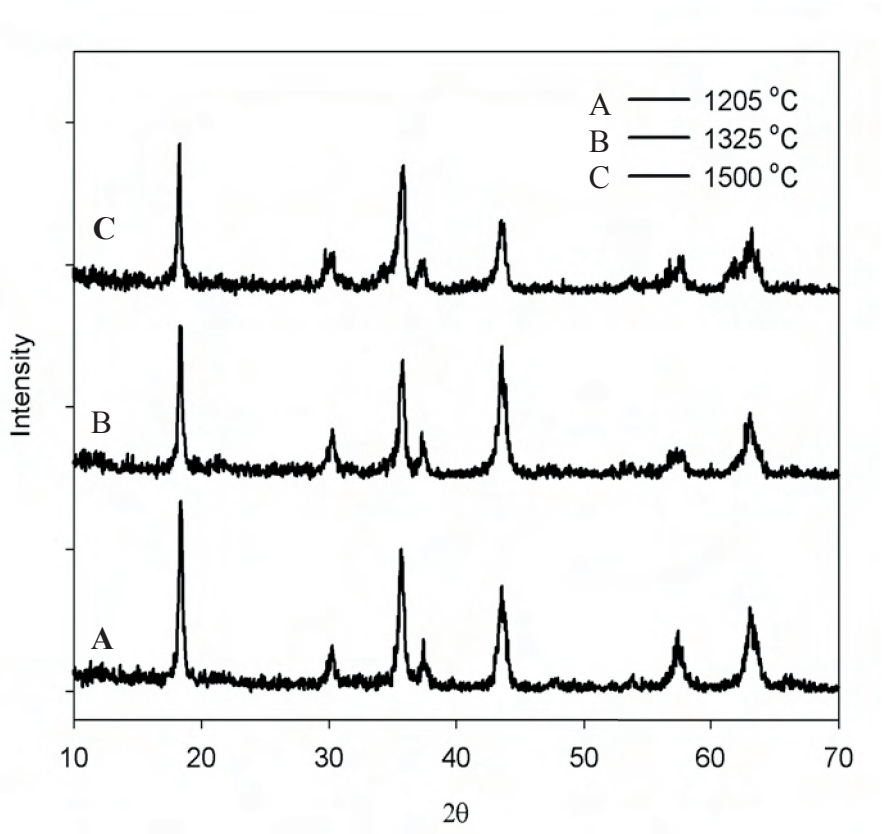

Figure 4.2 XRD pattern of the as-produced $LiNi_{0.5}Mn_{1.5}O_4$ powder from different flames.

The lattice constant *a* and the *d*-spacing of the powders made in the higher temperature flames (Flame B and C) are larger than those made at lower temperature (Flame A). This is consistent with the expectation that oxygen deficiency will be greater at higher

synthesis temperatures (Table 4.1). In addition, although disordered spinel $LiNi_{0.5}Mn_{1.5}O_4$ ($Fd\bar{3}m$ space group) has an oxygen-deficient structure, extended oxygen loss at higher temperature will cause the formation of impurities that may deteriorate the powder quality. Previous studies showed similar results that at elevated temperature, phase decomposition of spinel-$LiMn_2O_4$ caused the formation of the Mn_3O_4 impurity [73, 127]. Thus, to minimize the amount of impurity, a low temperature flame is preferred.

Table 4.1 Different pyrolysis flames and the crystallographic data of the as-synthesized powders.

Flame	Flow rate / lpm		Measured flame temperature / °C		Crystallographic data / Å	
	H_2	Atomizing gas N_2	1.5 cm HAB	Flame tip	*d*-spacing	Lattice parameter *a*
A	0.50	2.53	1205	1100	4.7835	8.285
B	0.82	2.28	1325	1165	4.7856	8.289
C	1.20	2.03	1500	1210	4.7901	8.297

4.1 Crystallographic Analysis

A comparison of the XRD patterns of the as-synthesized $LiNi_{0.5}Mn_{1.5}O_4$ powder and the powder annealed at 800 °C in air is shown in Figure 4.3. The as-synthesized powder shows broader XRD peaks, indicating a nanocrystalline structure, as seen in Figure 4.3a. The average grain size of the nanocrystalline $LiNi_{0.5}Mn_{1.5}O_4$ is about 16 nm as calculated from the Scherrer equation with the *fwhm* (full width at half maximum) of plane (400). The lattice parameter, *a* and cell volume, *V*, of the as-synthesized powder are 8.285Å and

568.76 $Å^3$, respectively, as determined by Rietveld cell refinement. These values are a bit higher than the experimental values obtained from other methods, e.g., 8.172 Å and 545.75 $Å^3$ from the molten salt method, and 8.180 Å and 547.34 $Å^3$ from spray pyrolysis [116, 176]. The reason for this may be due to the effect of high oxygen deficiency in the powder, which would reduce the average oxidation state of Mn^{n+} from 4+ to 3+. It is known that the ionic radius of Mn^{3+} is larger than Mn^{4+}, and thus an oxygen deficiency would increase the lattice parameter *a* and cell volume *V* [116]. In addition, as shown in the inset of Figure 4.3a, a small amount of impurity Mn_2NiO_4 (Mn^{3+}, Ni^{2+}) is detected. The (422) plane is a minor peak but the major peaks of Mn_2NiO_4 overlapped with the $LiNi_{0.5}Mn_{1.5}O_4$ spectrum at 2θ of 30° and 36°. The impurity Mn_2NiO_4 also has an $Fd\bar{3}m$ space group structure with a slightly larger lattice-parameter *a* of 8.370 Å. Thus, the existence of this impurity phase increases the average lattice constants during the cell-refinement calculation. The formation of this impurity phase may be due to a decomposition reaction of $LiNi_{0.5}Mn_{1.5}O_4$ at temperatures above 1000 °C.

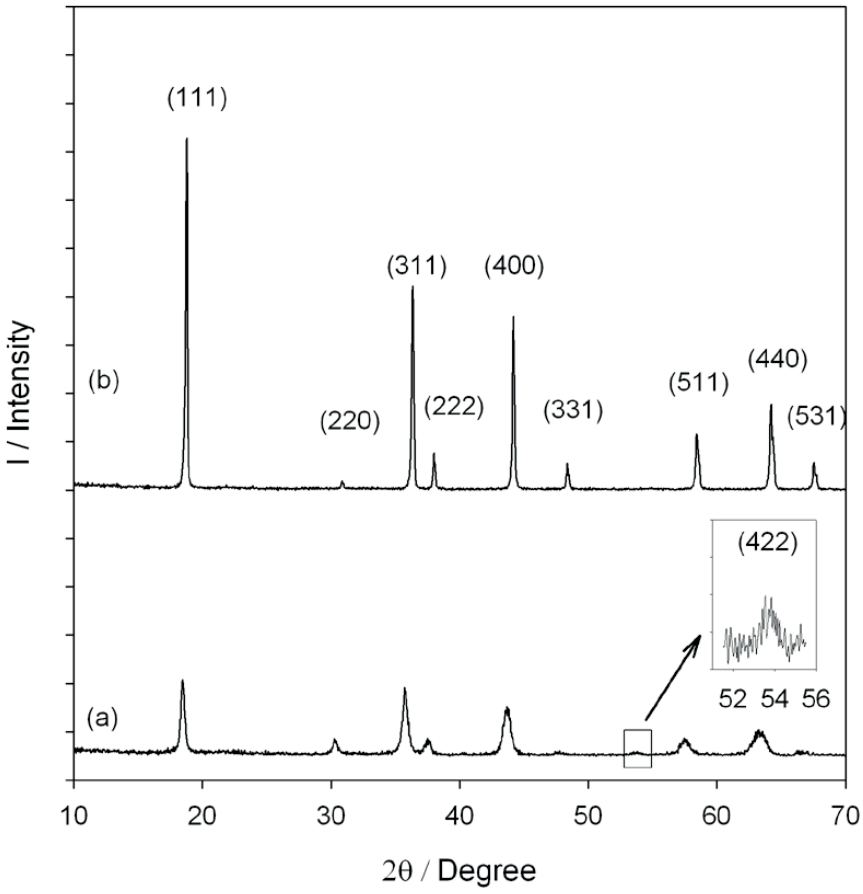

Figure 4.3 XRD patterns of the flame-synthesized $LiNi_{0.5}Mn_{1.5}O_4$ powder: (a) as-synthesized; (b) after annealing at 700 °C for 2hr.

For the as-synthesized powder, post heat-treatment is necessary to remove the impurity and reduce the oxygen defect. Annealing is also important to optimize the crystal structure of the powder. The $LiNi_{0.5}Mn_{1.5}O_4$ can have two different space group structures: $Fd\bar{3}m$ space group with weak oxygen deficiency, or $P4_332$ space group with no oxygen deficiency, and these structures are highly dependent on the heat treatment temperature. $LiNi_{0.5}Mn_{1.5}O_4$ can remain as $Fd\bar{3}m$ space group at low and high annealing temperatures. When the temperature is near 600 °C, a $P4_332$ space group structure may be produced [177]. In this experiment, 800 °C was chosen as the annealing temperature,

followed by slow cooling in air. After annealing in air at 800 °C for 2hr, the XRD spectrum shows good agreement with the pure-phase spinel $LiNi_{0.5}Mn_{1.5}O_4$ with an $Fd\bar{3}m$ space group, as seen in Figure 4.3b. No impurities are detectable and the XRD peaks are sharper and narrower, indicating better crystallinity and larger crystal size. Compared to the as-synthesized powder, the annealed powder has a higher average valence of Mn^{n+}, and the lattice-constants a (8.196 Å) and V (550.51 $Å^3$) are closer to those for powders made *via* the molten salt method (8.172 Å and 545.75 $Å^3$) and the spray-pyrolysis method (8.180 Å and 547.34 $Å^3$) [116, 176]. After annealing, the oxygen defect is considerably lowered than for the as-synthesized powder.

4.2 Powder Morphology

The improved crystallinity after annealing can also be directly observed by SEM and TEM analysis. The as-synthesized powder shows a similar morphology to the powder made by spray pyrolysis, being spherical in shape, as seen in Figure 4.4a and 4.4b. The particle sizes range from 30 nanometers to about 1 micron. After annealing, the small particles do not exist and the larger particles clearly show a faceted structure, as seen in Figure 4.4c and 4.4d. The crystallinity of the annealed powder appears to be better than the as-synthesized powder. The particle size distribution is expected to be the same.

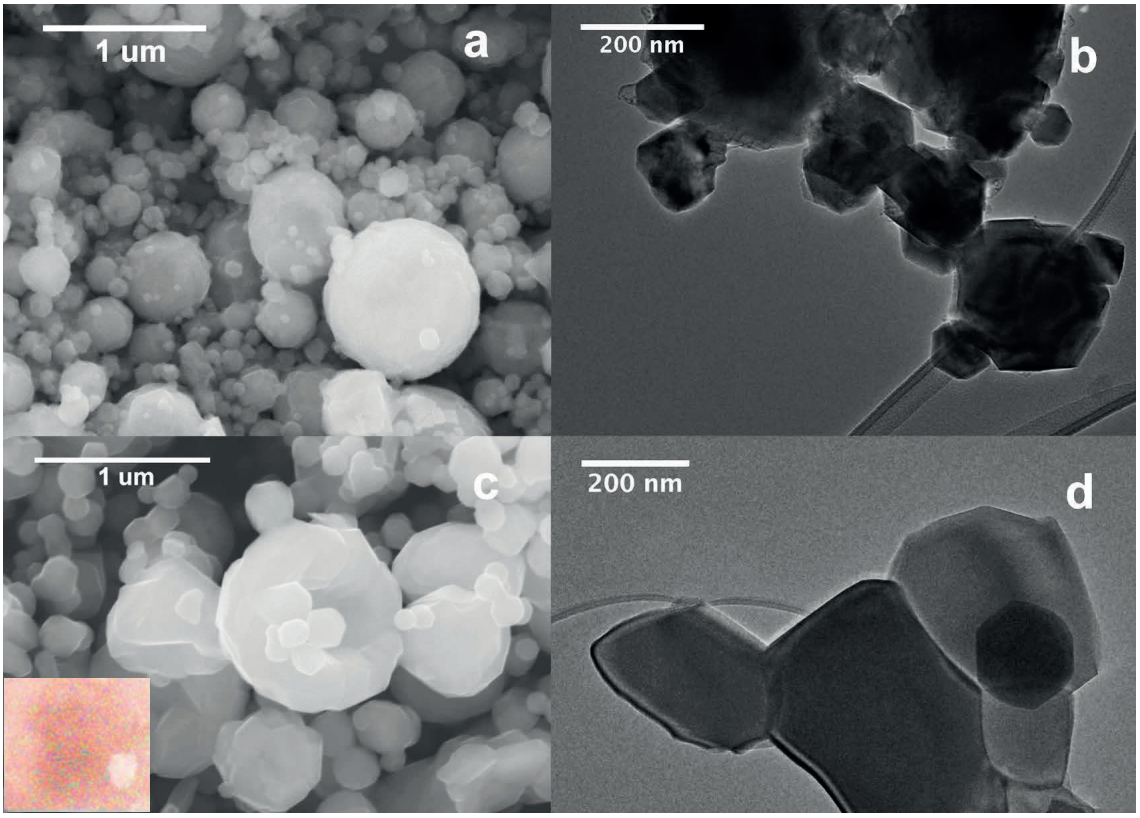

Figure 4.4 Morphology of the $LiMn_{0.5}Ni_{1.5}O_4$: (a) SEM photo of the powder before annealing; (b) TEM photo of the powder before annealing; (c) SEM photo of the powder after annealing; (d) TEM photo of the powder after annealing. Embedded figure in c is the elemental mapping of the particle surface using SEM-EDX (Red: Mn; Green: Ni).

4.3 Electrochemical Performance of 5 V Spinel-$LiNi_{0.5}Mn_{1.5}O_4$

4.3.1 Voltage Profile and Capacity

The electrochemical properties of the annealed $LiNi_{0.5}Mn_{1.5}O_4$ powder are evaluated with a 2032 coin-type test cell. The $LiNi_{0.5}Mn_{1.5}O_4$ powder, polyvinylidene-fluoride (PVdF) binder, and Super-P conductive-carbon-black are mixed at a ratio of 82:10:8 by mass in the cathode. A freshly assembled $Li/LiNi_{0.5}Mn_{1.5}O_4$ cell shows about a 2.7 V open-circuit-potential before charging, indicating that the cell is not short-circuit internally. In a Li-ion rechargeable-battery, Li^+ is the transported component during charge/discharge cycles. During charging, the Li^+ migrates from the host cathode $LiNi_{0.5}Mn_{1.5}O_4$ matrix where an oxidation reaction occurs towards the anode. A reduction reaction occurs at the cathode during discharging. In the experiment, the test cell was charged and discharged at a constant current of 14.9 mA g^{-1} at 30 °C with a cut-off voltage of 4.9 and 3.5 V, respectively. As seen in Figure 4.5, the voltage rises from 2.7 V to 4.9 V during charging, and then drops from 4.9 V to 3.5 V during discharging. The overall charge/discharge curves show good agreement with spinel $LiNi_{0.5}Mn_{1.5}O_4$ having an $Fd\bar{3}m$ space group structure [116, 176]. Two distinct plateaus (I and II) are observed around 4.7 V corresponding to a $Ni^{2+/4+}$ redox couple. A small plateau around 4.0 V is also observed during both charge and discharge, as indicated by arrows in Figure 4.5. This 4 V plateau is attributed to the $Mn^{3+/4+}$ redox couple. For the perfect $LiNi_{0.5}Mn_{1.5}O_4$ structure ($P4_332$

space group), the average oxidation state of the Mn is 4+. For the $Fd\bar{3}m$ structure, $LiNi_{0.5}Mn_{1.5}O_4$ remains as an oxygen-deficient spinel and the average oxidation state of the Mn is slightly lower than 4+. In other words, a small portion of the Mn appears as 3+ instead of 4+. As a result, the $Mn^{3+/4+}$ redox reaction, as seen in spinel $LiMn_2O_4$ will also be seen here at 4 V. This is consistent with the 4 V plateau during discharge being relatively long, which reduces the capacity of the cell at 4.7 V.

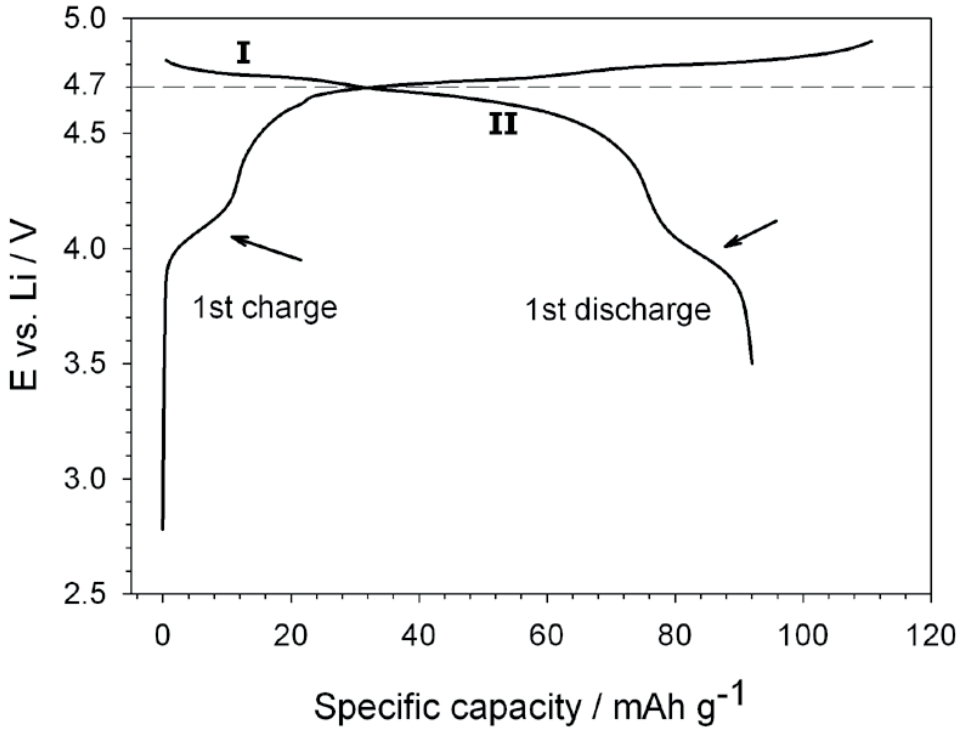

Figure 4.5 First charge/discharge curves of Li/$LiNi_{0.5}Mn_{1.5}O_4$ cell at C/10 rate at 30 °C. Powder for cathode was produced in Flame-A and annealed at 800 °C for 2 hr.

The cell shows a total charge capacity of 110 $mAhg^{-1}$, and total discharge capacity of 92 $mAhg^{-1}$ when summing the capacities at the 4 and 4.7 V plateaus, indicating a large irreversible capacity loss of about 18 $mAhg^{-1}$. The reason for this can be explained as a

result of the oxidation of the electrolyte EC/DEC at high voltage during the charge and discharge [53]. The capacity of the flame-synthesized $LiNi_{0.5}Mn_{1.5}O_4$ powder is consistent with that of the nanostructured powders made by emulsion drying and solid-state reaction, which is in range of 80 to 100 $mAhg^{-1}$ [48, 178]. Nonetheless, compared to bulk (micron-sized) material [46, 48, 49], the flame-synthesized powder shows a lower capacity.

4.3.2 Cycle Performance

Figure 4.6 shows the cycle performance of cell at C/10 rate between 3.5 and 4.9 V at room temperature. Despite the low capacity (*c.a.* 90 $mAhg^{-1}$), the flame-synthesized disordered $LiNi_{0.5}Mn_{1.5}O_4$ powder shows better cycle life over $LiMn_2O_4$. In $LiMn_2O_4$, the average valence state of Mn^{n+} is 3.5 due to the presence of an equal amount of Mn^{4+} and Mn^{3+}. The Mn^{3+} concentration in $LiMn_2O_4$ is considered high enough to induce the Jahn-Teller distortion and consequently the capacity fading. However, the Jahn-Teller disordering of Mn^{3+} is eliminated in $LiNi_{0.5}Mn_{1.5}O_4$ because Mn is mainly tetravalent and the $Ni^{4+/2+}$ redox couple drives the reaction across the two electrodes. As a result, the disordered $LiNi_{0.5}Mn_{1.5}O_4$ synthesized from the flame shows improved cycle life. As discussed earlier, the coulombic efficiency at the first cycle is low, due to the oxidation of electrolyte at high voltage and SEI layer formation. When the cycle test continues, the coulombic efficiency increases rapidly and is stabilized at 98%. After 100 cycles, approximately 94% of the initial capacity retains.

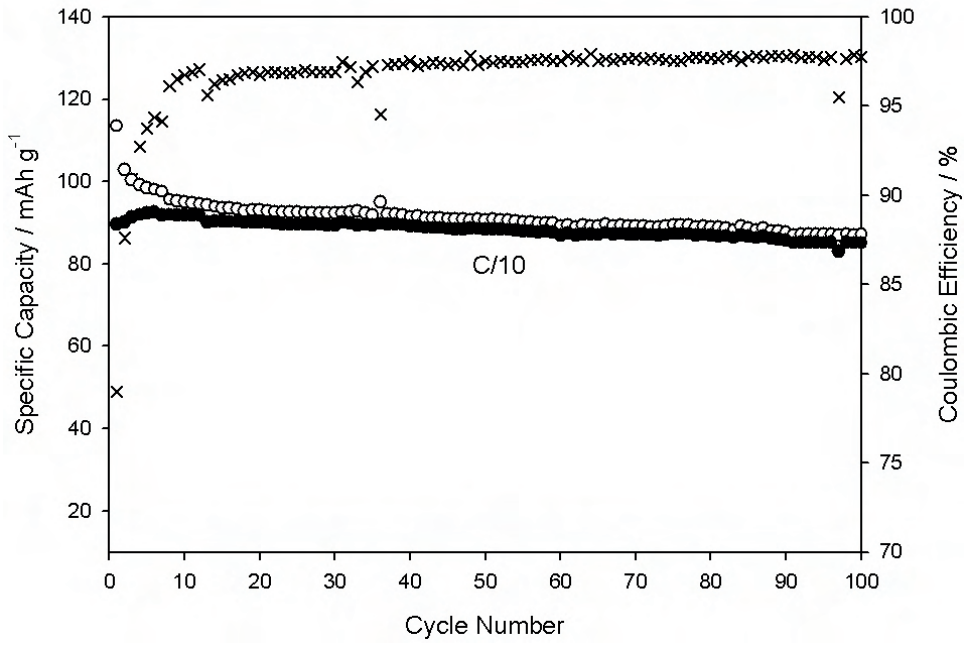

Figure 4.6 Cycle performance of Li/$LiNi_{0.5}Mn_{1.5}O_4$ cell at C/10 rate at 30 °C. Powder for cathode was produced in Flame-A and annealed at 800 °C for 2 hr. (Solid circle: discharge capacity; open circle: charge capacity; cross: coulombic efficiency)

4.3.3 Rate Performance

The rate performance test of the flame-made $LiNi_{0.5}Mn_{1.5}O_4$ powders is carried out by elevating C-rates every 10 cycles, from C/10 to 1C between 3.5 to 4.9 V. No significant capacity drop is observed during the rate test, as seen in Figure 4.7. After switching back the current density to C/10 rate, the capacity of $LiNi_{0.5}Mn_{1.5}O_4$ electrode is almost identical to the capacity at the first few cycles at C/10 rate. Therefore, no irreversible capacity loss occurred for $LiNi_{0.5}Mn_{1.5}O_4$. In the meanwhile, the coulombic efficiency of the $LiNi_{0.5}Mn_{1.5}O_4$ cell increases at elevated C-rates. At 1C rate, the coulombic efficiency exceeds 99%. However, the operation voltage drops significantly from 4.7 V at C/10 to

4.2 V at 1C due to a kinetic effect, as seen in Figure 4.8. Electrode formulation needs to be optimized to improve the rate capability of the $LiNi_{0.5}Mn_{1.5}O_4$.

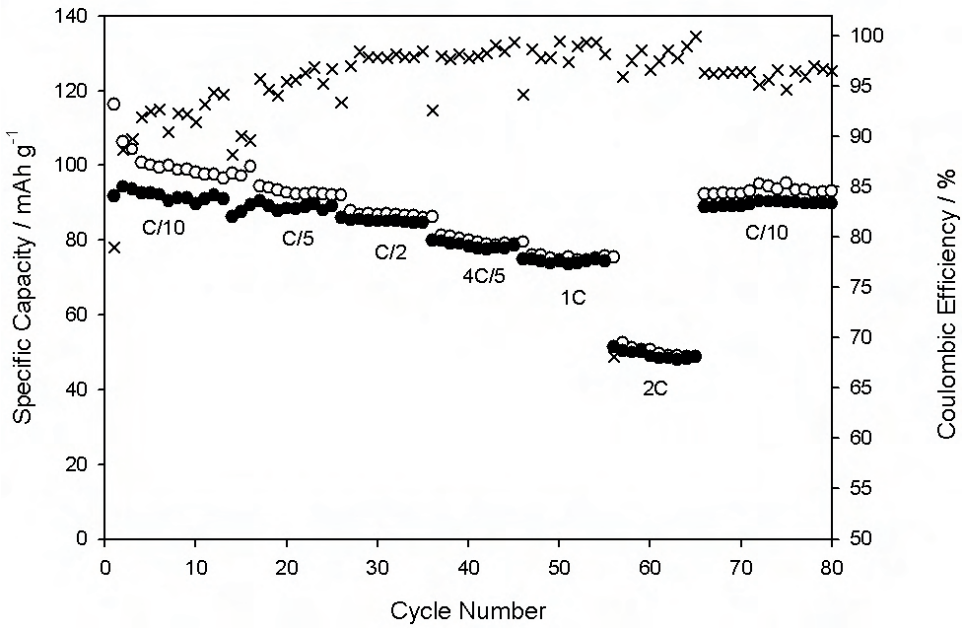

Figure 4.7 Rate performance of Li/$LiNi_{0.5}Mn_{1.5}O_4$ cell at room temperature. Powder for cathode was produced in Flame-A and annealed at 800 °C for 2 hr. (Solid circle: discharge capacity; open circle: charge capacity; cross: coulombic efficiency)

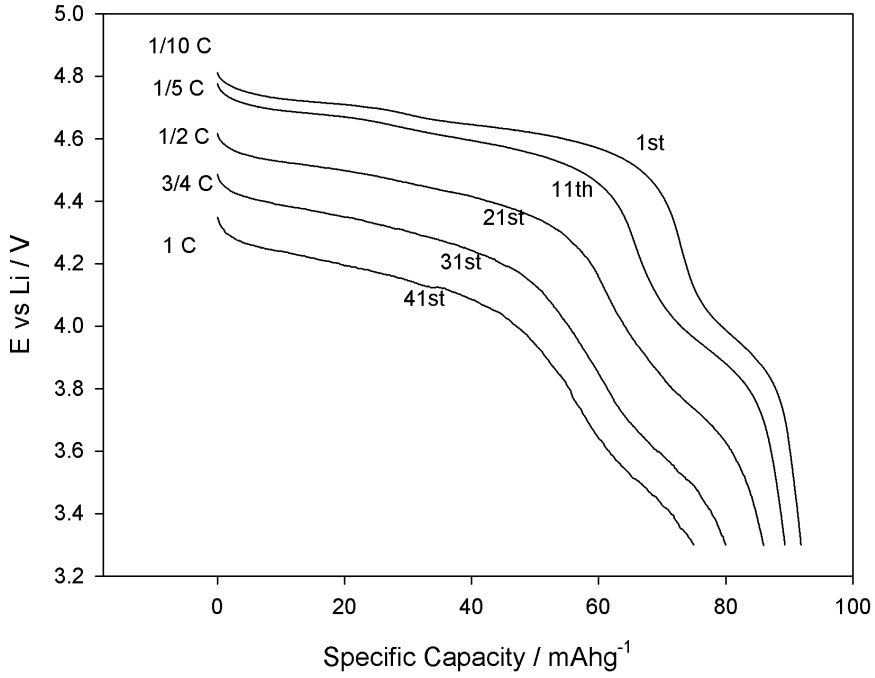

Figure 4.8 Discharge voltage profile of Li/$LiNi_{0.5}Mn_{1.5}O_4$ cell at elevated C-rates.

4.4 Summary

A flame spray pyrolysis process was developed to synthesize 5 V, spinel $LiNi_{0.5}Mn_{1.5}O_4$ cathode materials for lithium-ion batteries. The flame showed a unique appearance, being a combination of the emission characteristics of the metals in the precursors. The XRD analysis showed that the as-synthesized powder had a spinel-type structure and it is nanocrystalline. However, high oxygen deficiencies may lead to form Mn_2NiO_4 at elevated flame temperature. As-synthesized $LiNi0_{.5}Mn_{1.5}O_4$ from flame did not show significant amount of impurity phase due to its high thermostability, therefore no extensive oxygen loss can occur. To remove the defects in the powder and improve the

crystallinity, the powder was annealed at 800 °C for 2 hr in air. After annealing, $LiNi_{0.5}Mn_{1.5}O_4$ could be indexed as a single-phase spinel $Fd\bar{3}m$ structure with controllable oxygen deficiency (disordered spinel). No ordered spinel ($P4_332$) structure was observed in this study. SEM and TEM images also showed that the annealed powder had larger crystallite-sizes, and smooth, clean surfaces.

A test cell constructed from the annealed $LiNi_{0.5}Mn_{1.5}O_4$ powder as a cathode material showed that the powder was electrochemically active and had good performance. The initial charge capacity was about 110 $mAhg^{-1}$, and the discharge capacity was 92 $mAhg^{-1}$, which included capacity at both 4 and 4.7 V plateaus. The irreversible capacity loss was attributed to the oxidation of the chosen electrolyte at high voltage during charge/discharge. The flame-made spinel $LiNi_{0.5}Mn_{1.5}O_4$ powders also showed superior cycle life and rate capability over spinel $LiMn_2O_4$ by eliminating the Jahn-Teller effects. Nonetheless, the electrode made from this powder needs to be optimized to achieve a better rate capability. From these results, flame-assisted spray pyrolysis was shown to have potential for the production of valuable materials for energy storage applications.

Chapter 5

Layered-Layered Li-Ni-Mn-Oxide Composite Materials for High-Energy Li-ion Batteries [3]

[3] To be submitted to Electrochemical Communications, 2011

In the previous chapters, a flame process was discussed for the synthesis of Mn-based cathode materials, spinel $LiMn_2O_4$ and $LiNi_{0.5}Mn_{1.5}O_4$. These materials have shown comparable electrochemical performance to those synthesized *via* spray pyrolysis, solid-state reaction and wet-chemistry processes. Although Ni is added to the spinel framework to stabilize the structure and all the Mn cations therefore are tetravalent (to avoid Jahn-Teller effect), $LiNi_{0.5}Mn_{1.5}O_4$ spinels are only cycled in the 5 V region, displaying a capacity of *c.a.* 140 $mAhg^{-1}$. Many efforts have been reported to increase the capacity of Mn-based materials, by adopting a layered structure [33, 179-182]. Among them, the layered Li-excess $Li[Li_{(1/3-2a/3)}Ni_aMn_{(2/3-a/3)}]O_2$ ($0 < a < 1/2$) synthesized at high temperature can deliver over 200 $mAhg^{-1}$ between 2.0 and 4.6 V with a good cycle life [33, 179, 180, 182]. The Li-excess materials can be considered as an integration of two layer-structured materials: monoclinic Li_2MnO_3 (*C2/m*) and rhombohedral $LiNi_{0.5}Mn_{0.5}O_2$ ($R\bar{3}m$), forming a rock-salt-type α-$NaFeO_2$ structure with $R\bar{3}m$ space group [33, 183]. Therefore, they can be reformulated as layered-layered integrated composites $xLi_2MnO_3 \cdot (1-x)LiNi_{0.5}Mn_{0.5}O_2$ (where $0 \leq x \leq 1$). The two chemical formulas are equivalent with:

$$a=(1-x)/(2+x) \qquad (5.1)$$

The cation disordering in the transition metal layer between Li_2MnO_3 and $LiNi_{0.5}Mn_{0.5}O_2$ improves the stability of the overall structure, thus enhancing the cycle life. The initial charge of the layered-layered composite materials involves extraction of octahedral Li^+ and release of oxygen with a net loss of Li_2O, occurring above 4.5 V vs. Li [183-185].

The coulombic efficiency is low at the first cycle due to the irreversible loss of Li in form of Li_2O. Surface treatment, *e.g.,* acid etching and surface coating with phosphate, can enhance the rate and cycle capabilities, and also improve the coulombic efficiency, but adds complexity to the synthesis processes [183-185]. Due to the presence of monoclinic *C2/m* phase Li_2MnO_3, the high capacity over 200 $mAhg^{-1}$ can be only achieved at a very low current density, between C/20 and C/50 [33, 179, 180, 182]. Fortunately, by adopting nanostructured morphologies: porous and nano-size primary particles, these composite materials can show an improved rate capability [37, 99].

As discussed in Chapter one, coprecipitation process is the conventional process for synthesizing the nanostructured composite materials. The state-of-the-art high performance composite materials were initially demonstrated with a lab-scale coprecipitation process, which requires controlling the stirring speed, temperature, pH and concentration for producing high-quality materials [37, 99]. However, the stoichiometry of the powder may vary from batch to batch so that the product consistency can be a challenge. Meanwhile, the sodium from the coprecipitation agent (Na_2CO_3) may not be completely washed off from the precipitates, hence it becomes a major contaminant in the final powder. For these reasons, the coprecipitation process needs to overcome all these technical challenges and barriers at scale up. The spray pyrolysis process is environmental friendly, less resource and capital intensive, simpler and faster. Additionally, the process ensures a good uniformity and precise control of chemical composition within the particle and from particle to particle. In addition, no precipitation/chelating agent is required for the spray pyrolysis process. To date, no

studies have reported producing composite cathode materials with a capacity over 250 $mAhg^{-1}$ in the spray pyrolysis process. In this research, the synthesis of porous Li-excess $x Li_2MnO_3 \cdot (1-x) LiNi_{0.5}Mn_{0.5}O_2$ (where $0 \leq x \leq 1$) composite materials *via* a spray pyrolysis will be demonstrated.

5.1 Material Synthesis *via* Spray Pyrolysis

The spray pyrolysis uses a tubular aerosol flow reactor to produce Li-excess $x Li_2MnO_3 \cdot (1-x) LiNi_{0.5}Mn_{0.5}O_2$ ($0.3 \leq \boldsymbol{x} \leq 0.7$) composite materials, as shown in Figure 2.1. The precursor solution was prepared by dissolving $LiNO_3$, $Mn(NO_3)_2 \cdot 4H_2O$ and $Ni(NO_3)_2 \cdot 6H_2O$ at a stoichiometric ratio in the deionized water. The total molar concentrations of $Mn(NO_3)_2 \cdot 4H_2O$ and $Ni(NO_3)_2 \cdot 6H_2O$ is maintained at 2 $moleL^{-1}$. The corresponding Li concentration can be calculated based on the x values in the $x Li_2MnO_3 \cdot (1-x) LiNi_{0.5}Mn_{0.5}O_2$ composites. The precursor solution was aerosolized with a one-jet air-assisted nebulizer (Collison, BGI Inc.), where fine precursor droplets in the micron-size range were produced. Typically, the pressure of atomizing gas (air) was maintained at 40 psi and the corresponding gas flow-rate was 3.3 lpm. After aerosolization, the precursor aerosols flowed into a preheater maintained at 250 °C (wall temperature) and then a vertical ceramic tube furnace heated at 700 °C. At the preheater outlet, the gas temperature was measured to be 100 to 130 °C. Downstream of the reactor, the as-produced powders were collected by a membrane filter (Nuclepore™ track-etched polycarbonate membrane, pore size: 0.2 μm). The particle size distribution of the as-

synthesized powder was measured with an in-line electric-low-pressure-impactor (ELPI, DEKATI) at the furnace reactor outlet. The as-produced powders were commonly annealed at 800 °C for 2 hr and following by slow cooling at 3 °C min^{-1} unless it is specified otherwise in the research.

5.2 Elemental Analysis

The stoichiometry of the nitrate precursor solution was measured by ICP-MS before making powders with the spray pyrolysis system, as seen in Table 5.1. The precursor solutions with *x* between 0.3 and 0.7 have shown good agreement with the theoretical stoichiometry of the composite materials (±5% accuracy). The stoichiometry of powders before and after annealing was also evaluated using ICP-MS by digesting the powders in concentrated nitric acid and hydrochloric acid solution. An example of $0.5Li_2MnO_3 \cdot 0.5LiNi_{0.5}Mn_{0.5}O_2$ (or simply $Li_{1.2}Ni_{0.2}Mn_{0.6}O_2$) powders under different heat treatments is shown in Table 5.2. The as-synthesized powders are stoichiometric compounds, and this stoichiometry is well preserved after annealing at 800 °C from 2 hr to 10 hr. Therefore, no detectable Li loss from evaporation is observed in either the synthesis process or the post annealing process. Since the stoichiometry of the precursor solution is identical to the stoichiometry of the powders before and after annealing, the elemental ratio of the metals in the precursor solutions obtained from ICP-MS can represent the stoichiometry of the powders made from them.

Table 5.1 ICP-MS analysis of xLi$_2$MnO$_3$·(1-x)LiNi$_{0.5}$Mn$_{0.5}$O$_2$ precursor solution

Li_2MnO_3	*$LiMn_{0.5}Ni_{0.5}O_2$*	*Theoretical Stoichiometry*			*As-measured*		
x	**(1-x)**	**Li**	**Ni**	**Mn**	**Li**	**Ni**	**Mn**
0.3	0.7	1.13	0.30	0.57	1.08(8)	0.28(3)	0.51(7)
0.4	0.6	1.17	0.25	0.58	1.12(8)	0.25(0)	0.55(0)
0.5	0.5	1.20	0.20	0.60	1.20(9)	0.59(5)	0.20(5)
0.6	0.4	1.23	0.15	0.62	1.33(6)	0.16(2)	0.63(8)
0.7	0.3	1.26	0.11	0.63	1.31(6)	0.12(2)	0.67(8)

Table 5.2 ICP-MS elemental analysis of 0.5Li$_2$MnO$_3$ · 0.5LiNi$_{0.5}$Mn$_{0.5}$O$_2$ (or Li$_{1.2}$Ni$_{0.2}$Mn$_{0.6}$O$_2$) precursor and the powders under different heat treatment.

Samples	**Normalized Elemental Composition**		
	Li	**Mn**	**Ni**
As-synthesized	1.22	0.60	0.20
800 °C for 2 hr	1.24	0.60	0.20
800 °C for 10 hr	1.24	0.60	0.20
Stoichiometric Values	1.2	0.6	0.2

5.3 Particle Size Distribution

Figure 5.1 shows the particle size distribution of the as-synthesized xLi$_2$MnO$_3$·(1-x)LiNi$_{0.5}$Mn$_{0.5}$O$_2$ (*e.g.*, x = 0.5), as measured by ELPI. The particle size distribution displays a lognormal distribution with a geometric standard derivation of *c.a.* 1.46. The geometric mean diameter of this powder is *c.a.* 0.74 μm, so that the powders from the spray pyrolysis are generally considered as submicron particles, with a few of

them falling into nano size (40 nm) and micron size ranges (*c.a.* 8 μm). The particle number density is 4.8×10^{6} #cm^{-3}.

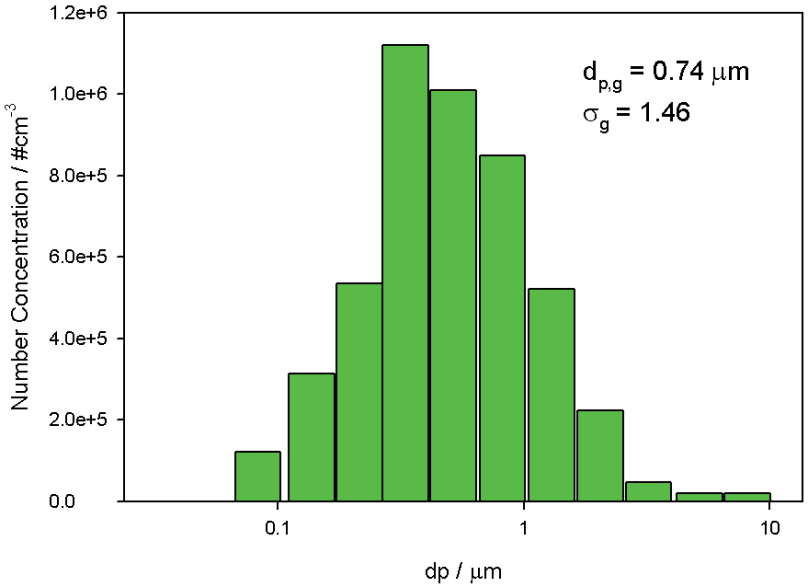

Figure 5.1 Particle size distribution of the as-synthesized composite material xLi$_2$MnO$_3$·(*1-x*)LiNi$_{0.5}$Mn$_{0.5}$O$_2$ as measured using ELPI.

5.4 Crystallographic Analysis

5.4.1 X-Ray Powder Diffraction

Layered composite materials with a general formula xLi$_2$MnO$_3$·*(1-x)*LiNi$_{0.5}$Mn$_{0.5}$O$_2$ ($0.3 \leq x \leq 0.7$) were synthesized *via* a spray pyrolysis process. The XRD patterns of the as-produced powders are shown in Figure 5.2. Due to the nano-size crystallite, the XRD peaks are very broad and certain peaks overlap between 35° and 40° (*2θ*). According to

research reports from Dahn *et al.,* the XRD pattern of this type can be indexed as either a spinel-type low-temperature $LiCO_2$ ($Fd\bar{3}m$) structure or layered ($R\bar{3}m$) structure [179, 180]. Nonetheless, the XRD patterns are also similar to that of the lithiated-$LiCoO_2$-type structure with a spinel $Fd\bar{3}m$ symmetry [186]. As the composite material is Li-excess and the synthesis temperature is sufficient high (700 °C), the as-produced powders are considered adopting the lithiated-$LiCoO_2$ type structure.

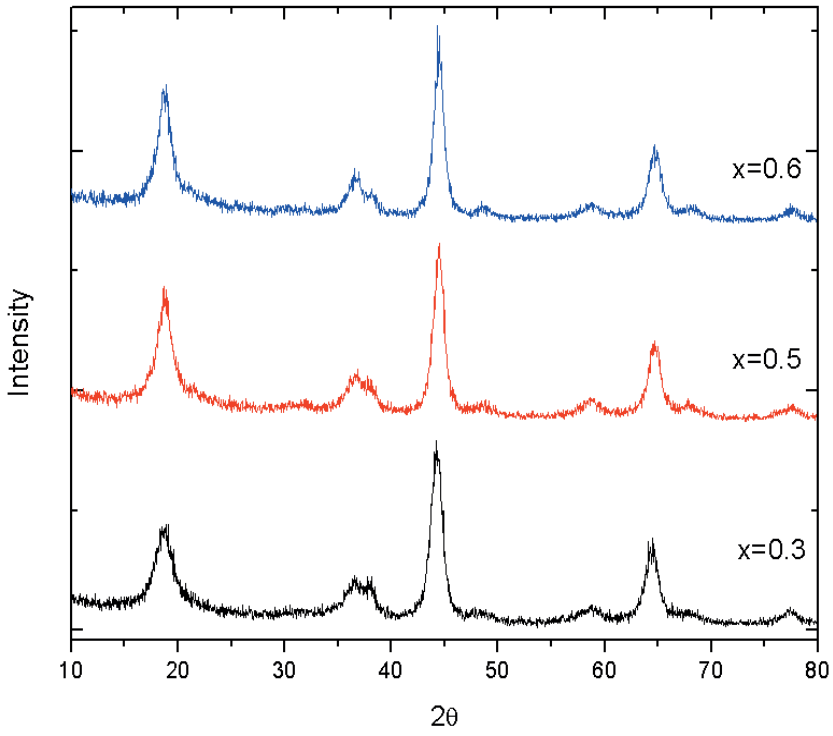

Figure 5.2 XRD pattern of as-produced (non-annealed) nanostructured $xLi_2MnO_3 \cdot (1-x)LiNi_{0.5}Mn_{0.5}O_2$ (where x = 0.3, 0.5 and 0.7) powders from spray pyrolysis.

After annealing at 800 °C for 2 hr, the layered-layered composite $x\mathrm{Li_2MnO_3}\cdot(1\text{-}x)\mathrm{LiNi_{0.5}Mn_{0.5}O_2}$ ($0.3 \leq x \leq 0.7$) can be clearly indexed as rhombohedral symmetry with the $R\bar{3}m$ space group , as seen in Figure 5.3. All the XRD spectrums of composite materials have shown a broad peak between 20 and 25° (2θ, arrow in Figure 5.3), indicating the superlattice ordering of Li and Mn cations in transition-metal layers for $\mathrm{Li_2MnO_3}$ (3a sites) [179, 187]. The broad XRD peak is considered as an evidence of the presence of the $\mathrm{Li_2MnO_3}$-type structure (*C2/m* symmetry) [37, 99]. Moreover, HRTEM shows that the nano-domains of the $\mathrm{Li_2MnO_3}$ structure integrate into the layered $R\bar{3}m$ structure, rather than forming a solid-solution between $\mathrm{Li_2MnO_3}$ and $\mathrm{LiNi_{0.5}Mn_{0.5}O_2}$ [188, 189]. The magnitude of the $\mathrm{Li_2MnO_3}$-type Bragg peaks increases with the amount of $\mathrm{Li_2MnO_3}$ in the composite materials, as seen in Figure 5.3. The (018) and (110) peaks near 65° (2θ) start to split as the x value increases due to the growing of the parent hexagonal cells with $R\bar{3}m$ symmetry and formation of a more compact structure [181, 189]. The $\mathrm{Li_2MnO_3}$-type structure is expected to be significant for maintaining structural stability and consequently the electrochemical properties of the composite materials.

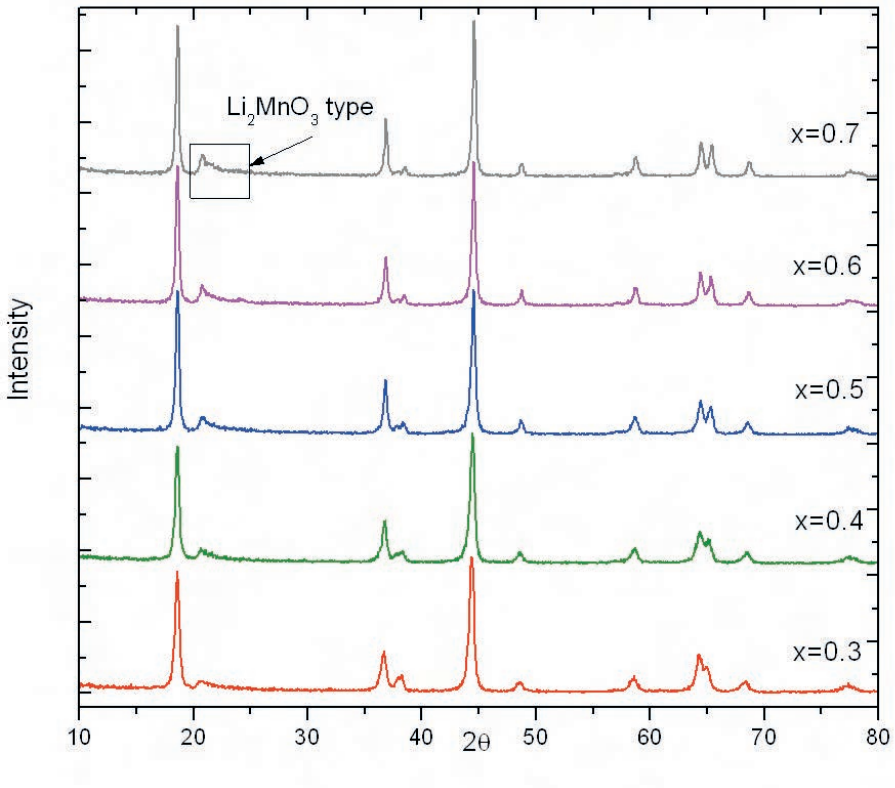

Figure 5.3 XRD pattern of composite material xLi$_2$MnO$_3$·(1-x)LiNi$_{0.5}$Mn$_{0.5}$O$_2$ (x = 0.3, 0.4, 0.5, 0.6 and 0.7) annealed at 800 °C for 2 hr.

5.4.2 Rietveld Cell Refinement

Figure 5.4 shows the XRD pattern of $0.5Li_2MnO_3 \cdot 0.5LiNi_{0.5}Mn_{0.5}O_2$ (or $Li_{1.2}Ni_{0.2}Mn_{0.6}O_2$) and the calculated XRD pattern based on the single-phase Rietveld cell refinement. The assumption is that the composite material $0.5Li_2MnO_3 \cdot 0.5LiNi_{0.5}Mn_{0.5}O_2$ adopted a single phase solid-solution $Li[Li_{0.2}Ni_{0.2}Mn_{0.6}]O_2$ structure, in which a small proportion of Li ions occupy the octahedral sites in the transition metal layer. It shows that, except for the broad peak between 20° and 25° from the Li_2MnO_3-type structure, the whole pattern can be indexed as the rhombohedral $R\bar{3}m$ structure.

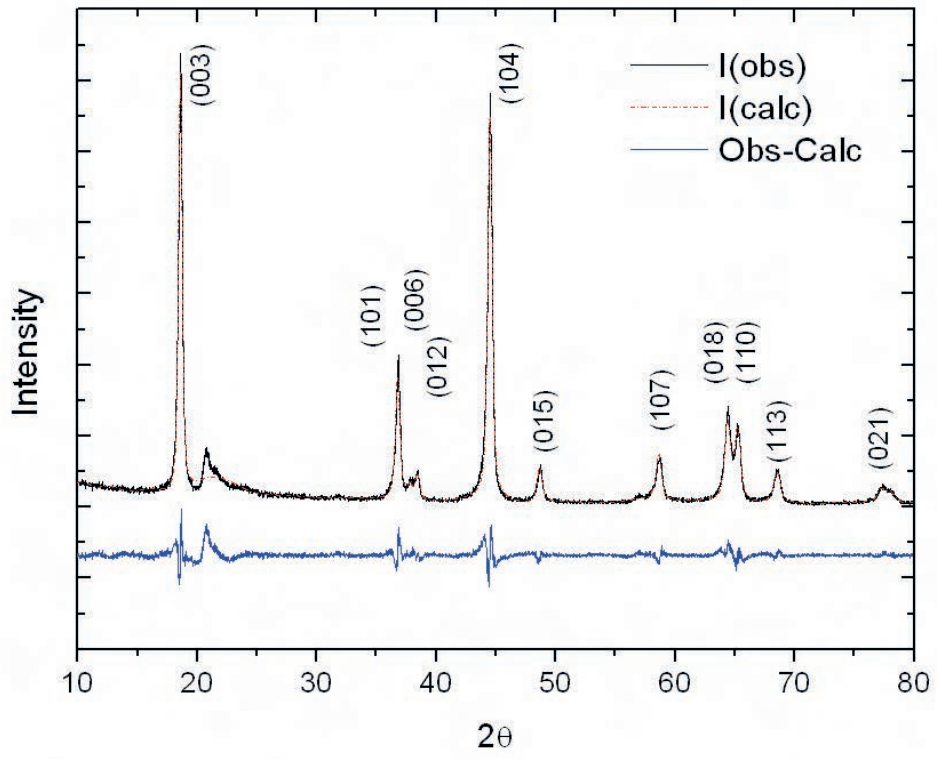

Figure 5.4 Single-phase Rietveld cell refinement of $0.5Li_2MnO_3 \cdot 0.5LiNi_{0.5}Mn_{0.5}O_2$ (or $Li_{1.2}Ni_{0.2}Mn_{0.6}O_2$) powder annealed at 800 °C for 2 hr. The structure parameter and the refined results are shown in Table 5.3.

The refined cell parameters in Table 5.3 also show good agreement with the results obtained using WPF method in Jade 9, as seen in Figure 6.4. Rietveld refinement result also confirms that some Ni ions exchange with the Li at (*3a*) sites, consistent with early observations by Dahn *et al.* [180]. The reason is understood to be the similar ionic radius of Ni^{2+} ($r_{Ni^{2+}}$= 0.69 Å) and Li^{+} ($r_{Li^{+}}$= 0.76 Å), which makes them exchangeable at *3a* Li sites. The reliability factor *wRp* and *Rp* are slightly higher than 10% due to the presence of Li_2MnO_3 phase. Therefore a two-phase Rietveld refinement is necessary to get a better fitting.

Table 5.3 Rietveld cell refinement parameters and results of the $0.5Li_2MnO_3 \cdot 0.5LiNi_{0.5}Mn_{0.5}O_2$ (or $Li_{1.2}Ni_{0.2}Mn_{0.6}O_2$) powder annealed at 800 °C for 2 hr.

atom	site	fractional coordinates			occupancy
Li1	**3a**	0	0	0	0.965
Ni2	**3a**	0	0	0	0.035
Mn1	**3b**	0	0	0.5	0.600
Ni1	**3b**	0	0	0.5	0.165
Li2	**3b**	0	0	0.5	0.235
O1	**6c**	0	0	0.243616	1.000
Space group	$R\bar{3}m$				
a / Å	2.856795				
c / Å	14.242840				
V / Å^3	100.667				
wRp	14.62%				
Rp	10.93%				
R(F2)	5.78%				
Chi^2	3.086				

5.5 Powder Morphology

The powders produced *via* spray pyrolysis, *e.g.*, $0.5Li_2MnO_3 \cdot 0.5LiNi_{0.5}Mn_{0.5}O_2$ (or simply $Li_{1.2}Ni_{0.2}Mn_{0.6}O_2$), are spherical in shape and in the nano to micron size range, as seen in Figure 5.5a. It is anticipated that the powders have a very high packing density with the smaller particles filling in the interparticle spacing of larger particles. The as-produced powder is nanocrystalline, and shows nano- to mesoporous morphology (Figure 5.5b). As the particle size increases to *c.a.* 5 to 10 μm, semi-spherical-shaped porous particles are also observed (SEM images not shown). The irregular-shaped particles can be removed by removing larger precursor droplets using a cyclone or an impactor prior to entering the furnace reactor.

After annealing at 800 °C for 2 hr, the spherical shape is preserved, and the particles appear to be more porous and coarsened, as shown in Figure 5.6. It also shows that for sample $x = 0.7$ (Figure 5.6c), the primary particles are larger and the surface is more porous than that of the other samples with smaller x values. Therefore, the ratio of Li_2MnO_3 and $LiNi_{0.5}Mn_{0.5}O_2$ in the materials has significant effect on sintering process of the composite materials. This morphology change was also observed during the synthesis of $Li_{(1+x)}Ni_{0.25}Mn_{0.75}O_{(2.25+x/2)}$ *via* coprecipitation process at Argonne National Laboratory [37]. Their observation indicates that a higher Li concentration will produce more coarsened secondary particles with larger primary particles under the same heat treatment. The reason is explained to be a sintering effect during lithiation and calcination processes.

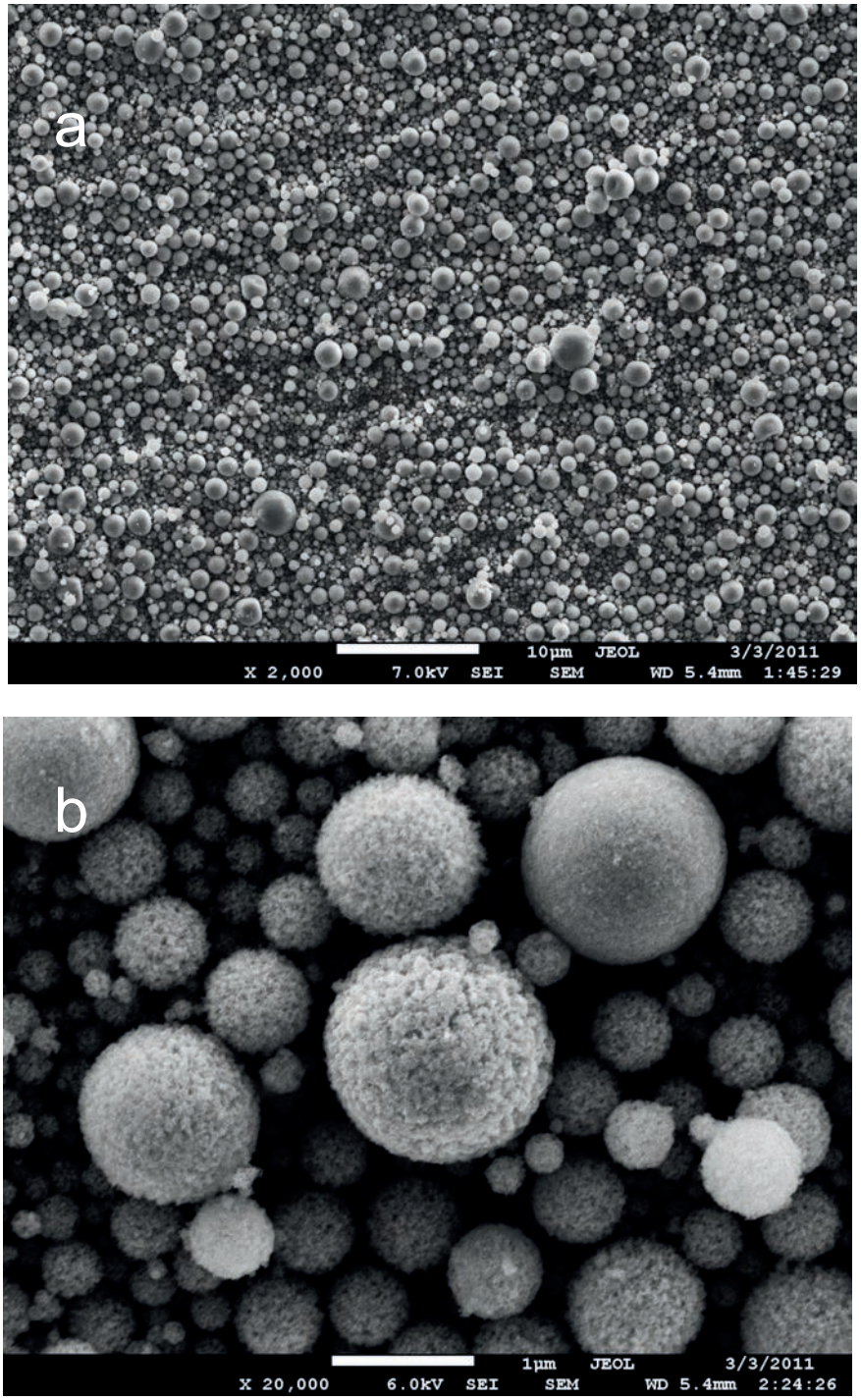

Figure 5.5 SEM photographs of as-produced (non-annealed) nanostructured $0.5Li_2MnO_3 \cdot 0.5LiNi_{0.5}Mn_{0.5}O_2$ (or simply $Li_{1.2}Ni_{0.2}Mn_{0.6}O_2$) powders from spray pyrolysis.

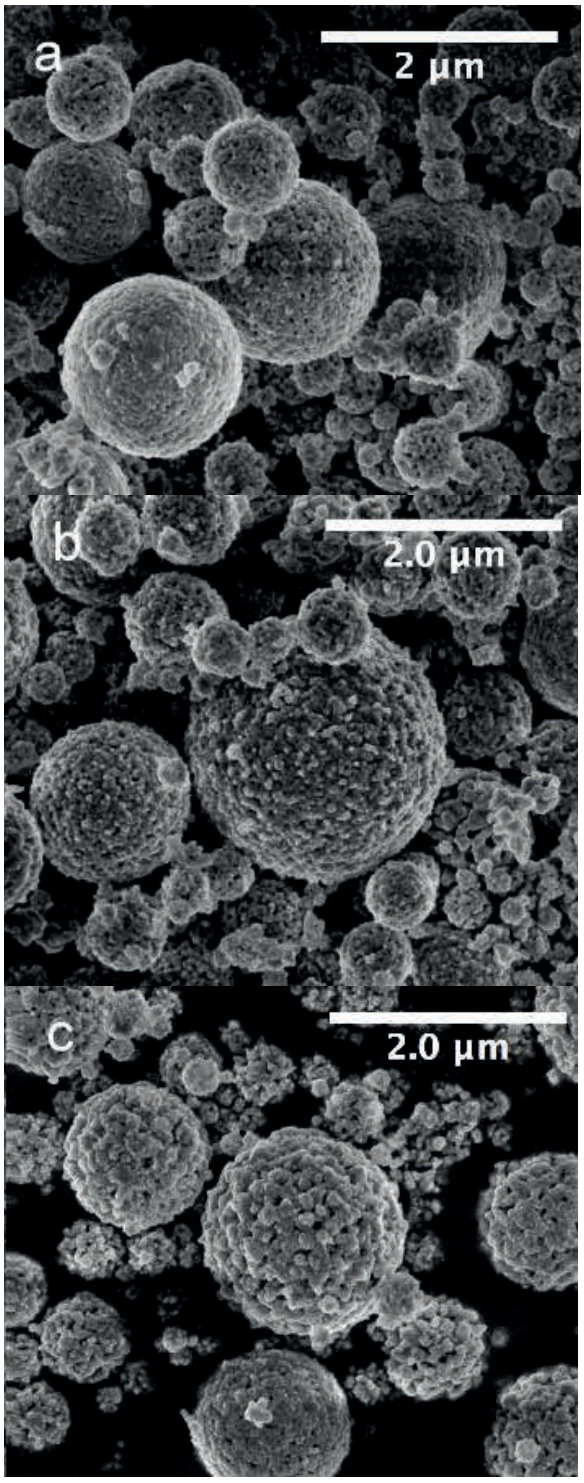

Figure 5.6 Porous morphology of composite materials xLi$_2$MnO$_3$·(1-x)LiNi$_{0.5}$Mn$_{0.5}$O$_2$ as observed by SEM: (a) x=0.3; (b) x=0.5; (c) x=0.7. The powders were annealed at 800 °C for 2 hr.

5.6 Electrochemical Performance

5.6.1 Voltage Profile and Capacity

Figure 5.7 shows the initial charge/discharge curves of $x\mathrm{Li_2MnO_3}\cdot(1\text{-}x)\mathrm{LiNi_{0.5}Mn_{0.5}O_2}$ (*e.g.*, x = 0.3, 0.4, 0.5 and 0.6) cells tested at a constant current density of 11.5 $\mathrm{mAg^{-1}}$ at room temperature (23 °C). All the cells show a two-step charge profile and a smooth discharge profile between 2.0 and 4.6 V. In the first cycle, the voltage slowly climbs from 3.5 V to 4.5 V due to the $\mathrm{Ni^{2+}/Ni^{4+}}$ redox couple during the extraction of Li. At *c.a.* 4.5 V, a voltage plateau appears, which is attributed to the removal of Li and O from $\mathrm{Li_2MnO_3}$ [33, 190]. The reactions in the composite materials during charging can be written as

$$LiNi_{0.5}Mn_{0.5}O_2 \rightarrow Li^+ + Ni_{0.5}Mn_{0.5}O_2 + e^- \qquad (5.2)$$

$$2\,Li_2MnO_3 \rightarrow 4\,Li^+ + 2\,Mn^{4+}O_3^{1.33-} + 4\,e^- \qquad (5.3)$$

(electrochemical oxidation)

$$2\,Mn^{4+}O_3^{1.33-} \rightarrow 2\,MnO_2 + O_2 \qquad (5.4)$$

(chemical redox reaction)

The net loss in the two-step Li-extraction reactions is $\mathrm{Li_2O}$ from the $\mathrm{Li_2MnO_3}$, after which the electrochemically active $\mathrm{MnO_2}$ component is produced. The composition of fully charged electrode can be written as $x\mathrm{MnO_2}\cdot(1\text{-}x)\mathrm{Ni_{0.5}Mn_{0.5}O_2}$ theoretically, where

Mn and Ni both are tetravalent and they occupy the octahedral sites. MnO_2 is also in a layered arrangement that the layered structure is not disrupted after the Li_2O extraction. The length of the 4.5 V plateau increases with x values, and on the other hand the capacity from Ni^{2+}/Ni^{4+} redox couple decreases. The turn-up of the voltage profile near the end of charge above 4.7 V may be from the oxidation of the electrolyte, which can provide excess capacity. During the discharge process, Li can be reinserted into the tetrahedral interstitial sites in MnO_2, forming $LiMnO_2$ ($Mn^{4+} \rightarrow Mn^{3+}$). From the ongoing discussion, the discharge of the $x MnO_2 \cdot (1-x) Ni_{0.5}Mn_{0.5}O_2$ electrodes from *c.a.* 4.6 V to 2.0 V is characterized by three steps: (1) Ni^{4+} is reduced to Ni^{3+} occurring between 4.6 and 3.9 V; (2) Ni^{3+} is further reduced to Ni^{2+} between 3.9 and 3.5 V; (3) reduction of Mn^{4+} to Mn^{3+} forming $LiMnO_2$ between 3.5 and 2.9 V. Therefore, the theoretical charge and discharge capacity of the composite electrodes $x Li_2MnO_3 \cdot (1-x) LiNi_{0.5}Mn_{0.5}O_2$ (*e.g.*, x = 0.3, 0.4, 0.5 and 0.6) can be easily calculated based on Faraday's law, as seen in Table 5.4. For example, a fully charged $0.5MnO_2 \cdot 0.5Ni_{0.5}Mn_{0.5}O_2$ electrode (or simply $Mn_{0.75}Ni_{0.25}O_2$ electrode from $0.5Li_2MnO_3 \cdot 0.5LiNi_{0.5}Mn_{0.5}O_2$), has a theoretical discharge capacity of 252 $mAhg^{-1}$, in which 63 $mAhg^{-1}$ comes from Ni^{4+}/Ni^{3+}, 63 $mAhg^{-1}$ is from Ni^{3+}/Ni^{2+} and 126 $mAhg^{-1}$ is from Mn^{4+}/Mn^{3+}. The discharge capacities of these composite materials between 4.6 and 2.9 V as measured using coin cells, have shown good agreement to their theoretical calculations. Moreover, for x = 0.5, the composite electrode shows a coulombic efficiency of *c.a.* 80% in the first cycle, which is the highest among the composite materials produced.

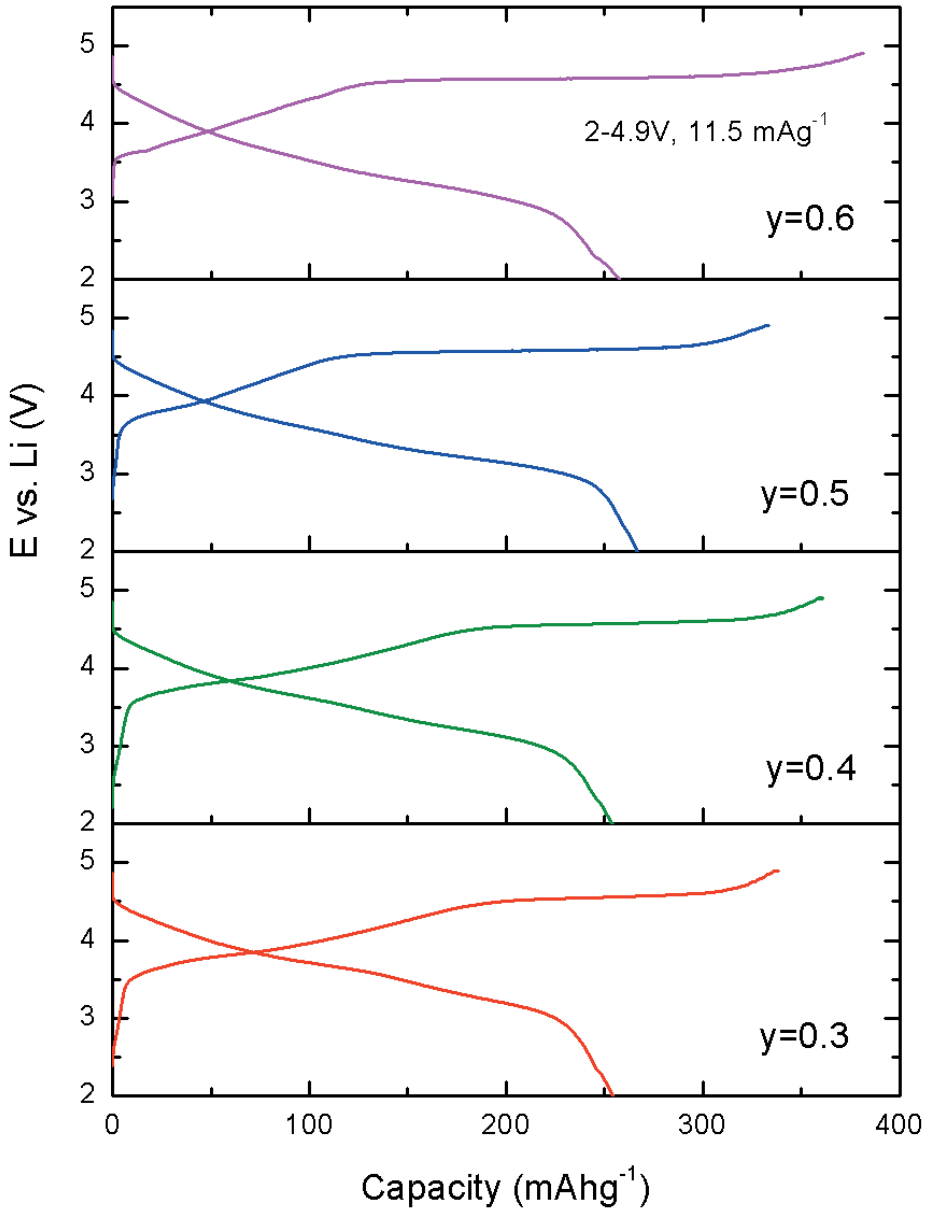

Figure 5.7 Initial charge-discharge voltage profile vs. capacity of the composite materials xLi$_2$MnO$_3$·(1-x)LiNi$_{0.5}$Mn$_{0.5}$O$_2$ (*e.g.*, x=0.3, 0.4, 0.5 and 0.6). The current density is 11.5 mAg^{-1}, with a cut-off voltage between 2.0 and 4.9 V. The test is performed at room temperature, 23°C

Table 5.4 Theoretical capacity of the layered composite materials $x$$Li_2MnO_3$·*(1-x)*$LiNi_{0.5}Mn_{0.5}O_2$ and the corresponding chemical formula in the solid-solution format.

$x$$Li_2MnO_3$· *(1-x)*$LiNi_{0.5}Mn_{0.5}O_2$	$Li[Li_{(1/3-2a/3)}Ni_aMn_{(2/3-a/3)}O_2$	Charge Capacity / $mAhg^{-1}$	Discharge Capacity / $mAhg^{-1}$		
x	a		Ni^{4+}/Ni^{2+}	Mn^{4+}/Mn^{3+}	Total
0.3	7/23	341	184	79	263
0.4	1/4	360	154	103	257
0.5	1/5	378	126	126	252
0.6	2/13	396	99	148	247

5.6.2 Cycle Performance

Figure 5.8 shows the cycle performance of the $x$$Li_2MnO_3$·(*1-x*)$LiNi_{0.5}Mn_{0.5}O_2$ (where x = 0.3, 0.4, 0.5 and 0.6) electrodes at a current density of 23 mAg^{-1} between 2.0 and 4.8 V. The cycle test is performed at room temperature 23 °C. For $x \geq 0.5$, the materials have better capacity retention and efficiency than those for $x < 0.5$, due to the presence of sufficient Li_2MnO_3-type phases stabilizing the structure. The surface area of these materials is also expected low due to the larger primary particle size, thus the side reactions (dissolution of active species and oxidation of electrolyte) can be minimized. With equal amount of Li_2MnO_3 and $LiNi_{0.5}Mn_{0.5}O_2$ phases, the composite material yields a superior cycleability and capacity: over 225 $mAhg^{-1}$ after 20 cycles with coulombic efficiency of over 98%. Moreover, the coulombic efficiency of $0.5Li_2MnO_3$·$0.5LiNi_{0.5}Mn_{0.5}O_2$ at the first cycle is the highest among the composite

materials tested. Nonetheless, an excess amount of Li_2MnO_3 phase for $x = 0.6$, is believe to decrease the electrochemical activity of the composite material and the capacity thereof, because Li_2MnO_3 is not electrochemically active. Capacity fading of electrodes with $x = 0.3$ and 0.4 is also observed, which is unlikely due to Jahn-Teller distortion of Mn^{3+} at deep discharge. It is known that in a fully discharged composite material, after the fist cycle, the electrode composition can be written as $x\text{LiMnO}_2 \cdot (1\text{-}x)\text{LiNi}_{0.5}\text{Mn}_{0.5}\text{O}_2$, where Mn is trivalent in $LiMnO_2$ and tetravalent in $LiNi_{0.5}Mn_{0.5}O_2$, and Ni is divalent. If x is less than 0.5, the average oxidation state of Mn is higher than +3.5 and the Jahn-Teller distortion would not play a significant role to deteriorate the structural stability of the composite electrodes. One possible reason for the capacity fading could be the smaller primary particle size in these materials ($x < 0.5$), which provides a sufficiently large surface area for size reactions. After a longer calcination time, the composite materials with less Li_2MnO_3 phase are expected to show a better capacity retention.

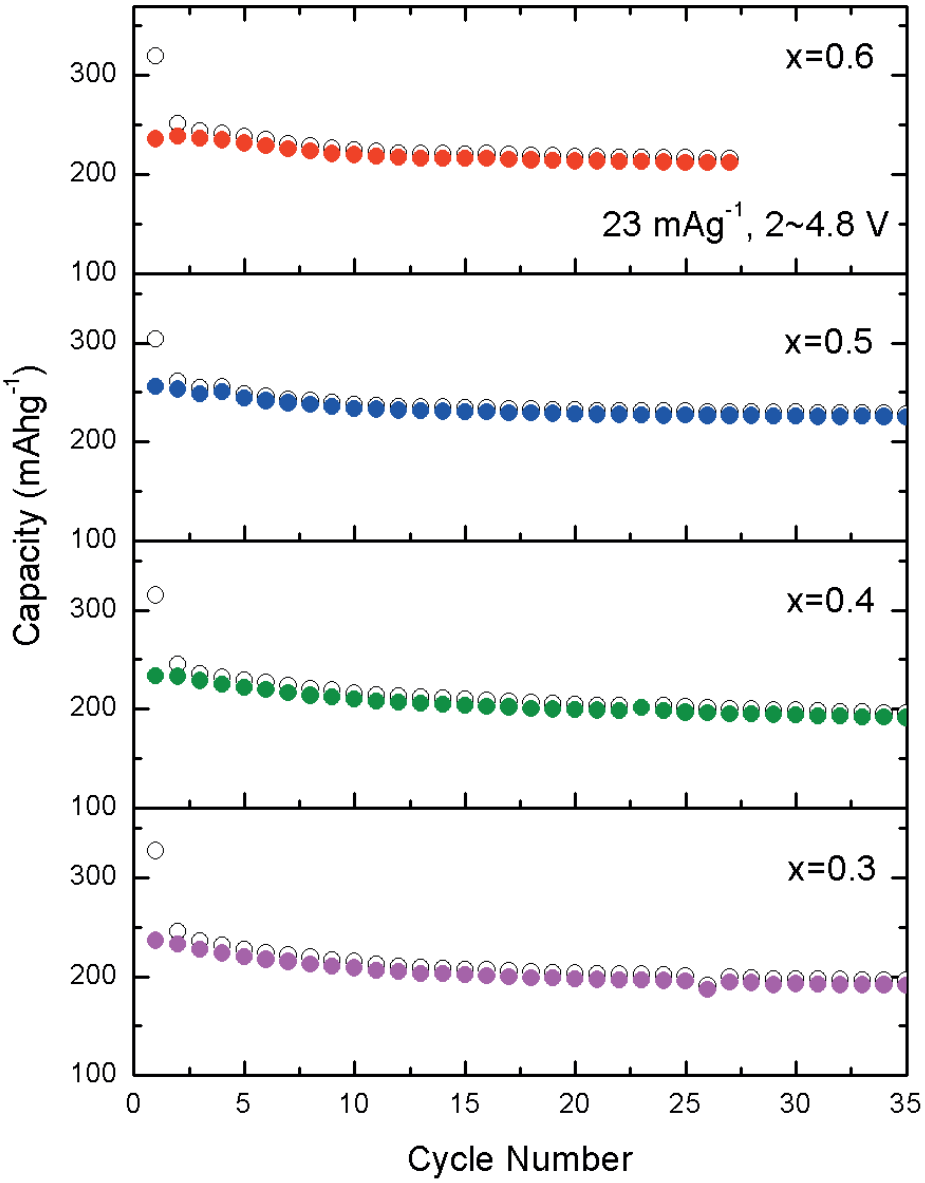

Figure 5.8 Cycling performance of the composite material xLi$_2$MnO$_3$·(1-x)LiNi$_{0.5}$Mn$_{0.5}$O$_2$ (where x=0.3, 0.4, 0.5 and 0.6). The current density is 23 mAg^{-1}, with a cut-off voltage between 2.0 and 4.8 V. The test is performed at room temperature, 23°C.

5.6.3 Rate Performance

$0.5Li_2MnO_3 \cdot 0.5LiNi_{0.5}Mn_{0.5}O_2$ (or $Li_{1.2}Ni_{0.2}Mn_{0.6}O_2$) is selected for the rate performance test, because it displays the highest capacity and the best cycleability. A slightly higher cut-off voltage, 4.9 V, is selected for the complete activation of the electrode in compensation for the kinetic effects. As seen in Figure 5.9, starting at 23 mAg^{-1}, the current density is increased every five cycles till it reaches 230 mAg^{-1}, and is then switched back to 23 mAg^{-1} for the future cycles. As previously observed, the coulombic efficiency of the test cell increases for the first few cycles before reaching an "efficiency plateau". At a constant current density of 115 mAg^{-1}, $0.5Li_2MnO_3 \cdot 0.5LiNi_{0.5}Mn_{0.5}O_2$ (or $Li_{1.2}Ni_{0.2}Mn_{0.6}O_2$) delivers roughly 200 $mAhg^{-1}$ with a 99% efficiency (Figure 5.9a). Divided by the discharge capacity at the first cycle (250 $mAhg^{-1}$), the normalized capacity is 80% at a 115 mAg^{-1} discharge rate. When the current density increases to 230 mAg^{-1}, the cell supplies *c.a.* 170 $mAhg^{-1}$ with a very high efficiency, 99.5%. At this current density, the normalized capacity retention is 70%, and no severe irreversible capacity loss is observed. After switching back to 23 mAg^{-1}, the $0.5Li_2MnO_3 \cdot 0.5LiNi_{0.5}Mn_{0.5}O_2$ electrodes can supply 240 $mAhg^{-1}$ with an average efficiency of 98.2%. The corresponding discharge voltage profiles of the $0.5Li_2MnO_3 \cdot 0.5LiNi_{0.5}Mn_{0.5}O_2$ at different C-rates are showing smooth curves. As the current density exceeds 46 mAg^{-1}, only a moderate polarization is observed.

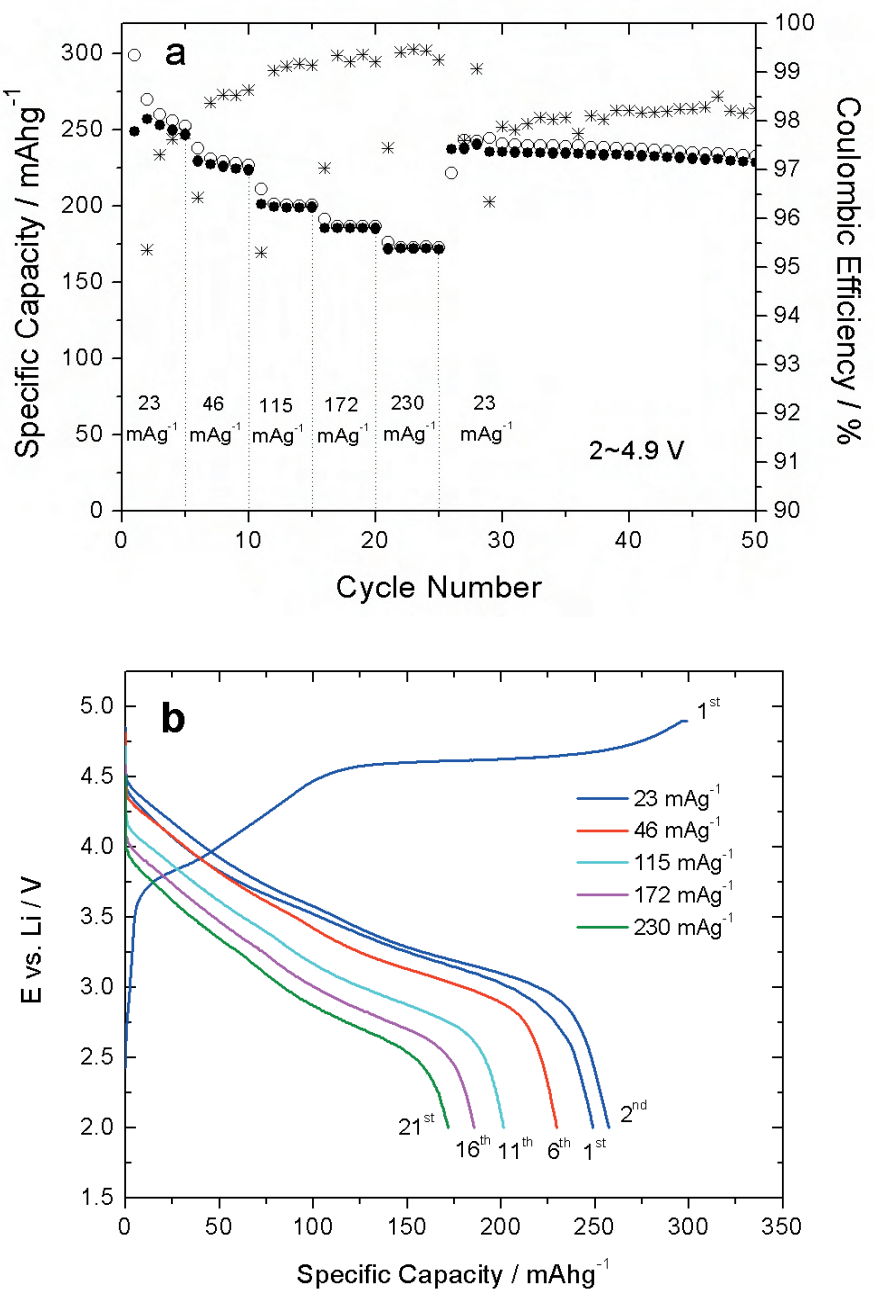

Figure 5.9 Cycle performance of $0.5Li_2MnO_3 \cdot 0.5LiNi_{0.5}Mn_{0.5}O_2$ (or $Li_{1.2}Ni_{0.2}Mn_{0.6}O_2$) after annealing at 800°C for 2 hr: (a) cycle life at elevated C-rates; and (b) corresponding voltage profile at elevated C-rates.

5.7 Annealing Conditions

The post annealing process is important to refine the crystal structure and grow the crystallites in the materials. In this research, $0.5Li_2MnO_3 \cdot 0.5LiNi_{0.5}Mn_{0.5}O_2$ composite material is annealed at different temperatures for different time periods. In order to maintain a good porosity for the powder, only a moderate temperature is applied in the post annealing process, *i.e.* 600 to 800 °C. At 600 °C, the grain size and primary particle size will not grow noticeably. Therefore, efforts are focused in the temperature range between 700 and 800 °C. $0.5Li_2MnO_3 \cdot 0.5LiNi_{0.5}Mn_{0.5}O_2$ annealed at 700 °C (2 hr) adopts lithiated-$LiCoO_2$-type structure, with a spinel-type $Fd\,\bar{3}\,m$ structure, due to exchange/mixing of Li and Ni cations in 16c and 16d sites [180, 186], which will be discussed in Chapter 6. The lithiated-$LiCoO_2$-type $0.5Li_2MnO_3 \cdot 0.5LiNi_{0.5}Mn_{0.5}O_2$ shows an inferior cycleability to the powder annealed at 800 °C.

A longer annealing time at the high-temperature, *i.e.,* 800 °C, is also studied. $0.5Li_2MnO_3 \cdot 0.5LiNi_{0.5}Mn_{0.5}O_2$ powders are annealed at 800 °C for 2 hr and 10 hr, and then fabricated into test cells. The ICP-MS data shows that the stoichiometry of the powder is preserved after annealing at 800°C for 2 hr and 10 hr, as shown in Table 5.2. As shown in Figure 5.10, $0.5Li_2MnO_3 \cdot 0.5Li\ Ni_{0.5}Mn_{0.5}O_2$ annealed at 800°C for 2 hr and 10 hr can be indexed as α-$NaFeO_2$ structure with $R\bar{3}m$ space group (rhombohedral symmetry). However, the powder annealed for 10 hr shows asymmetry peaks for (104) and (018) planes. The asymmetry of XRD peaks is believed to be due to the overlapping of XRD peaks with $R\bar{3}m$ structure and spinel $Fd\bar{3}m$ structure [37], or more likely

between $R\bar{3}m$ structure and monoclinic Li_2MnO_3 type ($C2/m$) structure. With stoichiometric amount of Li in the composite material, it is unlikely to form a spinel-type structure with tetravalent Mn. For this reason, the broadening of these peaks is considered to originate from the nano domains of the Li_2MnO_3-type structure. Nonetheless, the powder annealed for 10 hr remains porous and its primary particles appear to be larger, as observed by SEM (Figure 5.11a and 5.11b).

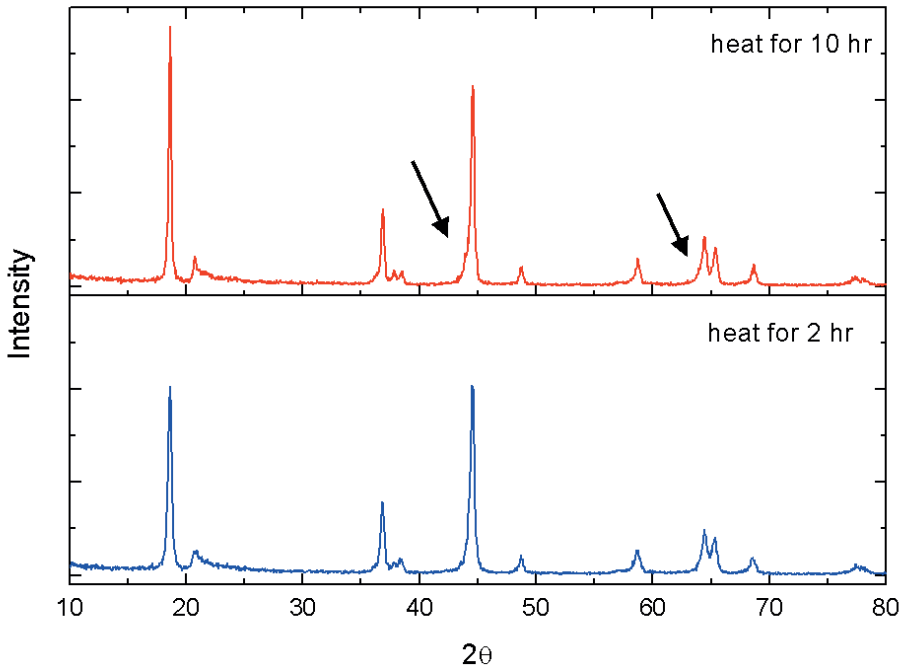

Figure 5.10 XRD pattern of $0.5Li_2MnO_3 \cdot 0.5LiNi_{0.5}Mn_{0.5}O_2$ (or $Li_{1.2}Ni_{0.2}Mn_{0.6}O_2$) after annealing at 800°C for 2 hr and 10 hr. Arrows indicate the broadening of peaks towards lower degrees (2θ).

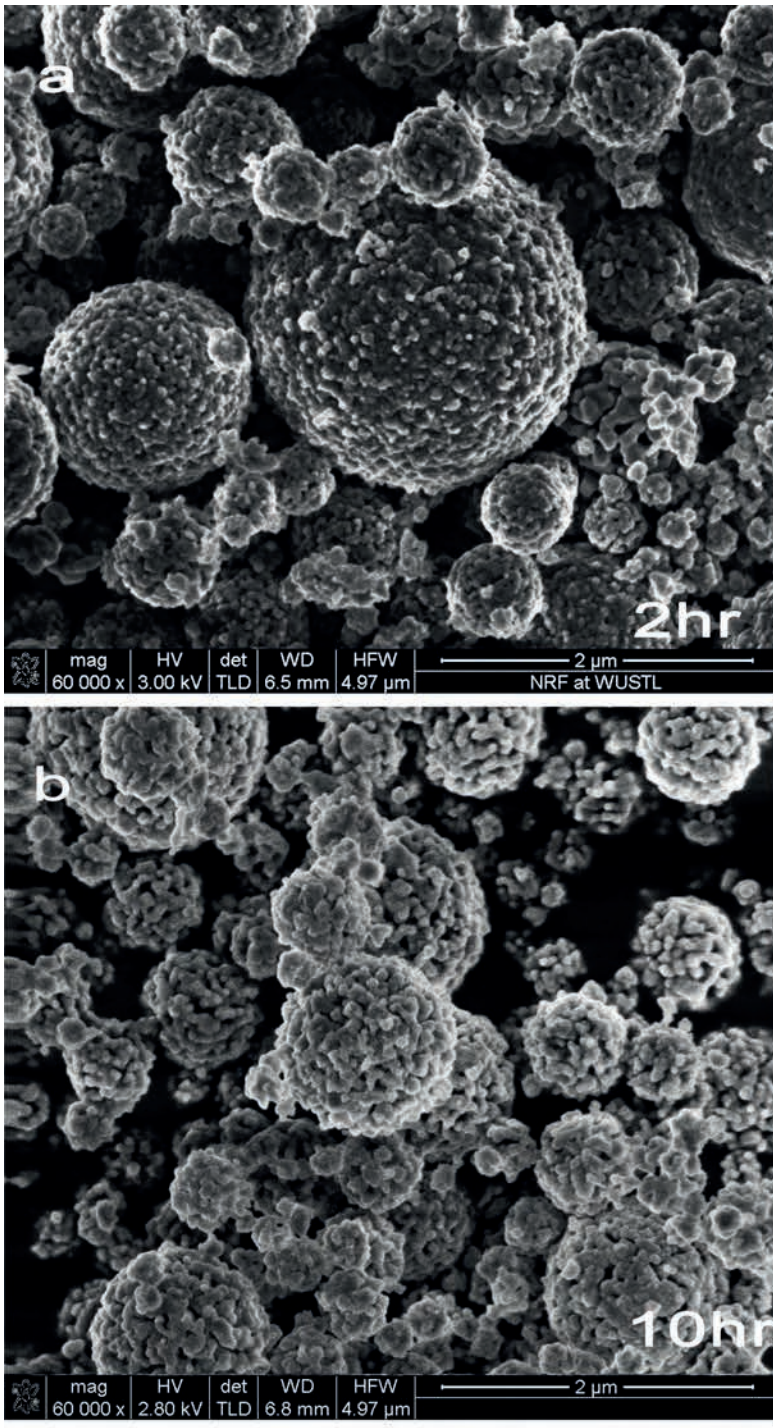

Figure 5.11 Porous morphology of composite materials $x\mathrm{Li_2MnO_3}\cdot(1\text{-}x)\mathrm{LiNi_{0.5}Mn_{0.5}O_2}$ preserved after annealing at 800 °C for 10 hr and 2 hr.

Figure 5.12 shows the cycle performance of the powder annealed for 2 hr and 10 hr. The 10 hr annealed powder experiences a slow activation process, *c.a.* 20 cycles, to achieve a capacity over 220 $mAhg^{-1}$ at 23 mAg^{-1} between 2.0 and 4.8 V. The reason for the slow activation process may possibly be due to the larger domains of Li_2MnO_3-type phase as previously observed. It is known that Li_2MnO_3 is electrochemically inactive, which can induce a large kinetic barrier for Li transportation.

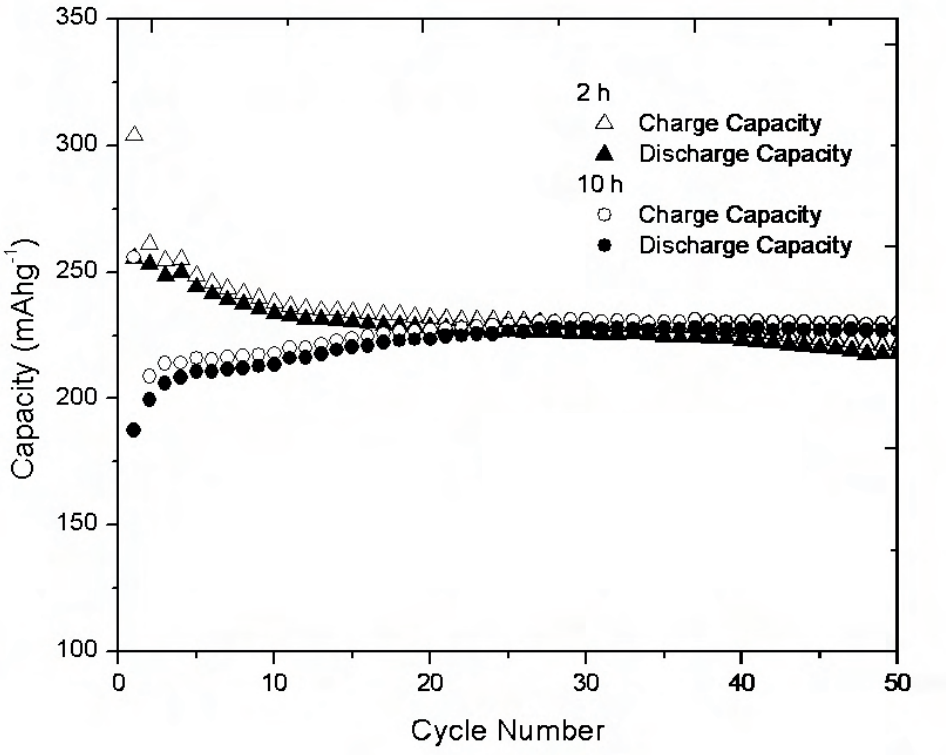

Figure 5.12 Cycle performance of $0.5Li_2MnO_3 \cdot 0.5LiNi_{0.5}Mn_{0.5}O_2$ (or $Li_{1.2}Ni_{0.2}Mn_{0.6}O_2$) after annealing at 800°C for 2 hr and 10 hr, at 23 mAg^{-1} between 2.0 and 4.8 V.

The BET specific surface area of the 10 hr powder is measured to be 13.34 m^2g^{-1} compared to 20.94 m^2g^{-1} of the 2 hr annealed powder. As seen in Figure 5.11, all the particles remain the spherical shape, so that the interparticle sintering effect is considered

very minor. For this reason, the increase in primary particle size predominantly accounts for the decrease in the specific surface area of the powder. The larger primary particle size may also lead to the slow electrochemical activation that the reconstitution reaction of Li_2MnO_3 is kinetically unfavorable due to the strains within the large primary particles. Therefore, the 10 hr annealed powder is not subjected to the rate performance test.

5.8 Summary

Mesoporous $x\mathrm{Li_2MnO_3}\cdot(1\text{-}x)\mathrm{LiNi_{0.5}Mn_{0.5}O_2}$ ($0.3 \leq x \leq 0.7$) composite materials have been synthesized *via* a spray pyrolysis process with post-annealing process (typically at 800 °C for 2 hr). All the powders produced are spherical in shape and submicron in size. Under the same synthesis condition, the powders appear to be more coarsened with larger primary particles as the *x* value increases from 0.3 to 0.7. The composite materials have a rock-salt type structure, which can be index as an rhombohedral $R\bar{3}m$ structure. $\mathrm{Li_2MnO_3}$-type structure is also observed for the composite material on the XRD spectrum, and its intensity increases with *x* values. Rietveld cell refinement of the XRD pattern of the composite material $0.5\mathrm{Li_2MnO_3}\cdot0.5\mathrm{LiNi_{0.5}Mn_{0.5}O_2}$ indicates that some of Ni ions exchange with (3a) Li ions due to similar ionic radius in the composite material. At the first charge, the composite materials show a smooth increase in voltage due to the $\mathrm{Ni^{2+/4+}}$ redox couple and then display a voltage plateau near 4.5 V due to electrochemical extraction of $\mathrm{Li_2O}$ from $\mathrm{Li_2MnO_3}$. The length of 4.5 V plateau increases with $\mathrm{Li_2MnO_3}$ content in the composite materials.

Among the composite materials synthesized, $0.5\mathrm{Li_2MnO_3}\cdot0.5\mathrm{LiNi_{0.5}Mn_{0.5}O_2}$ has shown the highest coulombic efficiency in the first cycle, and most importantly the highest discharge capacity and most superior cycle life: over 225 $\mathrm{mAhg^{-1}}$ after 20 cycles with an efficiency of *c.a.* 98.4% at 23 $\mathrm{mAg^{-1}}$ charge/discharge rates. Moreover, the $0.5\mathrm{Li_2MnO_3}\cdot0.5\mathrm{LiNi_{0.5}Mn_{0.5}O_2}$ composite shows excellent rate capability, *i.e.*, 200 $\mathrm{mAhg^{-1}}$ at 115 $\mathrm{mAg^{-1}}$ rates, which is the highest among all the materials that have

ever been synthesized *via* the spray pyrolysis process. When x is less than 0.5, the $x\mathrm{Li_2MnO_3}\cdot(1-x)\mathrm{LiNi_{0.5}Mn_{0.5}O_2}$ composites have very poor cycle life due to the extremely small primary particles that potentially can lead to side reactions. It is also found that powders annealed for a longer time require longer activation process in order to show a comparable capacity with the powders annealed for shorter periods of time, which might be due to either the larger domains of monoclinic $\mathrm{Li_2MnO_3}$ phase or the larger primary particle sizes.

Chapter 6

Integrated Layered-Spinel Li-Ni-Mn-Oxide Composite Materials for High-Energy Li-ion Batteries [4]

[4] Submitted to Journal of the Electrochemical Society, 2011 (under review).

Recently, a layered-spinel integrated composite lithium-nickel-manganese oxide $Li_{1.375}Mn_{0.75}Ni_{0.25}O_{2.4375}$ within the $LiMn_{1.5}Ni_{0.5}O_4$-Li_2MnO_3-$LiNi_{0.5}Mn_{0.5}O_2$ system was developed at Argonne National Laboratory [35, 37, 99, 191]. The material exhibits promising capacity, rate capability and cycle life. $Li_{1.375}Mn_{0.75}Ni_{0.25}O_{2.4375}$ can deliver 200 $mAhg^{-1}$ at a current density of 230 mAg^{-1}, which is the highest reported capacity among the Li-excess high-energy cathode materials [37]. This high performance is understood to be due to the layered-spinel ($R\bar{3}m$ + $Fd\bar{3}m$) integrated structure and the porous morphology composed of nano-sized primary particles [37]. This class of materials has a general formula given by $Li_{(1+x)}Mn_{0.75}Ni_{0.25}O_{(2.25+x/2)}$ ($0 \leq x \leq 1/2$), wherein the oxidation states of the metals are considered to be [Li^+], [Mn^{4+}] and [Ni^{2+}] [37, 99, 191]. $Li_{1.375}Mn_{0.75}Ni_{0.25}O_{2.4375}$ can be expressed as $Li_{1.1}Ni_{0.2}Mn_{0.6}O_{1.95}$, which can be considered as a Li-deficient $Li[Li_{(1/3-2a/3)}Ni_aMn_{(2/3-a/3)}]O_2$ material, wherein a equals 1/5. In this paper, the alternative formula $Li_{(1.2-\delta)}Ni_{0.2}Mn_{0.6}O_{(2-\delta/2)}$ ($0 \leq \delta \leq 1/10$) is employed, as it can better demonstrate the extent of Li deficiency in the composite materials.

The conventional method of synthesis of the composite materials involves coprecipitation of transition metal carbonates, post-lithiation and calcination at high-temperature [37, 99]. The powder is polycrystalline and shows a unique core-shell structure, where the electron diffraction pattern and preferred-growth direction of the core is different from that of the shell [37]. While the performance of Argonne's powder is excellent, the synthesis process is a multistep, slow, energy intensive process. In addition, the particle size and morphology produced from co-precipitation is not ideal, nor is the process readily scalable. Alternatively, we propose a novel spray pyrolysis method for synthesis of

porous high-energy cathode materials. In doing so, we also evaluate whether: (1) a capacity over 200 $mAhg^{-1}$ can be achieved without the unique core-shell morphology; (2) the integrated layered-spinel structure in Li-deficient $Li_{(1.2-\delta)}Ni_{0.2}Mn_{0.6}O_{(2-\delta/2)}$ ($0 \leq \delta \leq 1/10$) materials can be form with mixed precursors as opposed to post-lithiation; (3) a more uniform, spherical product can be produced for this promising class of materials, with improved nano- and microstructures. We will also evaluate the effect of annealed temperature on the electrochemical properties of the porous $Li_{(1.2-\delta)}Ni_{0.2}Mn_{0.6}O_{(2-\delta/2)}$ ($0 \leq \delta \leq 1/10$) materials.

6.1 Material Synthesis *via* Spray Pyrolysis

The spray pyrolysis method uses a tubular aerosol flow reactor, as shown in Figure 2.2, to produce Li-excess $Li_{(1.2-\delta)}Ni_{0.2}Mn_{0.6}O_{(2-\delta/2)}$ ($0 \leq \delta \leq 1/10$) composite materials. The precursor solution was prepared by dissolving $LiNO_3$, $Mn(NO_3)_2 \cdot 4H_2O$ and $Ni(NO_3)_2 \cdot 6H_2O$ at a ratio of (1.2-δ):0.6:0.2 in deionized water. The total molar concentrations of $Mn(NO_3)_2 \cdot 4H_2O$ and $Ni(NO_3)_2 \cdot 6H_2O$ were maintained at 2 $moleL^{-1}$. The corresponding Li precursor concentration can be calculated based on the δ values in $Li_{(1.2-\delta)}Ni_{0.2}Mn_{0.6}O_{(2-\delta/2)}$ composites. For example, for $\delta = 0$, the composite is $Li_{1.2}Ni_{0.2}Mn_{0.6}O_2$, and the precursor solution contained 1.5 $moleL^{-1}$ Mn, 0.5 $moleL^{-1}$ Ni, and 3 $moleL^{-1}$ Li cations.

The precursor solution was aerosolized with an air-assisted nebulizer (one-jet Collison nebulizer, BGI Inc.) to aerosolize the precursor solution, wherein fine precursor droplets in the micron-size range were produced. The flow rate of atomizing gas (air) was maintained at 3.3 lpm at 40 psi. After aerosolization, the precursor aerosols flowed into a preheater maintained at 200 to 300 °C (wall temperature) and then a vertical ceramic tube furnace. At the preheater outlet, the gas temperature was measured to be *c.a.* 100 to 130 °C, therefore, decomposition reactions did not occur for the nitrates during water evaporation in the preheater. The wall temperature of the tube furnace was kept at 700 °C, controlled by three independent temperature controllers. Downstream of the reactor, the as-produced powders were collected with a membrane filter. In this work, the powders were annealed at 700 and 800 °C for 2 hr following by slow cooling at 3 °C min^{-1}. To delineate the different powders, the annealing temperature will be shown in brackets after the material formula, *e.g.*, $Li_{1.2}Ni_{0.2}Mn_{0.6}O_2$ (800 °C) indicates the powder was annealed at 800 °C.

6.2 Elemental Analysis

ICP-MS analysis of the precursor solution for synthesizing $Li_{(1.2-\delta)}Ni_{0.2}Mn_{0.6}O_{(2-\delta/2)}$ powders shows good agreement with the stoichiometry of the material, as shown in Table 6.1. The composite powder is also believed to preserve the stoichiometry after the heat treatment for the reasons discussed in section 5.2.

Table 6.1 ICP-MS results for the precursor solution and theoretical charge/discharge capacities

Theoretical stoichiometry	Measured stoichiometry from ICP-MS			Initial Charge capacity $mAhg^{-1}$	Discharge capacity $mAhg^{-1}$	Coulombic efficiency %
	Li	Mn	Ni			
$Li_{1.1}Ni_{0.2}Mn_{0.6}O_{1.95}$	1.10(0)	0.59(3)	0.20(7)	352.9	240.6	68.2
$Li_{1.15}Ni_{0.2}Mn_{0.6}O_{1.975}$	1.16(2)	0.59(3)	0.20(7)	365.7	246.4	67.4
$Li_{1.2}Ni_{0.2}Mn_{0.6}O_2$	1.20(9)	0.59(5)	0.20(5)	378.2	252.2	66.7

***The numbers in brackets indicate the uncertainty.**

6.3 Particle Size Distribution

Figure 6.1 shows the particle size distribution of the as-synthesized composite materials $Li_{(1.2-\delta)}Ni_{0.2}Mn_{0.6}O_{(2-\delta/2)}$ ($\delta = 0$). The particle size distribution displays a lognormal distribution with a geometric standard derivation of 1.50, as measured by ELPI. The geometric mean diameter of the as-produced powder is *c.a.* 0.76 μm, so that the powders are predominately submicron particles, with a few of them falling into nano size (40 nm) and micron size ranges (*c.a.* 8 μm). The particle number density is *c.a.* 4.3×10^6 $\#cm^{-3}$.

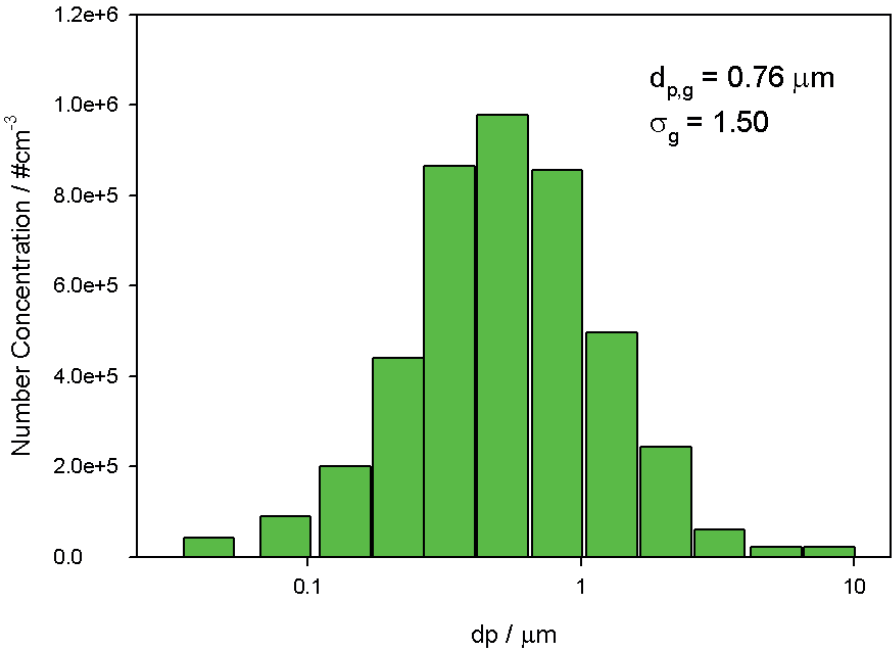

Figure 6.1 Particle size distribution of the as-synthesized composite material $Li_{(1.2-\delta)}Ni_{0.2}Mn_{0.6}O_{(2-\delta/2)}$ as measured using ELPI

6.4 Crystallographic Analysis

6.4.1 X-Ray Powder Diffraction

Figure 6.2 shows XRD patterns of $Li_{(1.2-\delta)}Ni_{0.2}Mn_{0.6}O_{(2-\delta/2)}$ (δ=0, 1/20, 1/10), after annealing at 700 °C and 800 °C. All of the XRD patterns show a broad peak between 20° and 25°, indicating the superlattice ordering of Li, Mn and Ni cations in the transition-metal layer (3a sites) [179, 187]. At the higher annealing temperature 800 °C, the XRD peaks of the powders are sharper indicating a larger grain size. $Li_{1.2}Ni_{0.2}Mn_{0.6}O_2$ (800 °C) shows a nearly identical XRD pattern to $Li_{1.1}Ni_{0.2}Mn_{0.6}O_{1.95}$ (700 °C), and the pattern can

be indexed to α-$NaFeO_2$-type structure with $R\bar{3}m$ space group. $Li_{1.2}Ni_{0.2}Mn_{0.6}O_2$ (700 °C) shows a single peak near 65° *2θ*, which may suggest that it is adopting a different crystal structure other than $R\bar{3}m$. An identical XRD spectrum was observed by Dahn's research group for $Li[Li_{(1/3-2a/3)}Ni_aMn_{(2/3-a/3)}]O_2$ with high Ni concentrations, *i.e.*, $x \geq 1/3$, when heated between 600 °C and 900 °C [180, 186]. In that work, the structure was considered to be isostructural to lithiated-$LiCoO_2$ with a spinel-type $Fd\bar{3}m$ structure, due to exchange/mixing of Li and Ni cations in the 16c and 16d sites [180, 186]. By decreasing the Li concentrations in the material, the exchange/mixing effect can be reduced. Therefore, $Li_{1.15}Ni_{0.2}Mn_{0.6}O_{1.975}$ (700 °C) and $Li_{1.1}Ni_{0.2}Mn_{0.6}O_{1.95}$ (700 °C) adopt predominately an $R\bar{3}m$ structure, as seen in the upper XRD patterns in Figure 6.2b and 6.2c.

Certain peaks in the XRD spectrum of $Li_{1.1}Ni_{0.2}Mn_{0.6}O_{1.95}$ (700 °C) are broadened towards smaller angles near 36°, 44° and 65° *2θ*, as indicated by the arrows in Figure 6.2c. This broadening is not observed for the layered $R\bar{3}m$ $Li_{1.2}Ni_{0.2}Mn_{0.6}O_2$ (800 °C). The peak broadening is similar to an earlier observation [37] on an integrated layered-spinel structure synthesized *via* coprecipitation with post-lithiation. Johnson *et al.* suggested that the spinel structure ($Fd\bar{3}m$) and the layered structure ($R\bar{3}m$) are structurally compatible and can mix physically at the atomic level forming an integrated composite [35, 37, 191]. The similarity of the XRD patterns produced from spray pyrolysis suggests that the $Li_{1.1}Ni_{0.2}Mn_{0.6}O_{1.95}$ (700 °C) may also have an integrated layered-spinel structure, as seen in Figure 6.3.

At a higher annealing temperature, $Li_{1.15}Ni_{0.2}Mn_{0.6}O_{1.975}$ (800 °C) and $Li_{1.1}Ni_{0.2}Mn_{0.6}O_{1.95}$ (800 °C) both undergo a phase transition from α -$NaFeO_2$ type structure ($R\bar{3}m$) to monoclinic Li_2MnO_3-type structure (more likely with *C2/c* space group) [99]. The observed monoclinic Li_2MnO_3-type structure was also detected in $Li_{(1+x)}Mn_{0.75}Ni_{0.25}O_{(2.25+x/2)}$ (where x=0, 1/4) prepared *via* coprecipitation of mixed metal oxide precursors [99]. The $R\bar{3}m$ phase and Li_2MnO_3-type phase may coexist in the material due to extensive overlapping of XRD peaks. However, there is no indication that the transformation occurs for $Li_{1.2}Ni_{0.2}Mn_{0.6}O_2$ (800 °C) heated at the same temperature. Therefore, more Li per formula unit helps retain the $R\bar{3}m$ symmetry at higher temperatures. With only a 4% decrease in total Li, the transformation tends towards the more thermodynamically stable structure.

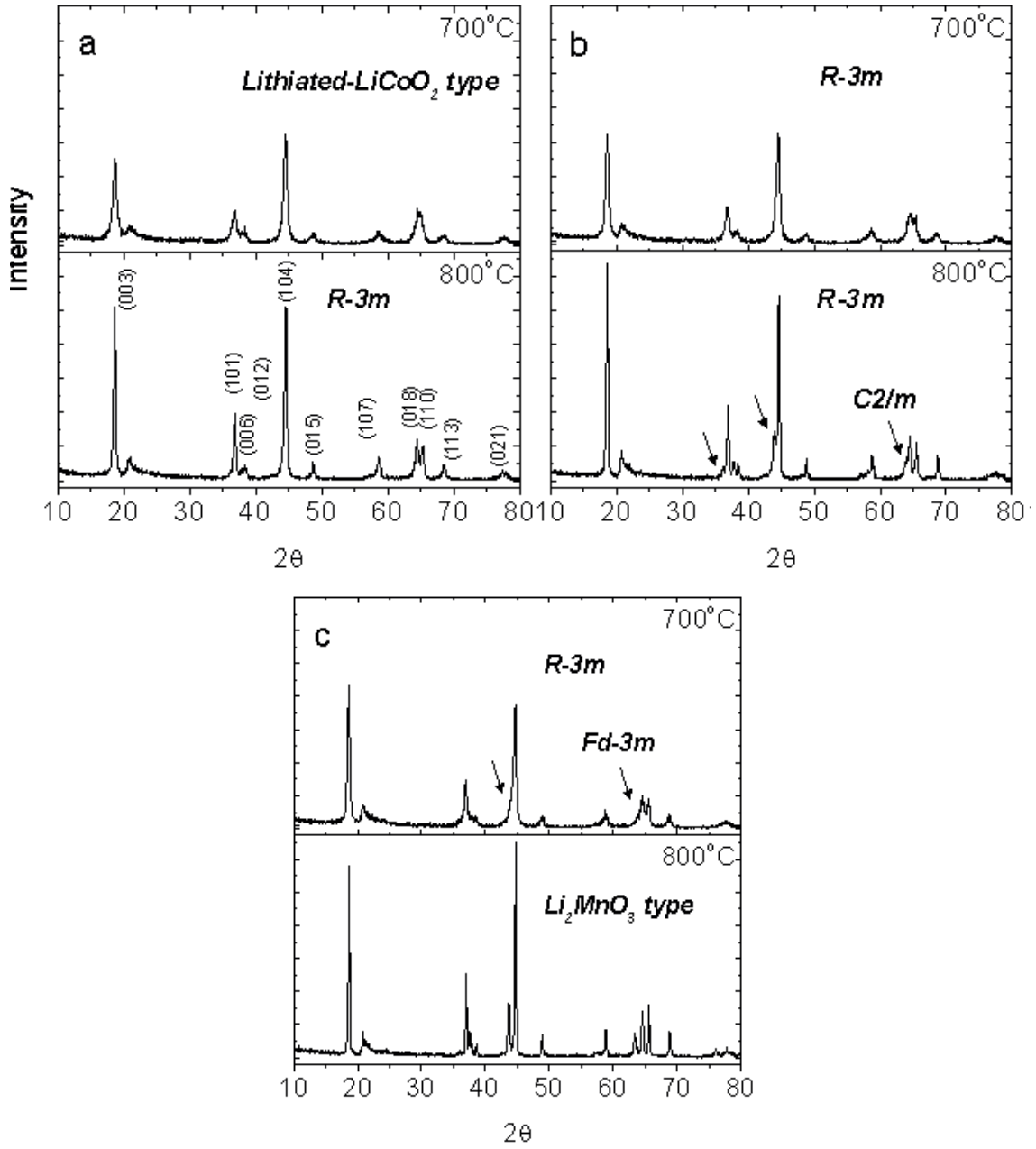

Figure 6.2 XRD pattern of the $Li_{(1.2-\delta)}Ni_{0.2}Mn_{0.6}O_{(2-\delta/2)}$ (δ=0, 1/20, 1/10) powders after annealing treatment: (a) δ=0; (b) δ =1/20; and (c) δ =1/10. The arrows indicate the broadening of the peaks. Solid circles show the splitting and separation of peaks, indicating the formation of Li_2MnO_3-type structures.

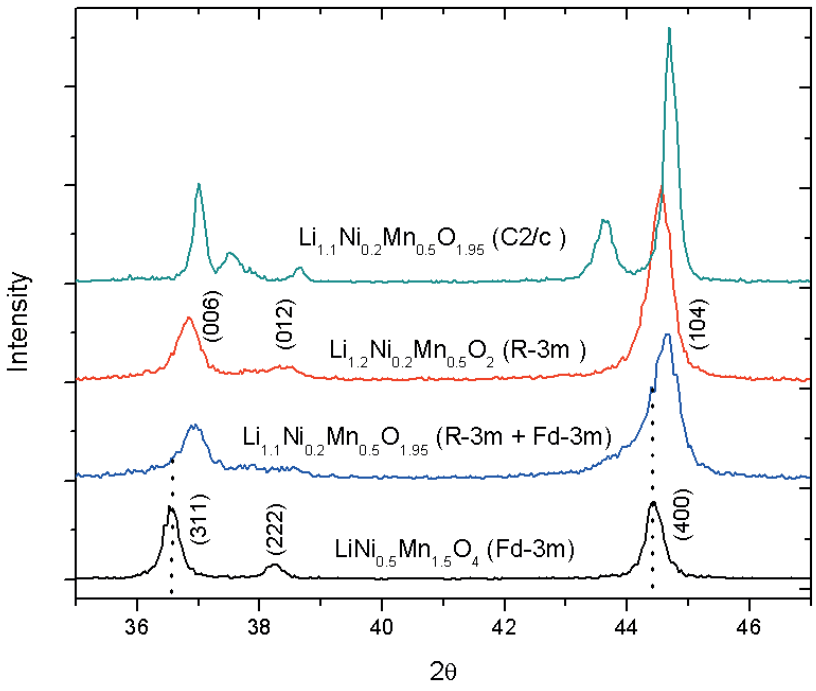

Figure 6.3 Stacking of XRD patterns of spinel-$LiNi_{0.5}Mn_{1.5}O_4$, layered $Li_{1.2}Ni_{0.2}Mn_{0.6}O_2$ and layered-spinel $Li_{1.1}Ni_{0.2}Mn_{0.6}O_{1.95}$.

6.4.2 WPF Cell Refinement

Cell refinement was applied to estimate the lattice parameters of the powders for the most predominated $R\bar{3}m$ structure. In the refinement, it was assumed that the rhombohedral $R\bar{3}m$ structure still dominates in $Li_{1.1}Ni_{0.2}Mn_{0.6}O_{1.95}$ (800 °C), as the XRD peaks of the $R\bar{3}m$ structure can overlap with that of the Li_2MnO_3-type structure with *C2/m* symmetry. As seen in Figure 6.4, the lattice constant *c*, the *c/a* ratio, and the unit cell volume decrease roughly linearly with Li content, while the lattice constant *a* increases.

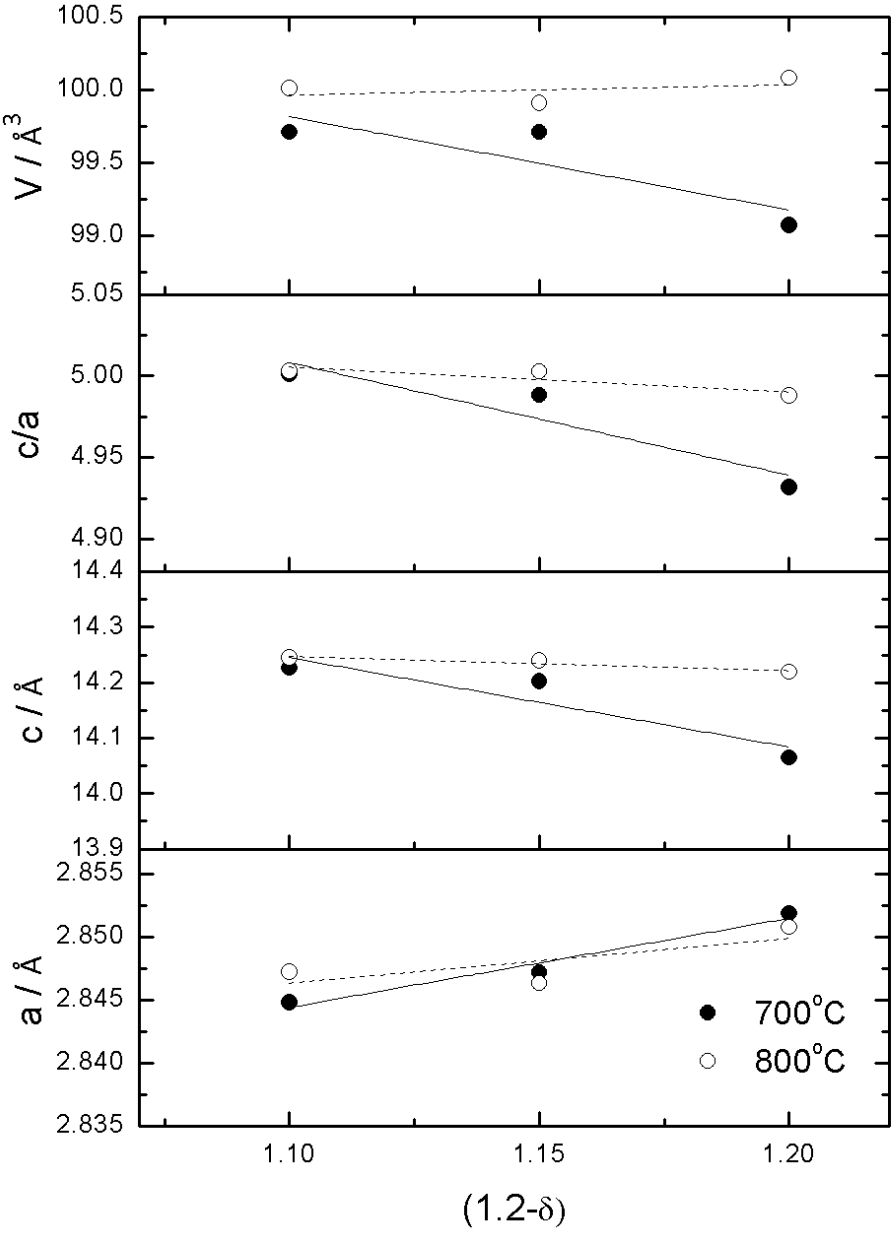

Figure 6.4 As-estimated lattice parameters of $Li_{(1.2-\delta)}Ni_{0.2}Mn_{0.6}O_{(2-\delta/2)}$ for different Li-content using WPF method.

The decrease in the *c/a* ratio and unit cell volume is consistent with the formation of the spinel-type structure for $Li_{1.1}Ni_{0.2}Mn_{0.6}O_{1.95}$ (700 °C). At an annealing temperature of 800 °C, the lattice constant *c*, the *c/a* ratio and the unit cell volume of the powders are

almost independent of Li-content, as seen by the open circles in Figure 6.4. $Li_{1.2}Ni_{0.2}Mn_{0.6}O_2$ (800 °C) and $Li_{1.1}Ni_{0.2}Mn_{0.6}O_{1.95}$ (700 °C) both adopt an $R\bar{3}m$ structure and show almost identical lattice constants *c* and unit cell volume. However, the *a* value is slightly higher for $Li_{1.2}Ni_{0.2}Mn_{0.6}O_2$ (800 °C). This may suggest that the excess Li may occupy the Li layers, which may supply more intercalatable Li.

6.4.3 Integrated Layered-Spinel Structure

The microstructure of $Li_{1.2}Ni_{0.2}Mn_{0.6}O_2$ (800 °C) and $Li_{1.1}Ni_{0.2}Mn_{0.6}O_{1.95}$ (700 °C) were studied by high-resolution TEM (HR-TEM), as shown in Figure 6.5. The former has a typical layered $R\bar{3}m$ structure. The measured interplanar spacing is 4.76 ± 0.18 Å along (001) plane. To identify the monoclinic Li_2MnO_3 phase, a Fourier transform was applied to this portion of the fringe structure on the HR-TEM image. The Fourier transform from the $Li_{1.2}Ni_{0.2}Mn_{0.6}O_2$ (800 °C) material has clear reflections from both rhombohedral $R\bar{3}m$ and monoclinic phases [36], as shown in the inserted image in Figure 6.5a. Therefore, it can be concluded that nano domains of $R\bar{3}m$ and monoclinic phases are present and integrated in the $Li_{1.2}Ni_{0.2}Mn_{0.6}O_2$ powders produced from spray pyrolysis.

The HR-TEM image of $Li_{1.1}Ni_{0.2}Mn_{0.6}O_{1.95}$ (700 °C) shown in Figure 6.5b, indicates that the nano domain of "non-layered" structures (5-10 nm) is structurally integrated with the layered structure. The Fourier transform of the selected area shows great similarity to the electron diffraction pattern of the spinel $LiMn_2O_4$ [192], as seen in Figure 6.5b. This

observation is consistent with the spinel feature obtained by XRD (Figure 6.2c and 6.3), which shows some peak broadening towards lower 2θ (see arrows). Therefore, $Li_{1.1}Ni_{0.2}Mn_{0.6}O_{1.95}$ (700 °C) is considered to be a layered-spinel integrated structure. The measured interplanar spacing is 4.72 ± 0.07 Å along the (001) planes, identical to the (111) inter-reticular distance of the spinel $LiMn_2O_4$ [192]. The decrease in interplanar spacing for $Li_{1.1}Ni_{0.2}Mn_{0.6}O_{1.95}$ (700 °C) is expected to be due to the lower occupancy of Li between the two consecutive layers. A thorough discussion of the compatibility of layered and spinel structure is given in reference [35, 37, 191, 193], utilizing phase-diagrams, TEM, XRD and MAS NMR results. In summary, the microstructure analysis indicates that the integrated layered-spinel structure exists in Li-deficient powders synthesized *via* spray pyrolysis using mixed nitrate precursors.

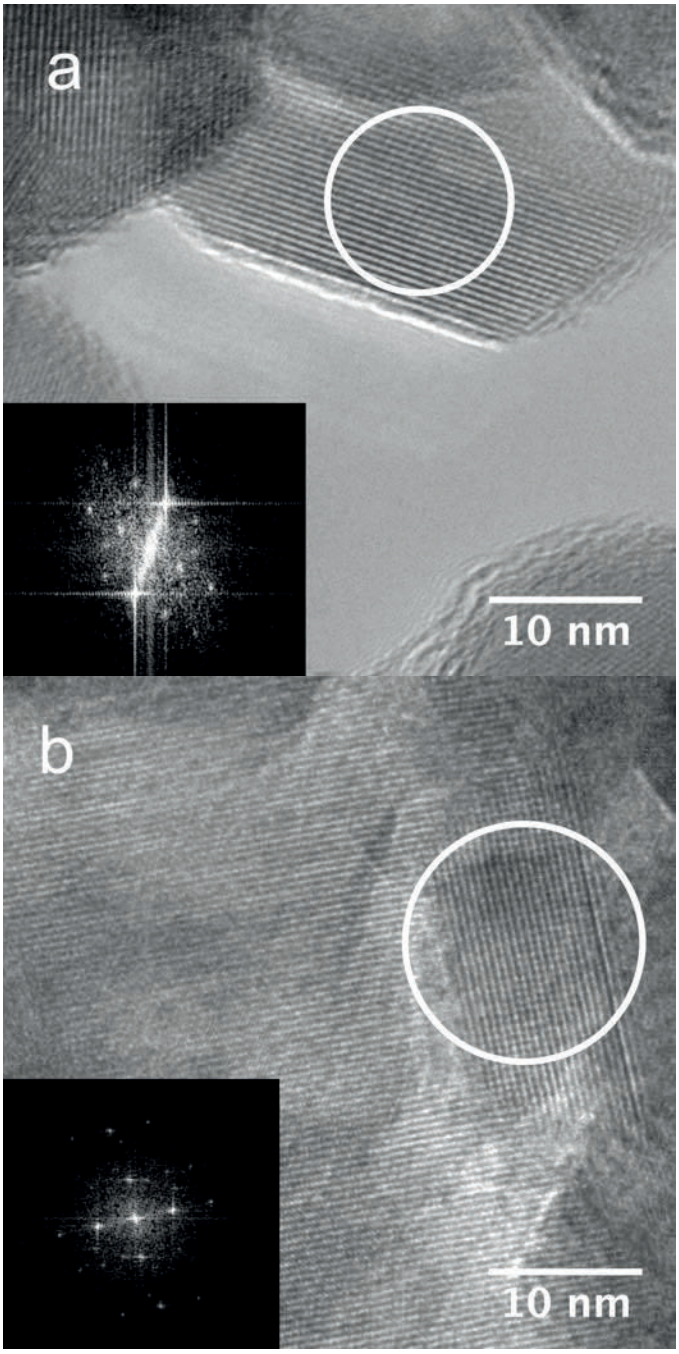

Figure 6.5 Microstructures of the powders obtained by HR-TEM and FFT: (a) $Li_{1.2}Ni_{0.2}Mn_{0.6}O_2$ (800 °C), and (b) $Li_{1.1}Ni_{0.2}Mn_{0.6}O_{1.95}$ (700 °C). Circles indicate the nano-domains of spinel structure that are integrated with the layered structure.

6.5 Powder Morphology

The morphology of the powders produced *via* spray pyrolysis and annealing at 700 °C and 800 °C was evaluated by SEM and TEM, as shown in Figure 6.6 and 6.7. The powders have a morphology that is common for powders produced by spray pyrolysis: they are spherical in shape, polycrystalline, and solid internally (*i.e.,* not hollow). The powders annealed at 700 °C preserve the shape and morphology of the as-synthesized powders. As the annealing temperature is increased to 800 °C, the powders undergo different degrees of sintering and coarsening. $Li_{1.2}Ni_{0.2}Mn_{0.6}O_2$ (800 °C) retains a porous structure with nano-sized primary particles, as shown in Figure 6.6b. In contrast, the $Li_{1.1}Ni_{0.2}Mn_{0.6}O_{1.95}$ (800 °C) powder is coarsened and the particle surface appears more faceted than that of the other powders (Figure 6.6f). This suggests that the Li content in the powder can significantly affect the sintering temperature, and consequently the powder morphology.

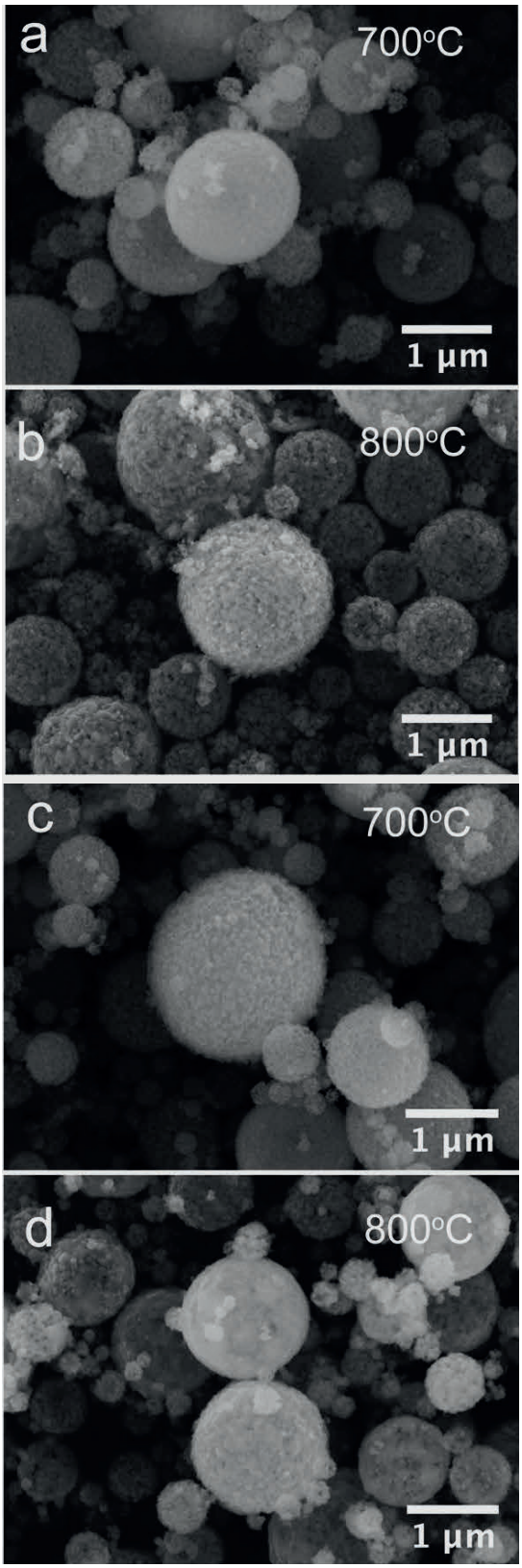
a
700°C
1 µm
b
800°C
1 µm
c
700°C
1 µm
d
800°C
1 µm

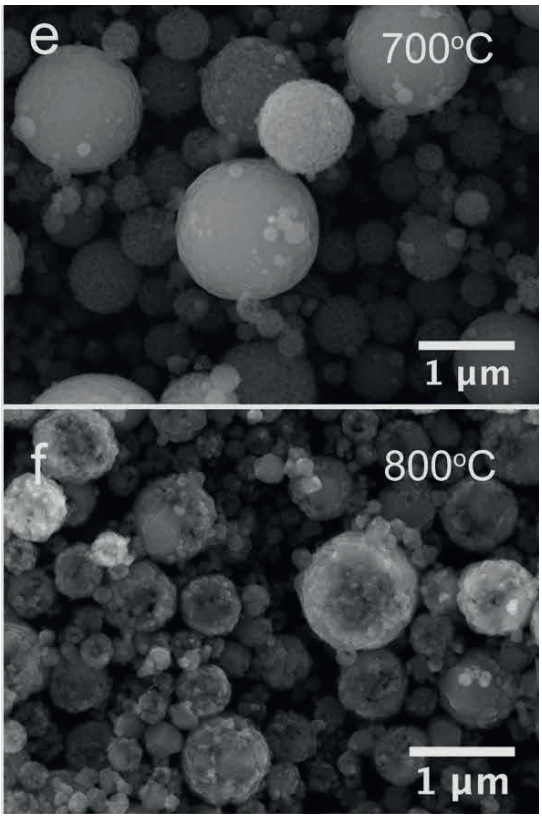

Figure 6.6 SEM photographs of the powders after annealing at 700 °C and 800 °C: (a, b) $Li_{1.2}Ni_{0.2}Mn_{0.6}O_2$; (c, d) $Li_{1.15}Ni_{0.2}Mn_{0.6}O_{1.975}$; and (e, f) $Li_{1.1}Ni_{0.2}Mn_{0.6}O_{1.95}$. The annealing temperature is shown on each photograph.

Porosity is considered important to improve the rate performance of high-energy cathode materials [37]. $Li_{1.2}Ni_{0.2}Mn_{0.6}O_2$ (800 °C) is particularly attractive due to the well-defined crystal structure and superior porous morphology observed in Figure 6.6. The TEM morphology of $Li_{1.2}Ni_{0.2}Mn_{0.6}O_2$ (800 °C) particles, as shown in Figure 6.7a, indicates a "dense" internal structure and nano-sized primary particles. The primary particles are *c.a.* 20 to 100 nm in size. As indicated by the arrows, nano-scale tunnels can be observed, indicating an open pore structure throughout the particle. The microtome result shown in Figure 6.7b reveals that the inner-particle is highly porous. The interparticle pore spacing

varies from few nanometers to tens of nanometers in size, and is distributed uniformly within the particle. This porous morphology may facilitate the interparticle transportation of lithium and the electrodes made from these mesoporous materials have the potential of having higher rate-capabilities than solid bulk materials.

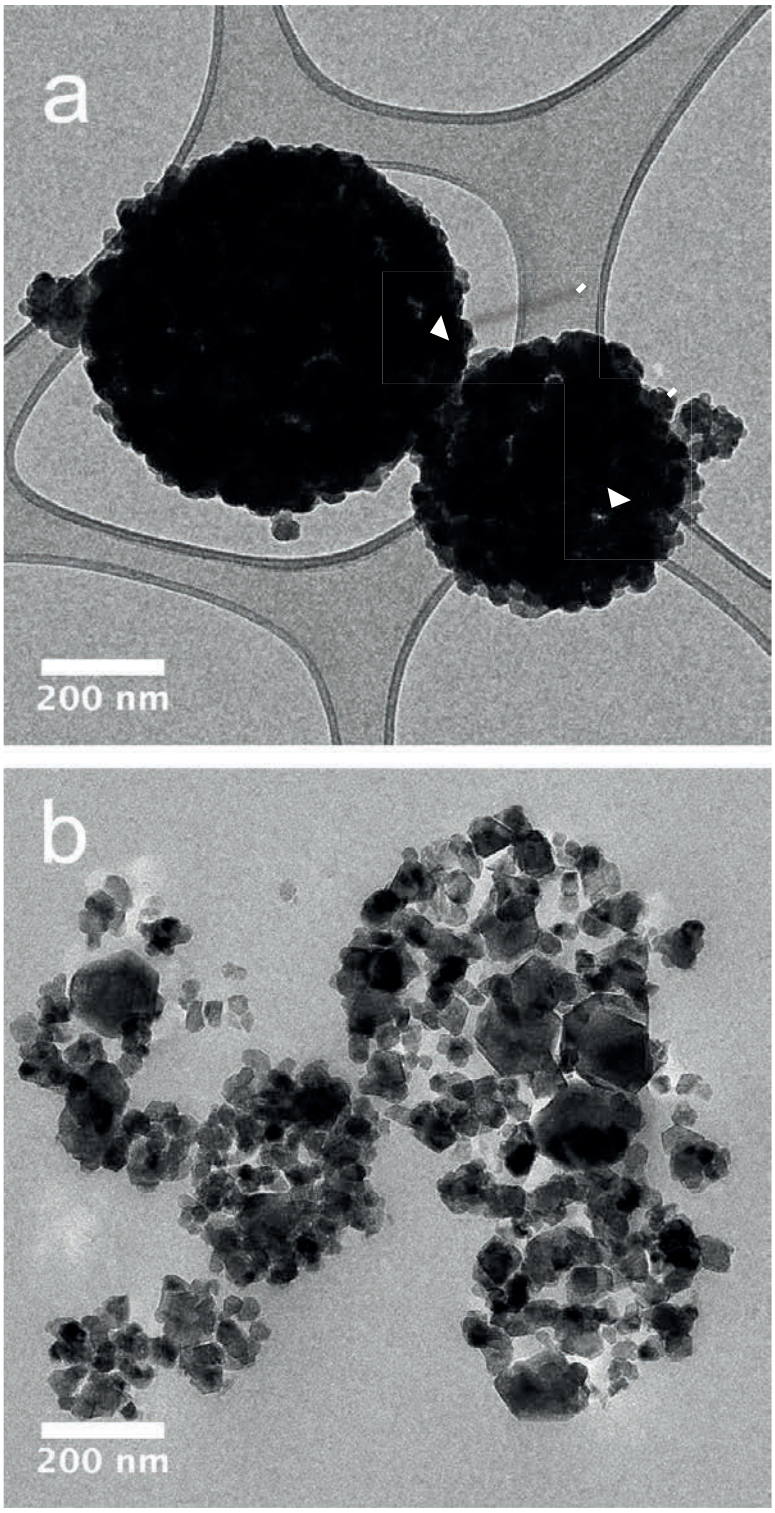

Figure 6.7 TEM photograph of the $Li_{1.2}Ni_{0.2}Mn_{0.6}O_2$ (800 °C) powders: (a) morphology of particle; and (b) a cross-section of the particles sliced using microtome.

6.6 Electrochemical Performance

6.6.1 Voltage Profile and Capacity

The electrochemical properties of all six powders were tested with coin cells. Figure 6.8 shows the initial charge/discharge between 2.0 and 4.9 V at a current density of 11.5 mAg^{-1}. The CCCV (Constant-Current, Constant-Voltage) charging procedure was applied to all test cells in this study. For the powders annealed at 700 °C, all three materials show a dominantly two-staged charge profile (except for the small kink near 3 V for $Li_{1.1}Ni_{0.2}Mn_{0.6}O_{1.95}$), and a very smooth discharge profile, as shown by the dash-lines in Figure 6.8. During the initial charge, the voltage slowly climbs from 3.5 V to 4.5 V owing to the Ni^{2+}/Ni^{4+} redox couple. At *c.a.* 4.5 V, a voltage plateau shows up, which is attributed to the removal of Li_2O from Li_2MnO_3 [33, 190]. The charge capacity increases with increasing initial Li content in the material, as expected since more Li can be extracted from the electrodes.

The $Li_{1.2}Ni_{0.2}Mn_{0.6}O_2$ composite material can be described as $0.5Li_2MnO_3 \cdot 0.5LiNi_{0.5}Mn_{0.5}O_2$, being composed of two compatible "layered-layered" structures in a 1:1 ratio. The theoretical charge capacity for $Li_{1.2}Ni_{0.2}Mn_{0.6}O_2$ is calculated to be 378 $mAhg^{-1}$ (Table 5.4), assuming that all of the Li can be extracted from the host materials [33, 190]. The ideal composition of a fully charged electrode can be written as $Mn_{0.75}Ni_{0.25}O_2$, wherein both Mn and Ni are tetravalent (Mn^{4+}, Ni^{4+}) [33]. The theoretical

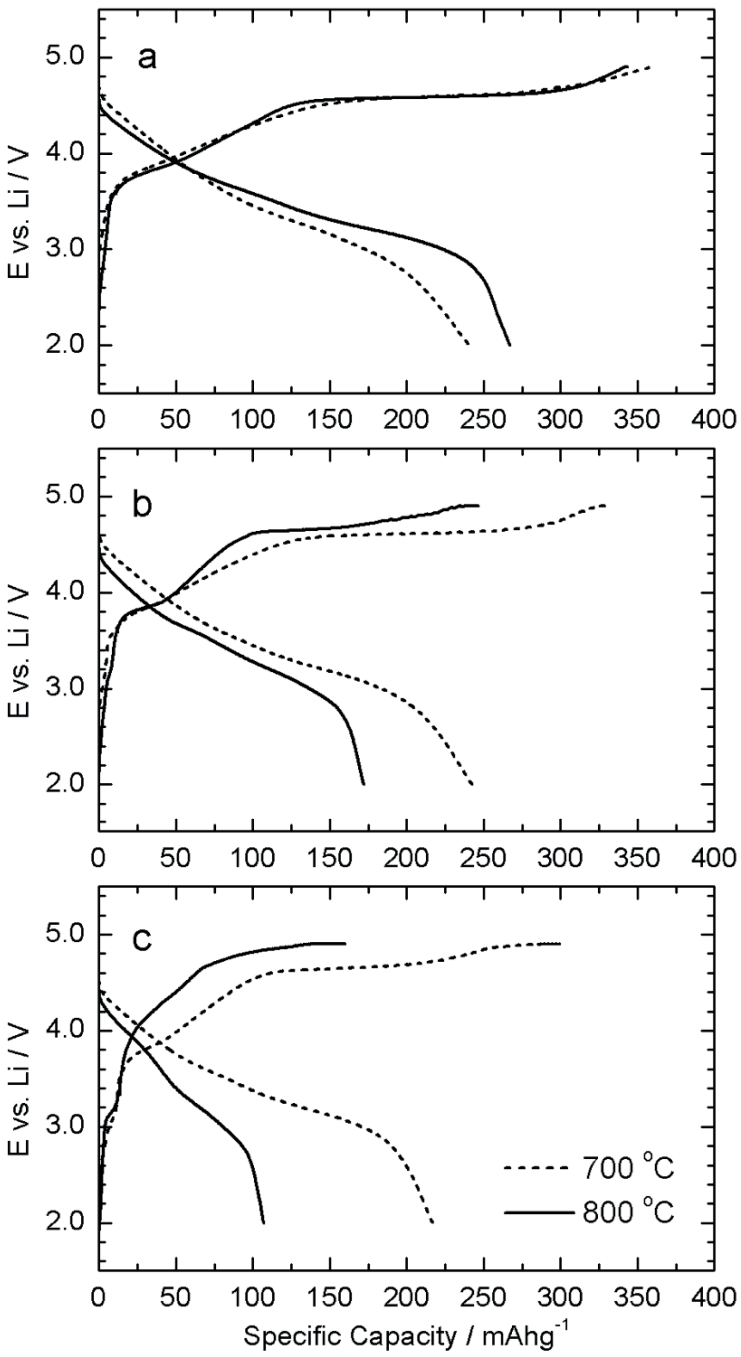

Figure 6.8 Initial charge/discharge voltage profiles of the cells at a constant current density of 11.5 mAg^{-1} between 2.0 and 4.9 V: (a) $Li_{1.2}Ni_{0.2}Mn_{0.6}O_2$; (b) $Li_{1.15}Ni_{0.2}Mn_{0.6}O_{1.975}$; and (c) $Li_{1.1}Ni_{0.2}Mn_{0.6}O_{1.95}$. (dash line: annealing temperature 700 °C; solid line: annealing temperature at 800 °C)

discharge capacity is 252 $mAhg^{-1}$, of which 126 $mAhg^{-1}$ is attributed to Ni^{4+}/Ni^{2+} redox couple and the other 126 $mAhg^{-1}$ is *via* the Mn^{4+}/Mn^{3+} redox couple. Based on the above calculations, the coulombic efficiency should be 67% for the first cycle. The experimental results show that at a constant current density of 11.5 mAg^{-1} (*c.a.* C/20), $Li_{1.2}Ni_{0.2}Mn_{0.6}O_2$ (700 °C) and $Li_{1.2}Ni_{0.2}Mn_{0.6}O_2$ (800 °C) have an initial charge capacity of 360 $mAhg^{-1}$ and 343 $mAhg^{-1}$, respectively. The former is almost identical to the theoretical charge capacity. The lower initial charge capacity of $Li_{1.2}Ni_{0.2}Mn_{0.6}O_2$ (800 °C) is possibly due to incomplete-activation at this current density, owing to the closed-packed crystal structure. As discussed earlier, $Li_{1.2}Ni_{0.2}Mn_{0.6}O_2$ (700 °C) consists of nano-sized primary particles with a lithiated-$LiCoO_2$ structure (spinel type). Thus, all of the Li can be extracted with a deep charge due to the short distance for Li diffusion. The discharge capacity for "spinel-type" $Li_{1.2}Ni_{0.2}Mn_{0.6}O_2$ (700 °C) is 240 $mAhg^{-1}$ with a coulombic efficiency of 67%, also identical to the calculated theoretical value. The layered $Li_{1.2}Ni_{0.2}Mn_{0.6}O_2$ (800 °C) shows an anomalous discharge capacity of 266 $mAhg^{-1}$, with a higher coulombic efficiency of 78%. The discharge capacity is also higher than its theoretical value. The reason for the excess capacity of this material has not been fully explained, but several hypotheses have been proposed in the literature, *e.g.,* surface/electrolyte reactions and capacitive effects, [183, 190].

Li-deficient composites $Li_{1.15}Ni_{0.2}Mn_{0.6}O_{1.975}$ and $Li_{1.1}Ni_{0.2}Mn_{0.6}O_{1.95}$ are designed to have the layered-spinel integrated structure, and can be formulated as $1/16[LiMn_{1.5}Ni_{0.5}O_4] \cdot 15/16[Li_2MnO_3 \cdot LiNi_{0.5}Mn_{0.5}O_2]$, and $1/8[LiMn_{1.5}Ni_{0.5}O_4] \cdot$

7/8[Li_2MnO_3·$LiNi_{0.5}Mn_{0.5}O_2$], respectively. Their actual structures may be more complex, and different from the ideal structure after heat treatment. The charge profiles of $Li_{1.1}Ni_{0.2}Mn_{0.6}O_{1.95}$ (both 700 °C and 800 °C) electrodes have a small capacity near 3 V (Figure 6.8c), indicating the presence of Mn^{3+} [99]. The 3 V region decreases for electrodes with higher Li-content, and eventually is absent in $Li_{1.2}Ni_{0.2}Mn_{0.6}O_2$. The 3 V capacity is considered to be evidence of the presence of spinel $LiMn_{1.5}Ni_{0.5}O_4$ [37]. Therefore, the charge voltage profile confirms the presence of spinel structure in $Li_{1.1}Ni_{0.2}Mn_{0.6}O_{1.95}$ (700 °C), consistent with XRD and HR-TEM results. As seen in Figure 6.3 and 6.5b, $Li_{1.15}Ni_{0.2}Mn_{0.6}O_{1.975}$ (700 °C) and $Li_{1.1}Ni_{0.2}Mn_{0.6}O_{1.95}$ (700 °C) show lower charge capacities, due to the lower Li content of these materials. In the ideal fully charged state, the electrodes are expected to have the same composition, $Mn_{0.75}Ni_{0.25}O_2$, identical to the fully delithiated $Li_{1.2}Ni_{0.2}Mn_{0.6}O_2$. Therefore, the discharge capacities of these electrodes are expected to be the same. However, as shown by the discharge voltage profiles in Figure 6.8b and 6.8c, $Li_{1.15}Ni_{0.2}Mn_{0.6}O_{1.975}$ (700 °C) and $Li_{1.1}Ni_{0.2}Mn_{0.6}O_{1.95}$ (700 °C) have a discharge capacity of 240 $mAhg^{-1}$ and 217 $mAhg^{-1}$, respectively. The initial capacity of $Li_{1.1}Ni_{0.2}Mn_{0.6}O_{1.95}$ (700 °C) is noticeably lower than the theoretical value, for undetermined reasons.

Nonetheless, "Li_2MnO_3-type" $Li_{1.15}Ni_{0.2}Mn_{0.6}O_{1.975}$ (800 °C) and $Li_{1.1}Ni_{0.2}Mn_{0.6}O_{1.95}$ (800 °C) have significantly lower capacities compared to those powders annealed at lower temperatures. $Li_{1.1}Ni_{0.2}Mn_{0.6}O_{1.95}$ (800 °C) has the lowest charge/discharge capacities (c.a. 50-100 $mAhg^{-1}$) among all the electrodes. The low capacity for Li_2MnO_3-type materials was also observed for Li-excess cathode materials and Li_2MnO_3 made at

high temperatures [29, 30, 99]. Moreover, the charge/discharge voltage profiles in Figure 6.8b and 6.8c for the powder annealed at 800 °C show severe polarization, indicating extremely slow reaction kinetics. This suggests that the phase transformation (rhombohedral to monoclinic) can induce a kinetic barrier for Li intercalation/deintercalation resulting a lower capacity.

6.6.2 Cycle Performance

The cycling performance of the electrodes was tested at a current density of 23 mAg^{-1} with a cut-off voltage between 2.0 and 4.8 V. In general, the powders annealed at 800 °C show better capacity retention over those annealed at 700 °C, as indicated by the circles and triangles, respectively, as seen in Figure 6.9. $Li_{1.2}Ni_{0.2}Mn_{0.6}O_2$ (800 °C) shows a capacity of 256 $mAhg^{-1}$ at the first cycle with a coulombic efficiency of 84%. In following cycles, both the charge and discharge capacities drop and stabilize at roughly 225 $mAhg^{-1}$, with an average coulombic efficiency above 98%. $Li_{1.2}Ni_{0.2}Mn_{0.6}O_2$ (700 °C), with the spinel-type lithiated-$LiCoO_2$ structure, shows a lower discharge capacity of 240 $mAhg^{-1}$ with a coulombic efficiency of 70% at the first cycle. However, the $Li_{1.2}Ni_{0.2}Mn_{0.6}O_2$ (700 °C) electrode fades very fast despite having a high efficiency. At the 50^{th} cycle, the electrode only retains 54% of its initial capacity, but with 99% coulombic efficiency. Capacity fading is also observed for the $Li_{1.15}Ni_{0.2}Mn_{0.6}O_{1.975}$ (700 °C) electrode, for which the crystal structure (XRD pattern in Figure 6.2a and 6.2b) is similar to that of $Li_{1.2}Ni_{0.2}Mn_{0.6}O_2$ (700 °C). After 50 cycles, the $Li_{1.15}Ni_{0.2}Mn_{0.6}O_{1.975}$

(700 °C) electrode has a capacity of only 140 $mAhg^{-1}$, 59% of its initial capacity. An identical result was also observed by Dahn *et al.* for the $Li[Ni_{1/3}Li_{1/9}Mn_{5/9}]O_2$ and $Li[Ni_{1/2}Mn_{1/2}]O_2$ electrodes with the spinel-type lithiated-$LiCoO_2$ structure [179, 194]. The reason for the fast capacity fading of $Li_{1.2}Ni_{0.2}Mn_{0.6}O_2$ (700 °C) and $Li_{1.15}Ni_{0.2}Mn_{0.6}O_{1.975}$ (700 °C) is possibly due to a structure failure caused by Jahn-Teller distortion for these spinel-type structures when a higher Li concentration is achieved towards the end of discharge [191].

The capacity fading for the materials annealed at 700 °C is suppressed in $Li_{1.1}Ni_{0.2}Mn_{0.6}O_{1.95}$ (700 °C) with the integrated layered-spinel structure, as indicated by the triangles in Figure 6.9c. The initial capacity of $Li_{1.1}Ni_{0.2}Mn_{0.6}O_{1.95}$ (700 °C) is only 150 $mAhg^{-1}$ at a constant current density of 23 mAg^{-1} between 2.0 and 4.8 V. After a few cycles, the capacity increases to 200 $mAhg^{-1}$, which is still much lower than its theoretical value and inferior to layered $Li_{1.2}Ni_{0.2}Mn_{0.6}O_2$ (800 °C). The reason for the poor capacity has not been determined. The coulombic efficiency of the layered-spinel increases from 82% in the first cycle, to c.a. 99% at the 40th cycle. The coulombic efficiency is slightly higher than that of layered $Li_{1.2}Ni_{0.2}Mn_{0.6}O_2$ (800 °C), possibly owing to more spinel structures in the composite.

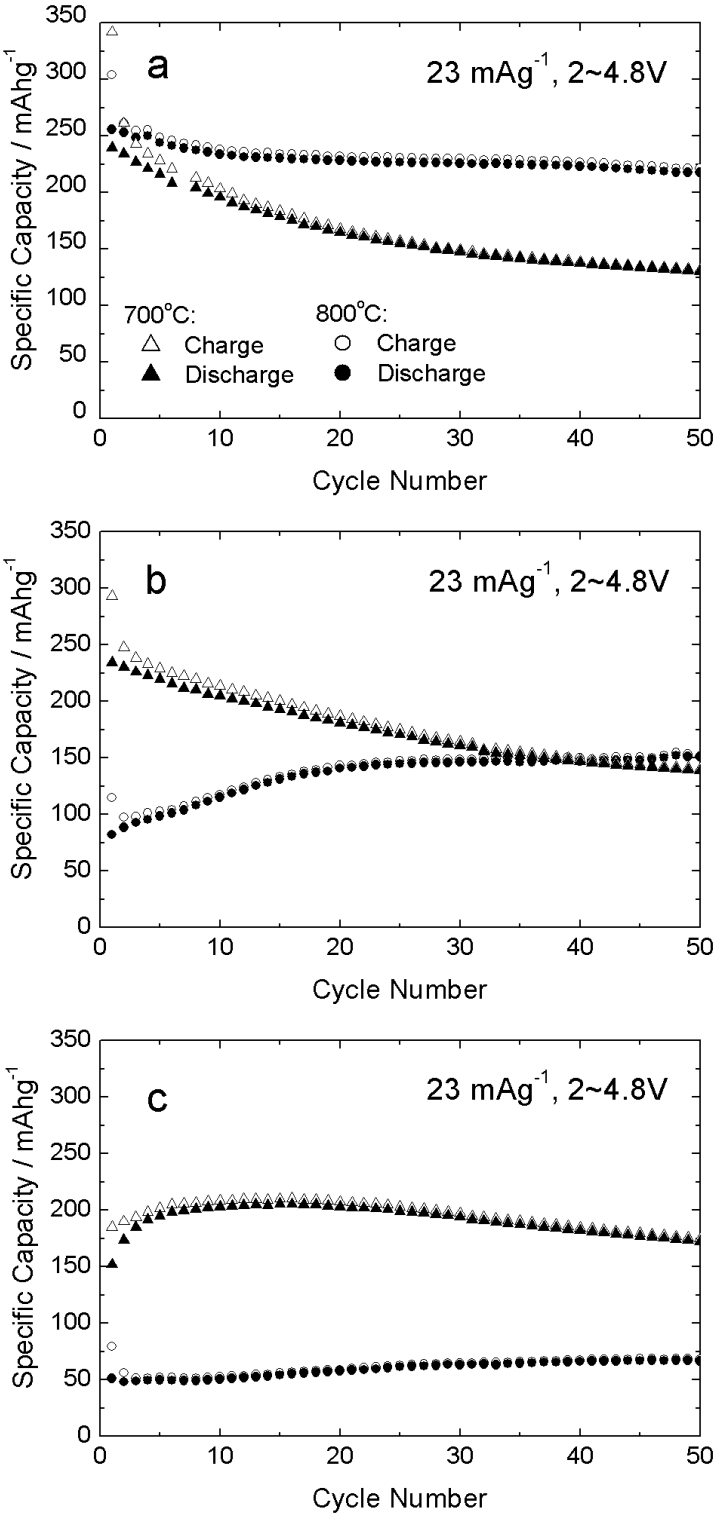

Figure 6.9 Cycling performance of the cells at a constant current density of 23 mAg^{-1} between 2.0 and 4.8 V: (a) $Li_{1.2}Ni_{0.2}Mn_{0.6}O_2$; (b) $Li_{1.15}Ni_{0.2}Mn_{0.6}O_{1.975}$; and (c) $Li_{1.1}Ni_{0.2}Mn_{0.6}O_{1.95}$. (triangles: annealing temperature is 700 °C; circles: annealing temperature is 800 °C)

Li_2MnO_3-type $Li_{1.15}Ni_{0.2}Mn_{0.6}O_{1.975}$ (800 °C) and $Li_{1.1}Ni_{0.2}Mn_{0.6}O_{1.95}$ (800 °C) have shown very low initial capacities at 23 mAg^{-1} (Figure 6.9b and 6.9c). The capacity climbs over repeated cycles, however extremely slowly for $Li_{1.1}Ni_{0.2}Mn_{0.6}O_{1.95}$ (800 °C). To electrochemically activate the electrodes, all three electrodes made from the cathode powders annealed at 800 °C were charged and discharged at 11.5 mAg^{-1} between 2.0 and 4.9 V for the first cycle, and then switched back to 23 mAg^{-1} between 2.0 and 4.8 V for future cycles. As seen in Figure 6.10b and 6.10c, the "activated" $Li_{1.15}Ni_{0.2}Mn_{0.6}O_{1.975}$ (800 °C) has a roughly constant discharge capacity of 150 $mAhg^{-1}$, and the capacity of $Li_{1.1}Ni_{0.2}Mn_{0.6}O_{1.95}$ (800 °C) has increased from *c.a.* 50 $mAhg^{-1}$ to 120 $mAhg^{-1}$. No significant capacity climbing is observed for $Li_{1.15}Ni_{0.2}Mn_{0.6}O_{1.975}$ (800 °C), indicating a successful activation under this condition. However, the $Li_{1.2}Ni_{0.2}Mn_{0.6}O_2$ (800 °C) activated at 11.5 mAg^{-1} only holds about 200 $mAhg^{-1}$ in subsequence cycles (Figure 6.10a), lower than the non-activated electrodes. A possible reason for this is the structure change or damage when the Li concentration is over-depleted during the initial charge process for the layered-type electrode [186]. Therefore, proper activation is critical to maximize the cycle life and capacity for the Li-excess mix-layered or layered-spinel materials.

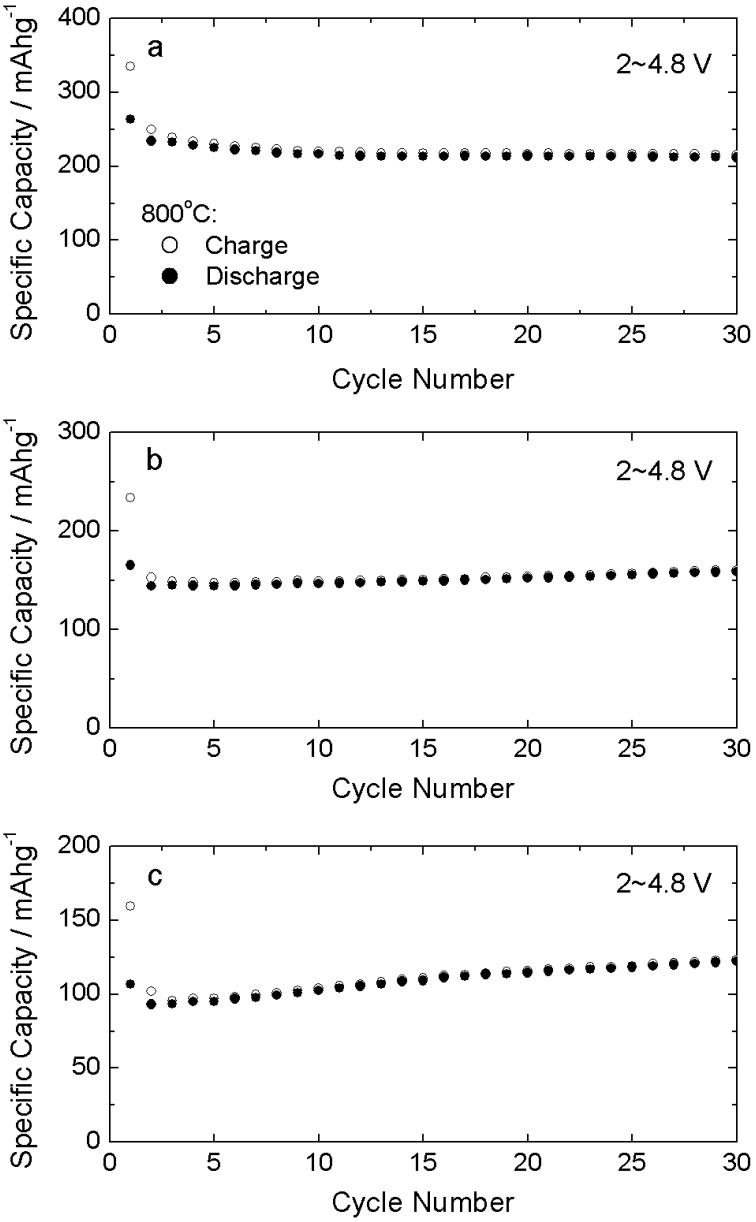

Figure 6.10 Cycling performance of the cells electrochemically activated at a constant current density of 11.5 mAg^{-1} between 2.0 and 4.9 V, and then cycled at 23 mAg^{-1} between 2.0 and 4.8 V: (a) $Li_{1.2}Ni_{0.2}Mn_{0.6}O_2$; (b) $Li_{1.15}Ni_{0.2}Mn_{0.6}O_{1.975}$; and (c) $Li_{1.1}Ni_{0.2}Mn_{0.6}O_{1.95}$. Annealing temperature is 800 °C for 10 hr.

6.6.3 Rate Performance

Layered-spinel $Li_{1.1}Ni_{0.2}Mn_{0.6}O_{1.95}$ (700 °C) was selected for rate performance test, to compare the layered $Li_{1.2}Ni_{0.2}Mn_{0.6}O_2$ (800 °C) composite material. As seen in Figure 6.11b, the performance of the $Li_{1.1}Ni_{0.2}Mn_{0.6}O_{1.95}$ (700 °C) electrode is very similar to that of the $Li_{1.2}Ni_{0.2}Mn_{0.6}O_2$ (800 °C) electrode, except for having slightly lower capacity. At a current density of 115 mAg^{-1} and 230 mAg^{-1}, the normalized capacities are 84% and 69%, respectively. When charged to 4.9 V, the $Li_{1.1}Ni_{0.2}Mn_{0.6}O_{1.95}$ (700 °C) cell was observed to reach 200 $mAhg^{-1}$ immediately, without a long activation process. One possible reason for this is that charging to 4.9 V may deplete the Li concentration to its proper level and contribute to the electrochemical activation. However, at elevated C-rates, $Li_{1.1}Ni_{0.2}Mn_{0.6}O_{1.95}$ (700 °C) shows inferior coulombic efficiencies, as compared to $Li_{1.2}Ni_{0.2}Mn_{0.6}O_2$ (800 °C). In summary, the $Li_{1.2}Ni_{0.2}Mn_{0.6}O_2$ (800 °C) powder with the highly mesoporous morphology shows better performance vis-a-vis energy density, rate capability and efficiency. Therefore, the spinel-layered structure does not significantly contribute to the rate capability and efficiency in this work.

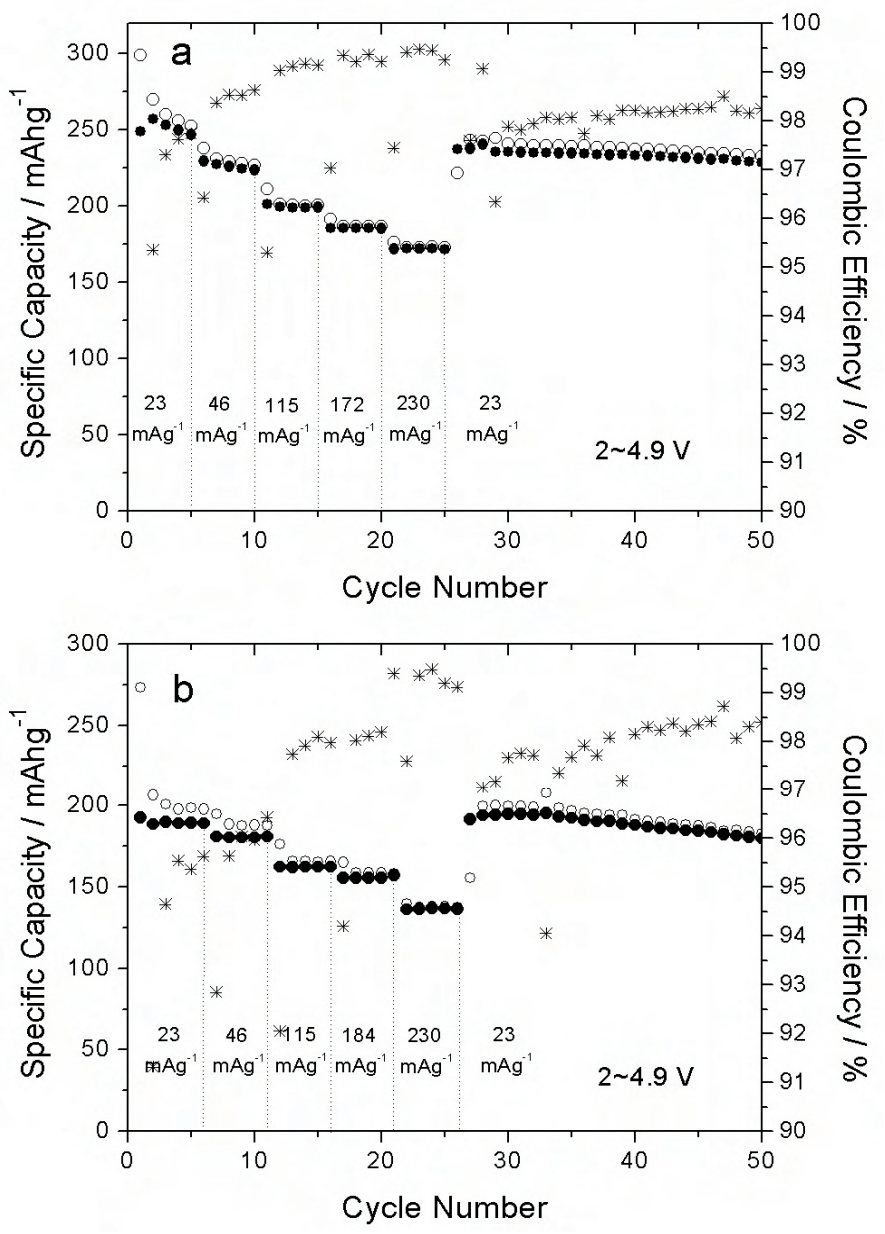

Figure 6.11 Rate performance of the cells at elevated current density between 2.0 and 4.9 V: (a) $Li_{1.2}Ni_{0.2}Mn_{0.6}O_2$ (800 °C); and (b) $Li_{1.1}Ni_{0.2}Mn_{0.6}O_{1.95}$ (700 °C). Coulombic efficiency corresponding to each charge/discharge cycle is calculated and plotted, as shown in the figures

6.7 Summary

Nanostructured $Li_{(1.2-\delta)}Ni_{0.2}Mn_{0.6}O_{(2-\delta/2)}$ (δ=0, 1/20, 1/10) high-energy materials were synthesized *via* a spray pyrolysis method with mixed nitrate precursors. With different Li content, the materials have shown different crystal structures, morphology and electrochemical properties, especially for those annealed at high temperatures (800 °C). $Li_{1.2}Ni_{0.2}Mn_{0.6}O_2$ preserves the $R\bar{3}m$ structure at high annealing temperature and shows a layered-layered integrated structure. At low annealing temperature (700 °C), $Li_{1.2}Ni_{0.2}Mn_{0.6}O_2$ shows a spinel-type lithiated-$LiCoO_2$ structure due to exchange/mixing of Li^+ and Ni^{2+} ions in the transition metal layers. With decreasing Li content, a layered-spinel integrated structure is observed for $Li_{1.1}Ni_{0.2}Mn_{0.6}O_{1.95}$ by XRD and TEM, and further validated by the cell voltage profiles. However, at high annealing temperatures, $Li_{1.1}Ni_{0.2}Mn_{0.6}O_{1.95}$ and $Li_{1.15}Ni_{0.2}Mn_{0.6}O_{1.975}$ undergo phase transformation, forming a Li_2MnO_3-type structure. The Li_2MnO_3-type materials have a very high activation barrier for Li transportation, exhibiting poor capacities and rate capabilities.

On the other hand, the stoichiometry of the powder has significant effect on the crystal structure and consequently the electrochemical performance of the composites materials. With stoichiometric Li content, layered $R\bar{3}m$ $Li_{1.2}Ni_{0.2}Mn_{0.6}O_2$ shows the best electrochemical performance with regards to capacity, capacity retention, rate performance and efficiency. The integrated layered-spinel structure, $Li_{1.1}Ni_{0.2}Mn_{0.6}O_{1.95}$ did not show superior electrochemical performance. The layered-layered $Li_{1.2}Ni_{0.2}Mn_{0.6}O_2$ powder that displayed the best rate-capability has a nano-structured

morphology, consisting of mesoporous secondary particles made up of nano-sized primary particles, allowing for a shorter Li diffusion distance. The spray pyrolysis process and powders synthesized from this process hold promise and require further optimization.

Chapter 7

Summary and Recommendations for Future Work

7.1 Summary of Results

The work presented in this dissertation studies the state-of-the-art aerosol processes, which are capable of synthesizing nanostructured cathode materials for Li-ion batteries. In particular, a prototype pyrolysis flame and a spray pyrolysis reactor were designed and employed for producing uniform, spherical powders by means of droplet-to-particle conversion processes. Flame process is widely used approach in the synthesis of ceramic powders and some functional materials. Of particular interest is the multicomponent metal-oxide powder for energy applications. In the flame synthesis, the exothermic reaction between fuel and air generates heat to create a high temperature environment, in which the heating is volumetric to provide uniform heating. The as-synthesis powders from flames show uniform morphology. In contrast, spray pyrolysis requires external heating, *i.e.*, electric heating, and the heat will be transferred to the gas and aerosol by conduction and convection. Therefore, no fuel is consumed in this process because electricity is supplied to heat the reactor. The spray pyrolysis process is environmentally friendly, less resource and capital intensive, simpler and faster. This process also ensures uniformity and precise control of chemical composition within the particle and from particle-to-particle. The spray pyrolysis reactor temperature is normally lower than the flame; therefore, spray pyrolysis process can be applied for temperature-sensitive material synthesis, *i.e.,* the composite materials; and the flame process is employed for synthesizing simple transition metal oxides, *i.e.,* the spinels. Beginning with the flame synthesis, a brief summary of the key results and findings in this dissertation is presented below.

7.1.1 Flame Pyrolysis

A good selection of precursors is critical for producing non-hollow particles and lowering the manufacturing cost. The precursors are selected among lithium nitrate, manganese nitrate and also nickel nitrate, which are dissolved in water or alcoholic solvent at stoichiometric ratio serving as the precursor solution. The nitrates are highly soluble in water and alcohol, and therefore the production rate of the final material is expected to be high. Another advantage for using the nitrates is because of the narrow decomposition temperature of Li, Mn and Ni nitrates, which allows uniform composition in each individual particle. When using metal acetates as precursors, hollow or shell-type morphology can be observed in the final powders. The acetates are less soluble in water and not stable from temperature variations. In this study, precipitates are observed in aged acetate solutions.

A prototype flame spray pyrolysis system is developed and has demonstrated being capable of synthesizing spherical spinel-$LiMn_2O_4$ and spinel-$LiNi_{0.5}Mn_{1.5}O_4$ metal oxides with good electrochemical performance. The flame spray pyrolysis system is mainly composed of a laminar hydrogen diffusion flame reactor and an atomizer. The precursor solution is combustible due to the presence of large amount of methanol serving as the solvent. In addition, the as-synthesized powder is non-hollow due to the high vapor pressure of methanol. The flame-made powder is nano to micron in size, spherical in shape, polycrystalline, free of agglomeration, and is expected to have a high packing

density due to the lognormal particle size distribution. As a result of the high flame temperature, an impurity Mn_3O_4 is detected from the decomposition of $LiMn_2O_4$ above 1000 °C. After a post-annealing treatment, the $LiMn_2O_4$ powder is recovered showing a single-phase spinel structure in $Fd\bar{3}m$ space group. However, the uneven (311) and (400) Bragg peaks indicated the presence of oxygen vacancies and these can harm the cycle life of the $LiMn_2O_4$ powders. The charge/discharge performance of the flame-made $LiMn_2O_4$ powders before and after post-annealing is in good agreement with the electrochemical characteristics of spinel $LiMn_2O_4$. Nonetheless, the annealed $LiMn_2O_4$ powder displays a much higher capacity than the as-synthesized powder in the 4 V range due to elimination of impurity phase and growing of the primary particles.

Oxygen loss is detrimental to the electrochemical performance of $LiMn_2O_4$, however it can be favorable for $LiNi_{0.5}Mn_{1.5}O_4$. $LiNi_{0.5}Mn_{1.5}O_4$ has two structures: primitive simple cubic $P4_332$ with stoichiometric oxygen and face-center cubic $Fd\bar{3}m$ with oxygen deficiency. Spray pyrolysis study shows that high calcination temperature (800 °C) leads to the oxygen deficient spinel ($Fd\bar{3}m$) and low calcination temperature (600 °C) produces the ordered spinel ($P4_332$). By utilizing the high flame temperature, disordered spinel $LiNi0_{.5}Mn_{1.5}O_4$ ($Fd\bar{3}m$) can be synthesized in the flame spray pyrolysis process. The as-synthesized $LiNi0_{.5}Mn_{1.5}O_4$ from flame does not show a significant amount of impurity phase due to its high thermostability, thus no extensive oxygen loss could occur. The flame-made disordered spinel $LiNi_{0.5}Mn_{1.5}O_4$ powder has lower capacity than that made from spray pyrolysis. The reason is understood to be the defects (oxygen vacancies, or dislocation) presented in the material from flame. Despite the low capacity, the cycle

performance of $Fd\bar{3}m$ $LiNi_{0.5}Mn_{1.5}O_4$ from flame has shown identical performance to the powders from spray pyrolysis in terms of operation voltage and cycleability. The flame process could produce high-quality cathode materials due to its high-temperature environment.

7.1.1 Spray Pyrolysis

Porous composite materials within Li-Ni-Mn-O system, *e.g.*, $x Li_2MnO_3 \cdot (1-x) LiNi_{0.5}Mn_{0.5}O_2$, have shown attractive properties including enormously high capacity, good cycle life and wide voltage window. However, it would be very challenging to synthesize high-quality composite material in the flame because the high flame temperature can lead to phase separation, significant sintering and loss of porosity. A state-of-the-art spray pyrolysis process is developed to produce the nanostructured composite materials using a tubular aerosol flow reactor. The composite materials produced from spray pyrolysis process are spherical in shape, submicron in size and composed of nanosized primary particles. Most importantly, the particles are highly porous and have no impurity phases, which are essential to the electrochemical performance of composite materials.

Composite materials within a binary system $x Li_2MnO_3 \cdot (1-x) LiNi_{0.5}Mn_{0.5}O_2$ ($0.3 \leq x \leq 0.7$) and a ternary system $LiNi_{0.5}Mn_{1.5}O_4$-Li_2MnO_3-$LiNi_{0.5}Mn_{0.5}O_2$ have been studied using the spray pyrolysis. The composite materials $x Li_2MnO_3 \cdot (1-x) LiNi_{0.5}Mn_{0.5}O_2$ ($0.3 \leq x \leq 0.7$) from spray pyrolysis display a rhombohedral $R\bar{3}m$ structure, which integrate

Li_2MnO_3 (C2/m) and $LiNi_{0.5}Mn_{0.5}O_2$ ($R\bar{3}m$) at the atomic level. Among the binary composite materials, uniform, spherical powders consisting of nanostructured $0.5Li_2MnO_3 \cdot 0.5LiNi_{0.5}Mn_{0.5}O_2$ (or simply $Li_{1.2}Ni_{0.2}Mn_{0.6}O_2$) has shown the best electrochemical performance including highest coulombic efficiency, excellent cycle life and rate capability. At the current density of 23 mAg^{-1}, $0.5Li_2MnO_3 \cdot 0.5LiNi_{0.5}Mn_{0.5}O_2$ attains over 250 $mAhg^{-1}$ at first cycle and over 220 $mAhg^{-1}$ at the 50^{th} cycle at deep discharge; and at 115 mAg^{-1}, it can achieve 200 $mAhg^{-1}$. Noticeable fading is observed for the powder with x less than 0.5 in $xLi_2MnO_3 \cdot (1-x)LiNi_{0.5}Mn_{0.5}O_2$, possibly due to the oxidation of the electrolyte from the large surface area of the powders with small primary particles. Nonetheless, the layered materials from spray pyrolysis have yielded some of the highest performance cathode materials as a result of uniform composition and high porosity.

By decreasing the Li content in $0.5Li_2MnO_3 \cdot 0.5LiNi_{0.5}Mn_{0.5}O_2$ (or simply $Li_{1.2}Ni_{0.2}Mn_{0.6}O_2$) and optimizing the heat-treatment conditions, a layered-spinel integrated composite material $Li_{(1.2-\delta)}Ni_{0.2}Mn_{0.6}O_{(2-\delta/2)}$ ($\delta = 1/10$) can be produced *via* the spray pyrolysis process. Nano domains (5-10 nm) of spinel-type structure from $Fd\bar{3}m$ $LiNi_{0.5}Mn_{1.5}O_4$ are observed by HR-TEM and XRD. Unfortunately, it is against the anticipation that the layered-spinel composites do not show noticeable improvement in rate capability, but they have shown a drop in overall capacity at deep discharge. Moreover, at elevated calcination temperatures, a phase transition from α-$NaFeO_2$ type structure ($R\bar{3}m$) to monoclinic Li_2MnO_3-type structure (*C2/m* or *C2/c*) occurs in composite materials $Li_{(1.2-\delta)}Ni_{0.2}Mn_{0.6}O_{(2-\delta/2)}$ ($\delta = 1/20$ and $1/10$), inducing a huge kinetic

barrier in the electrodes. For these reasons, it can be concluded that Li-content has significant impact on the crystal structure and the electrochemical performance of the composite materials. Although the layered-spinel integrated structure can be synthesized by altering the Li stoichiometry, the integrated layered-spinel structure is metastable which can convert into a new phase at an elevated temperature.

In summary, by using aerosol synthesis processes we have produced spherical, submicrometer- to micrometer-size particles with a unique, porous morphology. The size, shape and porous structure of the powders produced by spray-pyrolysis are considered superior to those produced by solid-state reactions and wet-chemistry processes. The materials from spray pyrolysis have high consistency in different batches and can preserve the stoichiometry of Li, Ni and Mn. The intraparticle and interparticle composition of the powders is also uniform. These composite materials have demonstrated reproducible high capacities and rate capabilities. However, little optimization of either the materials or electrodes has been performed. With optimization of size, morphology, chemical composition of the composite materials, the electrode formulation and cell fabrication, we can expect state-of-the-art powders approaching 300 $mAhg^{-1}$ (DOE's goal in 2011).

7.2 Recommendations for Future Work

7.2.1 Flame Pyrolysis

The flame process developed at this work used a hydrogen diffusion flame for powder synthesis. Due to the high flame temperature and long residence time of the particles in the flame, the primary particles are sintered together and an impurity phase is observed for some materials. Based on the results in this dissertation, it's recommended to make the following improvements and studies on the process and the materials:

1. Design of a low-temperature flame will help remove the impurity phase or defects in the powder. In the meantime, optimal residence time of the precursor in the flame should also be investigated to reduce the sintering effect and maintain a good porosity of the particles.
2. Methanol reacts as fuel in the flame process and also dissolves nitrate precursors as solvent. Although methanol is not expensive and more renewable than the metallic organics used in conventional flame-spray-pyrolysis (FSP) processes [125, 142], water-based precursor solution should be studied to minimize the cost of the flame process.
3. Particle size distribution may not be optimal for the powders as cathode materials. The fines (*c.a.* less than 100 nm) should be removed, which may potentially cause oxidation of electrolyte and dissolution of active species in the electrodes due to the high surface area.

4. High voltage $LiNi_{0.5}Mn_{1.5}O_4$ from flame process did not show significant amount of impurity phases, however it only delivered 90-100 $mAhg^{-1}$ at C/10 rate. A deep investigation should be made to understand the cause-effect of the performance.
5. Although turbulent flame has not been successful in this work, a continuing exploring of turbulent flame should be worthy for large-scale practicing.

7.2.2 Spray Pyrolysis

The spray pyrolysis process developed has produced high-quality powders. Several studies should be conducted for a better understanding of the aerosol process, and improvements should be made to optimize the system and the materials.

1. Optimize the reactor temperature and corresponding annealing conditions for an optimal porosity, primary particle size and crystal structure of the composition materials.
2. Impact of the secondary particle size distribution and primary particle sizes should be studied. More insights of the powder morphology and the formation mechanism, *e.g.*, hollow, irregular shaped and foam-like structured morphology, are highly recommended. Numerical model may help predict the morphology of the powders from various precursors.
3. The rate capability of the composite materials $xLi_2MnO_3 \cdot (1-x)LiNi_{0.5}Mn_{0.5}O_2$ ($0.3 \leq x \leq 0.7$) besides $x = 0.5$, should be studied. A systematic study of the

electrochemistry of these composite materials may give better understanding of the significance of Li_2MnO_3 in the integrated structures.

4. Battery modeling can aid in developing strategies to understand and optimize cell performance, particularly for new materials. A numerical model should be built to understand the transport phenomena of Li ions in the porous particles and electrode, and also to predict cycle life of the electrode.
5. New material composition should be studied, including doped materials with lightweight, or electrochemically active elements or both, to improve the cycle life, capacity and rate capability.
6. Cell optimization is essential to achieve the best performance of the powders. Reasonable efforts should be done to optimize electrode composition (binder and conductive material), cathode film thickness, electrode porosity, coupled anode chemistry, electrolyte and operation temperatures.
7. Study of scale-up to for large-scale production is also important to address the commercial viability of this process.

Appendix A

Spray Pyrolysis Synthesis of Spinel $LiMn_2O_4$

A.1 Precursor Effects on Particle Morphology

Precursor chemistry and its physical properties are essential to determine the particle morphology from spray pyrolysis processes. Metal nitrates and acetates, or a combination of them were tested at the early stage of the work with spray pyrolysis system. The precursors and experimental conditions are tabulated, as seen in Table A.1. Precursors were selected among Li nitrate and acetate, Mn (II) nitrates and acetate. The physical properties of these nitrates and acetates are shown in Table A.1. In general, the acetates have a lower decomposition temperature than the nitrates, and manganese compounds have a lower decomposition temperature than the lithium salts. Additionally, the lithium nitrates, for instance, has a higher solubility than the lithium acetate as the water temperature rises, which can potentially avoid precipitation of the salts, as seen in Figure A.1. Solid (non-hollow) and hollow morphology have been observed with various combinations of precursors during synthesizing $LiMn_2O_4$ powders, as shown in Table A.2. Hollow morphology is not desirable because it will decrease the packing density of the cell significantly. Heating temperature will also affect the morphology with certain

combinations of precursors. With $Li(HCOO)\cdot 2H_2O$ and $Mn(NO_3)_2\cdot 4H_2O$ precursors, slow heating (with the preheater on) will result in solid particles. However, rapid heating from room temperature to reactor temperature (700-800 °C) can produce hollow particles.

Table A.1 Physical properties of the precursors.

Compounds	Melting Point / °C	Boiling Point / °C	Decomposition Temperature / °C	Solubility g per 100 cc	
				Cold Water	Hot Water
$Li(HCOO)\cdot 2H_2O$	70	d.	338-470	30.0	very soluble
$LiNO_3$	264	d 600	600	89.8	234
$Mn(HCOO)_2\cdot 4H_2O$	120	N/A	120	33	N/A
$Mn(NO_3)_2\cdot 4H_2O$	25.8	129.4	200-300	426.4	∞

Source: Handbook of Chemistry and Physics College Edition, 48th Edition, 1967-1968; Ref. [195], [196]. (d: decompose)

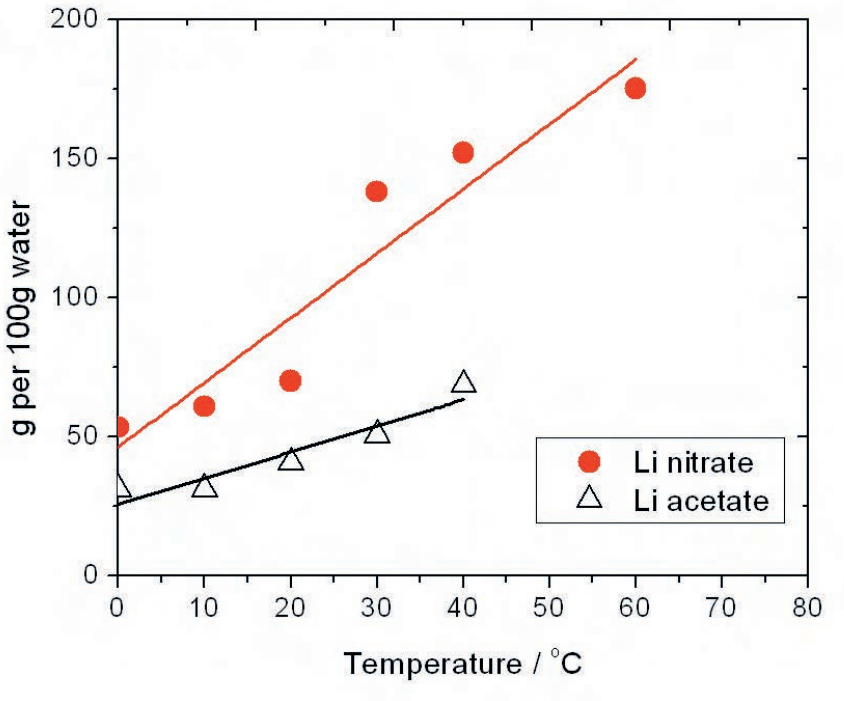

Figure A.1 Solubility of Li nitrate and acetate in water.

If mixing $Mn(NO_3)_2 \cdot 4H_2O$ precursor with either $Li(HCOO) \cdot 2H_2O$ or $LiNO_3$, the as-synthesized powders adopt a "solid" morphology that the internal of the particle is not hollow. In contrast, the powders produced from $Mn(HCOO)_2 \cdot 4H_2O$ and $Li(HCOO) \cdot 2H_2O$ precursors show a hollow morphology. The solubility of $Mn(HCOO)_2 \cdot 4H_2O$ is more than one order of magnitude lower than that of $Mn(NO_3)_2 \cdot 4H_2O$ in water; therefore, it can precipitate near the droplet surface during water evaporation. In the spray pyrolysis process, the first step for the precursor droplets is evaporation of the solvent, *i.e.*, water in this case. Near the droplet surface, the salt concentration tends to be higher than that in the droplet due to the evaporation of solvent. As a result if the salt solubility is low, precipitation could occur on the surface forming a thin solid layer. The precipitated product will further decompose into metal oxides, which is insoluble in water. Consequently, the oxide will sinter and form a thin crust on the surface that the hollow morphology can be produced. The hollow particle can burst and form shell structure under certain conditions, *e.g.*, from evaporation of internally trapped solvent. In contrast, both $LiNO_3$ and $Mn(NO_3)_2 \cdot 4H_2O$ have a much higher solubility than the acetates and the solubility of the former increases with temperature. Therefore, a homogeneous precipitation of the nitrates may occur in the precursor fine droplet during the evaporation of water solvent at elevated temperatures, forming dry precursor aerosols. After the thermal decomposition of the nitrates in the dry particles and a proper sintering process, a porous morphology is then developed.

Table A.2 Particle morphology with various precursors.

Precursor at 1:2 molar ratio		Preheater Temperature °C	Reactor Temperature °C	Morphology	Figure label
$Li(HCOO)\cdot 2H_2O$	$Mn(HCOO)_2\cdot 4H_2O$	300	700	Solid thin crust	A.2a
		N/A	700	Solid thin crust +shell	A.2b
$Li(HCOO)\cdot 2H_2O$	$Mn(NO_3)_2\cdot 4H_2O$	300	700	Porous thick crust	A.2c
		N/A	700	Porous + solid thick crust	A.2d
$LiNO_3$	$Mn(NO_3)_2\cdot 4H_2O$	300	700	Porous, non-hollow	A.2e

Carrier gas: air; flow rate: 3.3 lpm

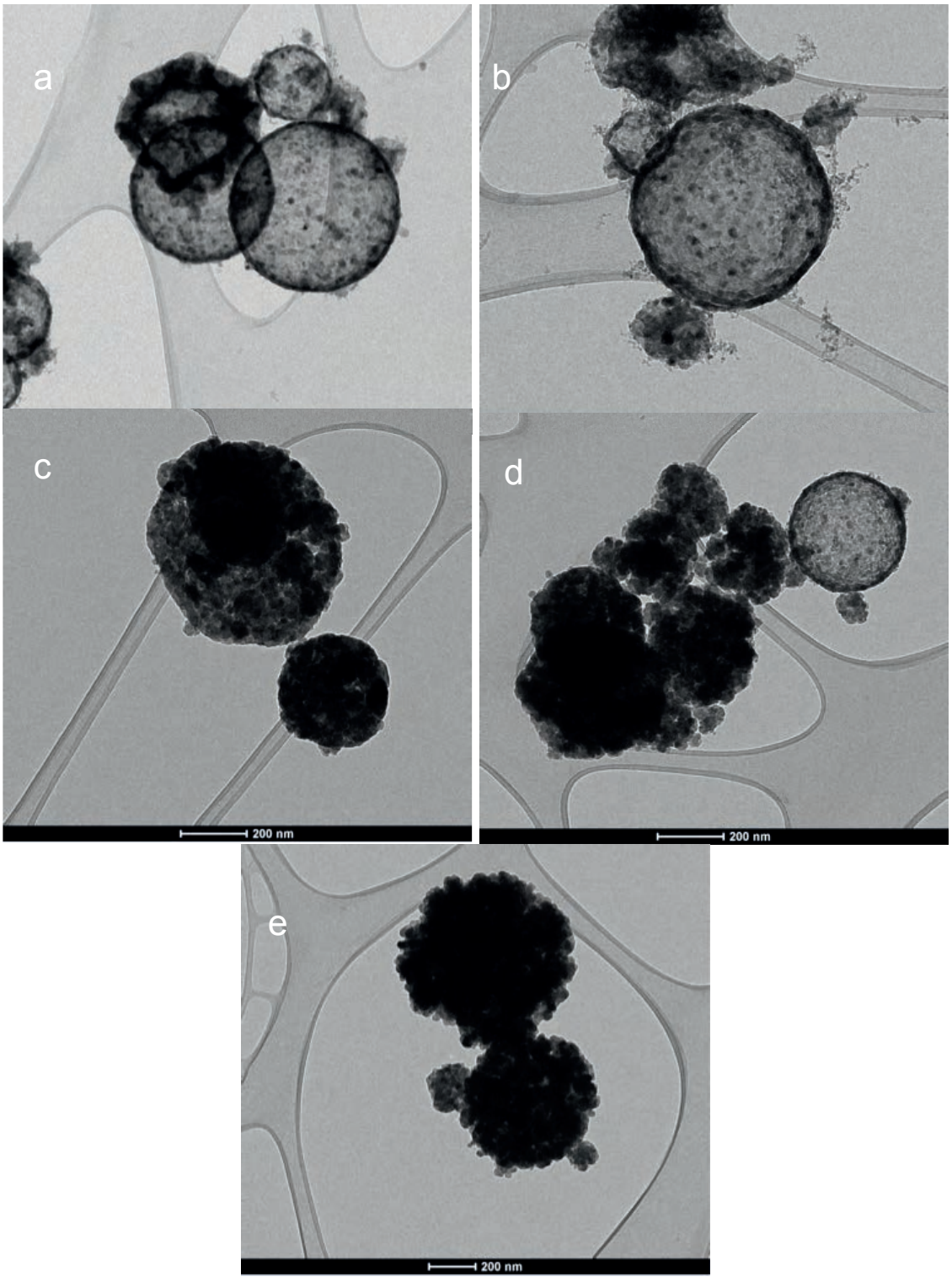

Figure A.2 Particle morphology as observed on TEM. Precursor and reactor temperature are listed in Table A.1.

A.2 Effects of Reactor Temperature

The flow reactor is used to explore the synthetic conditions for the spinel $LiMn_2O_4$. XRD analysis shows that at a wall temperature of 600 and 700 ºC, the as-synthesized powders are single-phase spinel with an $Fd\bar{3}m$ symmetry. When the wall temperature is elevated to 800 ºC, notable amount of Mn_3O_4 impurity is observed, as seen in Figure A.3. These results indicate that impurity phase formation (oxygen loss reaction) occurs at a lower temperature in the aerosol process. The reason may be explained as the small diameter ceramic tube and smaller particle sizes allow a more efficient heat transfer, leading to decomposition reaction. Therefore, high reactor temperature is not favorable for synthesizing spinel $LiMn_2O_4$. XRD analysis also shows that the powder at 700 ºC shows a sharper XRD pattern due to the better crystallinity as compared to that of the powder produced at 600 °C. Thus, the powder made at 700 ºC is selected for further test and optimization.

After annealing at 700 °C for 2 hours, the crystallinity of the powder is greatly improved as indicated by the sharper XRD peaks in Figure A.4. The annealed LiMn2O4 can be index as spinel type structure with a $Fd\bar{3}m$ symmetry. Cell refinement of the unannealed powder shows that the lattice constant a is 8.235 Å. After annealing, the lattice constant is reduced to 8.219 Å. The smaller lattice constant after annealing may be due to the better crystallinity.

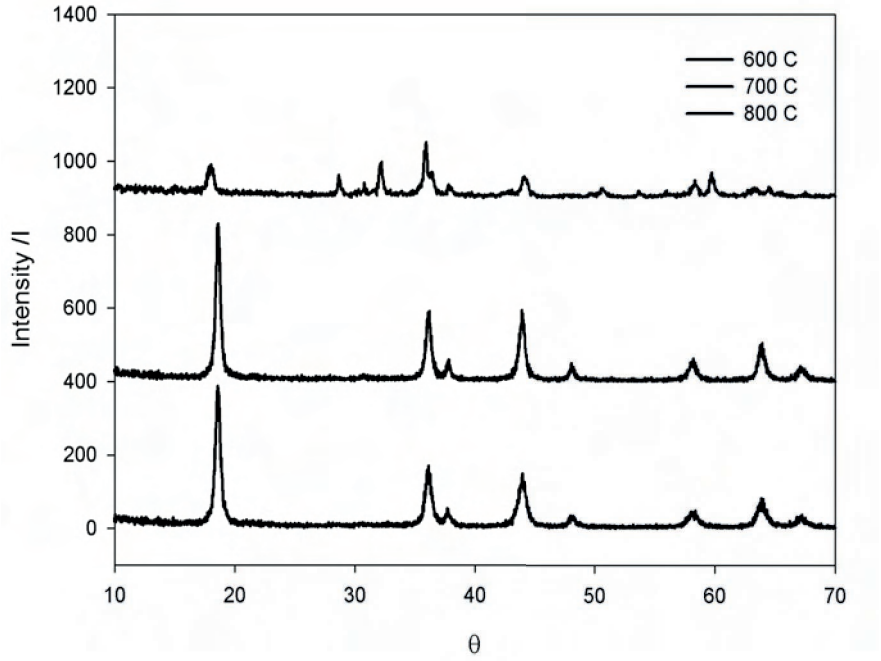

Figure A.3 XRD patterns of $LiMn_2O_4$ powder synthesized at 600 ºC (bottom), 700 ºC (middle) and 800 ºC (top).

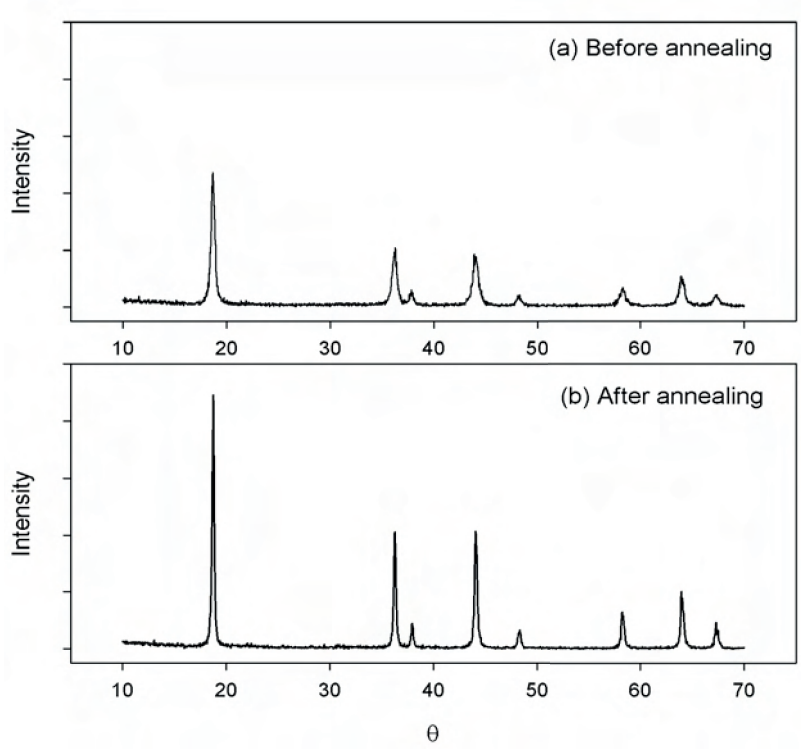

Figure A.4 XRD patterns of $LiMn_2O_4$ powders made in the aerosol flow reactor: (a) before annealing and (b) after annealing at 700 °C for 2 hr.

A.3 Particle Size Distribution and Morphology

Figure A.5 shows the size distribution of the as-produced $LiMn_2O_4$ powders with aqueous precursor solution consisting of 0.5 $moleL^{-1}$ $LiNO_3$ and 1.0 $moleL^{-1}$ $Mn(NO_3)_2 \cdot 4H_2O$ (total salt concentration: 1.5 $moleL^{-1}$). The preheater temperature is 300 °C and the reactor temperature is 700 °C. As measured by ELPI, the geometric mean diameter of the as-produced powder is *c.a.* 0.63 μm with a geometric standard derivation of 1.35, so that the powders are predominately submicron particles, with a few of them falling into nano size (20 nm) and micron size ranges (*c.a.* 2 μm). The particle number density is 6.5×10^6 $\#cm^{-3}$.

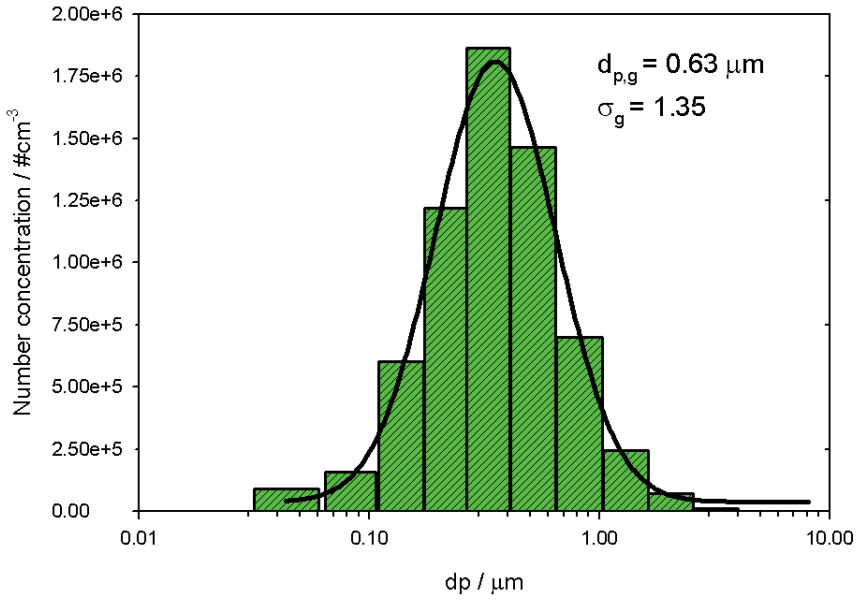

Figure A.5 Particle size distribution of $LiMn_2O_4$ from spray pyrolysis.

The as-synthesized powder shows a highly porous structure with nano-sized primary particles, and no hollow particle is observed, as seen in Figure A.6. This morphology is consistent with the $LiMn_2O_4$ powders made in different pyrolysis systems [112, 113]. After annealing for 2 hours, the primary particles are sintered together forming bigger crystallites. The annealed powder still remains polycrystalline and highly porous due to the short annealing time.

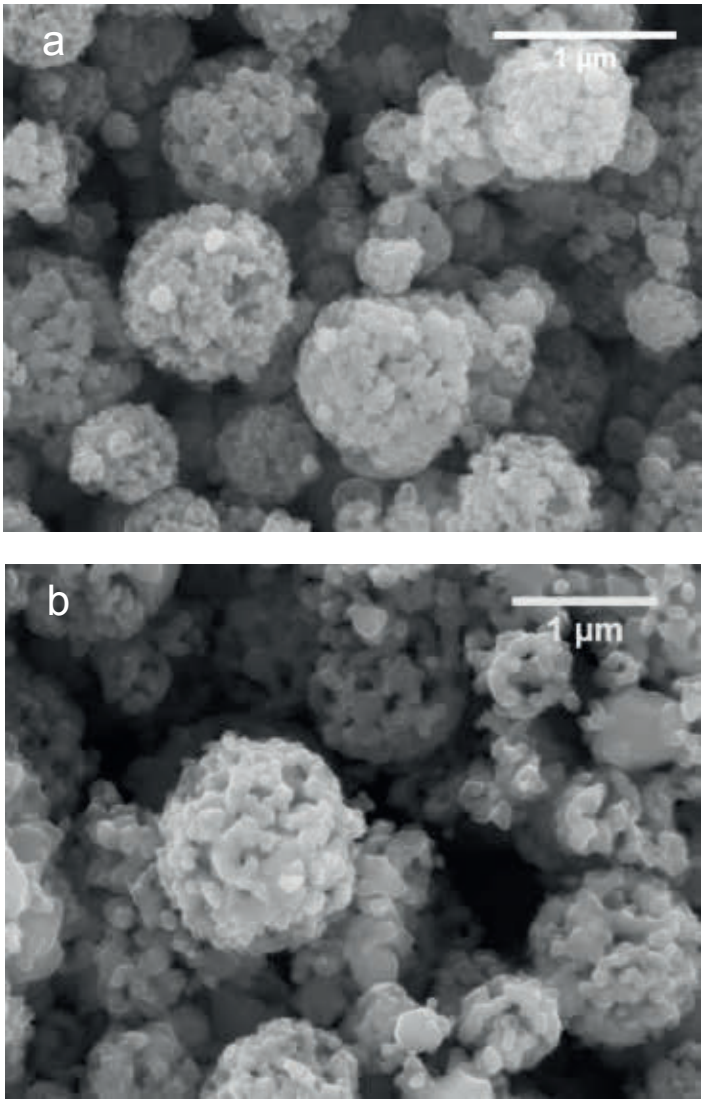

Figure A.6 Morphology of $LiMn_2O_4$ powders made in two-stage flow reactor: (a) before annealing and (b) after annealing at 700 °C for 2 hr.

A.4 Electrochemical performance

The initial charge/discharge cycles of the as-synthesized powder and annealed powder are shown in Figure A.7. The charge/discharge test was performed at C/10 rate between 3.0 and 4.3 V at LBNL. Both cells show the characteristic voltage plateaus at 4 V *vs.* Li, indicating lithium insertion/extraction into tetrahedral site (8a) in the spinel framework. The initial discharge capacity of unannealed powder is about 97 $mAhg^{-1}$, in contrast to 126 $mAhg^{-1}$ of the annealed powder. The low initial capacity of the as-synthesized powder may be due to the low crystallinity or the high surface area of the powder. As discussed before, poor crystallinity results in low structural integrity, leading to capacity loss.

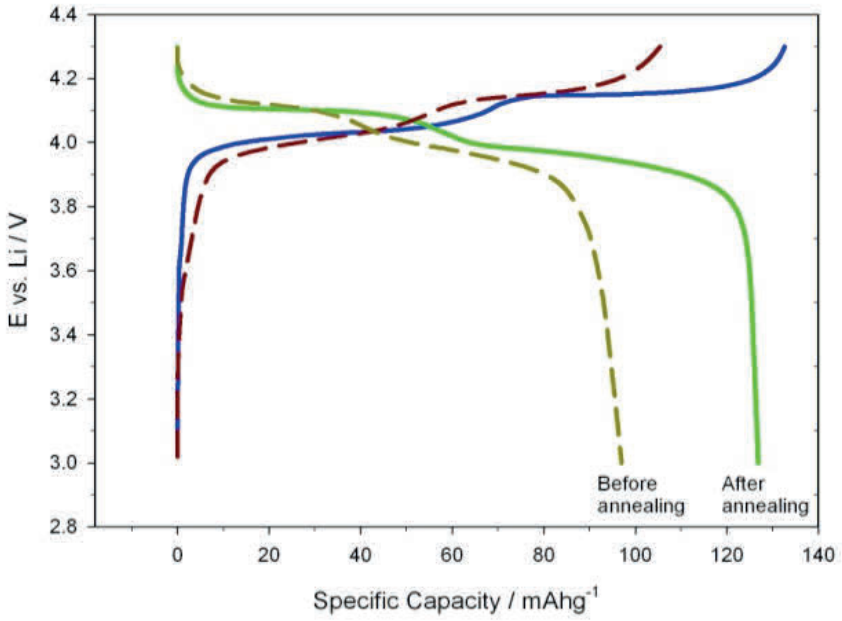

Figure A.7 Initial charge-discharge curves of $LiMn_2O_4$ powders (dash lines: as-synthesized powder; solid line: annealed powder).

The cycling performance of the annealed powder at C/10 charge/discharge rate was tested at WU, as shown in Figure A.8. The cell shows a higher initial capacity of over 130 $mAhg^{-1}$ and it fades slowly. The annealed $LiMn_2O_4$ also show high capacity retention in the first 17 cycles. At the 18^{th} cycle, the capacity drops and then remains flat for the rest three cycles. The fast capacity drop is expected due to the delamination of the thin film electrode on the current collector.

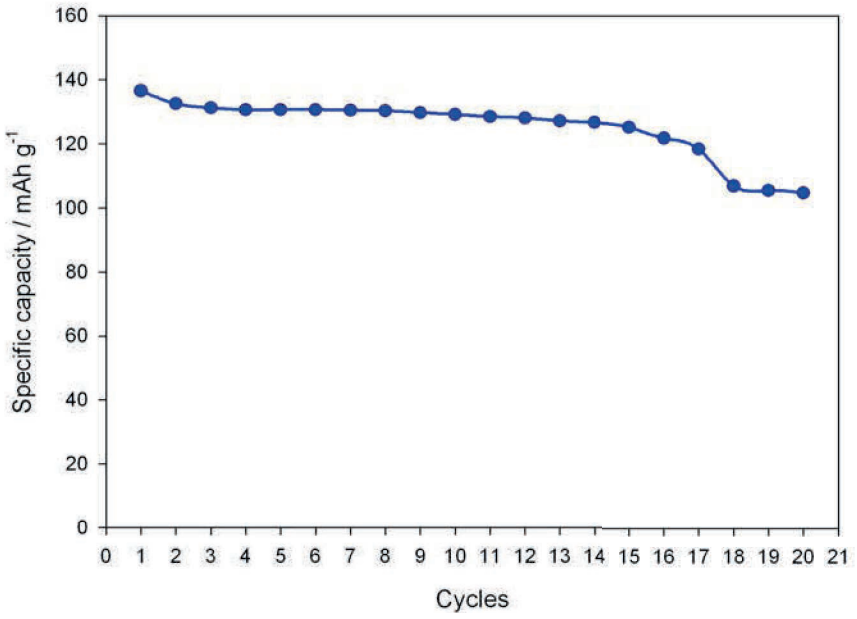

Figure A.8 Cycling performance of $LiMn_2O_4$ annealed at 700 °C, at C/10 rate.

Appendix B

Spray Pyrolysis Synthesis of Spinel $LiNi_{0.5}Mn_{1.5}O_4$

B.1 Effects of Reactor Temperature and Annealing Temperature

In the synthesis of $LiNi_{0.5}Mn_{1.5}O_4$ *via* spray pyrolysis process, stoichiometric amount of $LiNO_3$, $Ni(NO_3)_2 \cdot 6H_2O$ and $Mn(NO_3)_2 \cdot 4H_2O$ are dissolved in water with a total salt concentration 1.5 $moleL^{-1}$.The preheater temperature is kept at 300 °C, and reactor temperature varies between 400 °C and 800 °C. The powder produced at 700 °C is further annealed at 600 °C and 800 °C for 2 hr. Figure B.1 shows that the spinel type structure can be observed when the reactor wall temperature is as low as 400 °C, due to the narrow decomposition window of the nitrate mixture, as discussed in Chapter 3. As the reactor temperature increases to 700 °C, the spinel structure is more obvious in the as-synthesized powder. As the reactor temperature rises to 800 °C, impurity phase was produced. Therefore, the synthesis temperature of spray pyrolysis is significantly lower that in solid-state reaction process. Since total salt concentration is the same to the precursor solution for $LiMn_2O_4$ synthesis, the particle size distribution of $LiNi_{0.5}Mn_{1.5}O_4$ is expected to be the same, having a mean diameter in submicron range.

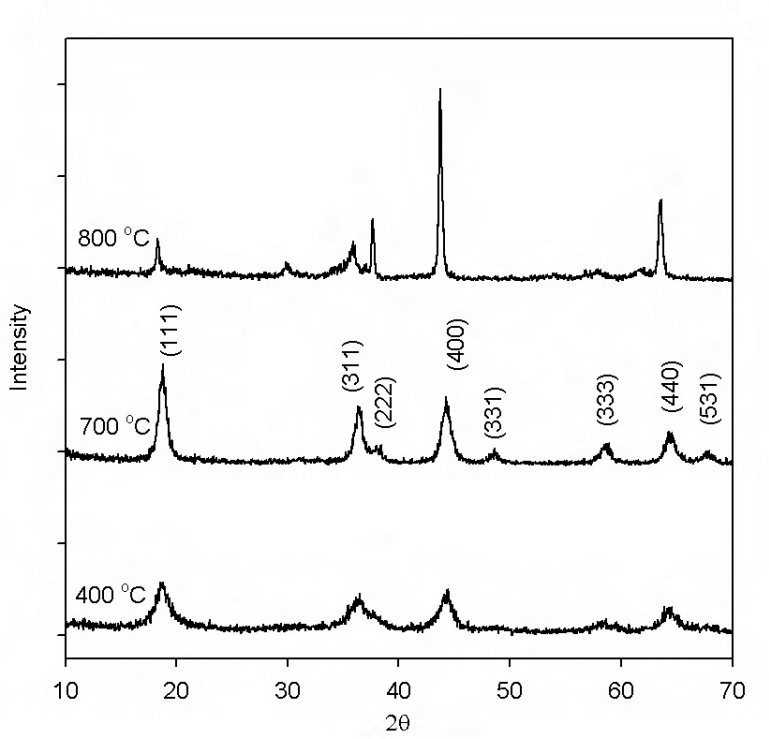

Figure B.1 XRD pattern of as-synthesized $LiNi_{0.5}Mn_{1.5}O_4$ at various temperatures *via* spray pyrolysis.

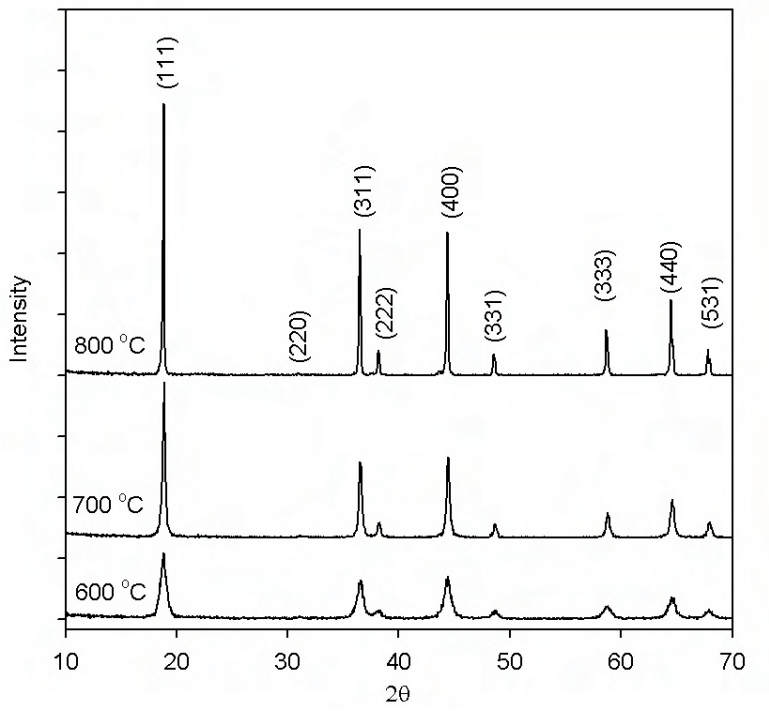

Figure B.2 XRD pattern of $LiNi_{0.5}Mn_{1.5}O_4$ after annealing at 600 °C, 700 °C and 800 °C. Powder is produced at 700 °C *via* the spray pyrolysis.

The $LiNi_{0.5}Mn_{1.5}O_4$ powder produced at 700 °C is further annealed for 2 hr at three different temperatures: 600 °C, 700 °C and 800 °C. The XRD pattern of the powder annealed at 600 °C is almost identical to the as-synthesized powder, which indicates no significant increase in crystallite size heated at 600 °C, as seen in Figure B.2. The TEM analyses also shows that no significant morphology changes occurs for the powder annealed at 600 °C, as shown in Figure B.3. In contrast, the powder annealed at 800 °C display a faceted morphology that the primary particles have sintered together forming a single crystal structure. The XRD pattern of the powder annealed at 800 °C appears sharper than the powders annealed at other temperatures, and it can be indexed as spinel structure. The 800 °C annealed powder is expected to be single-phase $LiNi_{0.5}Mn_{1.5}O_{4-\delta}$, due to the high calcination temperature. The powders annealed at 600 °C and at 700 °C have shown almost identical Bragg peaks to the 800 °C powder, except for the low intensities and broadened peak from nanosized crystallite. From the XRD spectrums, it is difficult to conclude that these powders are also oxygen deficient spinels $LiNi_{0.5}Mn_{1.5}O_{4-\delta}$ ($Fd\bar{3}m$). Another way to determine the structure is to measure the voltage profiles of the cells by assembling test cells with these powders. It is known that the average valence of Mn is 4+ in the perfect spinel $LiNi_{0.5}Mn_{1.5}O_4$ ($P4_332$) and it is *c.a.* 3.92 in $LiNi_{0.5}Mn_{1.5}O_{4-\delta}$ ($Fd\bar{3}m$) [50, 52]. Therefore, there is a redox reaction occurs for $LiNi_{0.5}Mn_{1.5}O_{4-\delta}$ ($Fd\bar{3}m$) between 3.0 and 4.3 V. For this reason, half-cells with powder annealed at 600 °C and 800 °C were assembled and tested.

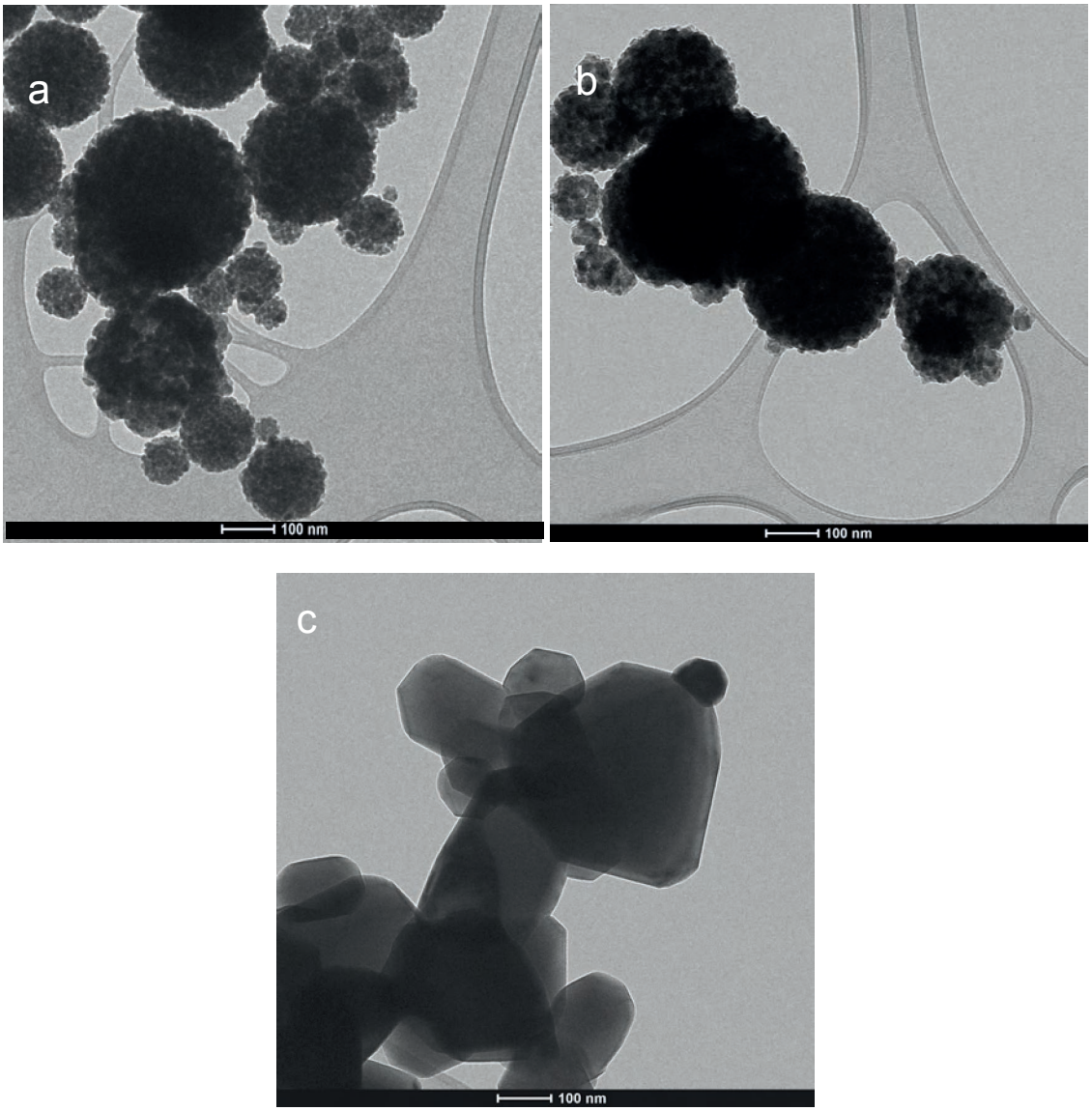

Figure B.3 Morphology of $LiNi_{0.5}Mn_{1.5}O_4$ as observed on TEM: (a) as-synthesize powder; (b) annealed at 600 °C for 2 hr; (c) annealed at 800 °C for 2hr. The 600 °C annealed powder shows an identical morphology to the as-synthesized powder.

Disordered spinel $LiNi_{0.5}Mn_{1.5}O_{4-\delta}$ can be converted into ordered spinel $LiNi_{0.5}Mn_{1.5}O_4$ under proper heat treatment by filling the oxygen vacancies with oxygen atoms. The weight change between the two structures is measureable. For this reason, TGA analysis is applied to study the oxygen vacancies in the spinel powders annealed at 600 °C and

800 °C as seen in Figure B.4. The sample temperature ramps from room temperature (23 °C) to 900 °C at 5 °Cmin^{-1} under an air flux, and then the samples follow an isotherm at 900 °C for 1 hour. The samples are cooled down to 23 °C at 5 °Cmin^{-1}. The perfect spinel $LiNi_{0.5}Mn_{1.5}O_4$ (*P4₃32*) annealed at 600 °C begins to lose weight slowly as the temperature rises, and then its weight drops rapidly at *c.a.* 700 °C possibly due to a severe oxygen loss reaction. After an isotherm at 900 °C for 1 hr, the total weight loss of perfect spinel is 4.5% (Figure B.4a). As the temperature cools down, the oxygen loss reaction is reversible and the sample weight remains constant, 97.7% of the initial weight. The 2.3% irreversible weight loss is possible due to the absorbed moisture in the porous $LiNi_{0.5}Mn_{1.5}O_4$ annealed at 600 °C, as seen in Figure 3.Bb. In contrast, the face-centered spinel $LiNi_{0.5}Mn_{1.5}O_{4-\delta}$ ($Fd\bar{3}m$) appears to be more stable because it starts to lose oxygen rapidly at *c.a.* 800 °C, which is higher than that of the $LiNi_{0.5}Mn_{1.5}O_4$ (*P4₃32*). The net weight loss is less than 2.5% after an isotherm at 900 °C for 1 hr. Most interestingly, the face-centered spinel $LiNi_{0.5}Mn_{1.5}O_{4-\delta}$ ($Fd\bar{3}m$) gains more weight at cooling, preferentially because it uptakes more oxygen forming the perfect spinel $LiNi_{0.5}Mn_{1.5}O_4$ (*P4₃32*). This result confirms that the powder annealed at 800 °C is an oxygen-deficient spinel $LiNi_{0.5}Mn_{1.5}O_{4-\delta}$ ($Fd\,\bar{3}\,m$). If assuming all the powders have the perfect spinel $LiNi_{0.5}Mn_{1.5}O_4$ structure, the oxygen deficiency δ in the $LiNi_{0.5}Mn_{1.5}O_{4-\delta}$ can be estimated by comparing the weight differences between heating and cooling on the TGA curves. With the TGA weight data acquired at 400 °C, the oxygen deficiency δ is calculated to be *c.a.* 0.03, therefore the chemical formula of the powder annealed at 800 °C is $LiNi_{0.5}Mn_{1.5}O_{3.97}$.

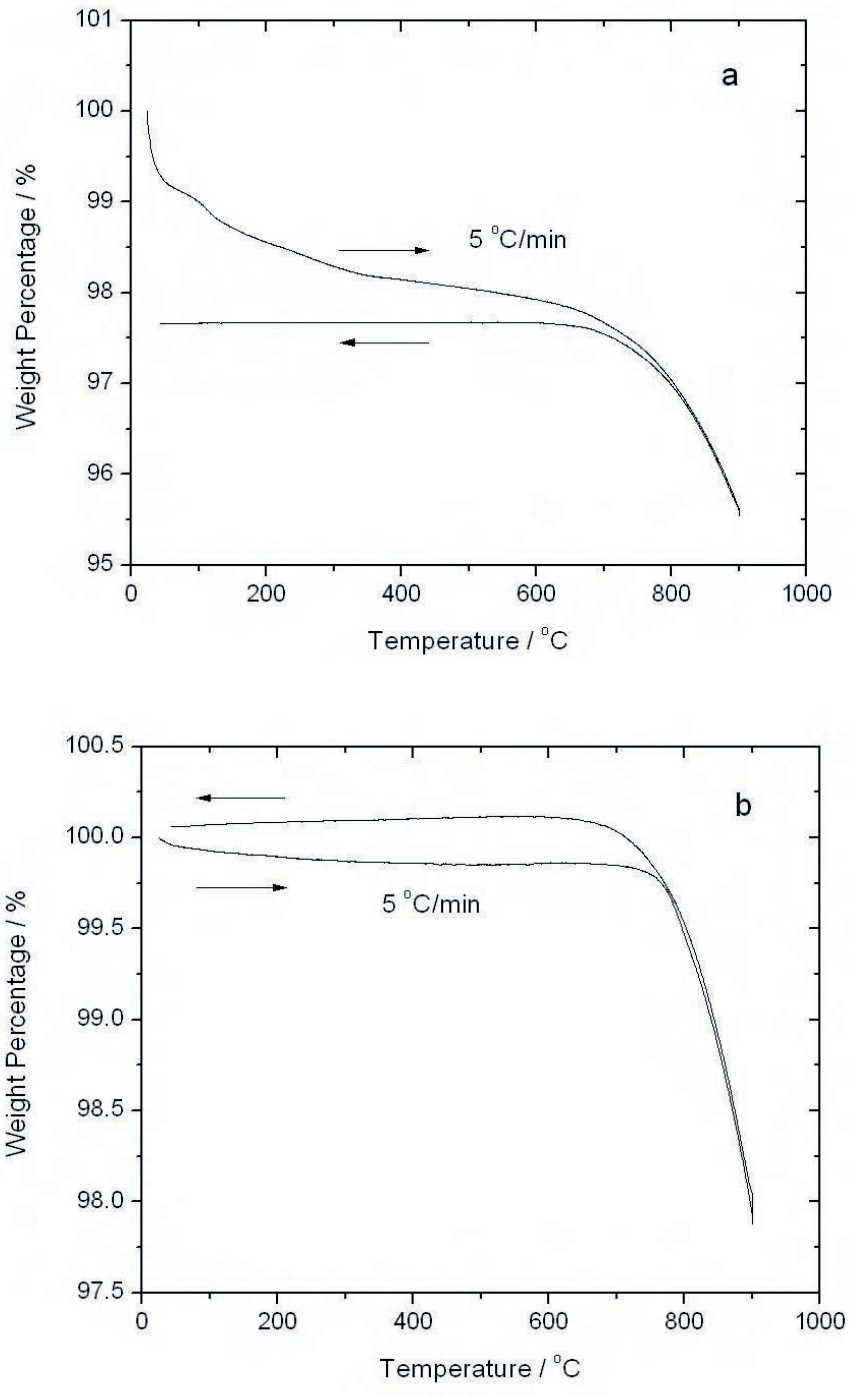

Figure B.4 TGA analysis of the powders annealed at 600 °C (a) and 800 °C (b).

B.2 Electrochemical performance

The discharge voltage profiles of cells with powders annealed at 600 °C and 800 °C are plotted and shown in Figure B.5. $LiNi_{0.5}Mn_{1.5}O_4$ annealed at 800 °C has a short voltage plateau near 4 V from $Mn^{4+/3+}$ redox couple and two-stage plateau near 4.7 V from $Ni^{4+/2+}$ redox couple. The average oxidation state of Mn therefore is less than 4+. For this reason, the powder annealed at 800 °C is considered as oxygen deficient spinel $LiNi_{0.5}Mn_{1.5}O_{4-\delta}$ ($Fd\bar{3}m$). The 4 V plateaus are missing for the powder annealed at 600 °C at various C-rates. This indicates that the $LiNi_{0.5}Mn_{1.5}O_4$ annealed at 600 °C adopts an ordered cubic spinel structure with $P4_332$ space group in which all the Mn cations are tetravalent.

The rate performance and cycle performance are combined in a single test, as shown in Figure B.6. Half-cells assembled with powders annealed at 600 °C and 800 °C are initially cycled at C/10 rate and then C-rates are increased every 10 cycles until it reached 1C. The cells are eventually cycled at C/10 rate after the rate performance test between C/10 and 1C. Disordered $LiNi_{0.5}Mn_{1.5}O_{4-\delta}$ ($Fd\bar{3}m$) shows better capacity retention over the nanostructured $LiNi_{0.5}Mn_{1.5}O_4$ ($P4_332$). After 150 cycles (including cycles at high C-rates), disordered $LiNi_{0.5}Mn_{1.5}O_{4-\delta}$ ($Fd\bar{3}m$) preserves over 91% of its initial capacity. In contrast, nanostructures $LiNi_{0.5}Mn_{1.5}O_4$ ($P4_332$) only hold 70% of its initial capacity after 100 cycles.

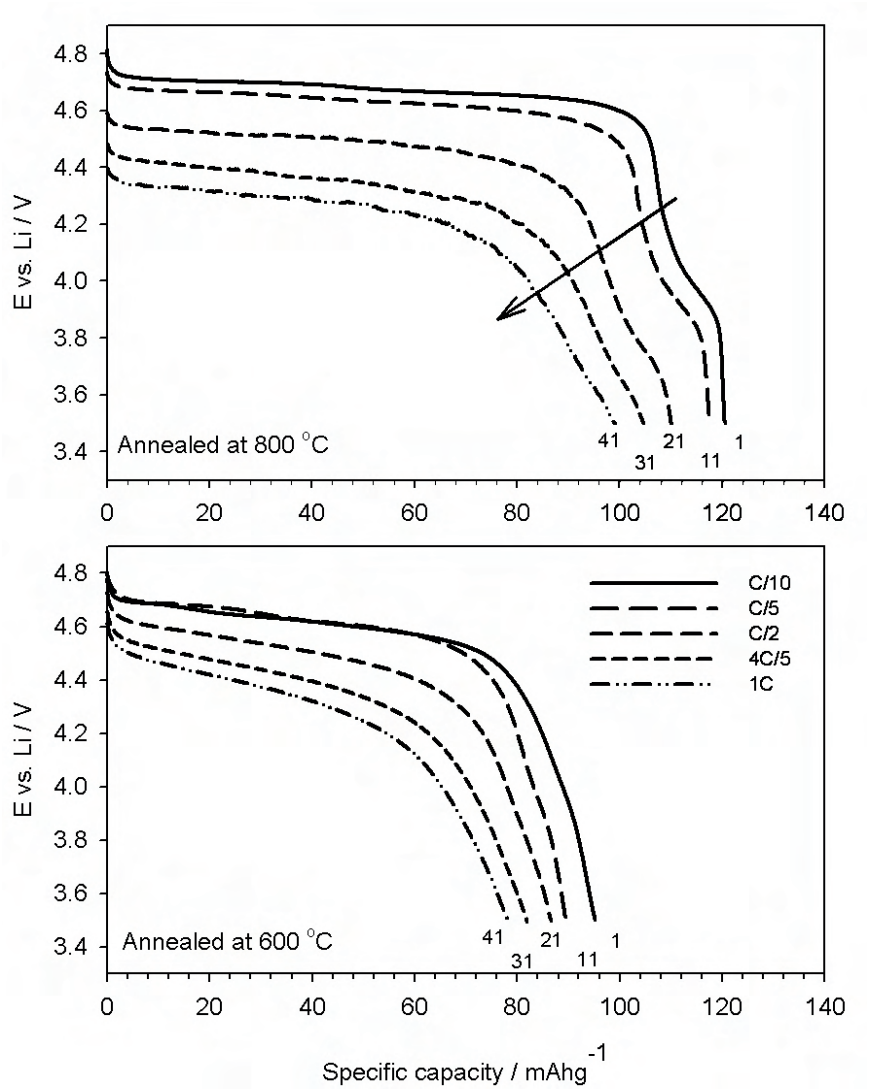

Figure B.5 Discharge voltage profile of electrodes with $LiNi_{0.5}Mn_{1.5}O_{4-\delta}$ (800 °C) and $LiNi_{0.5}Mn_{1.5}O_4$ (600 °C) powders.

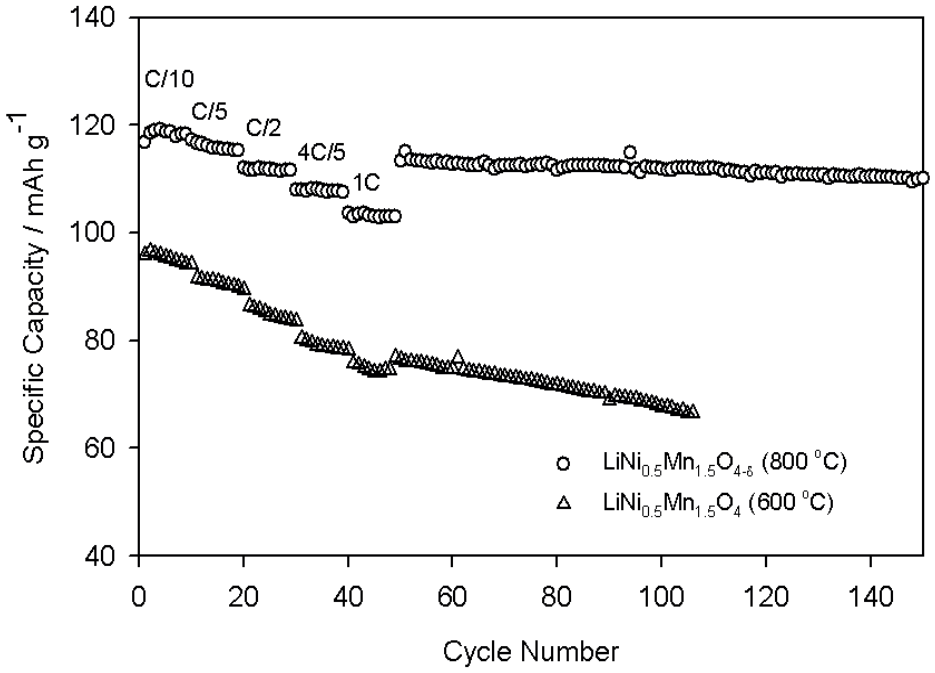

Figure B.6 Rate performance of $LiNi_{0.5}Mn_{1.5}O_{4-\delta}$ (800 °C) and $LiNi_{0.5}Mn_{1.5}O_4$ (600 °C) powders.

In summary, spray pyrolysis can produce disordered $LiNi_{0.5}Mn_{1.5}O_{4-\delta}$ ($Fd\bar{3}m$) and ordered $LiNi_{0.5}Mn_{1.5}O_4$ ($P4_332$) after simple heat treatments. Disordered $LiNi_{0.5}Mn_{1.5}O_{4-\delta}$ ($Fd\bar{3}m$) has superior capacity retention over the nanostructured ordered $LiNi_{0.5}Mn_{1.5}O_4$ ($P4_332$) material and $LiMn_2O_4$ from spray pyrolysis. Without electrode and cell optimization, disordered $LiNi_{0.5}Mn_{1.5}O_{4-\delta}$ ($Fd\bar{3}m$) also display good rate capability up to 1C. Therefore, spray pyrolysis is capable in producing high-quality high-power cathode materials with less energy and cost input.

Appendix C

Battery Performance Validation at National Laboratories

Battery fabrication and testing are new at the LACER lab, so it is necessary to validate these procedures employed in this research. An independent data validation can incrementally add to a higher level of confidence for this work. The independent validation was carried out at the Batteries for Advanced Transportation Technologies Fabrication Laboratory (BATT Fab lab) at LBNL and the Electrochemical Analysis and Diagnostics Laboratory at ANL for a variety of materials studied in this dissertation. An example is given using flame-made $LiNi_{0.5}Mn_{1.5}O_4$ powders, which were fabricated into electrodes for coin cells and tested at LBNL and WU separately. The composition of the electrodes is shown in Table C.1. The LBNL electrode has little more conductive carbon than the WU electrode does. In addition to that, a different electrolyte was used at LBNL.

Table C.1 Electrode composition and test condition for flame-made $LiNi_{0.5}Mn_{1.5}O_4$ powder.

	Electrode Composition Active material/PVdF/Carbon Black	**Electrolyte**	**C-rate**
WU	84:10:6	LiPF6 in EC+DMC (1:1)	1/10
LBNL	82:10:8	LiPF6 in EC+DEC (1:1)	1/10

Regardless of the differences mentioned above, the two $LiNi_{0.5}Mn_{1.5}O_4$ cells assembled at LBNL and WU almost have identical performance at C/10 rate, as seen in Figure C.1. The voltage profile near 4.7 V overlaps with one another at charge and discharge. In addition, the charge and discharge capacities of the two cells are almost identical (within 5% error). The minor difference can be considered to be due to the experimental uncertainties from the equipment and facilities. In summary, the WU test result is validated by LBNL test, and the other test results in the dissertation herein are considered true and accurate.

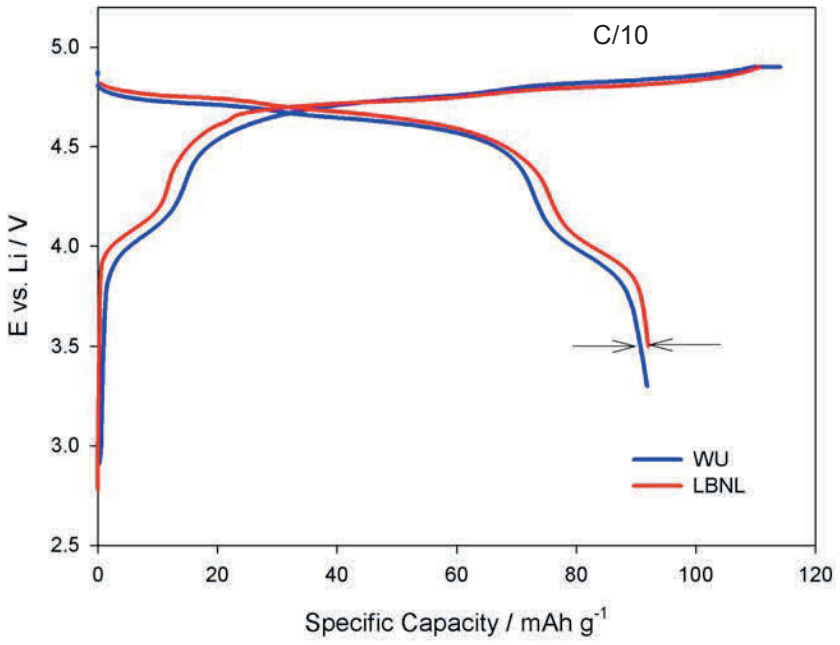

Figure C.1 Charge-discharge voltage profiles of $LiNi_{0.5}Mn_{1.5}O_4$ electrodes assembled at WU and LBNL.

Appendix D

Fabrication Procedure for Li-ion Coin Cells

The following procedures were developed and revised based on the one designed at LBNL specifically for the electrodes and coin cells consisting of spinel $LiMn_2O_4$, $LiNi_{0.5}Mn_{1.5}O_4$ and composite materials. The electrode composition or technical details may vary as new materials are developed. Detailed information regarding electrode and cell optimization, please contact LBNL for optimal procedures. (Last revised: 2011)

D.1 NMP-Based Binder Solution Preparation

Materials:

- Active material: spinel $LiMn_2O_4$, $LiNi_{0.5}Mn_{1.5}O_4$, and layered $x Li_2MnO_3 \cdot (1-x)LiNi_{0.5}Mn_{0.5}O_2$ composite materials , and such
- Conductive carbon: Super-P carbon black [TIMCAL]
- Binder: 12 % wt. polyvinylidene fluoride (PVdF) in N-methyl-pyrrolidone (NMP) [Kureha 1200 (solution)]
- Solvent: NMP [Sigma Aldrich]

Equipment:

- Vacuum oven
- Homogenizer: Polytron PT10-35
- Glove box with vacuum oven attached
- 100-300 ml jar
- Scale and balance
- Sonicator

Estimated time:

- Overnight drying + 2 to 4 hr mixing of the binder solution

(1) Determine binder solution composition

The binder solution is prepared to glue together the active cathode materials and also provide electronic conductive carbon black in the electrode. The composition of the binder solution depends on the cathode material chemistry and physical properties. The total weight of PVdF and carbon black, and the ratio of them are based on LBNL coin-cell fabrication procedure and information from literatures. The concentration of binder solution is not optimized yet.

Table D.1 Example of binder solution composition for $LiMn_2O_4$

Component	Chemistry	Weight %
Binder	PVdF	5
Conductive Carbon	Super-P carbon	3
Solvent	NMP	92

Table D.2 Example of binder solution composition for $Li_{1.2}Ni_{0.2}Mn_{0.6}O_2$

Component	Chemistry	Weight %
Binder	PVdF	3
Conductive Carbon	Super-P carbon	3
Solvent	NMP	94

(2) Pre-treat carbon black

1. Dry the acetylene black at 120-130 °C under high vacuum for at least 12 hours.
2. Store in glove box or under vacuum.

(3) Prepare binder solution

3. Calculate the amount of 12 % wt. Kureha binder solution, carbon black and NMP required for the electrode;
4. Take sufficient NMP from glove box and mix with Kureha binder solution in a glass or plastic bottle;
5. Weight carbon black and mixed with the PVdF-NMP solution;
6. Cap/seal the container and shake the as-prepared binder solution till a black solution is formed;
7. Homogenize the binder solution using sonicator for over 2 hr;
8. Store the binder solution in a ventilated place.

D.2 Electrode Preparation

Materials:

- Active material: spinel $LiMn_2O_4$, $LiNi_{0.5}Mn_{1.5}O_4$, and layered $xLi_2MnO_3 \cdot (1-x)LiNi_{0.5}Mn_{0.5}O_2$ composite materials and such
- Binder solution: as-prepared PVdF + Carbon black in NMP
- Current collector: aluminum foil

Equipment:

- Doctor blade (MTI)
- Variable-speed, vacuum drawdown coater (MTI)
- Calendering machine/roll press (MTI)
- Homogenizer: Polytron PT10-35
- Glove box with vacuum oven attached
- High-accuracy balance
- Micrometer
- Punches: 1/2", 9/16", 11/16" and 15 mm
- Hammer
- Small jars: 10 ml

Estimated time:

- Overnight drying at RT + 2 to 4 hr drying at 130 °C under vac. + 1 to 2 hr + overnight drying 130 °C under vac.

(4) Prepare Cathode Slurry

9. Weight enough active cathode powders (*c.a.* 1 g or more) into a 10 ml jar;
10. Calculate the amount of PVdF and conductive carbon for the electrode;
11. Extract enough binder solution using a pipette from the binder solution container;
12. Drip sufficient binder solution as calculated to the active material in the 10 ml jar, and recap the binder solution container;
13. Homogenize the slurry at a rate of 4000 rpm for at least 7 times (1 min each time) to completely mix active material with PVdF and carbon black. A dark slurry will form;
14. Remove the bubbles in the slurry by tapping the jar and resting it for few minutes;

Table D.3 Example of cathode slurry composition for $LiMn_2O_4$:PVdF:Carbon = 92:5:3

Component	Chemistry	Weight
Binder	PVdF	0.054 g
Conductive Carbon	Super-P carbon	0.033 g
Active material	NMP	1.0 g
Binder solution	PVdF/C in NMP	1.087 g

(4) Prepare Cathode Thin Film

15. Set casting speed at 7 or 8 of the film casting machine;
16. Adjust the blade height of the doctor blade applicator, the reading is in SI unit (*e.g.*, reading 10 = 100 μm);
17. Clean the perforated vacuum surface on top the casting machine;

18. Turn on vacuum and spread a Al foil (current collector) on the casting bench, wipe down the foil and remove the wrinkles and bumps on the Al foil surface that the current collector must be extremely flat;
19. Clean the flat Al surface with acetone and allow the acetone to evaporate before casting the cathode film;
20. Roughen the current collector surface can improve the adhesion of cathode film to the current collector to maintain a good lamination during drying.
21. Once everything is ready, pour the slurry on the Al foil across the front of the blade;
22. Begin casting the film at a constant speed (20-30 cm min^{-1}), the thin film generated should be a smooth shinning wet coating on the current collector;
23. Once the cathode films is casted, remove/clean the doctor blade/film applicator and cover the thin film with the plastic shield;
24. Dry the wet coating at room temperature overnight.
25.

(6) Prepare Cathode Disc

26. After the electrode film is dried in the casting machine, cut the film into 1" wide slices on a cutting board;
27. Transfer the cathode slices into vacuum oven, dry at 120-130 °C for 2-4 hr under vacuum (30-50 milli torr);
28. After the films are completely dried, remove them from vacuum oven and measure the thickness of active cathode film (= total cathode film thickness - Al foil thickness);

29. Optional: calender the electrode film using the calender machine, typically 90% to 100% to original thickness;
30. To calender the electrode, set the distance between the two rollers of the calender machine;
31. Feed the electrodes through the rollers and manually roll the roller until the entire film has been laminated;
32. Measure the thickness of the electrode with a micrometer; Repeat the process until the desired thickness is achieved;
33. Clean the punches (14 mm) and hammers before punch electrode discs;
34. Align the punch over the area and punch out electrode disc with a hammer gently;
35. Store the punched electrode in the jar and label the jar;
36. Continue punching electrode discs until the entire strip is done;
37. Dry the electrodes for at least 12 hr at 120-130 °C under vacuum (30-50 milli torr);
38. Measure the total weight of an electrode disc and the Al current collector weight, label each jar containing the electrode discs.

D.3 Coin Cell Assembly

Materials

- Coin cell parts (2032 type): coin cell cases (top and bottom), spring, gasket and spacer
- Anodes: lithium foil disc for half cells

- Cathodes: punched electrode discs
- Separator: Celgard 2400 and 2500
- Electrolyte

Equipment

- Coin cell crimper
- Glove box
- Latex gloves
- Punches for Li foil
- Pipette
- Plastic tweezers and weight boat

Estimated time:

- 10-20 minutes for each cell
-

(7) Assemble Coin Cells

39. Flatten the cathode disc and put it into the bottom coin cell case with the current collector facing down and attaching the case, center the electrode using a tweezer;
40. Confirm no dirt attached to the electrode surface or in the case;
41. Drip some electrolyte on the electrode till it's fully wet;
42. Center one or two separators on the wet electrode and add more electrolyte to the top separator surface till both components are fully wet;

43. Attach the Li disc to the spacer, and slightly press the Li foil to flatten the surface. Remove dendrite or any dirt if there is any;
44. The Li will contact with the separator facing down against the cathode;
45. Put spring on top of the spacer and center it;
46. Put the cap with gasket on top and seal the coin cell;
47. Check that all the components should be centered and aligned;
48. Flip over the coin cell and put it into the die of the battery crimper with anode side (-) facing down and cathode side (+) facing up, the coin cell should be centered and aligned with the die;

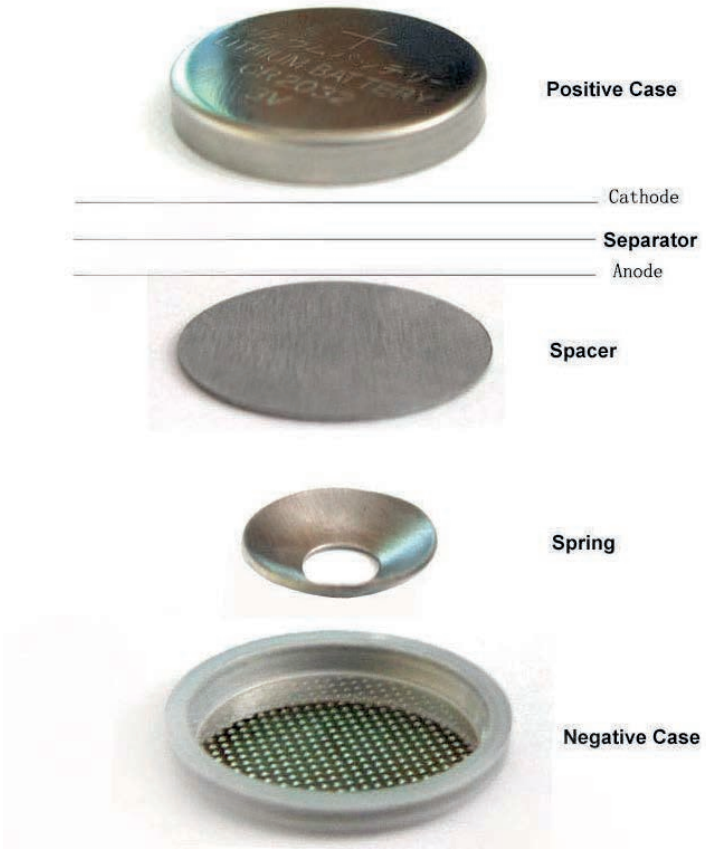

Figure D.1 Assembly of a 2032 coin cell.

49. Open the valve on the crimper and start to repeatedly press the rod, the die will move up with the coin cell in it;
50. When the die moves up and the coin cell contacts the upper die of the crimper, watch the pressure gauge and slowly press it up until the die is completely closed up, the pressure on the gauge should not exceed 800 psi;
51. Once the pressure reaches 700-800 psi, release the valve and the die will move down with a sealed coin cell;
52. Clean the electrolyte leaked during pressing and the coin cell is assembled;
53. Begin cycle test once the coin cells are transferred out of the glove box.

References

[1] J.M. Tarascon, M. Armand, Issues and Challenges Facing Rechargeable Lithium Batteries, *Nature*, 414 (2001) 359-367.

[2] M.S. Whittingham, Materials Challenges Facing Electrical Energy Storage, *MRS Bulletin*, 33 (2008) 411-419.

[3] D. Guyomard, J.M. Tarascon, Li metal-free rechargeable $LiMn_2O_4$/carbon cells: Their understanding and optimization, *J. Electrochem. Soc.*, 139 (1992) 937-948.

[4] M.S. Whittingham, Lithium batteries and cathode materials, *Chem. Rev.*, 104 (2004) 4271-4301.

[5] M.S. Whittingham, Electrical energy storage and intercalation chemistry *Science*, 192 (1976) 1126-1127.

[6] G.A. Nazri, G. Pistoia, Lithium Batteries: Science and Technology, Kluwer Academic Publishers, Boston, MA, 2004.

[7] L. Samuelson, I.P. Batra, Electronic-Properties of Various Stages of Lithium Intercalated Graphite, *Journal of Physics C-Solid State Physics*, 13 (1980) 5105-5124.

[8] S. Hashikawa, S. Yanase, T. Oi, Lithium isotope effect accompanying chemical insertion of lithium into graphite, *Z Naturforsch A*, 57 (2002) 857-862.

[9] P. Arora, R.E. White, M. Doyle, Capacity fade mechanisms and side reactions in lithium-ion batteries, *J. Electrochem. Soc.*, 145 (1998) 3647-3667.

[10] J. Vetter, P. Novak, M.R. Wagner*, et al.*, Ageing mechanisms in lithium-ion batteries, *J. Power Sources*, 147 (2005) 269-281.

[11] N. Imanishi, S. Ohashi, T. Ichikawa*, et al.*, Carbon-lithium anodes for lithium secondary batteries, *J. Power Sources*, 39 (1992) 185-191

[12] R. Yazami, K. Zaghib, M. Deschamps, Carbon fibers and natural graphite as negative electrodes for lithium ion-type batteries, *J. Power Sources*, 52 (1994) 55-59.

[13] H. Shimoda, B. Gao, X.P. Tang*, et al.*, Lithium intercalation into opened single-wall carbon nanotubes: Storage capacity and electronic properties, *Physical review letters*, 88 (2002) 015502.015501-015502.015504.

[14] H.M. Hsoeh, N.H. Tai, C.Y. Lee*, et al.*, Electrochemical properties of the multi-walled carbon nanotube electrode for secondary lithium-ion battery, *Rev. Adv. Mater. Sci.*, 5 (2003) 67-71.

[15] J. Yamaura, Y. Ozaki, A. Morita, *et al.*, High voltage, rechargeable lithium batteries using newly developed carbon for negative electrode material, *J. Power Sources*, 43 (1993) 233-239.

[16] A. Mabuchi, H. Fujimoto, K. Tokumitsu, *et al.*, Charge-discharge mechanism of graphitized mesocarbon microbeads, *J. Electrochem. Soc.*, 142 (1995) 3049-3051.

[17] Y.C. Chang, H.J. Sohn, C.H. Ku, *et al.*, Anodic performances of mesocarbon microbeads (MCMB) prepared from synthetic naphthalene isotropic pitch, *Carbon*, 37 (1999) 1285-1297.

[18] C.K. Chan, H. Peng, G. Liu, *et al.*, High-performance lithium battery anodes using silicon nanowires, *Nature Nanotechnology*, 3 (2008) 31-35.

[19] M.-H. Park, M.G. Kim, J. Joo, *et al.*, Silicon nanotube battery anodes, *Nano Lett.*, 9 (2009) 3844-3847.

[20] M. Green, E. Fielder, B. Scrosati, *et al.*, Structured silicon anodes for lithium battery applications, *Electrochem. Solid-State Lett.*, 6 (2003) A75-A79.

[21] Y. Cui, L.J. Lauhon, M.S. Gudiksen, *et al.*, Diameter-controlled synthesis of single-crystal silicon nanowires, *Applied Physics Letters*, 78 (2001) 2214-2216.

[22] M.S. Whittingham, The role of ternary phases in cathode reactions, *J. Electrochem. Soc.*, 123 (1976) 315-320.

[23] K. Mizushima, P.C. Jones, P.J. Wiseman, *et al.*, Li_xCoO_2 ($0<x\leqslant 1$): a new cathode material for batteries of high energy density, *Mater. Res. Bull.*, 15 (1980) 783-789

[24] M. Winter, J.O. Besenhard, M.E. Spahr, *et al.*, Insertion electrode materials for rechargeable lithium batteries, *Advanced Materials*, 10 (1998) 725-763.

[25] T. Ohzuku, A. Ueda, M. Nagayama, Electrochemistry and Structural Chemistry of $LiNiO_2$ (R-3m) for 4 Volt Secondary Lithium Cells, *J. Electrochem. Soc.*, 140 (1993) 1862-1870.

[26] J.R. Dahn, U. Vonsacken, C.A. Michal, Structure and Electrochemistry of $Li_{1\pm y}NiO_2$ and a New Li_2NiO_2 Phase with the $Ni(OH)_2$ Structure, *Solid State Ionics*, 44 (1990) 87-97.

[27] Y. Paik, C.P. Grey, C.S. Johnson, *et al.*, Lithium and deuterium NMR studies of acid-leached layered lithium manganese oxides, *Chem. Mater.*, 14 (2002) 5109-5115.

[28] G.R. Jain, J.S. Yang, M. Balasubramanian, *et al.*, Synthesis, electrochemistry, and structural studies of lithium intercalation of a nanocrystalline Li_2MnO_3-like compound, *Chem. Mater.*, 17 (2005) 3850-3860.

[29] A.D. Robertson, P.G. Bruce, Mechanism of electrochemical activity in Li_2MnO_3, *Chem. Mater.*, 15 (2003) 1984-1992.

[30] D.Y.W. Yu, K. Yanagida, Y. Kato, *et al.*, Electrochemical Activities in Li_2MnO_3, *J. Electrochem. Soc.*, 156 (2009) A417-A424.

[31] M.H. Rossouw, M.M. Thackeray, Lithium manganese oxides from Li_2MnO_3 for rechargeable lithium battery applications, *Mater. Res. Bull.*, 26 (1991) 463-473.

[32] C.S. Johnson, S.D. Korte, J.T. Vaughey, *et al.*, Structural and electrochemical analysis of layered compounds from Li_2MnO_3, *J. Power Sources*, 82 (1999) 491-495.

[33] C.S. Johnson, J.S. Kim, C. Lefief, *et al.*, The significance of the Li_2MnO_3 component in 'composite' $xLi_2MnO_3 \cdot (1-x)LiMn_{0.5}Ni_{0.5}O_2$ electrodes, *Electrochem. Commun.*, 6 (2004) 1085-1091.

[34] J.S. Kim, C.S. Johnson, J.T. Vaughey, *et al.*, Electrochemical and structural properties of $xLi_2M'O_3 \bullet (1-x)LiMn_{0.5}Ni_{0.5}O_2$ eIectrodes for lithium batteries (M' = Ti, Mn, Zr; $0 \leqslant x \leqslant 0.3$), *Chem. Mater.*, 16 (2004) 1996-2006.

[35] C.S. Johnson, N. Li, J.T. Vaughey, *et al.*, Lithium-manganese oxide electrodes with layered-spinel composite structures $xLi_2MnO_3 \bullet (1-x)Li_{1+y}Mn_{2-y}O_4$ ($0<x<1$, $0 \leqslant y \leqslant 0.33$) for lithium batteries, *Electrochem. Commun.*, 7 (2005) 528-536.

[36] F. Amalraj, D. Kovacheva, M. Talianker, *et al.*, Synthesis of Integrated Cathode Materials $xLi_2MnO_3 \cdot (1 - x)LiMn_{1/3}Ni_{1/3}Co_{1/3}O_2$ (x = 0.3, 0.5, 0.7) and Studies of Their Electrochemical Behavior, *J. Electrochem. Soc.*, 157 (2010) A1121-A1130.

[37] H.X. Deng, I. Belharouak, R.E. Cook, *et al.*, Nanostructured lithium nickel manganese oxides for lithium-ion batteries, *J. Electrochem. Soc.*, 157 (2010) A447-A452.

[38] M. Wakihara, Lithium Manganese Oxides with Spinel Structure and Their Cathode Properties for Lithium Ion Battery, *Electrochemistry*, 73 (2005) 328-335.

[39] M.M. Thackeray, W.I.F. David, P.G. Bruce, *et al.*, Lithium insertion into manganese spinels, *Mater. Res. Bull.*, 18 (1983) 461-472.

[40] T. Ohzuku, M. Kitagawa, T. Hirai, Electrochemistry of Manganese-Dioxide in Lithium Nonaqueous Cell .3. X-Ray Diffractional Study on the Reduction of Spinel-Related Manganese-Dioxide, *J. Electrochem. Soc.*, 137 (1990) 769-775.

[41] B.L. He, W.J. Zhou, Y.Y. Liang, *et al.*, Synthesis and electrochemical properties of chemically substituted $LiMn_2O_4$ prepared by a solution-based gel method, *Journal of Colloid and Interface Science*, 300 (2006) 633-639.

[42] C.J. Curtis, J. Wang, D.L. Schulz, Preparation and characterization of $LiMn_2O_4$ spinel nanoparticles as cathode materials in secondary Li batteries, *J. Electrochem. Soc.*, 151 (2004) 590-598.

[43] S.-H. Park, S.-T. Myung, S.-W. Oh, *et al.*, Ultrasonic spray pyrolysis of nano crystalline spinel $LiMn_2O_4$ showing good cycling performance in the 3 V range *Electrochim. Acta*, 51 (2006) 4089-4095.

[44] M.N. Obrovac, Y. Gao, J.R. Dahn, Explanation for the 4.8-V plateau in $LiCr_xMn_{2-x}O_4$, *Phys. Rev. B*, 57 (1998).

[45] S. Mandal, R.M. Rojas, J.M. Amarilla*, et al.*, High Temperature Co-doped LiMn2O4-Based Spinels. Structural, Electrical, and Electrochemical Characterization, *Chem. Mater.*, 14 (2002) 1598-1605.

[46] T. Ohzuku, K. Ariyoshi, S. Yamamoto, Synthesis and Characterization of $Li[Ni_{1/2}Mn_{3/2}]O_4$ by Two-Step Solid State Reaction, *J. Ceram. Soc. Jpn.*, 110 (2002) 501-505.

[47] C.P. Vicente, J.M. Lloris, J.L. Tirado, Understanding the voltage profile of Li insertion into $LiNi_{0.5-y}Fe_yMn_{1.5}O_4$ in Li cells, *Electrochim. Acta*, 49 (2004) 1963-1967.

[48] S.T. Myung, S. Komaba, N. Kumagai*, et al.*, Nano-crystalline $LiNi_{0.5}Mn_{1.5}O_4$ synthesized by emulsion drying method, *Electrochim. Acta*, 47 (2002) 2543-2549.

[49] S.H. Park, Y.K. Sun, Synthesis and electrochemical properties of 5 V spinel $LiNi_{0.5}Mn_{1.5}O_4$ cathode materials prepared by ultrasonic spray pyrolysis method, *Electrochim. Acta*, 50 (2004) 431-434.

[50] J.H. Kim, S.T. Myung, C.S. Yoon*, et al.*, Comparative study of LiNi0.5Mn1.5O4-delta and $LiNi_{0.5}Mn_{1.5}O_4$ cathodes having two crystallographic structures: Fd-3m and $P4_332$, *Chem. Mater.*, 16 (2004) 906-914.

[51] M. Kunduraci, G.G. Amatuccia, Synthesis and Characterization of Nanostructured 4.7 V $Li_xMn_{1.5}Ni_{0.5}O_4$ Spinels for High-Power Lithium-Ion Batteries, *J. Electrochem. Soc.*, 153 (2006) A1345-A1352.

[52] M. Kunduraci, G.G. Amatuccia, The effect of particle size and morphology on the rate capability of 4.7 V $LiMn_{1.5+\delta}Ni_{0.5-\delta}O_4$ spinel lithium-ion battery cathodes, *Electrochim. Acta*, 53 (2008) 4193-4199.

[53] K.M. Shaju, P.G. Bruce, Nano-$LiNi_{0.5}Mn_{1.5}O_4$ spinel: a high power electrode for Li-ion batteries, *Dalton T.*, (2008) 5471-5475.

[54] A.K. Padhi, K.S. Nanjundaswamy, J.B. Goodenough, Phospho-olivines as positive-electrode materials for rechargeable lithium batteries, *J. Electrochem. Soc.*, 144 (1997) 1188-1194.

[55] M. Manickam, K. Minato, M. Takataz, Lithium insertion into NASICON frameworks, *J. Electrochem. Soc.*, 150 (2003) A1085-A1089.

[56] A.K. Padhi, K.S. Nanjundaswamy, C. Masquelier*, et al.*, Mapping of transition metal redox energies in phosphates with NASICON structure by lithium intercalation, *J. Electrochem. Soc.*, 144 (1997) 2581-2586.

[57] H. Tukamoto, A.R. West, Electronic conductivity of $LiCoO_2$ and its enhancement by magnesium doping, *J. Electrochem. Soc.*, 144 (1997) 3164-3168.

[58] J. Guan, M.L. Liu, Transport properties of $LiMn_2O_4$ electrode materials for lithium-ion batteries, *Solid State Ionics*, 110 (1998) 21-28.

[59] C.M. Julien, A. Mauger, A. Ait-Salah*, et al.*, Nanoscopic scale studies of $LiFePO_4$ as cathode material in lithium-ion batteries for HEV application, *Ionics*, 13 (2007) 395-411.

[60] H. Huang, S.C. Yin, L.F. Nazar, Approaching theoretical capacity of $LiFePO_4$ at room temperature at high rates, *Electrochem. Solid-State Lett.*, 4 (2001) A170-A172.

[61] M.M. Doeff, Y.Q. Hu, F. McLarnon*, et al.*, Effect of surface carbon structure on the electrochemical performance of $LiFePO_4$, *Electrochem. Solid-State Lett.*, 6 (2003) A207-A209.

[62] H.K. Chung, S.K. Jang, H.W. Ryu*, et al.*, Effects of nano-carbon webs on the electrochemical properties in $LiFePO_4$/C composite. , *Solid State Communications*, 131 (2004) 549-554.

[63] H. Gabrisch, J.D. Wilcox, M.M. Doeff, Carbon surface layers on a high-rate $LiFePO_4$, *Electrochem. Solid-State Lett.*, 9 (2006) A360-A363.

[64] C.M. Julien, K. Zaghib, A. Mauger*, et al.*, Characterization of the carbon coating onto $LiFePO_4$ particles used in lithium batteries, *Journal of Applied Physics*, 100 (2006) -.

[65] C. Delacourt, P. Poizot, S. Levasseur*, et al.*, Size effects on carbon-free $LiFePO_4$ powders, *Electrochem. Solid-State Lett.*, 9 (2006) A352-A355.

[66] D.H. Kim, J. Kim, Synthesis of $LiFePO_4$ nanoparticles in polyol medium and their electrochemical properties, *Electrochem. Solid-State Lett.*, 9 (2006) A439-A442.

[67] M. Gabaerscek, R. Dominko, J. Jamnik, Is small particle size more important than carbon coating? An example study on $LiFePO_4$ cathodes, *Electrochemistry Conmmunications*, 9 (2007) 2778-2783.

[68] S.Y. Chung, J.T. Bloking, Y.M. Chiang, Electronically conductive phospho-olivines as lithium storage electrodes, *Nature Materials*, 1 (2002) 123-128.

[69] S.Q. Shi, L.J. Liu, C.Y. Ouyang*, et al.*, Enhancement of electronic conductivity of $LiFePO_4$ by Cr doping and its identification by first-principles calculations, *Phys. Rev. B*, 68 (2003) 195108.195101-195108.195105.

[70] M. Abbate, S.M. Lala, L.A. Montoro*, et al.*, Ti-, Al-, and Cu-doping induced gap states in $LiFePO_4$, *Electrochem. Solid-State Lett.*, 8 (2005) A288-A290.

[71] T.H. Teng, M.R. Yang, S.H. Wu*, et al.*, Electrochemical properties of $LiFe_{0.9}Mg_{0.1}PO_4$/carbon cathode materials prepared by ultrasonic spray pyrolysis, *Solid State Communications*, 142 (2007) 389-392.

[72] P. Nelson, K. Amine, A. Rousseau*, et al.*, Advanced Lithium-Ion Batteries for Plug-in Hybrid-Electric Vehicles, Argonne National Laboratory, 2007.

[73] J.M. Tarascon, W.R. McKinnon, F. Coowar, *et al.*, Synthesis conditions and oxygen stoichiometry effects on Li insertion into the spinel $LiMn_2O_4$, *J. Electrochem. Soc.*, 141 (1994) 1421-1431.

[74] V. Manev, A. Momchilov, A. Nassalevska, *et al.*, Rechargeable lithium battery with spinel-related λ-MnO_2. III: Scaling-up problems associated with $LiMn_2O_4$ synthesis, *J. Power Sources*, 54 (1995) 323-328.

[75] J.M. Tarascon, F. Coowar, G. Amatuci, *et al.*, The $Li_{1+x}Mn_2O_4$/C system materials and electrochemical aspects, *J. Power Sources*, 54 (1995) 103-108.

[76] M. Lanz, C. Kormann, H. Steininger, *et al.*, Large-agglomerate-size lithium manganese oxide spinel with high rate capability for Lithium-ion batteries, *J. Electrochem. Soc.*, 147 (2000) 3997-4000.

[77] Z.P. Guo, J.H. Ahn, H.K. Liu, *et al.*, Characterization of nanoparticles of $LiMn_2O_4$ synthesized by a one-step intermediate-temperature solid-state reaction., *J Nanosci Nanotechnol*, 4 (2004) 162-166.

[78] V. Massarotti, D. Capsoni, M. Bini, Nanosized $LiMn_2O_4$ from mechanically activated solid-state synthesis, *J. Solid State Chem.*, 179 (2006) 590?596.

[79] D.Y. Wang, L. Hong, Z.X. Wang, *et al.*, New solid-state synthesis routine and mechanism for $LiFePO_4$ using LiF as lithium precursor, *J. Solid State Chem.*, 177 (2004) 4582-4587.

[80] I. Belharouak, C. Johnson, K. Amine, Synthesis and electrochemical analysis of vapor-deposited carbon-coated $LiFePO_4$, *Electrochem. Commun.*, 7 (2005) 983-988.

[81] J.B. Lu, Z.L. Tang, Z.T. Zhang, *et al.*, Preparation of $LiFePO_4$ with inverse opal structure and its satisfactory electrochemical properties, *Mater. Res. Bull.*, 40 (2005) 2039-2046.

[82] S.H. Ju, D.Y. Kim, E.B. Jo, *et al.*, $LiMn_2O_4$ particles prepared by spray pyrolysis from spray solution with citric acid and ethylene glycol, *J. Mater. Sci.*, 42 (2007) 5369-5374.

[83] S.A. Needham, A. Calka, G.X. Wang, *et al.*, A new rapid synthesis technique for electrochemically active materials used in energy storage applications, *Electrochem. Commun.*, 8 (2006) 434-438.

[84] J.K. Kim, J.W. Choi, G. Cheruvally, *et al.*, A modified mechanical activation synthesis for carbon-coated $LiFePO_4$ cathode in lithium batteries, *Mater. Lett.*, 61 (2007) 3822-3825.

[85] J.K. Kim, G. Cheruvally, J.H. Ahn, *et al.*, Electrochemical properties of $LiFePO_4$/C composite cathode material: Carbon coating by the precursor method and direct addition, *J. Phys. Chem. Solids*, 69 (2008) 1257-1260.

[86] K.S. Park, J.T. Son, H.T. Chung, *et al.*, Synthesis of $LiFePO_4$ by co-precipitation and microwave heating, *Electrochem. Commun.*, 5 (2003) 839-842.

[87] S. Scaccia, M. Carewska, P. Wisniewski, *et al.*, Morphological investigation of sub-micron $FePO_4$ and $LiFePO_4$ particles for rechargeable lithium batteries, *Mater. Res. Bull.*, 38 (2003) 1155-1163.

[88] K.S. Park, K.T. Kang, S.B. Lee, *et al.*, Synthesis of $LiFePO_4$ with fine particle by co-precipitation method, *Mater. Res. Bull.*, 39 (2004) 1803-1810.

[89] K.F. Hsu, S.Y. Tsay, B.J. Hwang, Synthesis and characterization of nano-sized $LiFePO_4$ cathode materials prepared by a citric acid-based sol-gel route, *J. Mater. Chem.*, 14 (2004) 2690-2695.

[90] M. Gaberscek, R. Dominko, M. Bele, *et al.*, Porous, carbon-decorated $LiFePO_4$ prepared by sol-gel method based on citric acid, *Solid State Ionics*, 176 (2005) 1801-1805.

[91] M.A.E. Sanchez, G.E.S. Brito, M.C.A. Fantini, *et al.*, Synthesis and characterization of $LiFePO_4$ prepared by sol-gel technique, *Solid State Ionics*, 177 (2006) 497-500.

[92] K. Kimura, M. Miyayama, Li intercalation properties of $LiFePO_4$/carbon composites prepared by hydrothermal method, *Electroceramics in Japan Vii*, 269 (2004) 139-142.

[93] J. Zhang, S.Q. Liu, K.L. Huang, *et al.*, $LiFePO_4$: Hydrothermal synthesis and properties, *Chinese Journal of Inorganic Chemistry*, 21 (2005) 433-436.

[94] B. Jin, H.B. Gu, Preparation and characterization of $LiFePO_4$ cathode materials by hydrothermal method, *Solid State Ionics*, 178 (2008) 1907-1914.

[95] G. G. Meligrana, C. Gerbaldi, A. Tuel, *et al.*, Hydrothermal synthesis of high surface $LiFePO_4$ powders as cathode for Li-ion cells, *J. Power Sources*, 160 (2005) 516-522.

[96] N. Li, C.R. Martin, A High-Rate, High-Capacity, Nanostructured Sn-Based Anode Prepared Using Sol-Gel Template Synthesis, *J. Electrochem. Soc.*, 148 (2001) A164-A170.

[97] X. Huang, Q. Zhang, J. Gan, *et al.*, Hydrothermal Synthesis of a Nanosized $LiNi_{0.5}Mn_{1.5}O_4$ Cathode Material for High Power Lithium-Ion Batteries, *J. Electrochem. Soc.*, 158 (2011) A139-A145.

[98] C.-C. Chang, P.N. Kumta, Particulate sol-gel synthesis and electrochemical characterization of LiMO2 (M=Ni, $Ni_{0.75}Co_{0.25}$) powders, *J. Power Sources*, 75 (1998) 44-45.

[99] H.X. Deng, I. Belharouak, Y.K. Sun, *et al.*, $Li_xNi_{0.25}Mn_{0.75}O_y$ ($0.5 \leqslant x \leqslant 2$, $2 \leqslant y \leqslant 2.75$) compounds for high-energy lithium-ion batteries, *J. Mater. Chem.*, 19 (2009) 4510-4516.

[100] L.J. Fu, H. Liu, C. Li, *et al.*, Electrode materials for lithium secondary batteries prepared by sol-gel methods, *Prog Mater Sci*, 50 (2005) 881-928.

[101] T.T. Kodas, M.J. Hampden-Smith, Aerosol Processing of Materials, Wiley-VCH publication, 1999.

[102] K. Zaghib, K. Tatsumi, H. Abe, *et al.*, Optimization of the Dimensions of Vapor-Grown Carbon Fiber for Use as Negative Electrodes in Lithium-Ion Rechargeable Cells, *J. Electrochem. Soc.*, 145 (1998) 210-215.

[103] G.F. Ortiz, R. Alcántara, P. Lavela, *et al.*, Optimization of the Electrochemical Behavior of Vapor Grown Carbon Nanofibers for Lithium-Ion Batteries by Impregnation, and Thermal and Hydrothermal Treatments, *J. Electrochem. Soc.*, 152 (2005) A1797-A1803

[104] C.J. Unrau, R.L. Axelbaum, P. Biswas, *et al.*, Synthesis of single-walled carbon nanotubes in oxy-fuel inverse diffusion flames with online diagnostics, *Proc. Combust. Inst.*, 31 (2007) 1865-1872.

[105] C.J. Unrau, R.L. Axelbaum, Gas-phase synthesis of single-walled carbon nanotubes on catalysts producing high yield, *Carbon*, 48 (2010) 1418-1424.

[106] C.J. Unrau, V.R. Katta, R.L. Axelbaum, Characterization of diffusion flames for synthesis of single-walled carbon nanotubes, *Combust. Flame*, 157 (2010) 1643-1648.

[107] P. Fragnaud, R. Nagarajan, D.M. Schleich, *et al.*, Thin-film cathodes for secondary lithium batteries, *J. Power Sources*, 54 (1995) 362-366.

[108] T. Ogihara, Y. Saito, T. Yanagawa, *et al.*, Preparation of spherical $LiCoO_2$ powders by the ultrasonic spray decomposition and its application to cathode active material in lithium secondary battery, *J. Ceram. Soc. Jpn.*, 101 (1993) 1159-1163.

[109] P. Fragnaud, R. Nagarajan, D.M. Schleich, *et al.*, Thin-film cathodes for secondary lithium batteries *J. Power Sources*, 54 (1995) 362-366.

[110] T. Ogihara, N. Ogata, K. Katayama, *et al.*, Electrochemical properties of spherical, porous $LiMn_{2-x}Mg_xO_4$ powders prepared by ultrasonic spray pyrolysis, *Electrochemistry*, 68 (2000) 162-166.

[111] H. Aikiyo, K. Nakane, N. Ogata, *et al.*, Effect of particle morphology on electrochemical property of $LiMn_2O_4$, *J. Ceram. Soc. Jpn.*, 109 (2001) 506-510.

[112] H. Ogihara, H. Aikiyo, N. Ogata, *et al.*, Particle morphology and battery property of lithium manganate synthesized by ultrasonic spray pyrolysis, *J. Soc. Powder Technol.*, 38 (2001) 396-400.

[113] I. Taniguchi, C.K. Lim, D. Song, *et al.*, Particle morphology and electrochemical performances of spinel $LiMn_2O_4$ powders synthesized using ultrasonic spray pyrolysis method, *Solid State Ionics*, 146 (2002) 239-247.

[114] I. Taniguchi, D. Song, M. Wakihara, Electrochemical properties of $LiM_{1/6}Mn_{11/6}O_4$ (M = Mn, Co, Al and Ni) as cathode materials for Li-ion batteries prepared by ultrasonic spray pyrolysis method, *J. Power Sources*, 109 (2002) 333-339

[115] S.H. Park, S.W. Oh, S.G. Kang, *et al.*, Effects of molybdenum doping on the layered $Li[Ni_{0.5+x}Mn_{0.5-2X}Mo_x]O_2$ cathode materials for lithium secondary batteries, *Chem. Lett.*, 33 (2004) 2-3.

[116] S.H. Park, S.W. Oh, S.T. Myung, *et al.*, Effects of synthesis condition on $LiNi_{1/2}Mn_{3/2}O_4$ cathode material for prepared by ultrasonic spray pyrolysis method, *Solid State Ionics*, 176 (2005) 481-486

[117] I. Mukoyama, T. Kodera, N. Ogata, *et al.*, Synthesis and lithium battery properties of $LiM(M=Fe,Al,Mg)_xMn_{2-x}O_4$ powders by spray pyrolysis, *Key Eng. Mater.*, 301 (2006) 167-170.

[118] S.W. Oh, S.H. Park, J.H. Kim, *et al.*, Improvement of electrochemical properties of $LiNi_{0.5}Mn_{1.5}O_4$ spinel material by fluorine substitution, *J. Power Sources*, 157 (2006) 464-470.

[119] M.R. Yang, T.H. Teng, S.H. Wu, $LiFePO_4$/carbon cathode materials prepared by ultrasonic spray pyrolysis, *J. Power Sources*, 159 (2006) 307-311.

[120] S.H. Park, S.W. Oh, S.H. Kang, *et al.*, Comparative study of different crystallographic structure of $LiNi_{0.5}Mn_{1.5}O_{4-\delta}$ cathodes with wide operation voltage (2.0-5.0 V), *Electrochim. Acta*, 52 (2007) 7226-7230.

[121] S.H. Ju, Y.C. Kang, $LiFePO_4$/C cathode powders prepared by spray pyrolysis from the colloidal spray solution containing nano-sized carbon black, *Mater. Chem. Phys.*, 107 (2008) 328-333.

[122] S.M. Oh, S.W. Oh, C.S. Yoon, *et al.*, High-Performance Carbon-$LiMnPO_4$ Nanocomposite Cathode for Lithium Batteries, *Adv. Funct. Mater.*, 20 (2010) 3260-3265.

[123] H. Jang, C. Seong, Y. Suh, *et al.*, Synthesis of lithium-cobalt oxide nanoparticles by flame spray pyrolysis, *Aerosol Sci. Technol.*, 38 (2004) 1027-1032.

[124] S.H. Ng, T.J. Patey, R. Buechel, *et al.*, Flame spray-pyrolyzed vanadium oxide nanoparticles for lithium battery cathodes, *Phys. Chem. Chem. Phys.*, 11 (2009) 3748-3755.

[125] T.J. Patey, R. Büchel, M. Nakayama, *et al.*, Electrochemistry of $LiMn_2O_4$ nanoparticles made by flame spray pyrolysis, *Phys. Chem. Chem. Phys.*, 11 (2009) 3756 -3756

[126] T.J. Patey, R. Buchel, S.H. Ng, *et al.*, Flame co-synthesis of $LiMn_2O_4$ and carbon nanocomposites for high power batteries, *J. Power Sources*, 189 (2009) 149-154.

[127] X. Zhang, H. Zheng, V. Battaglia, *et al.*, Electrochemical performance of spinel $LiMn_2O_4$ cathode materials made by flame-assisted spray technology, *J. Power Sources*, 196 (2011) 3640-3645

[128] X. Zhang, H. Zheng, V.S. Battaglia, *et al.*, Flame synthesis of 5 V spinel-$LiNi_{0.5}Mn_{1.5}O_4$ cathode-materials for lithium-ion rechargeable-batteries, *Proc. Combust. Inst.*, 33 (2011) 1867-1874

[129] J.H. Yi, J.H. Kim, H.Y. Koo, *et al.*, Nanosized $LiMn_2O_4$ powders prepared by flame spray pyrolysis from aqueous solution, *J. Power Sources*, 196 (2011) 2858-2862.

[130] Z.P. Guo, H. Liu, H.K. Liu, *et al.*, Characterization of layered Li[Ni1/3Mn1/3Co1/3]O-2 cathode materials prepared by spray-drying method, *Journal of New Materials for Electrochemical Systems*, 6 (2003) 263-266.

[131] D.C. Li, A. Ito, K. Kobayakawa, *et al.*, Electrochemical characteristics of $LiNi_{0.5}Mn_{1.5}O_4$ prepared by spray drying and post-annealing, *Electrochim. Acta*, 52 (2007) 1919-1924.

[132] A. Ito, D. Li, Y. Lee, *et al.*, Influence of Co substitution for Ni and Mn on the structural and electrochemical characteristics of $LiNi_{0.5}Mn_{1.5}O_4$, *J. Power Sources*, 185 (2008) 1429-1433.

[133] K. Myoujin, M. Kojima, T. Ogihara, *et al.*, Synthesis and characterization of LiNi0.5Mn1.5O4 particle by internal combustion type spray pyrolysis and spray drying, *Transactions of the Materials Research Society of Japan*, 33 (2008) 985-988.

[134] I. Taniguchi, N. Fukuda, M. Konarova, Synthesis of spherical $LiMn_2O_4$ microparticles by a combination of spray pyrolysis and drying method, *Powder Technol.*, 181 (2008) 228-236.

[135] C.H. Chen, A.A.J. Buysman, E.M. Kelder, *et al.*, Fabrication of $LiCoO_2$ Thin-Film Cathodes for Rechargeable Lithium Battery by Electrostatic Spray-Pyrolysis, *Solid State Ionics*, 80 (1995) 1-4.

[136] D.Y. Kim, S.H. Ju, Y.C. Kang, Fine-sized $LiCoO_2$ particles prepared by spray pyrolysis from polymeric precursor solution, *Mater. Res. Bull.*, 42 (2007) 362-370.

[137] T. Ogihara, N. Ogata, S. Yonezawa, *et al.*, Synthesis of porous $LiNiO_2$ powders by ultrasonic spray pyrolysis and their cathode property, *Denki Kagaku*, 66 (1998) 1202-1205.

[138] S.B. Park, W.S. Eom, W.I. Cho, *et al.*, Electrochemical properties of $LiNi_{0.5}Mn_{1.5}O_4$ cathode after Cr doping, *J. Power Sources*, 159 (2006) 679-684.

[139] M. Kojima, I. Mukoyama, K. Myoujin, *et al.*, Mass production and battery properties of $LiNi_{0.5}Mn_{1.5}O_4$ powders prepared by internal combustion type spray pyrolysis, *Key Eng. Mater.*, 388 (2009) 85-88.

[140] S.L. Bewley, K. Konstantinov, G.X. Wang, *et al.*, Conductivity improvements to spray-produced $LiFePO_4$ by addition of a carbon source, *Mater. Lett.*, 58 (2004) 1788-1791.

[141] M. Konarova, I. Taniguchi, Preparation of $LiFePO_4$/C composite powders by ultrasonic spray pyrolysis followed by heat treatment and their electrochemical properties, *Mater. Res. Bull.*, 43 (2008) 3305-3317.

[142] F.O. Ernst, H.K. Kammler, A. Roessler, *et al.*, Electrochemically active flame-made nanosized spinels: $LiMn_2O_4$, $Li4Ti_5O_{12}$ and $LiFe_5O_8$, *Mater. Chem. Phys.*, 101 (2007) 372-378.

[143] T. Tani, L. Madler, S.E. Pratsinis, Homogeneous ZnO nanoparticles by flame spray pyrolysis, *J. Nanopart. Res.*, 4 (2002) 337-343.

[144] W.Y. Teoh, L. Madler, D. Beydoun, *et al.*, Direct (one-step) synthesis of TiO_2 and Pt/TiO_2 nanoparticles for photocatalytic mineralisation of sucrose, *Chem. Eng. Sci.*, 60 (2005) 5852-5861.

[145] H. Schulz, L. Madler, S.E. Pratsinis, *et al.*, Transparent nanocomposites of radiopaque, flame-made Ta_2O_5/SiO_2 particles in an acrylic matrix, *Adv. Funct. Mater.*, 15 (2005) 830-837.

[146] S.-H. Kang, J.B. Goodenough, L.K. Rabenberg, Effect of ball-milling on 3-V capacity of lithium-manganese oxospinel cathodes, *Chem. Mater.*, 13 (2001) 1758-1764.

[147] S.R. Sahaya Prabaharan, M. Siluvai Michael, T. Prem Kumar, *et al.*, Bulk synthesis of submicrometre powders of $LiMn_2O_4$ for secondary lithium batteries, *J. Mater. Chem.*, 5 (1995) 1035-1037.

[148] K. Kanamura, K. Dokko, T. Kaizawa, Synthesis of spinel $LiMn_2O_4$ by a hydrothermal process in supercritical water with heat-treatment, *J. Electrochem. Soc.*, 152 (2005) A391-A395.

[149] Y.-K. Sun, I.-H. Oh, K.Y. Kim, Synthesis of spinel $LiMn_2O_4$ by the sol-gel method for a cathode-active material in lithium secondary batteries, *Ind. Eng. Chem. Res.*, 36 (1997) 4839-4846.

[150] S. Komaba, N. Kumagai, M. Baba, *et al.*, Preparation of Li-Mn-O thin films by r.f.-sputtering method and its application to rechargeable batteries, *J. Appl. Electrochem.*, 30 (2000) 1179-1182.

[151] N. Treuil, C. Labrugere, M. Menetrier, *et al.*, Relationship between chemical bonding nature and electrochemical property of $LiMn_2O_4$ spinel oxides with various particle sizes: "Electrochemical Grafting" concept, *J. Phys. Chem. B*, 103 (1999) 2100-2106.

[152] A.A. Van Zomeren, E.M. Kelder, J.C.M. Marijnissen, *et al.*, The production of thin films of $LiMn_2O_4$ by electrospraying, *J. Aerosol Sci.*, 25 (1994) 1229-1235.

[153] C. Wan, Y. Nuli, Q. Wu, *et al.*, Submicro-sized $LiMn_2O_4$ prepared by a sol-gel, spray-drying method, *J. Appl. Electrochem.*, 33 (2003) 107-112.

[154] J.P. Tu, H.M. Wu, Y.Z. Yang, *et al.*, Spray-drying technology for the synthesis of nanosized $LiMn_2O_4$ cathode material, *Mater. Lett.*, 61 (2007) 864-867.

[155] K. Myojin, T. Ogihara, N. Ogata, *et al.*, Synthesis of non-stoichiometric lithium manganate fine powders by internal combustion-type spray pyrolysis using gas burner, *Adv. Powder Technol.*, 15 (2004) 397-403.

[156] R.L. Vander Wal, T.M. Ticich, Flame and furnace synthesis of single-walled and multi-walled carbon nanotubes and nanofibers, *J. Phys. Chem. B*, 105 (2001) 10249-10256.

[157] H.K. Kammler, L. Mädler, S.E. Pratsinis, Flame synthesis of nanoparticles, *Chem. Eng. Technol.*, 24 (2001) 583 - 596.

[158] W.J. Stark, S.E. Pratsinis, Aerosol flame reactors for manufacture of nanoparticles, *Powder Technol.*, 126 (2002) 103-108.

[159] G.P. Fotou, S.J. Scott, S.E. Pratsinis, The role of ferrocene in flame synthesis of silica, *Combust. Flame*, 101 (1995) 529-538.

[160] X. Qin, Y. Ju, S. Bernhard*, et al.*, Flame synthesis of Y_2O_3:Eu nanophosphors using ethanol as precursor solvents *J. Mater. Res.*, 20 (2005) 2960-2968.

[161] D.P. Dufaux, R.L. Axelbaum, Nanoscale unagglomerated nonoxide particles from a sodium coflow flame, *Combust. Flame*, 100 (1995) 350-358.

[162] R.L. Axelbaum, D.P. DuFaux, C.A. Frey*, et al.*, Gas-phase combustion synthesis of titanium boride (TiB_2) nanocrystallites, *J. Mater. Res.*, 11 (1996) 948-954.

[163] J.L. Barr, R.L. Axelbaum, M.E. Macias, Processing salt-encapsulated tantalum nanoparticles for high purity, ultra high surface area applications, *J. Nanopart. Res.*, 8 (2006) 11-22.

[164] R.L. Axelbaum, C.R. Lottes, J.I. Huertas*, et al.*, Gas-phase combustion synthesis of aluminum nitride powder, *Proc. Combust. Inst.*, 26 (1996) 1891-1897.

[165] Z. Wu, X. Dong, W. Jin*, et al.*, A dense oxygen separation membrane deriving from nanosized mixed conducting oxide, *J. Membr. Sci.*, 291 (2007) 172-179

[166] L. Forni, I. Rossetti, Catalytic combustion of hydrocarbons over perovskites, *Appl. Catal., B*, 38 (2002) 29-37.

[167] G.L. Chiarello, I. Rossetti, L. Forni, Flame-spray pyrolysis preparation of perovskites for methane catalytic combustion, *J. Catal.*, 236 (2005) 251-261.

[168] K.H. Stern, High temperature properties and thermal decomposition of inorganic salts with oxyanions, CRC Press, 2000.

[169] N. Kumagai, T. Saito, S. Komaba, Synthesis of ternary Li-Mn-O phase at a temperature of 260 degrees C and electrochemical lithium insertion into the oxide, *J. Appl. Electrochem.*, 30 (2000) 159-163.

[170] A. Yamada, K. Miura, K. Hinokuma*, et al.*, Synthesis and structural aspects of $LiMn_2O_{4\pm\delta}$ as a cathode for rechargeable lithium batteries, *J. Electrochem. Soc.*, 142 (1995) 2149-2156.

[171] J.Y. Lee, Y. Hideshima, Y.-K. Sun*, et al.*, The effects of lithium and oxygen contents inducing capacity loss of the $LiMn_2O_4$ obtained at high synthetic temperature, *J. Electroceram.*, 9 (2002) 209-214.

[172] C.-Z. Lu, G.T.-K. Fey, Nanocrystalline and long cycling $LiMn_2O_4$ cathode material derived by a solution combustion method for lithium ion batteries, *J. Phys. Chem. Solids*, 67 (2006) 756-761

[173] J.M. Tarascon, D. Guyomard, The $Li_{1+X}Mn_2O_4$/C rocking-chair System: a review, *Electrochim. Acta*, 38 (1993) 1221-1231.

[174] G. Liu, H. Ikuta, T. Uchida*, et al.*, The spinel phases LiMyMn2-yO4(M=Co,Cr,Ni) as the cathode for rechargeable lithium batteries, *J. Electrochem. Soc.*, 143 (1996) 178-182.

[175] N. Amdouni, K. Zaghib, F. Gendron*, et al.*, Structure and insertion properties of disordered and ordered $LiNi_{0.5}Mn_{1.5}O_4$ spinels prepared by wet chemistry, *Ionics*, 12 (2006) 117-126.

[176] J.H. Kim, S.T. Myung, Y.K. Sun, Molten salt synthesis of $LiNi_{0.5}Mn_{1.5}O_4$ spinel for 5 V class cathode material of Li-ion secondary battery, *Electrochim. Acta*, 49 (2004) 219-227.

[177] M. Kunduraci, J.F. Al-Sharab, J.M. Amarilla, High-Power Nanostructured $LiMn_{2-x}Ni_xO_4$ High-Voltage Lithium-Ion Battery Electrode Materials: Electrochemical Impact of Electronic Conductivity and Morphology, *Chem. Mater.*, 18 (2006) 3585–3592.

[178] A. Caballero, M. Cruz, L. Hernán*, et al.*, Nanocrystalline materials obtained by using a simple, rapid method for rechargeable lithium batteries., *J. Power Sources*, 150 (2005) 192-201.

[179] Z.H. Lu, D.D. MacNeil, J.R. Dahn, Layered Cathode Materials $Li[Ni_xLi_{(1/3-2x/3)}Mn_{(2/3-x/3)}]O_2$ for Lithium-Ion Batteries, *Electrochem. Solid-State Lett.*, 4 (2001) A191-A194.

[180] Z.H. Lu, L.Y. Beaulieu, R.A. Donaberger*, et al.*, Synthesis, Structure, and Electrochemical Behavior of $Li[Ni_xLi_{1/3-2x/3}Mn_{2/3-x/3}]O_2$, *J. Electrochem. Soc.*, 149 (2002) A778-A791.

[181] S.S. Shin, Y.K. Sun, K. Amine, Synthesis and Electrochemical Properties of $Li[Li_{(1-2x)/3}Ni_xMn_{(2-x)/3}]O_2$ as Cathode Materials for Lithium Secondary Batteries, *J. Power Sources*, 112 (2002) 634-638.

[182] S.H. Kang, Y.K. Sun, K. Amine, Electrochemical and ex situ X-ray study of $Li(Li_{0.2}Ni_{0.2}Mn_{0.6})O_2$ cathode material for Li secondary batteries, *Electrochem. Solid-State Lett.*, 6 (2003) A183-A186.

[183] M.M. Thackeray, S.H. Kang, C.S. Johnson*, et al.*, Li_2MnO_3-stabilized $LiMO_2$ (M = Mn, Ni, Co) electrodes for lithium-ion batteries, *J. Mater. Chem.*, 17 (2007) 3112-3125.

[184] S.H. Kang, C.S. Johnson, J.T. Vaughey*, et al.*, The effects of acid treatment on the electrochemical properties of $0.5Li_2MnO_3 \cdot 0.5\ LiNi_{0.44}Co_{0.25}Mn_{0.31}O_2$ electrodes in lithium cells, *J. Electrochem. Soc.*, 153 (2006) A1186-A1192.

[185] S.H. Kang, M.M. Thackeray, Enhancing the rate capability of high capacity $xLi_2MnO_3 \cdot (1-x)LiMO_2$ (M = Mn, Ni, Co) electrodes by Li-Ni-PO_4 treatment, *Electrochem. Commun.*, 11 (2009) 748-751.

[186] H.F. Wang, Y.I. Jang, B.Y. Huang*, et al.*, TEM study of electrochemical cycling-induced damage and disorder in $LiCoO_2$ cathodes for rechargeable lithium batteries, *J. Electrochem. Soc.*, 146 (1999) 473-480.

[187] C.S. Johnson, J.S. Kim, A.J. Kropf, *et al.*, The Role of Li_2MO_2 Structures (M=Metal Ion) in the Electrochemistry of $(x)LiMn_{0.5}Ni_{0.5}O_2 \cdot (1-x)Li_2TiO_3$ Electrodes for Lithium-Ion Batteries, *Electrochem. Commun.*, 4 (2002) 492-498.

[188] M.M. Thackeray, C.S. Johnson, J.T. Vaughey, *et al.*, Advances in manganese-oxide 'composite' electrodes for lithium-ion batteries, *J. Mater. Chem.*, 15 (2005) 2257-2267.

[189] Y.S. Meng, G. Ceder, C.P. Grey, *et al.*, Cation Ordering in Layered O_3 $Li[Ni_xLi_{1/3-2x/3}Mn_{2/3-x/3}]O_2$ ($0 \leqslant x \leqslant 1/2$) Compounds, *Chem. Mater.*, 17 (2005) 2386-2394.

[190] C.S. Johnson, N.C. Li, C. Lefief, *et al.*, Anomalous capacity and cycling stability of $xLi_2MnO_3 \cdot (1-x)LiMO_2$ electrodes (M= Mn, Ni, Co) in lithium batteries at 50 ˚C, *Electrochem. Commun.*, 9 (2007) 787-795.

[191] S.H. Park, S.H. Kang, C.S. Johnson, *et al.*, Lithium-manganese-nickel-oxide electrodes with integrated layered-spinel structures for lithium batteries, *Electrochem. Commun.*, 9 (2007) 262-268.

[192] L. Dupont, M. Hervieu, G. Rousse, *et al.*, TEM studies: The key for understanding the origin of the 3.3 V and 4.5 V steps observed in $LiMn_2O_4$-based spinels, *J. Solid State Chem.*, 155 (2000) 394-408.

[193] J. Cabana, S.H. Kang, C.S. Johnson, *et al.*, Structural and Electrochemical Characterization of Composite Layered-Spinel Electrodes Containing Ni and Mn for Li-Ion Batteries, *J. Electrochem. Soc.*, 156 (2009) A730-A736.

[194] Z.H. Lu, D.D. MacNeil, J.R. Dahn, Layered $Li[Ni_xCo_{1-2x}Mn_x]O_2$ Cathode Materials for Lithium-Ion Batteries, *Electrochem. Solid-State Lett.*, 4 (2001) A200-A203.

[195] M.A. Mohamed, S.A. Halawy, Kinetic and Mechanistic Study of the Nonisothermal Decomposition of Manganese(II) Acetate Tetrahydrate, *Thermochimica Acta*, 242 (1994) 173-186.

[196] Y.S. Lee, Y.K. Sun, K.S. Nahm, Synthesis and characterization of $LiNiO_2$ cathode material prepared by an adiphic acid-assisted sol-gel method for lithium secondary batteries, *Solid State Ionics*, 118 (1999) 159-168.

Vitae

Xiaofeng Zhang

Date of Birth 10/22/1980

Place of Birth Harbin, China

Education Ph.D. Energy, Environmental and Chemical Engineering, Washington University in St. Louis, St. Louis, MO, August 2011

M.S. Nuclear Science, Tsinghua University, Beijing, June 2006

B.S. Environmental Science and Engineering, Tsinghua University, Beijing, June 2003

Honors The Battery Division Student Travel Award, the 218th ECE meeting, The Electrochemical Society, Las Vegas, NV, 2010

Student Travel Grant, the 33rd International Symposium on Combustion, Beijing, China, 2010

Student Poster Competition Winner, 28th Annual Conference, AAAR, Minneapolis, MN, 2009

Charles & Marlene Buescher Scholarship, Washington University in St. Louis, St. Louis, MO, 2006

Excellent Master Thesis Award, Tsinghua University, Beijing, China, 2006

Volunteer Excellence Award, Tsinghua University, Beijing, China, 2001

Societies The American Association for Aerosol Research

The Combustion Institute

The Electrochemical Society

Publications Xiaofeng Zhang, Richard L. Axelbaum, Spray Pyrolysis Synthesis of Mesoporous Lithium-Nickel-Manganese-Oxides for High Energy Li-Ion Batteries, *Journal of the Electrochemical Society*, 2011 (Submitted)

Xiaofeng Zhang**,** Honghe Zheng, Vincent S. Battaglia, Richard. L. Axelbaum, Electrochemical Performance of Spinel $LiMn_2O_4$ Cathode Material Made by Flame-Assisted Spray Technology, *Journal of Power Source,* 2011, 196(7): 3640-3645

Xiaofeng Zhang**,** Honghe Zheng, Vincent S. Battaglia, Richard. L. Axelbaum, Flame Synthesis of 5 V Spinel $LiNi_{0.5}Mn_{1.5}O_4$ Cathode Materials for Lithium-Ion Rechargeable-Batteries, *Proceedings of the Combustion Institute*, 2011, 33(2): 1867-1874

Suyuan Yu, Xiaoli Yu, Xiaoyong Yang, Jie Wang, Ping Ye, Xiaofeng Zhang, Experimental Research on Synthesis of Multi-walled Carbon Nanotubes by

Methane-air Controlled Diffusing Flame, *Journal of Thermal Science and Technology*, 2007, 6(4)

Xiaofeng Zhang, Xiaoyong Yang, Suyuan Yu, Experimental Research on Synthesis of Carbon Nanotubes, *Journal of Engineering Thermophysics*, 2006, 27(2): 357-359

Patent Applications

Xiaofeng Zhang, Richard L. Axelbaum, High-Energy Cathode Materials Synthesized Using Spray Technology, 2011 (licensed to Xtend Energy, LLC, MO)

Xiaofeng Zhang, Richard L. Axelbaum, Synthesis of Nanostructured Cathode Materials for Lithium-Ion Secondary Batteries Using a Flame-Assisted Spray Technology (Serial No. PCT/US2011/46333)

Presentations

Xiaofeng Zhang, Richard. L. Axelbaum, High-Energy $Li_{(1+x)}Mn_{0.75}Ni_{0.25}O_{(2.25+x/2)}$ ($3/8 \leqslant x \leqslant 1/2$) Positive Electrodes with Integrated Layered-Spinel Structures Made from Spray Pyrolysis, 219th ECS meeting, Vancouver, Canada, 2011

Xiaofeng, Zhang, Richard. L. Axelbaum, A Comparative Study of Low- and High-Temperature Synthesis of 5 V Cathode Materials, 218th ECS meeting, Las Vegas, US, 2010

Xiaofeng Zhang, Honghe Zheng, Vincent S. Battaglia, Richard. L. Axelbaum, Flame Synthesis of 5 V Spinel $LiNi_{0.5}Mn_{1.5}O_4$ Cathode Materials for Lithium-Ion Rechargeable-Batteries, 33rd International Symposium on Combustion, Beijing, China, 2010

Xiaofeng Zhang, Richard. L. Axelbaum, Honghe Zheng, Vincent S. Battaglia, Electrochemical Performance of Spinel $LiMn_2O_4$ Produced in a Two-Stage Flow Reactor, 217th ECS meeting, Vancouver, Canada, 2010

Xiaofeng Zhang, Richard L. Axelbaum, Flame Synthesis of Spinel $LiMn_2O_4$ Cathodic Material for Lithium Ion Batteries, *The 6th U.S. National Combustion Meeting*, Ann Arbor, MI, US, May 2009

August 2011